
THE UNIVERSITY
*of* EDINBURGH

# Improving *the* Understanding *of* Fundamental Mechanisms that Influence Ignition *and* Burning Behavior *of* Porous Wildland Fuel Beds

by

Jan Christian Thomas

Doctor *of* Philosophy


The University *of* Edinburgh

2016

# Improving *the* Understanding *of* Fundamental Mechanisms that Influence Ignition *and* Burning Behavior *of* Porous Wildland Fuel Beds

by

Jan Christian Thomas

The thesis has been supervised by

Dr. Albert Simeoni

and

Dr. Rory Hadden

The examining committee consisted of

Dr. Eulàlia Planas

and

Dr. Stephen Welsh

**Declaration**

The thesis and work described within has been completed solely by Jan Christian Thomas at the Fire Laboratory of the Worcester Polytechnic Institute and the BRE Centre for Fire Safety Engineering of the University of Edinburgh, under the supervision of Dr. Albert Simeoni and Dr. Rory Hadden. Full reference is given where other sources are used. This work has not been submitted for any other degree or professional qualification.

Jan Christian Thomas

2016

*I dedicate this work to my parents, Angela and Ludger,*

*who have given me so much love and support to allow me pursue my dreams.*

*To my siblings, Christina, Alexander, Johannes and Maximilian,*

*without whom I wouldn't be the person I am today.*

**Abstract**

The phenomenon of a fire occurring in nature comes with a very high level of complexity. One central obstacle is the range of scales in such fires. In order to understand wildfires, research has to be conducted across these scales in order to study the mechanisms which drive wildfire behavior. The hazard related to such fires is ever more increasing as the living space of communities continues to increase and infringe with the wildland at the wildland-urban interface. In order to do so, a strong understanding on the possible wildfire behavior that may occur is critical.

An array of factors impact wildfire behavior, which are generally categorized into three groups: (1) fuel (type, moisture content, loading, structure, continuity); (2) environmental (wind, temperature, relative humidity, precipitation); and (3) topography (slope, aspect). The complexity and coupling of factors impacting various scales of wildfire behavior has been the focus of much experimental and numerical work over the past decades. More recently, the need to quantify wildland fuel flammability and use the knowledge in mitigating risks, for example by categorizing vegetation according to their flammability has been recognized. Fuel flammability is an integral part of understanding wildfire behavior, since it can provide a quantification of the ignition and burning behavior of wildland fuel beds.

Determining flammability parameters for vegetative fuels is however not a straight forward task and a rigorous standardized methodology has yet to be established. It is the intent of this work to aid in the path of finding a most suitable methodology to test vegetative fuel flammability. This is achieved by elucidating the fundamental heat and mass transfer mechanisms that drive ignition and burning behavior of porous wildland fuel beds.

The work presented herein is a continuation of vegetative fuel flammability research using bench-scale calorimetry (the FM Global Fire Propagation Apparatus). This apparatus allows a high level of control of critical parameters. Experimental studies investigate how varying external heat flux (radiative), ventilation conditions (forced

airflow rate, oxygen concentration, and temperature), and moisture content affect the ignition and burning behavior of wildland fuel.

Two distinct ignition regimes were observed for radiative heating with forced convection cooling: (1) convection/radiation for low heating rates; and (2) radiation only for high heating rates. The threshold for the given convection conditions was near 45 $kW.m^{-2}$.

For forced convection, ignition behavior is dominated by convection cooling in comparison to dilution; ignition times were constant when the oxygen flow rate was varied (constant flow magnitude). Analysis of a radiative Biot number including heat losses (convection and radiation) indicated that the pine needles tested behaved thermally thin for the given heating rates (up to 60 $kW.m^{-2}$). A simplified one-dimensional, multi-phase heat transfer model for porous media is validated with experimental results (in-depth temperature measurements, critical heat flux and ignition time). The model performance was adequate for two species only, when the convective Froude number is less than 1.0 (only one packing ratio was tested).

Increasing air flow rates resulted in higher heat of combustion due to increased pyrolysis rates. In the given experiments (ventilation controlled environment) combustion efficiency decreased with increasing $O_2$ flow rates. Flaming combustion of pine needles in such environments resulted in four times greater CO generation rates compared to post flaming smoldering combustion.

A link was made to live fuel flammability that is important for understanding the occurrence of extreme fire conditions such as crowning and to test if live fuel flammability contributes to the occurrence of a typical fire season. Significant seasonal variations were observed for the ignition and burning behavior of conditioned live pine needles. Variation and peak flammability due to ignition time and heat release rate can be associated to the growing season (physical properties and chemical composition of the needles).

Seasonal trends were masked when unconditioned needles were tested as the release of water dominated effects. For wet fuel, ignition time increases linearly with fuel moisture content (FMC, $R^2 = 0.93$). The peak heat release rate decreased non-linearly with FMC ($R^2 = 0.77$). It was determined that above a threshold of 60% FMC (d.w.), seasonal variation in the heat release rate can be neglected.

A novel live fuel flammability assessment to evaluate the seasonality of ignition and burning behavior is proposed. For the given case (NJ Pine Barrens, USA), the flammability assessment indicated that the live fuel is most flammable in August. Such assessment can provide a framework for a live fuel flammability classification system that is based on rigorous experimentation in well controlled fire environments.

## Lay Summary

Wildland fires are a global problem affecting millions of people around the world. This is also a natural phenomenon because some ecosystems have adopted fire in order to sustain their habitat. The phenomenon of a fire occurring in nature comes with a very high level of complexity that is impossible to untangle all at once. One central obstacle is the vast scale of such fires. In order to understand wildfires, research has to be conducted on various scales in order to study particular mechanisms that drive their wildfire behavior. The need to adequately protect the wildland-urban interface is paramount for land managers and authorities having jurisdiction. In order to do so, a strong understanding on the possible wildfire behavior that may occur is critical. A part of this understanding is knowledge of how vegetative fuel burns – how well does it ignite and how intense does it burn. The ignition and burning characteristics (flammability) of dead and live fuel is impacted by external factors, such as wind and moisture content. These factors are also very dynamic, and therefore indicate that the flammability is not a static parameter. The work presented in this thesis (experimental and theoretical) aims to help in understanding the fundamental mechanisms that drive the ignition and burning behavior of wildland fuel. By understanding the processes at a small scale, better predictions of the risks associated with wildfires can be undertaken.

**Selected Publications and Refereed Proceedings**

Simeoni A., Thomas J.C., Bartoli P., Borowieck P., Reszka P., Colella F., Santoni P.A., and Torero J.L., (2012) Flammability Studies for Wildland and Wildland–Urban Interface Fires Applied to Pine Needles and Solid Polymers, *Fire Safety Journal* 54: 203-217.

Thomas J.C., Everett J. N., Simeoni A., Skowronski N., and Torero J.L. "Flammability Study of Pine Needle Beds," *Proceedings of the 7th International Seminar on Fire and Explosion Hazards*, Providence, RI, USA, (2013).

Thomas J.C., Simeoni A., Gallagher M., and Skowronski N.S. "An Experimental Study Evaluating the Burning Dynamics of Pitch Pine Needle Beds Using the FPA," *Proceedings of the 11th International Symposium on Fire Safety Science*. Christchurch, New Zealand, (2014) pp. 1406-1419.

Lamorlette A., El Houssami M., Thomas J.C., Simeoni A., and Morvan D. (2015) A Dimensional Analysis of Forest Fuel Layer Ignition Model: Application to the Ignition of Pine Needle Litters. *Journal of Fire Science* 33: 320-335.

El Houssami M., Thomas J.C., Lamorlette A., Morvan D., Chaos M., Hadden R., and Simeoni A. (2016) Experimental and Numerical Studies Characterizing the Burning Dynamics of Wildland Fuels. *Combustion and Flames* 168: 113-126.

Thomas J.C., Hadden R.M., Simeoni A. "Experimental Investigation of the Impact of Oxygen Flux on the Burning Dynamics of Forest Fuel Beds." *Proceedings of the 12th International Symposium on Fire Safety Science*. Lund, Sweden, (2017). (accepted)

**Acknowledgements**

First and foremost, I would like to thank my advisors Dr. Albert Simeoni and Dr. Rory Hadden for their superb guidance and mentoring. Thank you Albert for finding me in WPI's lab and giving me the opportunity to do initial research during my Masters, which lead to this thesis. I sincerely enjoyed our relationship during this journey, including the many hours spent in your office, the lab, the pub, or on the road discussing science (foremost fire of course), politics, humanity, history and the world; your knowledge truly has no boundaries. Thank you Rory for the countless hours of discussions and guiding me through this journey. Thanks also for showing me the perfect Old Fashion!

I would like to thank Eric Mueller and Dr. Mohamad El Houssami, who have been with me through this entire journey. We were a great team and our time spend together was truly paramount to making this journey memorable, worthy and as best as it could be. Thank you for walking this path with me.

A big thank you goes to Dr. Kenneth Clark, Dr. Nicholas Skowronski and Michael Gallagher, who were always ready to answer any Ecology questions I had. Thank you also for tedious task of collecting and sending me pine needles to Edinburgh and making sure they are chilled well enough. I will never forget the hours spent together at the field station, preparing equipment, talking about wildfire, discussing the weather ("when do you think we will burn?") and enjoying one or two cold ones. Mayo's … nuff said!

Thank you to all my friends and colleagues in Edinburgh's Fire Group who have welcomed me with open arms. Special thanks go to Dr. Juan Hidalgo, Dr. Martyn McLaggen and Michal Krajcovic who helped me get settled in the lab, taught me the ways of the FPA and always had a helping hand in the fire lab. Thank you Juan for being a great flat mate! It is truly special to be part of this phenomenal group of friends.

I would also like to thank my friends and colleagues at the WPI Fire Group, with whom I was able to work in the first part of my journey. Special thanks go to Randy Harris, Dr. Kathy Notarianni, and Dr. Nicholas Dembsey. My interest for fire dynamics was raised significantly in Nick's course, which made me want to work in the lab (since there was no lab course at the time). Thank you Kathy and Randy for providing me the opportunity to work in the lab, which eventually led to me meeting Albert. Thank you Randy for teaching me proper lab etiquette, techniques, methodologies and how to set things on fire safely.

I would like to thank FM Global and the US Fire Service for their financial support.

Special thanks also to Dr. Marcos Chaos at FM Global for numerous discussions about flammability testing, the FPA, and everything fire.

I'm grateful to have met my friends Ryan Thomann and John Desrosier during my undergraduate years, without whom I would not have found my way into the Fire Protection Engineering discipline. Thank you for being such great friends and brothers … In Τ.Κ.Φ.

To all my dear friends (USA, Scotland, Germany and elsewhere) who have endured this journey with me, thank you for support.

Finally, thank you to my parents and family, who have always encouraged me to go as far as I can go and never stopped supporting me. I love you all.

Thank you.

## Content

**List of Figures**

**List of Tables**

*This page is intentionally left blank.*

## Abbreviations and Nomenclature

| | |
|---|---|
| A | sample cross-section area [$cm^{-2}$] |
| a | surface absorptivity [-] |
| All | OG and NG tests |
| ASTM | ASTM International |
| Avg. | mean |
| B | Stefan-Boltzmann constant [$W.m^{-2}.K^{-4}$] |
| Bi | Biot number |
| C | empirical coefficient for correlation [-] |
| $C_B$ | Babrauskas correction factor [-] |
| $c_p$ | specific heat [$kJ.kg^{-1}.K^{-1}$] |
| $C_T$ | Thomas correction factor [-] |
| CACC | Controlled Atmosphere Cone Calorimeter |
| CDG | carbon dioxide generation calorimetry |
| closed | closed sample basket (0% perforation, open only at top side) |
| cond. | fully dehydrated |
| d | diameter or side of needle [mm] |
| D | sample basket diameter [cm] |
| d.w. | dry weight |
| Dead | brown/yellow needles |
| Drierite | drying agent (desiccant) |
| DSC | Differential Scanning Calorimetry |
| E | energy constant [$kJ.g^{-1}$] |
| EDI | University of Edinburgh |
| EMC | equilibrium moisture content [% d.w.] |
| F | flammability parameter/factor or forced convection [-] |
| FMC | fuel moisture content (dry weight basis) [% d.w.] |
| Fo | Fourier number |
| FPA | FM Global Fire Propagation Apparatus |
| Fr | convective Froude number |
| g | gravitational acceleration [$m.s^{-2}$] |
| Gr | Grashof number |
| H | sample thickness [cm] |
| h | heat transfer coefficient [$W.m^{-2}.K^{-1}$] |
| $H_c$ | heat of combustion [$kJ.kg^{-1}$] |
| $H_{vap}$ | heat of vaporization (water) [$kJ.kg^{-1}$] |

| | |
|---|---|
| HF | high flow, forced convection |
| HHF | extra high flow, forced convection |
| I | irradiance [$kW.m^{-2}$] |
| $I_B$ | Byram's fireline intensity [$kW.m^{-1}$] |
| IR lamp | infrared heating unit |
| K | radiation extinction coefficient or permeability [$m^{-1}$] or [$m^2$] |
| k | thermal conductivity [$W.m^{-1}.K^{-1}$] |
| $k_R$ | Rosseland approximation [$W.m^{-1}.K^{-1}$] |
| L | characteristic length [m] |
| LF | low flow, forced convection |
| LFL | lower flammability limit |
| Live | green needles |
| LOC | limiting oxygen concentration |
| m | mass [g] |
| M | molar mass [$kg.mol^{-1}$] |
| N | number of data points/tests |
| NDVI | Normalized Difference Vegetation Index |
| NF | no flow, natural convection |
| NG | new generation needle |
| NJ | New Jersey, USA |
| NT | no tube |
| Nu | Nusselt number |
| OC | oxygen consumption calorimetry |
| OG | old generation needles |
| open | open sample basket (63% perforation) |
| P | pressure [bar] |
| pHRR | peak heat release rate [kW] |
| PIV | particle image velocimetry |
| PMMA | Poly methyl methacrylate |
| Pr | Prendtl number |
| PR | Pinus resinosa, Red pine |
| PRI | *Pinus rigida*, Pitch pine |
| PS | Pinus strobus, White pine |
| PW | Pickard and Wraight correlation |
| q | heat flux (pHRR from sample or heat flux from FPA lamps) [$kW.m^{-2}$] |
| R | rate of spread, therm. resistance or univ. gas const. [$m.s^{-1}$], [$K.W^{-1}$], or [$J.mol^{-1}.K^{-1}$] |
| $R^2$ | coefficient of determination |

| | |
|---|---|
| Ra | Rayleigh number |
| Re | Reynold number |
| $Re_{porous}$ | Reynold number for porous medium (packed bed) |
| S | surface area [$m^2$] |
| SD | spring dip |
| St. Dev. | standard deviation |
| SVR | surface area-to-volume ratio [$m^{-1}$] |
| t | time [s] |
| T | temperature, thickness of needle, or tube [°C or K], [mm] |
| Tube | quartz tube |
| uncond. | natural state (no drying) |
| v | Velocity [$m.s^{-1}$] |
| V | volume or velocity [$m^3$] or [$m.s^{-1}$] |
| VBA | Visual Basic for Applications |
| VOC | volatile organic compound |
| w | mass fraction [$g.g^{-1}$] |
| WPI | Worcester Polytechnic Institute |
| X | molar fraction [$mol.mol^{-1}$] |
| x or z | coordinates |
| $y_{O2}$ | oxygen volume fraction [%] |

Greek

| | |
|---|---|
| $\alpha$ | thermal diffusivity or volume fraction [$m^2.s^{-1}$] or [$m^3.m^{-3}$] |
| $\beta$ | thermal expansion factor [-] |
| $\Delta$ | differential |
| $\delta$ | thermal or radiation penetration depth [mm] |
| $\varepsilon$ | Emissivity [-] |
| $\theta$ | temperature differential |
| $\mu$ | dynamic viscosity [$kg.m^{-1}.s^{-1}$] |
| $\rho$ | Density [$kg.m^{-3}$] |
| $\sigma$ | SVR |
| $\tau$ | thermal time constant [s] |
| $\Phi$ | oxygen depletion factor or equivalence ratio [-] |
| $\chi$ | combustion efficiency [-] |

| Subscripts | |
|---|---|
| all | OG and NG |
| c | convective |
| comb | combustibility |
| cond | conduction |
| conv | convection |
| density, ρ | evaluated at density |
| dry | conditioned |
| equiv or eq | equivalent mass |
| exp or ex | experimental |
| ext | external heat flux from the FPA lamps |
| f | forced convection |
| flames | refers to flames above fuel |
| FMC | evaluated at FMC |
| g or ∞ | gas phase or ambient |
| i | induction time |
| ign or ig | ignition, ignitibility |
| L | refers to evaluation at characteristic length |
| lamps | refers to FPA heating lamps |
| liquid | refers to liquid |
| m | mixing time |
| max | maximum |
| min | minimum |
| month | refers to the month of test |
| N | natural convection |
| needle | refers to needle |
| ng | New generation needle |
| norm | normalized |
| OC | refers to oxygen consumption calorimetry |
| og | old generation needle |
| p | pyrolysis time |
| piloted | piloted ignition |
| PW | Pickard and Wraight correlation |
| r | radiative |
| rad | radiation |
| rad,losses | radiative heating with convective and reradiative losses |
| s | solid phase |

| | |
|---|---|
| sample | refers to sample |
| smoldering | smoldering ignition (time when transition to flaming) |
| spontaneous | spontaneous ignition |
| T | total |
| theory or th | theoretical |
| total | either (og + ng) or (ign + comb) |
| total | refers to measurement |
| wet | unconditioned |
| zero (0) | initial, or dry |

Superscript

| | |
|---|---|
| (·) | per second |
| (*) | bulk density, normalized temperature or corrected model (PW) |
| (') | per unit length |
| (") | per unit area |
| (0) | ambient |

*This page is intentionally left blank.*

# Chapter 1

*Introduction*

## *1.1. Motivation*

### *1.1.1. The wildfire problem*

The understanding of the fundamental mechanisms of fire spread and the dynamics of combustion is not only critical in the built environment, but just as much in the natural environment, i.e. the wildland environment. With the extension of the wildland-urban interface (WUI), communities experience increasing danger from wildfires [1.1-1.3]. This danger must be mitigated to the extent that a safe living space for humans is granted. Economic and ecologic objectives are critical and drive the process of creating a safe environment. These objectives deal with land management issues, such as fire prevention and firefighting and are limited by monetary means, personnel and the knowledge about the ecosystems and physical phenomena.

On the one hand, it must be determined how much money can be spent on, for example fire prevention, i.e. clearing out dead and live matter to reduce the fuel loading. On the other hand, it must be carefully studied what the effects of removing fuels from an ecosystem are. This is commonly done by mechanical removal or prescribed burning [1.4, 1.5]. Prescribed burning does not only remove dead material, but also live vegetation. The balance of how much human interaction in the ecosystem warrants a small enough impact on flora and fauna, but still reduces the danger from a fire to society, must be evaluated.

Furthermore, spending of resources on firefighting is the most prevailing means to provide a level of safety for communities in the WUI. Extinguishing fires can have adverse effects, for example allowing the buildup of dead vegetation that would be otherwise consumed in a natural wildfire [1.5, 1.6].

It becomes evident, that researchers from many disciplines must get together and study various aspects of the wildfire problem. These fields range from socio-economics, to policy making, to ecology, to physics and engineering [1.7]. Fire dynamics is one field

that is essential in tackling the monumental task of understanding the wildfire problem. Knowledge of fire chemistry, material science, fluid and thermodynamics and heat transfer can be applied to study the fundamental mechanisms which drive wildfire behavior. The work presented in this thesis falls into this field. The primarily focuses are on the flammability of vegetative fuel beds and how it is impacted by external factors, such as wind and fuel moisture content.

### *1.1.2. The challenges*

The phenomenon of a fire occurring in nature comes with a very high level of complexity that is impossible to untangle at once. A wildfire always has an initial ignition point, intentional or accidental, from which it starts to develop. If conditions permit, it can grow into a blaze encompassing thousands of square kilometers. It is not only the scale and the influence of the external parameters that make this phenomenon so complex, but also the nature, and structure of the fuel. Vegetative fuels vary widely in size and chemical composition. Live foliage chemical composition may even vary over time (season), because they are living organisms that have a natural metabolism governed by soil and climate conditions, as well as plant health and physiological processes.

For modeling purposes, vegetative fuels are considered porous fuel packages [1.8-1.17], because in most cases it is not feasible to model wildfire at small enough resolution. Heterogeneity of the particle distribution and the bulk properties of the vegetation layer, play a major role in the burning dynamics of wildland fuels, for example in the consideration of the dominant modes of heat transfer.

The wildfire problem can be approached at different scales. On a micro scale, the combustion of fuel particles is related to their chemical composition [1.18-1.22]. On this scale, detailed reaction kinetics is analyzed. Results provide constants for kinetic reactions, such as activation energy, which can then be used as input parameters in larger scale physical models that are used for wildfire spread models. Investigation in

ignition behavior and flammability ranking can also be performed as was illustrated by [1.19, 1.20]. Challenges here are that structural integrity (physical properties) of the fuel is lost by homogenizing (grinding) it.

A large number of bench-scale studies investigate the flammability of foliage in either stationary fires [1.23-1.51] or burning behavior of spreading fires [1.52-1.60] under a broad spectrum of parameters. These studies focus on variability in flammability between species (classification) or understanding fundamental heat and mass transfer mechanisms in porous fuel beds and what factors have significant impacts on them.

Fire spread studies continue on into medium to larger scales (large bench or field scale) [1.61-1.74]. In these scales, fundamental mechanisms are also the main focus, with attention to various fire phenomena, such as fire spread, fire intensity, crowning potential, firebrand generation and extreme fire behavior (e.g. fire eruptions). Experimental data is collected to validate computational models (empirical, semi-physical, fully-physical).

On the largest scale, two topics become the focus: (1) Fire risk assessment and (2) wildfire-atmosphere interaction. The latter focus is plume development and emissions from wildfire [1.75-1.79]. Large amounts of hazardous gases and aerosols are transferred from the fire into the atmosphere. This can impact the carbon balance in the atmosphere, which can have adverse effects on the global climate causing socio-economic challenges.

Fire risk assessments are tools that allow authorities having jurisdiction to estimate the current (daily) fire hazard for a large area. An assessment generally includes simplified fuel and fire behavior models into which current meteorological data is fed. For example, in the United States, the assessment is the National Fire Danger Rating System (NFDRS) [1.81]. The sophistication of these models (in terms of representing the physics) is usually kept as low as possible to prevent the requirement of significant computational power, but still high enough to justify underlying simplifications. This

is mainly because these are operational tools that require real time analysis. This is not possible with sophisticated fully-physical models, e.g. Fire Dynamics Simulator (FDS) [1.82, 1.84]. These more sophisticated models are however used for research purposes in order to study the wildfire phenomena.

In each scale, one can find dominating parameters that drive the dynamics of a wildfire and studies referred to above have aided in developing comprehensive understanding of the critical relationship between influencing parameters and their effect. The complexity of the physical phenomena that drive wildfire is acknowledged in the community, however coupling of phenomena (temporal and spatial) is not fully understood yet. Moritz et al [1.85] provided a clear picture of the complexity of the wildfire in a systematic manner.

The research presented here is driven by the principles of flammability as applied to the built environment. Flammability characterizations are obtained from strict standardized combustion tests, e.g. the Cone Calorimeter [1.86], FM Global Fire Propagation Apparatus (FPA) [1.87], or Lateral Ignition and Flame Spread Test (LIFT) [1.88], which allow material classification according to their ignition and burning behavior. It must be understood, how a fuel ignites, how well it sustains a flame and how intensely it burns, in order to identify the risks posed by the material in a fire scenario. It is thus beneficial for a quantification of the risk to have test methodologies with adequate control of the test environment (e.g. heating condition), but which also have provide good repeatability.

### *1.1.3. From flammability to fire behavior*

The two terms, *flammability* and *fire behavior* are closely related. Flammability is a term that describes the response of a material subjected to heat insult. A general definition of flammability can be stated as a quantification of some parameter(s) that characterize the ignition and burning behavior of a combustible material. Flammability is commonly characterized with ignitibility, sustainability, and combustibility as

defined by Anderson [1.23]. In its basic understanding, it is a material property (for a given environment), and can be quantified with several components: (1) how well does a material ignite, and (2) how well does it burn. These are generally associated to ignitibility (time to ignition), and combustibility (energy release rate), respectively. Sustainability refers to the ability of a material to sustain a flame.

When discussing a wildfire, two important fire behavior characteristics are (1) the rate at which a fire spreads and (2) with what intensity it burns. The former can be fundamentally described as a series of ignition of adjacent unburned fuel particles (ignition behavior) [1.89-1.95]. The latter can be linked to various definitions of energy release parameters (burning behavior), for example heat release rate (mean or peak), total energy released, or similar metrics based on the mass consumption [1.94-1.96].

One can identify the similarities of the definitions of fire behavior and flammability. However, they are not necessarily interchangeable. Flammability is used when discussing the fire behavior as a property of the fuel under defined conditions, which will be the case in this work. Therefore, a fuel bed that is more flammable may be associated to stronger fire behavior. The same factors that impact flammability also drive fire behavior. This is because fuel flammability is an integrated part of the wildfire behavior. A schematic given in Fig. 1.1 highlights this concept.

It is evident that many factors may impact the flammability and thus can cause a fire to extinguish or become more extreme. In this conceptualization (Fig. 1.1), the physical phenomena of wildfire behavior are related to the flammability, because this is where the fundamental mechanisms of heat and mass transfer have to be evaluated (ignition and burning behavior). Thus, understanding the flammability is paramount and will aid in the development of understanding wildfire behavior.

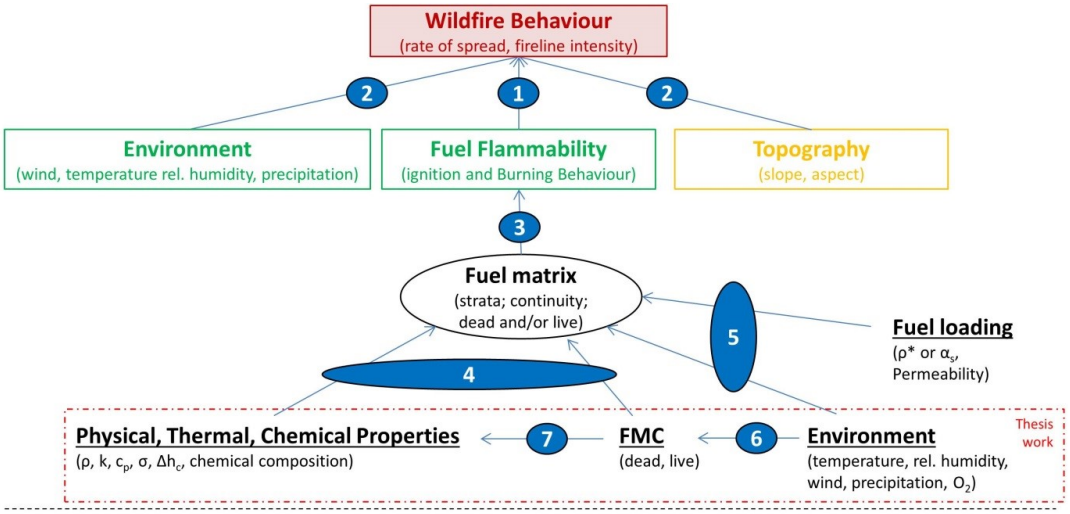


***Comments:***

Requirement for wildfire

No requirement for wildfire behaviour, but enhance or detract it

1) Defines location of fire and provides the pathway for fire spread; Governs phenomena of wildfire behavior by defining ignition and burning behavior
2) External effects on the fire that enhance or detract heat and mass transfer mechanisms
3) Heat and mass transfer mechanisms are defined
4) Internal factors
5) External factors (the environment affects fire behavior on two scales)
6) Temperature, humidity, and wind govern FMC (live FMC is also dependent on soil conditions and plant metabolism)
7) FMC can alter particle properties

**Fig. 1.1. Conceptualization of wildfire behavior. Environment, flammability and topography are integrated parts to characterize wildfire behavior.**

### Factors impacting flammability

A typical flammability assessment is conducted with standardized tests, where external factors are controlled (e.g. heating condition). This allows classification of materials based on their response to a specific heat insult. The ignition behavior is closely related to their thermophysical properties as these define the heat transfer within the material.

The porosity ($\alpha_g$) of wildland fuels introduces a complexity that is ignored for solid material, and is explained by bulk properties. This porosity is also highly variable depending on the location of the fuel package (e.g. in the litter layer or in the canopy). Changing the porosity in a fuel package (by varying fuel loading) and keeping other parameters constant will impact the flammability because heat and mass transfer mechanisms are altered (e.g. [1.39, 1.41, 1.47]). For example, radiation is able to

penetrate further into the fuel matrix when the porosity is increased, which will affect the heating and subsequent combustion of solid particles [1.97]. At the same time, higher porosity increases oxygen availability, which improves combustion dynamics [1.47].

If it is desired to classify wildland fuels according to their flammability, as a baseline, this must be done at a constant porosity, airflow magnitude and oxygen concentration, and FMC. This is mainly because each one is highly dynamic in a real wildfire scenario. Forced convection airflow is a special case because it also affects particles differently, depending on size, i.e. at a constant flow velocity, smaller particles are cooled more effectively compared to larger particles; thus the net energy received varies.

Beyond this baseline, a strategic analysis of the flammability as a function of one or more factors may then be formulated. Thus, a full flammability assessment of wildland fuel is a multidimensional problem (depending on the number of external factors) and should be reported as such.

The work presented in this thesis is an extension of the research on wildland fuel flammability with the FPA that has been conducted in the past decade [1.39-1.51]. Highlighted are the impact of forced convection and FMC on the ignition and burning behavior. It is not the intent of this thesis to provide a final solution for wildland fuel flammability assessment, but to provide another stepping stone into the right direction. Still much research is needed to assess all the factors (Fig. 1.1) and their relations to flammability parameters. A novel flammability assessment for live foliage is presented here. The proposed assessment can be used as a framework for a new wildland fuel flammability classification. Furthermore, the knowledge may be used to understand wildfire behavior phenomena.

### *1.2. Research goals and thesis outline*

This chapter provides background information for the thesis and explains important aspects that are discussed throughout the thesis. Chapter 2 outlines fuel characterization, sample preparation, experimental apparatus (setup and methodologies), heat release rate calculations, and test conditions for each analysis chapter. The analysis portion of the manuscript is split into two major parts. In the first half, Chapter 3 and 4, investigations focus on the impact of forced convection on the flammability (ignition and burning behavior) of dead forest fuel beds. In the second half of the thesis, Chapter 5 and 6, the focus turns towards the seasonal trends of flammability of live foliage and impact of fuel moisture content. Finally, Chapter 7 provides a summary of the works, concluding remarks and future work. Several Appendices are available that provide supporting material.

The goal of this work is to aid in the development of the fundamental knowledge on the burning dynamics of vegetative fuel beds, with respect to heat and mass transfer. This is achieved by conducting laboratory scale combustion experiments under a wide range of test conditions. Furthermore, the experimental data shall provide a database that can be used for model validation exercises. The analysis techniques applied in this work shall also provide theoretical descriptions of the physical phenomena and aid in the understanding of (1) the thermal behavior of fine forest fuel particles and (2) their fundamental burning dynamics.

#### Chapter 2

This chapter includes all the important information about the experimentation (fuel, sample test apparatus, test conditions, and analysis techniques). It was desired to have a comprehensive fuel and sample characterization, which is required for a successful interpretation of the experimental results.

**Chapter 3**

The goal of this chapter is to analyze the heat and mass transfer mechanisms that govern ignition and burning behavior of forest fuel beds, and assess the impact of changing ventilation condition and external heat flux. Changing ventilation conditions here are: ventilation area, flow magnitude, flow temperature and flow oxygen concentration.

Variations in time to ignition are analyzed with respect to (a) radiant heat flux, (b) convective heat transfer, (c) airflow oxidizer mass flux, and (d) airflow temperature. Testing these conditions, allows de-coupling the effects imposed by forced convection: cooling of the solid phase and dilution of the gas phase. A second objective is to evaluate the combustion dynamics (emissions, combustion efficiency and combustion intensity), by analyzing the pyrolysis and combustion gases, oxygen consumption and time of the flaming period with respect to the same parameters (a – d).

**Chapter 4**

The goal is to assess, to what extent a simplified two phase physical model (energy conservation) can be used to predict the ignition behavior of porous forest fuel beds. Experimental results developed in Chapter 3 are used to validate the performance of this model. The model is validated with experimental results for in-depth temperature distribution, critical heat flux, and ignition times for two pine needle species. Current limitations of the model are described. Thermal analyses are performed on the scale of the sample and needle to (1) estimate a convective heat transfer coefficient and (2) assess the thermal behavior of the sample and needle.

**Chapter 5**

The goal in this chapter is to assess the flammability in terms of ignition and burning behavior of live, fully dehydrated foliage and determine any seasonal trend. It was

desired to determine if live fuel flammability correlates with the occurrence of a typical fire season. A novel framework for live fuel flammability assessment is developed, which can also be used for fuel classification. This is achieved by conducting combustion tests over the period of one year. Variations in flammability are linked to ignition time and heat release rate results from combustion tests, and were obtained for two needle generations (young growing and mature). Finally, the monthly live fuel flammability assessment is compared to historic fire data to evaluate any correlation.

**Chapter 6**

The goal in this chapter is to assess the flammability in terms of ignition and burning behavior of live unconditioned foliage and determine any seasonal trend. The novel framework for live fuel flammability assessment from Chapter 5 is extended to unconditioned needles. A comparison of conditioned and unconditioned fuel flammability is made to analyze the effect of FMC. Finally, it is attempted to correlate flammability assessment of unconditioned to fully conditioned foliage. This is achieved by determining the relationship between ignition time and *FMC* and the relationship between peak heat release rate and *FMC*. As was the case in Chapter 5, the live unconditioned flammability assessment is also compared to historic fire data to evaluate any correlation. The novel assessment presented in Chapter 5 and 6 results in the definition of live fuel flammability as a two dimensional parameter, depending on time (season) and FMC.

**Chapter 7**

This chapter provides a summary of the key findings of the studies conducted in this thesis. Finally, it provides some guidance for the direction of future research and concludes with some final remarks.

## *1.3. Background and literature review*

The following sections provide information from past research and describe the fundamental concepts that are studied in this work. Global concepts, such as the wildfire behavior and the occurrence of a fire season are discussed first. The framework of analyzing wildfire behavior with respect to fuel flammability parameters is presented. A discussion is presented to explain wildland fuel considerations. Then, more detail is provided in what drives fuel flammability and what factors impact it. Furthermore, the mechanisms are further detailed into the physical phenomena, heat and mass transfer.

### *1.3.1. Introduction*

In every fire scenario it is essential to know what is burning. It was discussed in Section 1.1.3 that the fire behavior depends on the flammability of the fuel (see Fig. 1.1). It is however, not the sole component that needs to be considered. Topography and environmental factors are two other components that impact the wildfire behavior on a larger scale. It was shown that external factors, e.g. wind, impact fire behavior by varying the flammability of the fuel bed. Many other considerations must be made, such as the distinction between dead and live fuel. Differentiations for dead and live fuel are made, because these generally exist in different fuel strata (e.g. ground or canopy).

In the wildland environment there are arrays of different species that can have different levels of flammability. Furthermore, the arrangement of the fuel is heterogeneous. A wildfire can occur only if certain conditions are met: (1) combustible material is present; (2) fuel bed loading and continuity are adequate; (3) environmental conditions (temperature, relative humidity and wind) are favorable; and (4) the FMC is low.

Condition (1) can be assessed with the flammability of the fuel. Condition (2) is a variable depending on local conditions. As discussed previously, the flammability may

be considered for specific fuel loading (porosity). However, fuel bed continuity is critical to allow fire spread. Condition (3) governs not only the ambient conditions, but also the inherent FMC (condition 4) of the fuel. Condition (4) is also driven by soil conditions and plant health for live foliage.

It is common that wildfire prone areas have distinct seasons in which the frequency of fires is high [1.98]. It is likely that during this time of the year the factors impacting the flammability (Fig. 1.1), and by extension fire behavior, are favorable. However, it is not fully understood what the dominant factor driving the occurrence of a fire season is. It is the intent of this thesis to shed some light onto this phenomenon. The NJ Pine Barrens is used as the ecosystem of interest, mainly because the fuel studied in this thesis (Pitch pine; *Pinus rigida*; PRI) is a dominant species therein.

**Seasonality**

The ecosystem of interest, the NJ Pine Barrens, experiences all four seasons throughout the year. Each one has typical meteorological conditions which drive phenological cues, such as the start or end of growing season [1.99]. Evergreen conifer plants, like the Pitch pine (*Pinus rigida*), lie dormant over the winter, which means that no (or limited) photosynthetic activity takes place. In the spring, photosynthetic activity is triggered by the rise in temperature and/or solar radiation [1.99]. This is followed by bud break and green-up, which mark the start of the growing season [1.99]. New foliage grows over the spring and summer month until they reach full maturity in the fall. Aalto et al [1.100] indicated that the growth period of pine needles (*Pinus sylvestris* L.) is approximately 100 days. It begins with shoot elongation and minor elongation of the needles. When the shoot is sufficiently long and stable, needles begin to elongate more rapidly. At the same time, existing foliage undergoes an aging (if generations stay for multiple years) or a decaying process in the fall. When foliage is sufficiently decayed, indicated by a change in pigmentation (yellowing), they will

fall off the tree. At the end of the fall, plants prepare for the upcoming dormancy period, by reducing photosynthetic activity.

Phenological cues can be observed from visual inspection. However, modern technologies, such as remote sensing, allowed the determination from satellite imagery [1.101, 1.102]. A common technique includes the Normalized Difference Vegetation Index (NDVI) [1.101]. Spectral reflectivity of the earth's surface is the basis to obtain the NDVI [1.101]. The reflectivity of a surface depends on its color [1.101]. Satellite images can be used to observe the "greenness" of a specific landscape. The analysis of NDVI (from satellite imagery) of a landscape can then be interpreted to reveal typical growing seasons within a year [1.101]. A large collection of data can be found on the Oak Ridge National Laboratory Distributed Active Archive Center for Biogeochemical Dynamics (ORNL DAAC) [1.103]. Representation of the NJ Pine Barrens is for example the Cedar Bridge data site [1.104]. NDVI data shows a typical growing season starting in April and ending in November.

It was shown by Jolly et al [1.31] and McAllister et al [1.34] that seasonality introduces a change in live fuel chemistry. By extension, this means that, fuel flammability is also affected by seasonality, which was confirmed by both (time to ignition). Seasonality of flammability was also observed by [1.38]. It was concluded that, the seasonal nature of the ignition time is in part due to the FMC of live fuel, which also has seasonal variation. However, McAllister et al [1.34] found that foliage with similar FMC collected in different times of the year have different ignition times. So for example, foliage ignited faster in the summer months, compared to the spring. Thus other factors besides FMC must play a role. A strong relation between ignition time and FMC is obvious (as will be discussed later), but it is still uncertain to what extent other factors, such as chemical composition play a role in the seasonality of live fuel flammability.

Aalto et al [1.100] indicated a rise in the emissions of volatile organic compounds (VOC) during the growing phase of new needles, which might allude to a higher

flammability. Alessio et al [1.105] showed that the monoterpene content and emissions varies significant over the year. They concluded that FMC is a predominant factor for the flammability, composition is only minor. Jolly et al [1.31] also showed that the particle density has significant seasonal variation, which contributes to changing flammability. A change in particle density affects the thermal responds (thermal mass) and can lead to faster or slower ignition.

The following definition should be kept in mind when reading this thesis:

Seasonality – The characteristic growth cycle of foliage as can be observed for a single plant species or in an ecosystem; this relates to characteristic change in live fuel properties as a function of state of growth or decay and explains, in part, existing variation in fuel flammability, as determined by combustion tests.

**Fire season in the NJ Pine Barrens**

In NJ, the major fire season occurs in the spring, at which time most fires are observed. This can be illustrated with historical data. The NJ Office of Emergency Management [1.106] establishes an action plan (e.g. the New Jersey 2014 State Hazard Mitigation Plan) based on collected incident data, which includes wildfire. An extensive database includes significant fires (1905-2012), which shows that most occur in April (a significant fire in this data set is defined as being larger than 100 acres; it is not shown here, but the largest fires also occurred in the spring time). However, it is not uncommon to see significant fire during the fall months, provided that the weather conditions are favorable [1.107]. The data from [1.106] was evaluated by summing significant fires in each month (1905-2012). Results are shown in Fig. 1.2 and identify the seasonal trend of fire occurrence in the spring.

However, this particular data set does not indicate the occurrence of significant fires in the fall, which is likely due to the definition of a “significant fire”. Forman and

Boerner [1.108] have explored the fire frequency in the NJ Pine Barrens and have also illustrated that the spring has the months with the highest fire frequency.

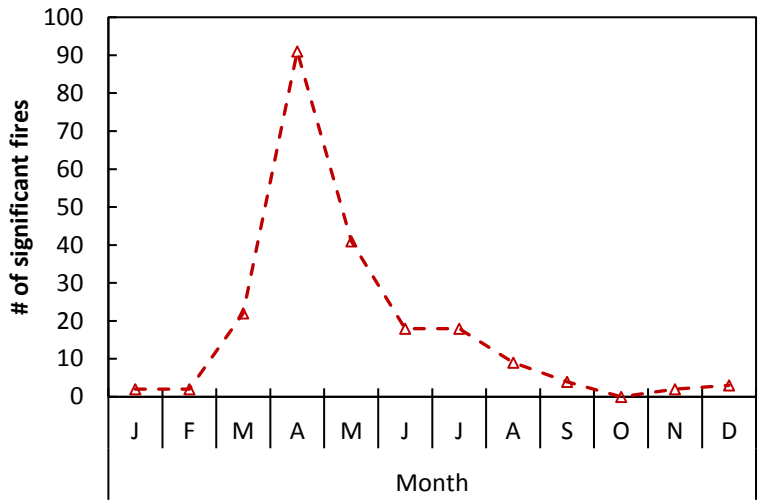


**Fig. 1.2. Historic fire data in NJ, USA (1905-2012) [1.106].**

As was discussed above, the reason for this seasonal trend is the variation in particular conditions that impact fire behavior. These conditions are, external factors (fuel loading and environmental conditions), and internal factors (fuel properties and FMC). The exact relations and whether or not one is dominant over another is not well understood. Environmental conditions and FMC are linked (Fig. 1.1), especially dead FMC, as will be explained in Section 1.3.3. Furthermore, FMC and intrinsic fuel properties are also linked (as will be discussed later). Thus, weather is likely a dominant factor driving a fire season. Detailed meteorological are available for the NJ Pine Barrens. Therefore, these can be evaluated and correlated readily to the major fire season.

### Weather conditions (environment) in the NJ Pine Barrens

Fuel is very difficult to ignite when it is wet or cold. Therefore, favorable fire weather conditions are certainly high temperatures and low relative humidity. Ambient temperatures have indirect effects, because elevated temperatures assist in the

dehydration of dead fuel (item (6) in Fig. 1.1). Wind has a strong influence on the ignition and combustion intensity (e.g. [1.13, 1.39, 1.41, 1.44]). Similar to high temperatures, high wind also assists in the dehydration of dead fuel.

The graphs in Fig. 1.3 show typical weather condition in the NJ Pine Barrens. This particular data collection site is located in Wrightstown, NJ, which is near where the fuel for this study was collected (~16 km). The graphs were extracted from WeatherSpark [1.109], which provides typical weather data (historic and forecast).

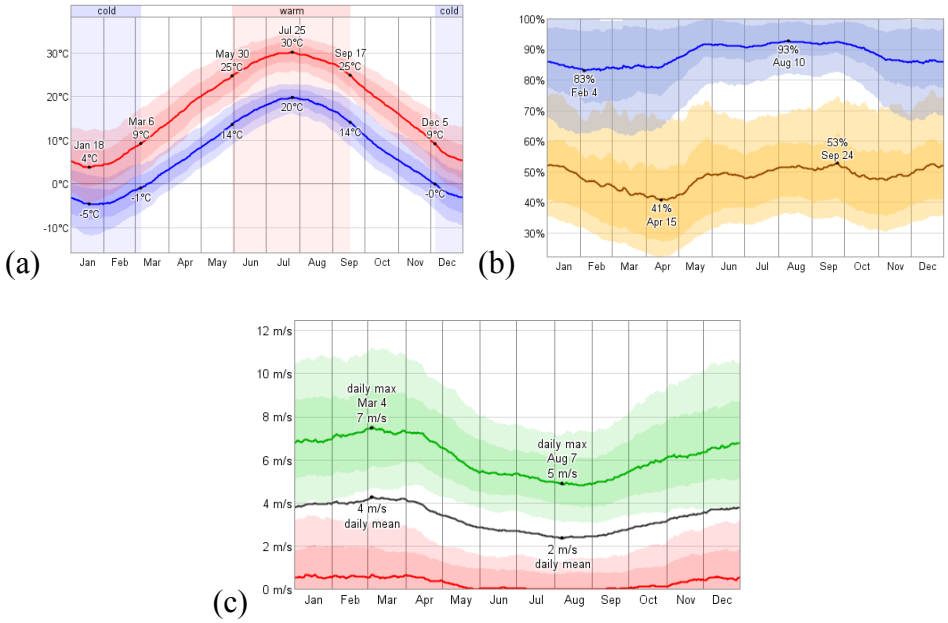


**Fig. 1.3. Typical yearly ambient temperatures (a), relative humidity (b) and wind speed (c) in the NJ Pine Barrens [1.109]. (a) daily average low: blue and high: red; (b) daily average low: brown and high: blue; (c) daily average low: red, high: green, and average: black. Inner percentile bands: 25$^{th}$ and 75$^{th}$. Outer percentile bands: 10$^{th}$ and 90$^{th}$.**

In summary, the spring season has moderate ambient temperatures, low relative humidity, and strong winds. This suggests a correlation between the weather and timing of the fire season.

The discussion above indicates that, the occurrence of a fire season is a complex problem impacted by many factors (weather, fuel flammability, FMC, loading). In order to understand the hazards from wildfire it is paramount to evaluated, why typical

fire seasons occur. This will lead to a better understanding of how to mitigate the hazard and investigate resources.

### *1.3.2. Framework for analysis of wildfire behavior*

#### Wildfire spread mechanism

The fundamental mechanisms of heat and mass transfer drive the ignition and combustion processes for forest fuel beds. On the one side, the fuel bed needs to heat up in order to pyrolyze. On the other hand, combustion products need to mix with available oxidizer in order to form a flammable mixture. If pyrolysis produces enough volatiles, mix with oxygen to reach a lower flammable mixture (LFL) and reach a critical temperature, a sustained chemical chain reaction can take place, which is the exothermic combustion reaction [1.94, 1.95]. Wildfire spread can be idealized as shown in Fig. 1.4.

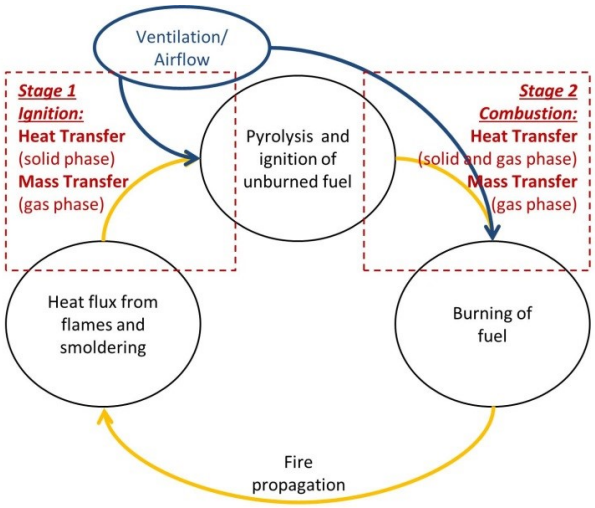


**Fig. 1.4. Feedback loop that illustrates the relation between fire and unburned fuel particles. It highlights the influence of an airflow on heat and mass transfer.**

It becomes evident, that fire spread, if associated to the ignition time, is strongly dependent on the burning behavior of the fuel. The fire behavior of a flame front (mass transfer) governs the intensity of the combustion, which in turn provides the heat

feedback (heat transfer) to the adjacent unburned fuel, i.e. there is a two-way relation between both mechanisms; heat transfer ↔ mass transfer.

Feedback loop: In natural convection with unlimited oxygen, sufficient pyrolysis has to take place in order for a flammable mixture to develop. In the presence of an ignition source this mixture will ignite. A steady burning and flame propagation is established, when the pyrolysis rate continues to be sufficient and uninterrupted. The flames and smoldering particles provide the heat source (either via radiation and/or convection) for the pyrolysis of unburned fuel. If this circle is interrupted at any stage, fire spread will cease.

Besides the flame heat flux feedback, solid phase combustion (smoldering) is also impacted by an increase in oxygen availability. The rate of the smoldering reaction will increase because more oxygen is available. This will increase the local solid phase temperature, which increases heat losses via radiation. Heat losses from glowing particles will then contribute to the overall heat transfer to unburned particles.

Both mechanisms, heat flux from flames and smoldering, and additionally the increased rate at which smoldering occurs, increase the pyrolysis rate, which feeds the required fuel vapor for combustion. This feedback can be described as a loop as shown in Fig. 1.4 and illustrates the inherent linkage between heat and mass transfer. In this schematic, Stage 1 refers to the ignition behavior (pre-ignition stage) and Stage 2 to the combustion behavior (post-ignition stage).

Altering the ventilation scenario (Oxygen availability) influences both the heat balance and mass transfer: In stage 1, it influences the pyrolysis rate by changing the net heat transfer to the solid phase. This impact is carried on during the burning phase (stage 2), because the solid phase cooling effect does not stop after ignition, and gas phase products may also be cooled. Additionally, pyrolysis products need to mix with sufficient oxygen in order to produce a flammable gas mixture (mass transfer in stage 1). In stage 2 (post ignition), ventilation condition impacts the combustion dynamics

by providing the necessary oxygen for the combustion reaction (gas phase). The mass flow of oxygen will also determine the intensity of any surface reaction.

This cycle may be interrupted when (1) the convective cooling of the fuel particles is higher than the heating of the particles from the flames; or (2) when the oxygen supply to the reaction zone is insufficient. The first case is therefore a function of the heat transfer, whereas, the latter is a function of the mass transfer, and as was just described, both mechanisms can be linked to the ventilation/airflow condition.

### Ignition and burning behavior

#### *Ignition behavior*

It is defined as the time from first incident radiative heat flux exposure to flaming ignition. Piloted ignition conditions are desired for the tests with the assumption that in forest fires, the flame front (or glowing particles) act as the ignition source for an advancing fire.

Time to ignition ($t_{ig}$) is given as the sum of the pyrolysis time ($t_p$), mixing time ($t_m$) and induction time ($t_i$) [1.89-1.95]:

$$t_{ig} = t_p + t_i + t_m \approx t_p \qquad \textbf{Eq. 1.1}$$

Pyrolysis time is the time required for a material to reach the temperature at which pyrolysis starts. Mixing time is associated to the time required for a flammable mixture (pyrolysis products and oxidizer) to form above the fuel bed. Induction time is associated to the time required for the flammable mixture to reach its critical temperature at which a thermal runaway (chemical chain reaction, or combustion) occurs. It is commonly assumed that under natural flow conditions and with the use of a pilot flame, $t_i$ and $t_m$ can be considered negligible (e.g. [1.89]). The mixing of fuel

gases and oxygen is assumed to be fast. The pilot flame induces the chemical chain reaction due to its high temperature.

Tewarson and Ogden [1.110] have shown that ignition times of solids are not significantly impacted by a forced flow (bench scale calorimeter similar to the FPA). This was however found to be different for porous wildland fuel beds (e.g. [1.47]). When forced flow is introduced, the pyrolysis time can be delayed due to convective cooling of the particles. The differences between solid and porous fuel indicates that the convection cooling is significantly higher for porous fuel beds, which can be attributed to the particle size and fuel bed bulk density. The mixing time may vary depending on the flow magnitude and oxygen concentration. Forced flow can promote better mixing between the pyrolysis products and the oxidizer. However, this mixing may also dilute the gas such that a flammable mixture cannot be established in the location of the pilot, therefore delaying ignition. The exact behavior is not well understood and depends on the balance of oxidizer and pyrolysis gas flow rates.

Ignition can occur in three modes: 1) piloted, where the combustion gases are ignited at the pilot flame; 2) auto-/spontaneous, where the gases ignite in the absence of a pilot flame; and 3) smoldering to flaming, where the gases ignite (transition to flaming) due to the presence of smoldering fuel. Mode 1 is commonly studied because it allows the most repeatable ignition conditions, which is ideal for flammability studies [1.93].

In this scenario (mode 1) the spreading fire front acts as the pilot flame to induce ignition of the pyrolysis gases that develop from the adjacent virgin fuel [1.49]. Mode 2 occurs when a flammable gas mixture develops and is continuously heated, in the absence of a pilot flame, until it reaches a critical temperature (auto-ignition temperature). In this mode, $t_i$ is not short, because it is the time required to for a fuel/air mixture to reach the ignition temperature (in the presence of a pilot flame it is assumed that $t_i \rightarrow 0$ s). When the gas temperature is high enough, the chemical reaction reaches a thermal run-away. The third mode may occur frequently in wildfire, because

vegetative fuel is prone to smolder, or described in more accurate terms, factors are present that inhibit a flaming combustion and cause flame extinction (cooling and dilution); FMC (acting as a heat sink in solid and gas phase), and wind (cooling and dilution). A common scenario of the smoldering mode is ignition of combustible structures or porous fuel beds via an accumulation of firebrands that are generated and expelled from a wildfire [1.74, 1.111-1.113]. The time scale of these three modes is such that

$$t_{piloted} < t_{smoldering} \approx t_{spontaneous} \quad \textbf{Eq. 1.2}$$

Piloted ignition is the fastest because the strong ignition sources means that the induction time is negligible compared to pyrolysis time of the solid and the mixing is commonly assumed to be fast. In Mode 3 the induction time or transition time from glowing solid phase to flaming gas phase combustion, due to the smolder (hot spot) is longer than in mode 1. In Mode 1 and 3 the induction time is small compared to other time parameters, such as pyrolysis time. However, in mode 2 this induction time component is long because it is related to the chemical reaction time and the time it takes for a combustible gas mixture to reach its auto-ignition temperature. The interest in this work lies in mode 1, because it is desired to obtain repeatable, controlled ignition conditions. However, Mode 2 is frequently observed in the experimentation, for example at low external heat flux with airflow (Chapter 3), at very high FMC levels (Chapter 6), or at low oxygen concentrations (Chapter 3).

*Burning behavior*

When combustion tests are evaluated (Chapter 3, 5 and 6), calorimetry calculations are performed in order to determine the heat release rate (HRR) and total energy release from a burning fuel.

The HRR estimations used here are based on the principle of oxygen consumption calorimetry (OC) [1.114-1.124]. Huggett [1.114] has determined that, when typical hydrocarbon fuels combust in air (assuming complete combustion), the energy released per unit mass of oxygen is relatively constant ($E_{O2}$). A mean value of 13.1 +/- 0.7 kJ.g$^{-1}$ (oxygen) was proposed [1.114], and is widely applied today. The advantage is that detailed knowledge of chemistry of the material is not required to estimate the energy release rate, although estimations are improved if it is known [1.120-1.122].

The applicability of this to forest fuel was shown by [1.39, 1.42] for typical Mediterranean forest fuels using the FPA. Bartoli et al [1.42] concluded that a value of 14.15 kJ.g$^{-1}$ (oxygen) is more accurate when conducting tests with forest fuel. For pine needles, they found that the standard value will result in under-estimation of the HRR of approximately 6.7%. A similar value for the energy constant was found by Santoni et al [1.53]. An abundance of studies are available (e.g. [1.120-1.124]) that have reviewed the principle of OC and have illustrated the derivation in detail. This also includes comparison to the principle of carbon dioxide generation calorimetry (CDG) (e.g. [1.122]). A recent work done by Hidalgo [1.124] applied the technique to building insulation material and includes a comprehensive set of equations and comparison of the two principles, OC and CDG. The HRR ($\dot{Q}_{OC}$; in [kW]) of a material burning in air can be estimated by the amount of oxygen consumed in the combustion process [1.117] and can be formulated as

$$\dot{Q}_{OC} = E_{O_2} \Delta \dot{m}_{O_2} \qquad \textbf{Eq. 1.3}$$

Where $E_{O_2}$ the oxygen consumption energy coefficient [kJ.g$^{-1}$(oxygen)], and $\Delta \dot{m}_{O_2}$ is the mass of oxygen consumed [g] in the combustion. More detail on the calculations and uncertainties is given in Chapter 2.

**Fire spread rate and fireline intensity**

Two critical wildfire behavior characteristics are flame spread rate [$m.s^{-1}$] and fireline intensity [$kW.m^{-1}$]. In context to flammability these can be related to ignition and burning behavior, respectively. As discussed earlier, flame spread can be described by a series of ignition of adjacent unburned particles. Fireline intensity can be associated to the burning behavior by evaluating the energy release rate.

Theories for both, spread rate and intensity, include parameters that account for the fuel loading. The importance of the fuel loading becomes evident when examining Byram's definition of the fireline intensity [$kW.m^{-1}$] [1.125]:

$$I_B = H\, w_a R \qquad \textbf{Eq. 1.4}$$

Where $H$ is the net low heat of combustion [$kJ.kg^{-1}$], $w_a$ is the fuel consumption in the fire front [$kg.m^{-2}$], and $R$ is the linear rate of spread [$m.s^{-1}$]. The mass component is evident. Additional fuel specific information will be captured in the heat of combustion considered. Santoni et al [1.53] were able to relate this quantity ($I_B$) to laboratory measurements. They were able to determine the fireline intensity using oxygen consumption calorimetry. It is concluded that $I_B$ overestimated the heat release by 13-23% for their specific fuel beds. This is attributed to the lack of consideration of combustion efficiency in $I_B$. Besides fireline intensity, importance of the fuel loading can be found in traditional wildfire spread theory (e.g. [1.10, 1.11]). The rate of spread ($R$) can be defined as:

$$R = \frac{energy\ available}{(Bulkd\ density) * (energy\ required\ for\ ignition)} \qquad \textbf{Eq. 1.5}$$

The available energy is defined by the heat flux (radiant or convective) from the flames [$kW.m^{-2}$], whereas, the energy required for ignition can be defined as the heat of

combustion of the fuel [kJ.kg]. The bulk density [kg.m$^{-3}$] is used to account for the porosity and amount of fuel in the bed.

### *1.3.3. Wildland fuels*

In this work, wildland fuels refer to foliage (dead and live). In a global definition it also includes larger fuel particles, e.g. tree trunks. Species used in this work are: (1) White pine (*Pinus strobus*), (2) Red pine (*Pinus resinosa*) and (3) Pitch pine (*Pinus rigida*) [1.126]. Detailed fuel characterization is included in Chapter 2. It is important to obtain a number of fuel properties, such as the SVR, density, specific heat, and others, as these are important to analyze specific fire phenomena, for example ignition.

#### Porous media

Wildland fuels have to be considered as a porous media, because in reality it is not a single particle burning that governs the combustion process but rather a volume with a number of particles. In this scale one must consider a fuel matrix that consists of a solid phase (the leaf/needle) and a gas phase (normally air). The porosity may be described from the solid volume fraction, $\alpha_s$:

$$\alpha_g = 1 - \alpha_s \qquad \textbf{Eq. 1.6}$$

Where $\alpha_s$ is the solid volume fraction (packing ratio), which is determined from the bulk density, $\rho^*$ and the particle density, $\rho$:

$$\alpha_s = \frac{\rho^*}{\rho} \qquad \textbf{Eq. 1.7}$$

The variation of the porosity is high, because it depends on what location of the fuel matrix under consideration. The porosity of for example pine needle litter is lower than

foliage in the tree canopy (litter: 2-5%, shrub: 2-5‰, canopy: 0.2-0.5‰) [1.49]. The influence of porosity on the burning dynamics is evident, because it creates spaces that allow oxygen to enter the fuel matrix. A simple example of this is illustrated by the combustion of wood cribs [1.127-1.130]. Extensive research has been conducted by changing crib configuration and evaluating the mass loss and heat release rate data. Furthermore, McAllister and Finney [1.128-1.130] have provided a discussion on the relevance to wildland fuel burning dynamics.

The large volume of air in the fuel matrix increases oxygen availability, which is advantageous for improved combustion processes. On the other side the void space allows forced airflow, such as wind, to become an important factor in the ignition process as well. The variability of wind is a large contribution to the unpredictability of real wildfire. This is due to the influences on the fundamental mechanisms that drive the ignition and burning behavior. A forced airflow influences the heat transfer within the fuel matrix, by increasing the convection cooling mechanism. At the same time, it affects mass transfer by either direct influence due to the change in oxidizer mass flow rate, but also indirectly due to the cooling mechanism, which impacts the pyrolysis rate. These mechanisms will be further discussed in the subsequent sections.

As discussed previously, the porosity means that additional parameters are required for the fuel characterization, which is negligible for solid fuels. These are the bulk density which is related to the fuel loading (mass per unit area), and the porosity which is related to the bulk density and particle density. Bartoli et al [1.42] have defined a correlation for the permeability for pine needle beds as a bulk property that depends on the porosity and particle size. Permeability describes the ability of a fluid to pass through a porous medium [1.42]. Porosity (Eq. 1.6) does not distinguish between particle sizes. It merely defines what fraction of the volume is gas and what solid. The definition of the permeability by Bartoli et al is based on Darcy's law, and takes porosity (bulk and particle density) and particle size into account. Therefore, it is a fuel and bed specific property. They used this parameter to analyze the HRR.

### Fuel loading

Fuel loading may vary drastically in time and space. Depending on the fuel stratum of interest (ground, surface of canopy) distinction also has to be made for dead and live fuel. It is not the intent of this thesis to identify variations in fuel loading, nor the impact on the ignition and burning behavior. It is however, important to point out the significance of fuel loading as was first discussed in terms of fire spread rate and intensity.

Discussion in Section 1.3.2 first indicated that fuel loading is critical, because it is widely understood that, fires spread mainly on the ground in continues fuel beds. If there is not enough fuel present, ignition and spread of fire are less likely. This was a topic of much research in the past. Bartoli [1.43] and Jervis [1.51] showed that the ignition time (FPA) is not significantly impacted unless fuel loading becomes very low (only for natural convection; forced convection significant affects the ignition). Jervis [1.51] also showed that the peak heat release rate (pHRR) increases with increasing fuel loading, but reaches a limiting value (~1.2 $kg.m^{-2}$ or 40 $kg.m^{-3}$). Bartoli et al [1.42] and Simeoni et al [1.47] (more detailed in [1.43]) have related fuel bed permeability to mean HRR. Permeability increases with porosity ($K \propto \alpha_g^3$) (i.e. decreases with fuel loading) [1.42]. They found that mean HRR increases with permeability (i.e. decreases with fuel loading). The increase is attributed to changes in heat and mass transfer, e.g. radiation penetration depth and oxygen availability inside the fuel matrix. Fuentes and Consalvi [1.131] performed small scale experimentation with fuel beds of different loading and found a non-monotonic behavior analyzing the mass loss rate (MLR). Peak MLR initially increased with increasing fuel load, but further increasing the fuel load reduced the peak MLR. These works are contradicting, indicating that the exact mechanism is not certain. Certainly, oxygen availability increases, which should increase HRR. The energy received by the solid phase is more uncertain. For more porous fuel beds, radiation penetrates further involving more fuel in the pyrolysis process. On the other hand, in denser fuel beds radiation does not penetrate as far and

the energy is absorbed closer to the surface and heating up particles in this zone more quickly.

Fire spread experimentations (bench scale) with varying fuel loading were carried out by [1.52-1.55]. The spread rate increases with increasing fuel load. This is attributed to higher combustion intensity, which provides higher heat feedback to adjacent unburned fuel. Energy release rates measured from experimental fires showed the increase with fuel loading. The amount of live fuel present in the canopy is considered to have a large impact on the likelihood of crown fires [1.70, 1.71]. Another factor for crowning is the ladder fuel that is an aid for flames to travel into the canopy.

**Fuel moisture content (FMC)**

This condition has to be divided into two categories, dead and live FMC, because both are governed by different mechanisms. Dead FMC is governed by meteorological conditions, whereas, live FMC is governed by physiological plant processes.

The mechanism driving dead FMC is the ability of a fuel particle to absorb or release from or into the surrounding air. The relationship between environmental condition and dead particles is often characterized with the Nelson model (physical model based on heat and moisture transfer) [1.132, 1.133] (or others as summarized by Lopes et al [1.134]). Fine fuel particles react faster to environmental conditions than larger particles. This is typically described with a time lag [1.133], which relates the time it takes for a particle to reach 63% of the equilibrium moisture content (EMC) [1.133]. Fine fuels, such as dead foliage is categorized as 1-hr fuel, which means that a dead particle will reach 63% of the EMC within one hour [1.133]. This category includes particles < 6.35 mm (0.25”) in diameter [1.133]. The linkage between the weather and dead FMC is evident. Dry and windy conditions in the spring are significant factors that keep the dead FMC low. In the summer, high temperatures also reduce the dead FMC, however, relative humidity tends to be higher during this time.

In a live plant, water is drawn from the soil and distributed internally, from the roots through the trunk and branches to the foliage. Transpiration causes water loss from the foliage. However, plants are designed to store water and minimize losses, because it is required for survival. Therefore, live FMC is less susceptible to changing weather conditions. It is however, susceptible to plant health [1.32].

Live FMC in NJ Pitch pine foliage has been monitored over the course of five years prior to the start of this study. Results (Fig. 1.5) from this long term monitoring showed a low FMC in the spring (April/May) and a peak FMC in summer (July/August). The low value in the spring refers to the spring dip (SD) which is a characteristic of pine foliage (for example [1.135-1.139]). The high peak indicates new foliar generation growth (No attempts were made to separate individual needle cohorts).

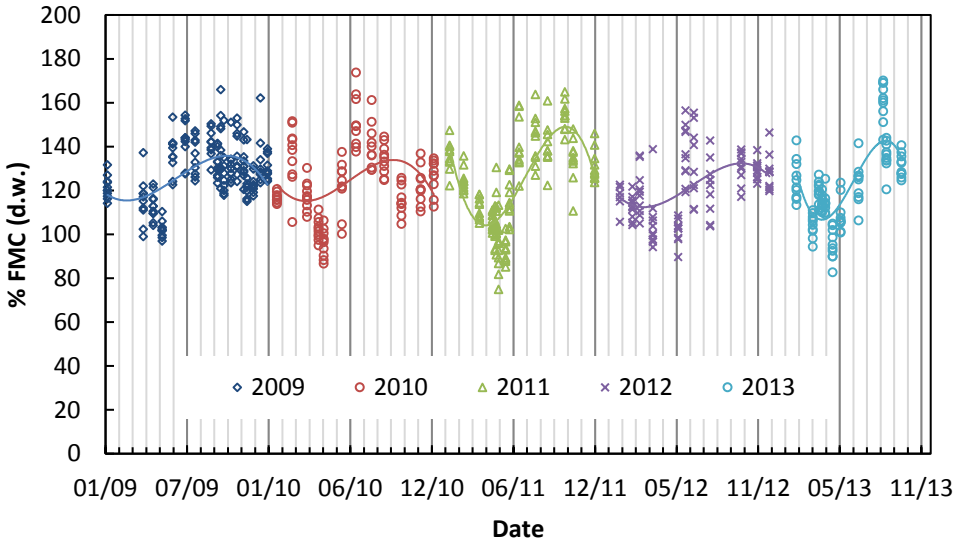


**Fig. 1.5. Live FMC measurements of NJ Pitch pine needles (2009-2013). No separation of generations. Data collected by [1.140].**

The low live FMC value in the spring suggests that unconditioned live fuel is most flammable during this period, on the account that water content is low, which means that ignition can occur faster and combustion intensity is higher [1.45, 1.50]. Jolly et al [1.31, 1.137] have determined that this low value is not only due to reduced water

content but also due to a rise in dry matter, which has the same effect on the FMC (dry weight) calculations:

$$\%FMC\ (d.w.) = \frac{m_{water}}{m_{dry}} \times 100 \qquad \textbf{Eq. 1.8}$$

This was determined by detailed analysis of the particle density and chemical composition.

### *1.3.4. Flammability of wildland fuels*

Two critical wildfire behavior characteristics are fire spread and fireline intensity as previously discussed. In context to flammability these can be related to ignition and burning behavior. Two definitions should be kept in mind when reading this work:

Ignitibility – The ease at which a material ignites in a (sustained) flaming state when subjected to a heat source; this is determined from combustion experiments where the time from first heat exposure until the appearance of a sustained flame (in the presence of a pilot flame) is measured; the experimental parameter is the time to piloted ignition ($t_{ign}$) [s].

Combustibility – The (peak) intensity of the combustion of a material after ignition; this is determined from combustion experiments where the energy release is calculated from oxygen consumption calorimetry principles (see Chapter 2); the experimental parameter is the (peak) heat release rate per unit area (cross-section on the sample; pHRR) [kW or $kW.m^{-2}$].

Past studies have focused on a range of different parameters to describe flammability of foliage (species properties, heating rate, wind, fuel loading, and others). These studies focus on various time parameters (e.g. ignition) [1.23-1.32, 1.34-1.38, 1.45-1.51], or heat release rates [1.27-1.30, 1.36, 1.37, 1.39-1.51], and other factors (length

of flaming, smoldering, fuel chemistry or flame height) [1.37, 1.60]. Ignition time, duration of flaming and smoldering, flame height, and temperatures are common parameter to quantify flammability because little equipment is required in laboratory experiments. Mass loss or heat release rate measurements require precision scales and/or gas analyzer that are not always available and are expensive. However, these latter parameters have been described as vital to understand the fire hazard (e.g. Babrauskas [1.115]).

Many of these studies portray interesting and revealing characteristics of the ignition and burning dynamics and a few suggest forest fuel rankings. Fuel was ranked according to individual flammability parameter, for example time to ignition [1.26-1.30], or heat release rate/heat of combustion [1.28, 1.30]. Varner et al [1.60] used a slightly different approach, in which several fire behavior characteristics (e.g. spread rate, flame height, smoldering and others) are grouped together. Besides [1.60], there is little work that attempted to develop a classification that accounts for several flammability traits simultaneously. These rankings are useful as guidance for home owners (WUI) and land managers, because it can be gauged if the local species are more or less hazardous. This helps mitigate any potential risks. Recently, researchers [1.28, 1.30] have highlighted the needs for a standardized flammability assessment for wildland fuels, which currently does not exist.

The difficulty is to de-couple factors that are known to influence ignition and burning dynamics (see Fig. 1.1). However, this is necessary if one wishes to study the fuel flammability. In this work, experimentation is carried out in a systematic fashion where all but certain test parameters are kept constant. Therefore, differences found in the results of the combustion experiments are solely a function of test parameter under investigation. Details on the experimentation with the FPA are discussed in Chapter 2.

The benefit of standardized combustion experiments such as the FPA is the control of critical parameters, but also the repeatability of the results. In order to interpret the

flammability of wildland fuel, the heat and mass transfer mechanisms must be assessed, as they govern the ignition and burning behavior. The following section explains these mechanisms in more detail.

### *1.3.5. Heat transfer in porous fuel beds*

The heat transfer can be due to three modes: (1) conduction, which is the transfer of energy from one object to another by direct contact; (2) convection, which is the transfer of energy due to the bulk motion of a fluid over a solid surface; and (3) radiation, which is the transfer of energy from one object to another via molecular motion [1.141]. Solid materials generally experience a heat insult via convection and/or radiation at their surface. This energy (heat) is then transferred into the solid via conduction. In the same process, the solid experience heat loss due to re-radiation (at the surface) and can experience losses due to convection if the heat insult is only due to radiation. Porous fuels may be heated via radiation and/or convection. However, conduction in the fuel matrix is ignored due to the high porosity (contact area between adjacent particles is assumed much smaller than total surface area). Instead, heat transfer is due to radiation and convection. Each one of these modes is further explained in detail in the following subsections.

In realistic wildfire scenario, heating conditions of a given fuel package (or a single particle) change with respect to the given fire. Initially, far away from a moving fire front, unburned particles are at equilibrium with ambient (cold) air. When a fire front approaches, particles begin to experience a radiant heating from the flames and simultaneous convection cooling due to colder airflow. As the distance between the unburned particles and fire front reduces, radiation transfer intensifies and convection cooling continues to be unchanged (assuming constant flow velocity). At some point in time, it is fair to assume that the ambient air temperature will increase and thus convection cooling will reduce until eventually convective cooling will become

convective heating. Finally, particles will be submerged in the flames at which point radiation and convection heating are at their maximum.

This transient heat transfer problem is very complex. Assuming steady state conditions, and/or ignoring various heat transfer mechanisms, are significant simplifications that can produce uncertainty in analyses. For example, a pure convection heating only condition is likely to be never fully true, because there is always radiant heating from flames. At the same time, radiant heating only condition is also very unlikely because there will always be some convection cooling or heating. It is therefore, desirable to consider a combination of radiant and convective heat transfer condition, but also to determine when a simplified condition produces acceptable error.

The next sections explain the heat transfer consideration that need to be considered in order to study the ignition and burning behavior of forest fuel beds. The discussion is split into pre- and post-ignition stages (see also Fig. 1.4).

### Pre ignition

A schematic of the heat transfer scenario for the porous fuel bed is given in Fig. 1.6. In this stage the external heat flux ($\dot{q}''_{ext}$) is a predetermined radiant flux from the FPA heating units. Heat losses may occur at the interphase (solid and gas phase) via convection and re-radiation.

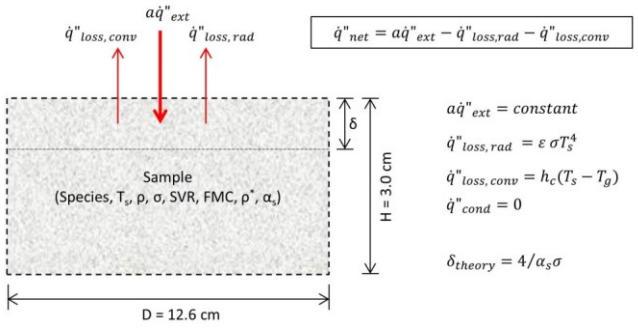


**Fig. 1.6. Sample schematic with simplified heat transfer balance (Stage 1).**

Radiation, $\dot{q}''_{ext}$, can enter the fuel matrix to a certain depth, $\delta$. Therefore, particles are not only heated at the surface of the fuel package, but within a volume underneath the surface of the matrix. This in-depth heating depends on the radiation intensity, source of radiation, particle properties, as well as fuel bed properties.

Convection heat transfer is altered, for example by imposing a forced convection through the fuel matrix. The convection transfer coefficient, $h_c$, is strongly influenced by flow magnitude and particle size. Bulk properties may become important when changed significantly [1.51], as they also alter the flow through the porous bed.

*Radiation heat transfer*

Heat is transmitted in-depth into the fuel volume because the fuel package is porous and does not have a well-defined surface area, as do solid materials. Radiation can penetrate to a certain depth. The energy supplied by the radiation is attenuated in this depth and causes the fuel particles to heat up. The distance to which radiation enters the fuel matrix is described as the radiation penetration depth ($\delta$) [1.16, 1.47, 1.97]. At this depth the irradiance has reduced by 63% from the irradiance experienced by the surface. The radiation attenuation can be assessed with the Beer-Lambert law

$$I(z) = I_0 e^{-Kz} \qquad \textbf{Eq. 1.9}$$

where *I(z)* is the irradiance at depth $z$, $K$ is radiation attenuation (or extinction) coefficient, which is defined as

$$K = \frac{1}{\delta} \qquad \textbf{Eq. 1.10}$$

Simeoni et al [1.47] have conducted an experimental series with pine needle fuel beds to determine $\delta$. In this study [1.47] they measured the heat flux at the bottom of the

fuel bed that was subjected to a constant and known heat flux ($I_0$) at the surface. Using Eq. 1.9 and 1.10 they calculated an experimental value, $\delta_{ex}$ = 5.88 mm (*Pinus halepensis* needle beds with fuel load of 1.2 kg.m$^{-2}$). The experimentation was repeated for the species used in this work to obtain corresponding values for δ.

De Mestre et at [1.12] have shown that a simple correlation can be used to estimate the radiation penetration depth. This is

$$\delta_{th} = \frac{4}{\alpha_s \sigma} \qquad \textbf{Eq. 1.11}$$

Where $\alpha_s$ is the solid volume fraction and $\sigma$ is the particle SVR. The drawback of this correlation is that it was only validated for isotropic particles and beds (spheres). Forest fuel beds however, are highly non-isotropic. It was noted in [1.47] that the estimation can significantly underestimates the radiation attenuation, i.e. giving larger $\delta$. For *Pinus halepensis* needle beds as studied in [1.47], $\delta_{th}$ = 10.99 mm, which is almost twice the experimental value. As will be discussed later in Chapter 4, this estimation should be used with caution when used to describe the radiation penetration in forest fuel beds.

Radiant heat transfer in a porous media is strongly dependent on the porosity of the fuel bed (see Eq. 1.11). Radiation is attenuated stronger in dense fuel beds [1.97]. This means, that the radiant energy is transferred to the solid phase in a smaller volume when the porosity is low. The particles in this volume will heat up faster, because more energy is received compared to particles in fuel beds with higher porosity (less radiant energy is absorbed by individual particles). The temperature gradient thus depends on the radiation penetration depth, i.e. the porosity.

In solid material, the temperature gradient is driven by the thermal diffusivity, $\alpha = k/\rho c_p$, where $k$ is the thermal conductivity, $\rho$ the density and $c_p$ the heat capacity. A

heat wave propagates faster through a material with high diffusivity (e.g. [1.89]). Contrarily when it is low, the surface of the material heats up but energy is transferred slower into the solid. This is different for porous media, because the conductivity is considered negligible. Therefore, another parameter needs to be introduced to describe the in-depth radiation transfer. It was attempted by Simeoni et al [1.48] to introduce the Rosseland approximate, which linearizes the radiant heat transfer problem. This parameter, $k_R$, replaces the conduction heat transfer term in a general heat balance equation and can be defined as

$$k_R = \frac{16}{3K} BT^3 \qquad \textbf{Eq. 1.12}$$

where $B$ is Stefan-Boltzmann constant ($5.67 \times 10^{-8}$ $W.m^{-2}.K^{-4}$), $T$ the solid phase temperature and $K$ the radiation attenuation coefficient (Eq. 1.10). It is evident, that this parameter depends on the particle size and fuel bed density (in $K$). When the porosity of a fuel bed increases, for example due to lower fuel loading, K decreases which causes $k_R$ to increase. (For simplicity the solid phase temperature is considered constant). The increasing $k_R$ means that radiant energy is transferred more easily, with fewer obstructions through the porous media. This is analogous to thermal conductivity; a material with higher conductivity transfers energy better (faster) than a material with lower conductivity.

When energy transfer in a solid material is more efficient (e.g. higher conductivity which leads to a higher thermal diffusivity) it results in lower rise in surface temperatures because the energy is not stored at or in close proximity to the surface. The same can be said for porous media, where the conductivity of the sample is replaced by the linearized radiation constant (Eq. 1.12). A visualization of this can be made when plotting Eq. 1.9 (with constant $\sigma$). This is done in Fig. 1.7 in a normalized form.

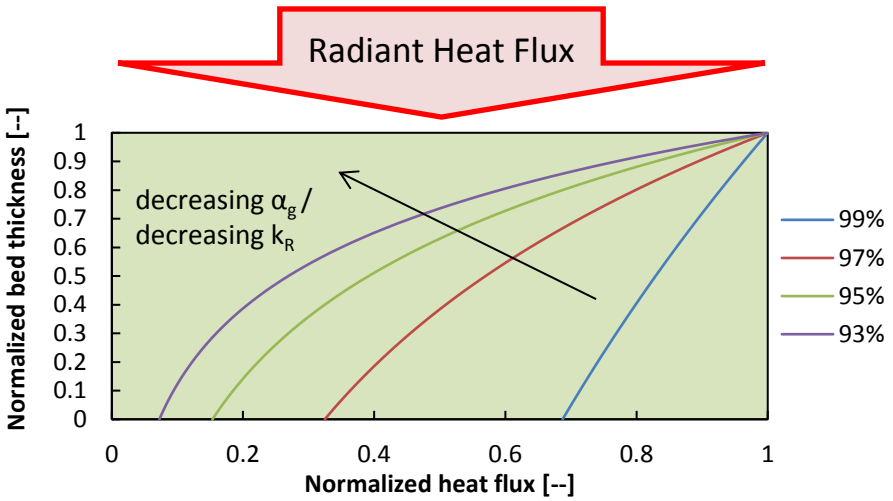


**Fig. 1.7. Normalized heat flux attenuation in a porous medium with different porosities. Bed thickness=1 is the surface exposed to an incident radiant flux. Zero is the back face of the bed. No other heat losses are considered. Illustrated in a 1-dimensional system.**

The normalization was done with the prescribed heat flux ($I_0$ = 30 kW.m$^{-2}$) and a sample thickness ($z(max)$ = 3 cm). At the surface of the fuel bed heat flux is at a maximum. Four lines in this graph represent four fuel bed porosities. The heat flux is attenuated in the beds at different rates depending on the porosity. Through the bed (surface: 1 and backface: 0 on the y-axis), the radiant energy is attenuated by 31.3% when the porosity is 99%. However, when the porosity is 93%, the energy is attenuated by as much as 92.7%. This clearly shows that denser fuel beds store more energy compared to less dense fuel beds. They do so over the entire thickness of the fuel bed, but more near the surface, which is described by the non-linear trend. The stored energy is used to raise the temperature of the solid phase, finally leading to pyrolysis, ignition and combustion. This change in heat transfer attenuation leads to different temperature profiles and can, in part, explain faster ignition of denser fuel beds.

The above explanation is only for the case of radiant heating, ignoring convective cooling. However, ignoring convection in a wildfire scenario is not always realistic.

*Convection heat transfer*

Convection can either be cooling (ambient airflow), competing against the heating due to radiation or it can be heating (hot combustion gases and flame contact) aiding the overall heating process. In either case convection is due to the bulk motion of fluid (in this case air) inside the fuel matrix. The mechanism depends strongly on the particle size and porosity: (1) particle size, because heat transfer increases with decreasing particle diameter, and (2) porosity, because it influences the movement of air (velocity). In recent developments Finney et al [1.61] have described that flame spread in wildfires is mainly due to convection heat transfer. They have determined that radiation alone is not enough to allow flame spread in fine, porous wildland fuels. This is a critical development, because many existing models implement radiation heat transfer as the mechanism of flame spread (e.g. [1.11]). Finney's work [1.61] is important in the study of flame spread and it shows how much of the physical mechanism is still unknown or misrepresented in current models. However, their work represents a specific fuel bed characteristic: vertically oriented fuel particles, with a very high porosity. This type of fuel bed can represent grasslands, but probably less so conifer forest litter. This is because forest litter (for example pine needles) has a much higher bulk density.

It is likely that convection and radiation transfer each play an important role in the flame spread depending on the given scenarios. This was explored by Morvan [1.83] and Morandini and Silvani [1.63], who concluded that there are two wildfire spread regimes: (1) plume driven, in which radiation is the dominant mode of heat transfer; and (2) wind driven, in which convection is the dominant mode.

Convection affects increase with decreasing particles size, because the particles SVR increases, which means that a larger surface area is available for cooling. At the same time the larger surface area also means that more radiation can be absorbed. However, these heat transfer effects are not balanced equally. Radiant heating will occur mainly

from one side, whereas cooling will occur around the entire particle perimeter. This will lead to enhanced cooling and therefore reduced net heat transfer to the solid phase, or in other words a much higher radiant heating is required to cause a small particle to ignite compared to a larger particle in the same condition.

The addition of convection introduces additional complexity in solving the heat transfer. For example, should each individual particle be described to have its individual boundary layer, or can the boundary condition be lumped together into a single boundary layer described for the entire fuel bed?

In order to define the convection heat transfer, one has to determine the convection heat transfer coefficient, $h_c$. This factor depends strongly on the particle size, particle arrangement and flow field. For individual particles the boundary condition can be represented by a cylinder in cross-flow or inline-flow. This is represented in Fig. 1.8.a.

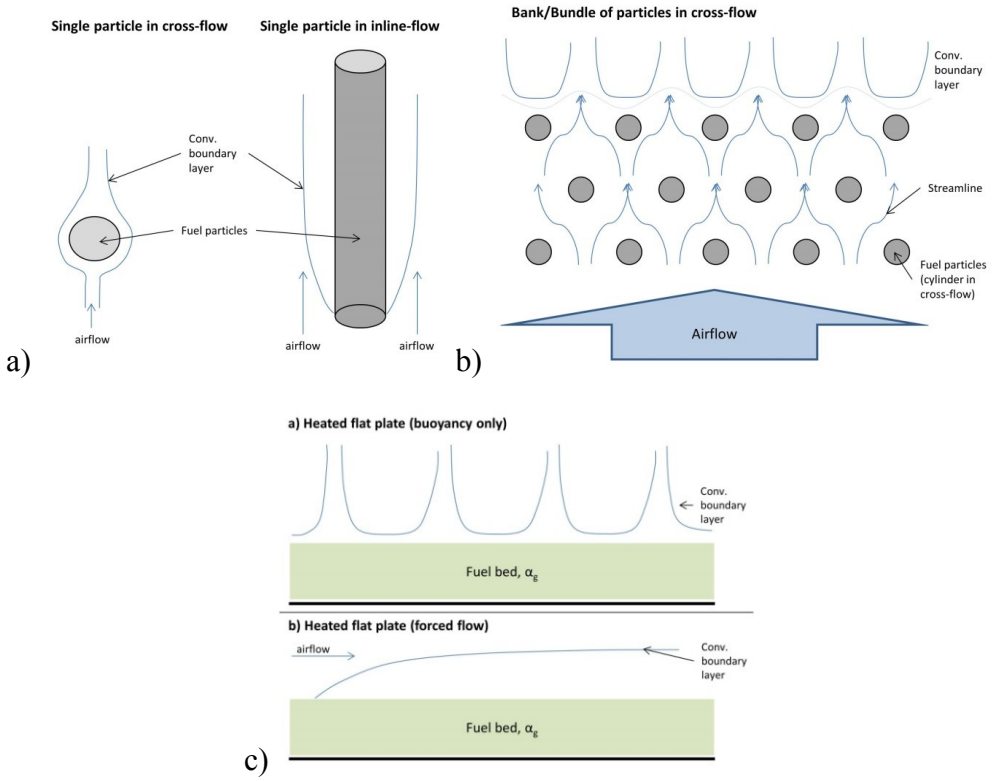


**Fig. 1.8. Schematic of a) single particle in cross-flow and inline-flow condition, b) bank of particles in cross-flow condition and c) flat plate (heated) in buoyancy (top) and wind driven (bottom) flow condition**

The boundary layers have similar shape in buoyancy or wind driven conditions. This representation is the most accurate and detailed one. However, as mentioned earlier, computational models are not able to represent individual fuel particles, because the model will be too expensive (in terms of computational cost). Therefore, a more feasible representation is on a larger scale, the one for a porous fuel bed. This can be described by bundles of cylinders in cross-flow which is depicted in Fig. 1.8.b. Illustrated are only three rows of particles. In reality a fuel bed will have many rows. Also, particles are shown in a staggered formation instead of in-line. This is still a significant simplification, because it does not account for heterogeneity of a fuel bed. However, for this work it will be assumed an acceptable simplification.

On the largest scale, the fuel bed can be considered as a flat plate that is heated by the fire front (radiation from flames). The boundary layer takes on different shapes when the flat plate is in quiescent air or if a wind blows over it (see Fig. 1.8.c.). In no wind condition the boundary layer forms due to buoyancy forces due to the heating of the fuel layer. In a wind driven condition, the layer depends on the flow velocity (but also surface conditions such as roughness).

In each of these considerations one can determine the relation between convection and conduction in the boundary layer. This is commonly done with the Nusselt number, $Nu_L$, in order to estimate a convective heat transfer coefficient:

$$Nu_L = \frac{h_c L}{k_{air}} \qquad \textbf{Eq. 1.13}$$

where $k_{air}$ is the thermal conductivity of the fluid (air). For the arrangements shown in Fig. 1.8 researches have determined many different empirical correlations which can be found in traditional heat transfer text books such as Incropera et al [1.141]. Only a number of correlations that suite the given scenario will be discussed in this thesis (see "Modeling porous fuel beds" section below).

**Post ignition**

After ignition, radiation from the flames increases the net heat flux $\dot{q}''_{net}$, altering the energy balance. A new consideration of the external heat flux, $\dot{q}''_{ext}$, has to be formulated to account for the addition heat flux from the flames (besides heat flux from lamps).

$$(a\dot{q}'')_{ext} = (a\dot{q}'')_{lamps} + (a\dot{q}'')_{flames} \quad \textbf{Eq. 1.14}$$

The subscript "lamps" refers to the prescribed heat flux from the heating units. The subscript "flames" refers to the heat flux from the flames, after ignition has occurred. Note that, each heat flux is accompanied by the absorptivity, *a*. Fuel surface absorptivity is dependent on temperature at which a source radiates energy (spectral dependence) as was described in detail by [1.142]. It was shown that the effective absorptivity of wood decreases with the temperature of the radiating body. Several other authors have explored the spectral behavior of vegetative fuels [1.143-1.145] and showed significant spectral behavior of vegetative fuel. It is also shown that the behavior can be different for dead and live foliage.

It is important to understand this behavior in order to accurately formulate an energy balance. Specifically, for the FPA experiments conducted in this work, because the heating units are IR lamps. Furthermore, the lamps are protected by quartz glass, which acts as a filter. The transmissivity significantly reduces for wavelength greater than 2 μm [1.142, 1.146]. This is further enhanced when using the quartz tube in the experimental set-up (see Chapter 2).

Explicitly for pine needle beds in the FPA, Houssami et al [1.17] have illustrated the change in surface absorptivity with source temperature similar to the study done by Chaos [1.142] for wood. They concluded that, effective surface absorptivity of dead pine needles heated by flames is 0.85-0.95 ($a_{flame}$). Contrarily, for radiation from

infrared heater (FPA heating units), it is ~ 0.64 ($a_{lamp}$), which is significantly lower and should not be ignored. This analysis technique [1.17, 1.142] was extended to live foliage in this thesis (see Chapter 5).

The radiant heat flux from the flames, $\dot{q}''_{flames}$, may be related to the flame shape. Changing ventilation conditions will impact the flame shape when for example a forced convection stretches the flames. The stretching is caused by the inertial forces that act on the flame sheet. This deformation impacts the view factor [1.141, 1.147] and therefore, the heat flux feedback from the flames to the surface.

The heat flux feedback from flames can also change when the ventilation condition is limited by reduction of the oxygen concentration. It was shown by [1.148, 1.149] that, the radiative power of flames is strongly dependent on the oxygen concentration of the environment; the radiative power increases with oxygen concentration. This is attributed to the increase in soot production with increasing oxygen concentrations, which increases the luminosity of the flame [1.148, 1.149]. Tewarson et al [1.148] mainly tested at oxygen concentration above ambient, whereas Santo et al [1.149] studied concentrations below ambient (to 18% by vol.). The increased heat flux feedback than impacts the pyrolysis rate as shown by Marlair et al [1.150] and Mulholland et al [1.151].

The explanations provided in the preceding paragraphs indicate that changing the ventilation in one way or another (blocking natural entrainment, increasing forced convection, altering oxygen concentration) will inherently impact the heat transfer. Most dominantly it alters the heat flux feedback from the flames (besides continuously cooling solid particles and gases). It is likely that smoldering combustion also changes (depending on the oxygen availability), which impacts the pyrolysis rate (heat flux from smoldering). However, this is extremely difficult to de-couple from the effects of the flame heat flux feedback. Part of this thesis explores this relationship (Chapter

3). At this stage, it is assumed that heat flux from the flames is the dominant phenomenon that drives the pyrolysis rate.

**Simplified heat transfer model for porous fuel beds**

Modeling work in this thesis includes the validation of a simplified ignition model that was developed by Simeoni et al [1.48]. The purpose of this model is to understand if a simplified formulation based on energy conservation is sufficient to predict the ignition of porous fuel beds.

This model is based on the energy conservation equation for a porous medium. It is simplified to a one-dimensional, two phase formulation. Thermal equilibrium is assumed between solid and gas phase. The fuel package is considered as a semi-infinite solid with the energy balance performed at the surface:

$$\left(\alpha\rho c_p\right)_s \frac{\partial T}{\partial t} + \left(\alpha\rho c_p\right)_g V_{g,x} \frac{\partial T}{\partial x} = k_R \frac{\partial^2 T}{\partial x^2} + a\dot{q}''_{ext} K e^{-Kx} \qquad \textbf{Eq. 1.15}$$

With the boundary conditions

$$x = 0, \quad -k_R \frac{\partial T}{\partial x} = h_T (T(0,t) - T_\infty) \qquad \textbf{Eq. 1.16}$$

$$t = 0, x \to \infty, T = T_\infty \qquad \textbf{Eq. 1.17}$$

The diffusive heat transfer coefficient, $k_R$, is due to radiative transfer. As discussed in [1.48] (and in the subsection "Radiation heat transfer"), the radiative extinction coefficient, $K$, can be estimated from the mean free path of radiation, $\delta$ (Eq. 1.10). The radiative heat transfer was linearized with the Rosseland approximation (Eq. 1.12) [1.48]. Under natural convection, the flow velocity, $V_{g,x}$, is zero. For forced airflow conditions, energy transfer in the fuel matrix is not only due to radiation but also due

to convection. This is described by the advection term in Eq. 1.15. Surface heat losses are considered to be due to convection ($h_c$) and re-radiation ($h_r$) and are lumped into a total heat transfer coefficient ($h_T$).

Assumptions that are employed here include considerations of: (1) no conduction heat transfer, (2) a semi-infinite fuel bed, (3) a thermal equilibrium between solid and gas phase, and (4) thermally thin behaving particles (ignoring heat transfer within particles).

In a first assessment, Simeoni et al [1.48] have shown the applicability of the model for natural convection conditions, but only limited experimental data was available for forced convection conditions. It is applicable for natural convection because convection heat transfer is minimized, thus radiation is prevailing. Furthermore, the model was only assessed with ignition time data. It is necessary to evaluate the performance of the model with in-depth temperature measurements, in order to confirm the predictive capability (ignition time) of the model.

It can be recognized that several input parameters are required (for gas and solid phase), for example $\rho$, $c_p$ and $a$. Such parameters can be obtained from detailed fuel characterization, which is described in detail in Chapter 2.

The criterion for ignition is the ignition temperature. A value of 300 °C is referred to as a benchmark ignition temperature for vegetative fuels, but it can vary significantly [1.2, 1.23, 1.34]. To provide a best possible validation procedure, ignition temperatures for the fuel used here is determined experimentally.

Critically, appropriate heat transfer coefficients ($h_c$ and $h_r$) are required, in order to quantify the heat losses. A value for $h_r$ can be estimated with [1.141]

$$h_r \approx \varepsilon B T_{ig}^3 \qquad \textbf{Eq. 1.18}$$

where $\varepsilon$ is the surface emissivity of the needles (~0.9 at ignition temperature), $B$ is the Stefan-Boltzmann constant (5.67 x $10^{-8}$ W.m$^{-2}$.K$^{-4}$), and $T_{ig}$ is the ignition temperature. $h_c$ can be determined from a detailed thermal analysis and calculating an appropriate Nusselt number ($Nu_L$).

$$h_c = \frac{k_{air} Nu_L}{L} \qquad \textbf{Eq. 1.19}$$

As was discussed in the previous subsection, convection heat transfer consideration in porous fuel beds is not straight forward, and may change drastically depending of the flow field and fuel bed properties. In order to estimate an appropriate value for $h_c$, a detailed thermal analysis is required. Such analysis is also required to verify assumptions (2) and (4).

*Correlations to determine a convection heat transfer coefficient*

Various dimensionless numbers are applied to the given problem to estimate $Nu_L$: (1) heated, horizontal flat plate (Eq. 1.20) [1.141, 1.152]; (2) bundle of cylinder in cross-flow (Eq. 1.21) [1.153, 1.154]; and (3) single cylinder in natural convection (Eq. 1.22) [1.155]

$$Nu_L = 0.54\, Ra_L^{1/4} \qquad \textbf{Eq. 1.20}$$

$$10^4 \leq Gr_L \leq 10^7; \quad \text{Pr} \geq 0.7$$

---

$$Nu_L = C Re_L^n Pr^m \qquad \textbf{Eq. 1.21}$$

$$10 \leq Re_{L,max} \leq 100$$

$$C = 0.9,\ n = 0.4,\ m = 0.36$$

---

$$\overline{Nu}_N = \left[0.60 + 0.387Ra^{1/6}/\left(1 + (0.559/Pr\ )^{9/16}\right)^{8/27}\right]^2 \quad \textbf{Eq. 1.22}$$

$$Ra \leq 10^{12}$$

The correlation for a bundle of cylinder in cross flow (Eq. 1.21) is for a staggered arrangement with many rows and is an averaged value for interior cylinder [1.154]. The Prandtl number (*Pr*) is evaluate at a single temperature (i.e. $Pr/Pr_s$=1 [1.154]). Summary of non-dimensional numbers used:

- Rayleigh number

$$Ra = Gr_L\ \mathrm{Pr} \quad \textbf{Eq. 1.23}$$

- Grashof number

$$Gr_L = \frac{\rho_{air}^2 g\beta\Delta T_{ig} L^3}{\mu_{air}} \quad \textbf{Eq. 1.24}$$

- Prandtl number

$$\mathrm{Pr}\ = \frac{c_{p,air}\mu_{air}}{k_{air}} \quad \textbf{Eq. 1.25}$$

- Reynolds number: (1) standard form (Eq. 1.26); and (2) porous beds (Eq. 1.27) [1.156]

$$Re_L = \frac{\rho_{air} vL}{\mu_{air}} \quad \textbf{Eq. 1.26}$$

$$Re_{L,porous} = \frac{\rho_{air} vL}{\mu_{air}\alpha_g} \quad \textbf{Eq. 1.27}$$

It is suggested in [1.141] that mixed convection, due to buoyancy and inertial forces, should be considered when the convective Froude number

$$Fr_L = \frac{v^2}{gL} \qquad \textbf{Eq. 1.28}$$

is small ($Fr_L < 1$). Only when $Fr_L < 0.1$, may forced convection be ignored [1.141]. In order to accommodate both, natural and forced convection, one must consider a modified Nusselt number that is a composite including both phenomena. Incropera et al [1.141] suggest that for mixed convection the actual Nusselt number is a combination of forced and natural, thus:

$$Nu^n = Nu_f^n + Nu_N^n \qquad \textbf{Eq. 1.29}$$

where $f$ denotes forced convection and $N$ natural convection. For cylinders in transverse flow condition, as is the case for needles, the exponent is defined as $n$=4; Considerations for other geometries and flow conditions can be found in [1.141].

Using these correlations, it is possible to determine an appropriate value for $h_c$ that can be used as input for the porous ignition model (Eq. 1.15) [1.48]. Furthermore, this parameter can also be used to explore the thermal behavior of the fuel bed and a single needle within the fuel bed, which depends on the external heating/cooling conditions described by radiation and convection.

*Thermal behavior of a fuel bed*

Traditionally, the thermal behavior of a material is evaluated with assessing the internal and external thermal resistance [1.141]. These are evaluated with an energy balance under steady state conditions:

$$\dot{q}_{in}^{"} - \dot{q}_{out}^{"} = 0 \qquad \textbf{Eq. 1.30}$$

Considering a pure convection boundary condition (heating) this results in the standard definition of the Biot number [1.141]:

$$\frac{k}{L}\left(T_{surface,sample} - T_{backface,sample}\right) = h_c\left(T_\infty - T_{surface,sample}\right) \qquad \textbf{Eq. 1.31}$$

$$\frac{\left(T_{surface,sample} - T_{backface,sample}\right)}{\left(T_\infty - T_{surface,sample}\right)} = \frac{h_c L}{k} = Bi_{conv} \qquad \textbf{Eq. 1.32}$$

where $T_\infty$ is the gas temperature. The Biot number now describes the thermal response (temperature) of the material to the given convection heat transfer conditions. In other words, it describes the relationship between convective to conduction heat transfer. The condition of the thermal behavior is strongly dependent on the heating conditions, i.e. the external thermal resistance which is convection here, but also on the conduction heat transfer, i.e. the internal thermal resistance.

When the external thermal resistance is high compared to the internal thermal resistance, then the particle heats up more uniformly and a single temperature can be assumed for the entire body. On the contrary, if the external thermal resistance is low compared to the internal thermal resistance, heat transfer within the body can be considered slow, resulting in a significant temperature differential within the body of the particle. The first condition is commonly known as a thermally thin behavior, whereas, the latter one is known as a thermally thick behavior [1.94].

In this case, the external thermal resistance is described with the convection heat transfer coefficient ($h_c$), $R_{conv} = 1/h_c$. The internal thermal resistance is described with the thermal conductivity (k), $R_{cond} = L/k$, where $L$ is the characteristic length of the

particle of interest. Finally, a thermally thin behavior occurs when $R_{conv} >> R_{cond}$. Vice versa, a thermally thick behavior occurs when $R_{conv} << R_{cond}$ [1.94].

The standard Biot number applies to convective cooling or heating with no internal heat generation (or external radiant heating). When $Bi < 0.1$, the material can be considered thermally thin. Contrarily when it is large, $Bi_{conv} > 0.1$, the material behaves thermally thick. For each condition specific analysis techniques have been developed [1.141] and using one, for example the analysis for thermally thin conditions (*lumped capacitance analysis*), when it is actually thermally thick will result in significant uncertainties.

It was discussed previously that, convection heating is likely not the only external heat transfer and that, conduction heat transfer within the porous bed is considered negligible. Therefore, the traditional analysis requires adaptation.

Benkoussas et at [1.157] have considered a different approach to estimate the thermal behavior of forest particles. They have concluded that a radiative boundary condition is more appropriate compared to the convective boundary condition from the standard Biot number (Eq. 1.32). Their definition of the Biot number takes the form

$$Bi_{rad} = \frac{a\dot{q}^{"}_{ext}L}{k\Delta T_{ig}} \qquad \textbf{Eq. 1.33}$$

This definition only accounts for radiative heating without heat losses and with internal conduction heat transfer. (Remark: this will be further discussed in the next section on the scale of the needle)

This definition can be adopted for the porous fuel bed by replacing the the thermal conductivity in Eq. 1.33 with the Rosseland approximation (Eq. 1.12), and considering the characteristic length of the sample and not the particle.

This definition ignores heat losses, which can be significant if forced convection (wind) is present (cooling). Therefore, development of this definition should include heat losses, which was done in this work. A new boundary condition, for radiative heating with heat losses can be considered (in-depth radiative transfer):

$$\frac{k_R}{L}\left(T_{surface,sample} - T_{backface,sample}\right) = \\ = a\dot{q}''_{ext} - h_T\left(T_{surface,sample} - T_\infty\right) \quad \textbf{Eq. 1.34}$$

$$\frac{\left(T_{surface,sample} - T_{backface,sample}\right)}{\left(T_{surface,sample} - T_\infty\right)} = \\ = \left(\frac{a\dot{q}''_{ext}}{\left(T_{surface,sample} - T_\infty\right)} - h_T\right)\frac{L}{k_R} \quad \textbf{Eq. 1.35}$$

The definition indicates a transient condition, due to the dependence on temperature ($T_{surface,sample} - T_\infty$). For a first approximation, the evaluation can be done at a constant surface temperature, corresponding to the ignition temperature (the same as in Eq. 1.33). Finally, a new Biot number can be defined as:

$$Bi_{rad,losses} = \left(\frac{a\dot{q}''_{ext}}{\left(\Delta T_{ig}\right)} - h_T\right)\left(\frac{L}{k_R}\right) \quad \textbf{Eq. 1.36}$$

A significant simplification of this definition is still the internal heat transfer (inside fuel matrix), i.e. radiation only. Therefore, it requires validation to what extent this definition can be used. Furthermore, the Rosseland approximate, $k_R$, depends strongly on the temperature ($k_R \propto T^3$). Therefore, the coefficient is transient. This is true for the thermal conductivity as well, because the fuel property changes with temperature [1.141]. So effectively, using a constant value for the thermal conductivity is already a substantial approximation on its own.

Additionally, the Rosseland approximation depends also on the mean path of radiation. At the time of ignition, maximum radiative heat transfer is at the surface. The transfer weakens with decreasing temperature inside the sample. For simplification, the Rosseland approximation can be averaged over the temperature spectrum that is considered here, ambient to ignition temperature.

Inherently, this also depends strongly on the bulk density of the samples. When the bulk density increases, the radiation attenuation (extinction) coefficient ($K$) increases because the solid volume fraction, $\alpha_s$, in Eq. 1.11 increases. Finally, an increasing K means that $k_R$ decreases (Eq. 1.12), which means that, radiant energy is absorbed closer to the surface of the fuel bed rather than transmitted further into the sample. This is analogous to conduction heat transfer, i.e. a lower thermal conductivity means that the thermal diffusivity is lower, and thus, the heat wave propagates slower through the material and the material heats up faster at the surface.

Using the analysis of the developed Biot number, with heat losses and in-depth radiative transfer, provides acceptable means to assess the thermal behavior of the porous media considered in this work. Experimental data will be used to verify this behavior.

This analysis can now also be adopted on the scale of the needle (as was first done by Benkoussas et al [1.157]), to provide insight into the thermal behavior of fine forest fuel particles.

*Thermal behavior of a particle in the fuel bed*

In a mathematical representation of a wildfire, the computational domain and mesh size has to be selected, so that it does not become incredibly expensive in terms of computational time. On the other hand, the mesh size has to be selected so that physical phenomena such as heat and mass transfer are still represented to an acceptable degree of uncertainty. In an ideal simulation this would mean that mesh sizes should be on

sub-foliage size scale. In a computational domain that can extend hundreds of meters or even kilometers this would make the model extremely expensive (computational time) and render it not feasible, because it would require enormous computing power. To accommodate this, computer simulations can be run with mesh size of sup-foliar size scales, where the cell represents a porous medium consisting of two phases. In doing this, the physical phenomena have to be described for porous media as discussed above.

In simulations, it is commonly assumed that, particles exhibit a thermally thin behavior (e.g. [1.17]). This assumption allows the simulation of the porous fuel beds without solving explicitly the heat transfer within the particles. Simulations become less complex and computationally expensive, but also lose a level of sophistication. Therefore, this assumption requires validation in order to assess the acceptability and limitation of it and aid in the quantification of uncertainties.

On the scale of a single particle the heat transfer can be expressed in a similar manner as was discussed on the scale of the fuel bed. The same complexity of the heating and cooling condition applies here (via radiation and/or convection). The internal heat transfer is now due to conduction (as opposed to radiative and convective for the fuel bed).

Biot number consideration

A traditional thermal analysis includes the calculation of the standard Biot number (Eq. 1.32) to determine if a *lumped capacitance analysis* (single temperature for solid particle) is appropriate [1.141]. As was discussed, this definition may not be the most accurate representation of the heating condition. Remark: the temperature term ($T_{backface}$) in Eq. 1.31, 1.32 and Eq. 1.34, 1.35 is adjusted to account for the new scenario, i.e. to represent the internal temperature at the characteristic length used.

The radiative Biot number defined by Benkoussas et al [1.157] (Eq. 1.33) is a more appropriate consideration. However, it is likely to be accompanied by large uncertainties when heat losses are high (e.g. forced convection cooling due to wind).

It is evident from Eq. 1.33 that the thermal behavior of a particle strongly depends on the external heat flux, and that there exists a threshold heat flux, above which a particle starts to behave thermally thick. Benkoussas et al [1.157] concluded that typical fine forest fuel particles transition from thermally thin to thick behavior in the range of typical wildfire heat flux levels.

The transient behavior is not a surprise, because the same is true for the convection boundary condition. If the heating rate due to convection increases, i.e. $h_c$ increases, $Bi_{conv}$ increases as well and at some point a transition from thermally thin to thick will be observed. It is however, more comprehensible to discuss the energy output of a wildfire in terms of radiative heat flux, because it can be quantified and measured in the field (e.g. [1.66]). This is a critical assessment for modeling, because if fuel particles behave as predominantly thermally thick, it suggests that models that assume thermally thin particles include a high degree of uncertainty, due to neglecting heat transfer in the solid phase [1.157].

As was discussed in the previous subsection, a drawback from Eq. 1.33 is that it does not include heat losses. Not including heat losses due to convective cooling for example, over-estimates the heating rate (under-estimates external thermal resistance) and thus under-estimates the heat flux at which particles transition to thermally thick behavior. Effectively, the convection cooling dampens the heating rate.

Physically, this goes back to the balance of the thermal resistances, internal and external, which were described in the previous subsection. For the radiative boundary condition, the external thermal resistance is due to radiation heat transfer. For a given particle the internal thermal resistance does not change. Therefore, when the heat flux increases, this means that the external thermal resistance decrease and internal

resistance becomes more important, i.e. the particle becomes thermally thick. When wind is also present, it is not only radiation that governs the external thermal resistance, but also convection. It is evident that considering a radiation only boundary condition is a significant simplification, because convection cooling is ignored.

Therefore, it is required to further develop the radiative definition of the Biot number (Eq. 1.33) in order to assess the uncertainty that arises from ignoring heat losses. This may be achieved by evaluation Eq. 1.36 with the characteristic length of the particle and substituting $k$ for $k_R$.

Besides assessing the thermal behavior and determining critical conditions at which a transition from thermally thin to thick behavior occurs ($Bi_{rad,losses}$ = 0.1), this analysis has another advantage. This is the theoretical evaluation of the critical heat flux required to overcome heat losses and can be achieved when evaluating $Bi_{rad,losses}$ = 0.

A study of the transient heat transfer problem is a useful technique to further assess the validity of a "no loss" condition (Eq. 1.33).

Transient condition

For transient heat transfer condition, the Fourier number (non-dimensional time) is used in the assessment of the particle temperature evolution and determination of wether the particle or material can be estimated as semi-infinite [1.141].

$$Fo = \frac{\alpha t}{L^2} \qquad \textbf{Eq. 1.37}$$

When the Fourier number is less or equal to 0.2 a particle can be idealized as semi-infinite [1.141]. Substituding 0.2 for $Fo$ and solving for $L$ results in

$$L = \delta \approx 2\sqrt{\alpha t} \qquad \textbf{Eq. 1.38}$$

which is referred to as the thermal penetration depth [1.141]. It defines how far the heat wave propagated into the solid at time *t*. This is analogous with the Eq. 1.11 for radiation heat transfer in porous beds. With this, one can calculate at what time the heat wave propaged through the entire solid; at this time a thermally thick, semi-infinite, behavior is no longer valid.

If the particle is thermally thin ($Bi < 0.1$) the temperature of the body is uniform and change in temperature due to heating (or cooling) can be approximated as an exponential function and the product of *Bi* and *Fo* [1.141]:

$$\theta^* = \frac{\theta}{\theta_0} = \frac{(T - T_\infty)}{T_0 - T_\infty} = \mathrm{e}^{-BiFo} \qquad \textbf{Eq. 1.39}$$

Where *T* is the particle temperature, $T_0$ is the particle initial temperature and $T_\infty$ is the gas temperature. The parameter $\theta^*$ is the non-dimensional particle (body) temperature, and plotting this parameter against time (or *Fo*) allows the assessment of the particle temperature evolution under the given heat transfer condition. A value of unity refers to no temperature change (initial condition). Contrarily, a value of zero means that the particle has reached its equilibrium temperature. The product of the Biot and Fourier number depends on the boundary condition that is considered. For a convective boundary condition it is

$$Bi_{conv}Fo = \frac{h_c \alpha t}{kL} = \frac{h_c \alpha t A}{kV} = \frac{h_c A}{\rho c_p V} t \qquad \textbf{Eq. 1.40}$$

Constant parameters can be lumped together

$$\tau_{conv} = \left[\frac{h_c A}{\rho c_p V}\right]^{-1} = \left[\frac{h_c \sigma}{\rho c_p}\right]^{-1} \qquad \textbf{Eq. 1.41}$$

$$Bi_{conv}Fo = \frac{t}{\tau_{conv}} \quad \textbf{Eq. 1.42}$$

Tau ($\tau$) is the thermal time constant [1.141]. It represents the time required for a particle to reach 63% of its equilibirum temperature. For example, for a convective boundary condition with a hot gas at 500 °C , it is the time required to reach 315 °C . For a radiative boundary condition, the concept is the same. However, the association to the final/equilibrium temperature is unknown, because the boundary condition is a heat flux condition, not a temperature boundary condition. With the same steps, $\tau$ can be calculated for the radiative boundary conditions for the ”no loss” and “loss”, respectively:

$$\tau_{rad} = \left[\frac{a\dot{q}_e^{''}\sigma}{\Delta T_{ig}\rho c_p}\right]^{-1} \quad \textbf{Eq. 1.43}$$

$$\tau_{rad,losses} = \left[\left(\frac{a\dot{q}_e^{''}}{(\Delta T_{ig})} - h_T\right)\frac{\sigma}{\rho c_p}\right]^{-1} \quad \textbf{Eq. 1.44}$$

Increasing $\tau$ corresponds to slower change in body temperature. Plotting $\theta^*$ and comparing values of $\tau$ at a range of heating and cooling conditions allows the evaluation of the “no loss” condition [1.157] and determine acceptable limitations.

*Water (liquid) in the solid phase*

At ambient temperature (and pressure) water is in its liquid form and is encapsulated within the fuel particle, either as free water, or bound water (within the cell tissue). The presence of water changes the effective (apparent) fuel properties (e.g. $k$, $\rho$, $c_p$), which are critical for heat transfer mechanism. Thus, changing either one of these properties will inherently change the thermal response of the particle, i.e. the particle

will heat up slower or faster. For example, if the density goes up, thermal mass ($\rho c_p$) increases and thus, time to ignition is longer, because it takes longer for the particle to reach its ignition temperature [1.94, 1.95]. This is also reflected by the behavior of $\tau$ in Eq. 1.41, 1.43, and 1.44.

Specific heat will likely also be a function of the FMC, as is the case for wood [1.158-1.160]. The study of Taoukil et al [1.160] is included here because it evaluates various models for each thermophysical property. It shows how the effects of these parameters are competing, and a similar scenario for live forest fuel is likely (composite material: needle matter and water).

Liquid water in the particle does not only change effective properties, but it also adds an additional term in an energy balance, that must be accounted for. This term is the latent heat of vaporization of water [1.141], and describes a heat sink in the energy balance. Additional heat (energy) is required to vaporize the water. Under constant heating conditions, particles at 0% FMC would utilize this energy to raise the solid temperature and initiate pyrolysis, thus resulting in a faster ignition. Therefore, the amount of water that is taking part in the vaporization process should correlate to the time to ignition.

The amount of water that is present is also critical. The more water is present the more energy is required to evaporate sufficient amounts before ignition can commence, which will further delay the time to reach ignition. Past research (e.g. [1.33]) has shown that not all water is required to have been evaporated before ignition of live foliage. This was mainly attributed to the content of flammable extractives (e.g. terpenes), which vaporize at temperatures lower than water [1.161]. Quantification of the amount of water remaining in the fuel at the point of ignition is important, but has yet to be fully established. For example Jolly and Butler [1.33] have indicated that it changes depending on the initial amount of water (FMC) in the fuel. Furthermore, it is also likely that it strongly depends on the heating rate (external thermal resistance).

The complexity of the phenomenon of the water release mechanism requires more research to fully understand it. Part of this thesis aims to provide additional analysis and supplement past work.

*Live foliage*

Under a heat insult, water is vaporized and released from the needle. The water vapor acts as a heat sink in the gas phase, cooling the gas mixture and flames. Additionally, it also displaces oxygen from the reaction zone. These phenomena describe the quenching of the flames. If the rate of evaporation is high enough, flaming will not be sustained. This marks the moisture of extinction described in [1.26]. If an external heat flux is still present to drive the pyrolysis, combustion may continue when sufficient water has been evaporated.

For dry fuel, flaming is sustained because the heat flux feedback to the fuel surface is high enough to pyrolyze the fuel. For sustained flaming to continue above wet needle samples, a similar heat flux feedback needs to exist to drive pyrolysis. This feedback can be related to the flame height (via a view factor), flame temperature ($T_{flame}$) and emissivity ($\varepsilon$).

Water vapor will cool the flames, directly impacting the heat flux feedback, by reducing $T_{flame}$. At the same time, $\varepsilon$ depends on the flame temperature. If the flame height is not impacted by the water vapor, the view factor for dry and wet samples is the same. This is, however, an assumption that is challenging to uphold, because the ability of water vapor to displace oxygen will affect the combustion reaction zone. The displacement of oxygen means that flammable fuel vapor has to travel further in order to react with a sufficient amount of oxygen. During this extra travel time gas temperature drop, at which point a combustion reaction will not occur any more, even if the mixture is flammable. This will lead to less efficient combustion and smaller flame heights, which also reduces the heat flux feedback.

Discussion of the impact of water, in the solid and gas phase, describes why wet fuel particles take longer to ignite and why it can be expected that, combustion intensity decreases with increasing water content.

Various works have observed such tendencies in experimentation on various scales. Most frequently, a positive linear trend between ignition time and FMC has been documented [1.24-1.29, 1.31, 1.34, 1.36-1.38, 1.50. 1.93]. Less common is the documentation of combustion intensity with respect to FMC. Babrauskas [1.96], Baker [1.162] and Possell and Bell [1.163] determined an exponential relation between pHRR and FMC. Jervis et al [1.50] showed a negative linear relationship, however, only with limited data (FPA tests with pine needles). Thomas et al [1.45] showed a polynomial relationship (FPA tests with pine needles). This polynomial relationship compared well with studies conducted by Weise et al [1.28] and Etlinger and Beall [1.36], who tested vegetation fuel beds in the Cone Calorimeter and intermediate scale calorimeter.

### *1.3.6. Mass transfer in porous fuel beds*

As was discussed previously, mass transfer in porous media is also critical for understanding the ignition and burning behavior of porous wildland fuel. Under natural convection, flow fields are driven by buoyancy forces that are induced by temperature differences. Contrarily, for forced convection, flow fields are driven by inertial forces. It was discussed that the convective Froude number (Eq. 1.28) can be used to determine when one condition prevails over the other.

The next sections explain the mass transfer consideration that need to be considered in order to study the ignition and burning behavior of forest fuel beds. The discussion is again split into pre- and post-ignition stages (see Fig. 1.4). The mass transfer, pyrolysis and oxygen mass flow rates, are critical for the formation of a flammable gas mixture before ignition. After ignition, the mass transfer is important in controlling the combustion intensity and efficiency.

### Pre ignition

A flammable gas mixture (see Fig. 1.9) needs to be formed above the fuel bed for ignition to occur. This is driven by the mass transfer of oxidizer (oxygen in this case), $\dot{m}_{O_2}$, and pyrolysis gases, $\dot{m}_p$. The pyrolysis rate is governed by the energy received by the solid phase, i.e. the external heat flux in this phase. The introduction of an oxidizer flow (as opposed to a 0% oxygen environment) can alter the pyrolysis rate by appearance of oxidative pyrolysis [1.164-1.169]. Although oxidative pyrolysis is of interest in wildfire combustion dynamics, it is not explicitly explored in this thesis.

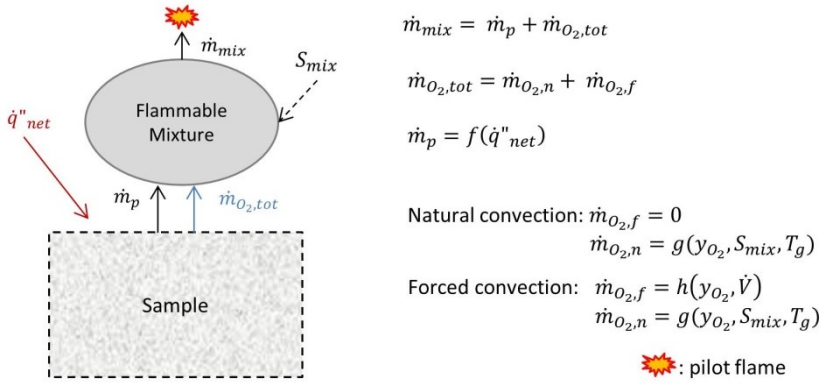


**Fig. 1.9. Schematic of sample with mass transfer considerations before ignition (Stage 1).**

The oxygen mass flow rates shown in Fig. 1.9 are due to natural entrainment, $\dot{m}_{O_2,n}$, driven by buoyancy forces, and forced airflow, $\dot{m}_{O_2,f}$, driven by inertial forces. The delivery of oxygen due to natural entrainment depends on the oxygen concentration of the environment, $y_{O_2}$, a characteristic surface area through which oxygen can be entrained, $S_{mix}$, and the temperature of the gas phase, $T_g$, which drive the buoyancy forces.

In a natural convection condition, $\dot{m}_{O_2,n}$ is the only oxygen mass flow requirement, because $\dot{m}_{O_2,f} = 0$. When a forced convection is imposed, $\dot{m}_{O_2,f} \neq 0$, and becomes a function of the oxygen concentration, $y_{O_2}$, and flow magnitude, $\dot{V}$. It becomes evident

that the ignition behavior (time to ignition) may be impacted by either a change in $\dot{m}_p$ or $\dot{m}_{O_2,tot}$.

### Post ignition

In this stage, the mass transfer scenario is depicted in Fig. 1.10 below. After ignition, pyrolysis gases are produced and mix with oxygen ($\dot{m}_{O_2,n}$) in the reaction zone (flame sheet).

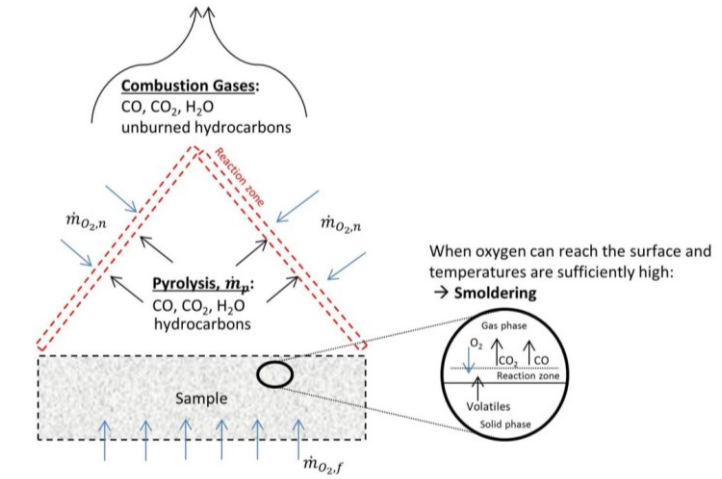


**Fig. 1.10. Schematic of sample with mass transfer considerations after ignition (Stage 2).**

Smoldering combustion (heterogeneous surface reaction) can occur only when oxygen reaches the solid interface. It is evident that a forced oxygen flow ($\dot{m}_{O_2,f}$) will have a significant impact on the oxygen reaching the fuel surface and increasing the surface reaction. Additionally, it can also cause a change of flaming regime, because oxygen (from $\dot{m}_{O_2,f}$) and pyrolysis products can mix within the fuel bed before reaching the reaction zone (flame sheet). The change in flaming regime is a transition from diffusion to premixed type, which will be discussed. This phenomenon needs to be understood, because it was observed in the experimentation discussed in Chapter 3. The importance lies in the fundamental difference in mass transfer, but also the resulting impact on the heat flux feedback from changing flame properties.

*Flaming regimes (diffusion and premixed)*

Typically, burning in the open (natural convection) results in diffusion flames (e.g. [1.94, 1.95]). The simplest example for a diffusion flame is a candle flame. In these types of flames, combustible gases and oxidizer enter the reaction zone as separate streams. These may be laminar or turbulent (compare a candle flame to a bonfire flame), depending on the local mass balance of pyrolysis rate and oxidizer flow rate. Alternatively, flames may be a premixed type, as for example a jet flame or an acetylene torch. In such flame types, both combustible gases and oxidizer are premixed in a single stream before entering the reaction zone (Fig. 1.10).

*Occurrence of transition from diffusion to premixed flaming*

The transition between flaming regimes occurs when the oxygen in the environment around the combustion zone is reduced. This is a well-known phenomenon that has been identified by several researchers in various experimental apparatuses [1.170-1.172]. An early study by Simmons and Wolfhard [1.170] identified limiting oxygen concentrations (LOC) for diffusion and premixed flames. The LOC for premixed flames is lower than the LOC for diffusion flames [1.170]. They also concluded that an exact threshold between flame regimes is not only a function of the oxygen concentration ($y_{O_2}$), but also of the flow rates of the oxygen and combustible gas [1.170]. Marquis et al [1.171] observed the transition from diffusion to premixed and finally to no-flaming regime (~ 10% oxygen) for PMMA samples using the Controlled Atmosphere Cone Calorimeter (CACC). Biteau et al [1.172] observed a transition for a fuel mixture of starch, lactose and potassium nitrate using the FPA. The threshold was 17% oxygen. A no-flaming state was not observed, because the fuel mixture included oxidizer (potassium nitrate). Jervis [1.51] did not report a transition between diffusion and premixed regimes for wood products, but found a LOC for the no-flaming state around 14%.

Simmons and Wolfhard [1.170] and others [1.171, 1.172, 1.173] have attributed this LOC of diffusion (or premixed) flames to the change in thermal capacity of the gas-air mixture, induced by the gas used to dilute the atmosphere (this thesis nitrogen). The flame temperature reduces when oxygen concentration in the atmosphere decrease (decreasing soot production). It reduces until a limiting temperature is reached. Below this threshold, combustion will cease, due to insufficient energy. It is highlighted in [1.173] that the gas used for the dilution is important and will impact the flame temperature and thus extinction condition. Marlair et al [1.150] have shown the impact of different dilution gases on the combustion dynamics (pyrolysis rate). Changing flame properties has an inherent effect on the heat flux feedback to the solid phase as was previously discussed in the "heat transfer" section.

Understanding this process aids in analyzing combustion test data, such as duration of flaming period, mass loss rates, heat release rates, and others. In this thesis, it will be shown that transition from diffusion to premixed type flaming at reduced oxygen environment was observed when burning pine needle beds in the FPA.

*Ventilation condition*

A variation of ventilation conditions was tested in this study. In the context of this work, ventilation conditions refers to either (1) a varying area through which air can be entrained or (2) varying forced convection (magnitude of airflow). A detailed understanding of the combustion behavior of fuel in changing ventilation regimes was explained by Tewarson and Steciak [1.175]. In fact, their exploration utilized the FM Small-Scale Combustibility Apparatus which is a predecessor of the FPA used in this thesis. They explained that fundamentally, combustion will change from fuel controlled to ventilation controlled when: (1) the velocity or density of a supplied forced ventilation flow, or the ventilation area is decreased; (2) the oxygen concentration of the forced ventilation flow is decreased; (3) the heat flux from flames is increased; or (4) external heat flux is increased.

Several of these mechanisms are explored experimentally in this thesis in conjunction with porous forest fuel beds (1, 2 and 4). Changes in heat flux feedback (3) are a consequence of changing the ventilation condition (1, 2 or 4), which will be explained in detail in Chapter 3. If desired, a change in heat flux feedback may be induced by using fuel that is chemically different, i.e. produces different pyrolysis gases that react in the combustion, or vary the fuel load, which will alter the pyrolysis rate.

Various authors [1.175-1.177] have established a parameter that allows the quantification of the combustion scenario. This is known as the equivalence ratio (Φ), which is the actual fuel-to-air ratio, normalized by the stoichiometric fuel-to-air ratio. If Φ is equal to one, the reaction is at its stoichiometric balance. If $\Phi < 1$, excess oxygen is present and the combustion is well-ventilated. When $\Phi > 1$, excess fuel is present and the combustion is oxygen limited. The two ventilation scenarios (well- and under-ventilated) are summarized in Table 1.1.

Table 1.1. Summary of two ventilation conditions.

| Ventilation condition | Relationship between mass flow rate of oxidizer and pyrolysis gases | Combustion dynamics |
|---|---|---|
| 1. Well-ventilated (fuel lean) | $\Phi < 1$ | Fuel controlled, $\dot{m}_p$ |
| 2. Under-ventilated (fuel rich) | $\Phi > 1$ | Ventilation controlled, $\dot{m}_{O_2,tot}$ |

In scenario (1) the pyrolysis rate governs the combustion, whereas, in (2) combustion is governed by the oxygen flow rate. The occurrence of one scenario over the other can be achieved by either varying $\dot{m}_p$ or $\dot{m}_{O_2,tot}$.

The pyrolysis rate, $\dot{m}_p$ is impacted mainly by the heat transfer, $\dot{q}''_{net}$ (Fig. 1.9), and smoldering intensity. In the given experimentation $\dot{m}_p$ is not explicitly controlled, but inherently impacted by a change in heat flux feedback as explained previously.

Two mechanisms that may be used to alter the oxygen flow rate, $\dot{m}_{O_2,tot}$ are: (1) the flow magnitude, $\dot{V}$, which also impacts the heat transfer (convective cooling), and (2)

the oxygen concentration, $y_{O_2}$, which does not change the heat transfer (at constant flow magnitude). As described by Tewarson [1.175] changing these two variables will change the combustion dynamics. Both of these mechanisms are explored experimentally in this thesis.

The importance of understanding these phenomena is because they affect the pyrolysis and combustion processes. It was identified in the past that pyrolysis and combustion in oxygen limited environments can generate different products which is attributed to reaction chemistry [1.148, 1.175-1.185]. Both pyrolysis and combustion in oxygen limited scenarios mainly result in elevated generation of CO and reduced generation of $CO_2$ (e.g. [1.177]). Most research in this topic is associated to fundamental fire dynamics (combustion dynamics and flame properties) [1.148, 1.149, 1.175, 1.184] and enclosure fire dynamics [1.175-1.178, 1.182, 1.185]. A major cause of deaths in enclosure fires is the inhalation of toxic gases, one of which is CO [1.185, 1.186]. The relevance for wildfire research lies in a more global or large scale view, where atmospheric conditions are impacted by the emissions of wildfire [1.75-1.77]. Changing atmospheric conditions will have inherent effects on the climate. Therefore, exploring the origins of emissions from wildfire is crucial in understanding the impact on climate changes.

High levels of incomplete combustion in oxygen limited environments reduce the combustion efficiency and thus the combustion intensity. The heat release rate ($\dot{Q}$; [kW]) of a material can be estimated as given in [1.94, 1.95]:

$$\dot{Q} = \chi \Delta h_c \dot{m} \qquad \textbf{Eq. 1.45}$$

where $\chi$ is the combustion efficiency [-], $\Delta h_c$ is the heat of combustion [kJ.kg$^{-1}$] and $\dot{m}$ is the burning rate [kg.s$^{-1}$]. When the combustion is complete (ideal scenario), $\chi$ is one; for incomplete combustion, $0 < \chi < 1$. It is evident that when the combustion efficiency decreases, the combustion intensity decreases. This shows the important position of

the combustion efficiency in an accurate determination of the combustion intensity. It was discussed in Section 1.3.2, that one disadvantage in the definition of Byram's fireline intensity (Eq. 1.4) is the lack of quantification of the combustion efficiency, which was explored in detail by Santoni et al [1.53].

*Limited oxygen conditions in wildfire*

Wildfires occur in the open and thus combustion in limited oxygen conditions is not necessarily apparent, which means that it is likely that combustion efficiency is generally high. However, it is likely that certain scenarios exist that may promote elevated levels of incomplete combustion: (1) limited ventilation area created by topography (slope of canyons), or very dense vegetation; (2) combustion within the interior of a large fire front, or combustion of particles that are located within the plume (canopy fuel); and (3) released water vapor, as the fuel is heated, into the combustion zone has the equivalent effect to blocking the entrainment air, or reducing the oxygen concentration of the environment. The water vapor displaces oxygen (and other components) from the combustion zone, therefore, limiting the oxygen availability. Besides displacing oxygen, water vapor acts as a heat sink in the gas phase and cools pyrolysis gases and flames, which further impact the combustion efficiency and heat flux feedback and thus the pyrolysis rate.

## *1.4. Chapter summary and conclusions*

This chapter has laid out the motivation, challenges, and research goals that provide the basis for the work presented in the following chapters. It has provided background information to the importance on flammability and the relation to wildfire behavior and wildfire research as a whole. Critical aspects that define flammability of a material, such as the ignition and burning behavior are explained. It has been discussed that fundamental heat and mass transfer mechanisms must be explored in order to adequately characterize the flammability of wildland fuels. Discussion of literature

illustrated the still ongoing search for a unified methodology for wildland fuel flammability. Background information concerning the heat and mass transfer mechanisms in porous wildland fuel beds is presented. This includes topics such as in-depth radiation, convection heat transfer considerations, fuel bed and particle thermal behavior, FMC effects and ventilation conditions.

### *1.5. References*

[1.1] D.M. Theobald, W.H. Romme. Expansion of the US Wildland-Urban Interface. Landscape and Urban Planning 83 (2007) 340-354.

[1.2] R.B. Hammer, S.I. Stewart. V.C. Radeloff. Demographic Trends, the Wildland-Urban Interface, and Wildfire Management. Society and Natural Resources 22/8 (2009) 777-782.

[1.3] V.C. Radeloff, R.B. Hammer, S.I. Stewart, J.S. Fried, S.S. Holcomb, J.F. McKeefry. The Wildland-Urban Interface in the United States. Ecological Applications 15/3 (2005) 799-805.

[1.4] J.K. Agee, C.N. Skinner. Basic Principles of Forest Fuel Reduction Treatments. Forest Ecology and Management 211 (2005) 83-96.

[1.5] E.D. Reinhardt, R.E. Keane, D.E. Calkin, J.D. Cohen. Objectives and Considerations for WIldland Fuel Treatment in Forested Ecosystems of the Interior Western United States. Forest Ecology and Management 256 (2008) 1997-2006.

[1.6] J. Cohen. The Wildland-Urban Interface Fire Problem. Fremontia 38/2-38/3 (2010) 16-22.

[1.7] W.E. Mell, S.L. Manzello, A. Maranghides, D. Butry, R.G. Rehm. The Wildland-Urban Interface Fire Problem – Current Approaches and Research Needs. International Journal of Wildland Fire 19 (2010) 238-251.

[1.8] H.E. Anderson. Heat Transfer and Fire Spread. Research Paper INT-69. US Forest Service, Northern Forest Fire Laboratory, Missoula, Montana, USA (1969)

[1.9] W.H. Frandsen. Fire Spread through Porous Fuels from the Conservation of Energy. Combustion and Flames 16 (1971) 9-16.

[1.10] R.C. Rothermel. A Mathematical Model for Predicting Fire Spread in Wildland Fuels. INT-115. USDA, Forest Service, Ogden, UT, USA (1972).

[1.11] F.A. Albini. Wildland Fire Spread by Radiation – a Model Including Fuel Cooling by Natural Convection. Combustion Science and Technology 45 (1986) 101-113.

[1.12] N.J. de Mestre, E.A. Catchpole, D.H. Anderson, R.C. Rothermel, Uniform Propagation of a Plana Fire Front Without Wind. Combustion Science and Technology 65 (1989) 231-244.

[1.13] B. Porterie, D. Morvan, J.C. Loraud, M. Larini. Fire Spread Through Fuel Beds: Modeling of Wind-Aided Fires and Induced Hydrodynamics. Physics of Fluids 12/7 (2000) 1762-1782.

[1.14] A. Simeoni, P.A. Santoni, M. Larini, J. Belbi. Reduction of a Multiphase Formulation to Include a Simplified Flow in a Semi-Physical Model of Fire Spread Across a Fuel Bed. International Journal of Thermal Science 42 (2003) 95-105.

[1.15] F. Morandini, A. Simeoni, P.A. Santoni, J.H. Balbi. A Model for the Spread of Fire Across a Fuel Bed Incorporating the Effects of Wind and Slope. Combustion Science and Technology 177/7 (2005) 1381-1418.

[1.16] A.M. Grishin. Mathematical Modeling Forest Fire and New Methods Fighting Them. Publishing House of Tomsk University, Tomsk, Russia, 1997.

[1.17] M. El Houssami, J.C. Thomas, A. Larmorlette, D. Morvan, M. Chaos, R. Hadden, A. Simeoni. Experimental and Numerical Studies Characterizing the Burning Dynamics of Wildland Fuels. Combustion and Flames 168 (2016) 113-126.

[1.18] D.J. Nowakowski, J.M. Jones. Unanalyzed and potassium-catalyzed pyrolysis of the cell-wall constituents of biomass and their model compounds. Journal of Analytical and Applied Pyrolysis 83 (2008) 12-25.

[1.19] S. Liodakis, D. Bakirtzis, A. Dimitrakopoulos. Ignition Characteristics of Forest Species in Relation to Thermal Analysis Data. Thermochimica Acta 390 (2002) 83-91.

[1.20] S. Liodakis, T. Kakardakis, S. Tzortzakou, V. Tsapara. How to Measure the Particle Ignitibility of Forest Species by TG and LOI. Thermochimica Acta 477 (2008) 16-20.

[1.21] A.A. Pappa, N.E. Tzamtzi, M.K. Statheropoulous, G.K. Parissakis. Thermal analysis of Pinus halepensis pine-needles and their main components in the presence of (NH4)2HPO4 and (NH4)2SO4. Thermochimica Acta 261 (1995) 165-173.

[1.22] M.K. Statheropoulous, M. Liodakis, N.E. Tzamtzi, A.A. Pappa, A. Kyriakou. Thermal Degradation of Pinus Halepensis Pine-Needles Using Various Analytical Methods. Journal of Analytical and Applied Pyrolysis 43/2 (1997) 115-123.

[1.23] H.E. Anderson. Forest Fuel Ignitibility. Fire Technology 6/4 (1970) 312-319.

[1.24] B. Ubysz, J.C. Valette. Flammability: Influence of Fuel on Fire Initiation. In Towards Integrated Fire Management- Outcomes of the European Project Fire Paradox. J.S. Silva, F. Rego, P. Fernandes, E. Rigolot (editors). European Forest Institute Research Report 23 (2010).

[1.25] C. Moro. Flammability measurements for Erica arborea, INRA, Le Ruscas (1989 – 2007), relation between ignition time and moisture content. EU FIRE LAB. < http://www.eufirelab.org/specific_view.php?unit=2&ID_encour=191&type=1>.

[1.26] A.P. Dimitrakopoulos, K.K. Papaioannou. Flammability Assessment of Mediterranean Forest Fuels, Fire Technology, 37(2) (2001) 143-152.

[1.27] A.C. Dibble, R.H. White, P.K. Lebow. Combustion characteristics of north-eastern USA vegetation tested in the cone calorimeter: invasive versus non-invasive plants. International Journal of Wildland Fire, 16 (2007) 426-443.

[1.28] D.R. Weise, R.H. White, F.C. Beall, M. Etlinger. Use of the Cone Calorimeter to Detect Seasonal Differences in Selected Combustion Characteristics of Ornamental Vegetation. International Journal of Wildland Fire 14 (2005) 321-338.

[1.29] R.H. White, D.R. Weise, K. Mackes, A.C. Dibble. Cone Calorimeter Testing on Vegetation: An Update. Proceedings of the 35th International Conference on Fire Safety. Columbus, OH, USA (2002) 1-12.

[1.30] R.H. White, W.C. Zipperer. Testing and Classification of Individual Plants for Fire Behavior: Plant Selection for the Wildand-Urban Interface. International Journal of Wildland Fire 19 (2010) 213-227.

[1.31] W.M. Jolly, J. Hintz, R.C. Kropp, E. Conrad. Physiological drivers of the live foliar moisture content 'spring dip' in Pinus resinosa and Pinus banksiana and their relationship to foliar flammability. Proceedings of the 7th International Conference on Forest Fire Research. Coimbra, Portugal (2014).

[1.32] W.M. Jolly, et al. Relationships between moisture, chemistry, and ignition of Pinus contorta needles during the early stages of mountain pine beetle attack. Forest Ecology and Management 269 (2012) 52-59.

[1.33] W.M. Jolly. B.W. Butler. Final Report for JFSP-Funded Project entitled: "Linking Photosynthesis and Combustion Characteristics in Live Fuels: The Role of Soluble Carbohydrates in Fuel Preheating". JFSP Project ID: 10-1-08-6.

[1.34] S. McAllister, I. Grenfell, A. Hadlow, W.M. Jolly, M. Finney, J. Cohen. Piloted ignition of live forest fuels. Fire Safety Journal, 51 (2012) 133-142.

[1.35] S. McAllister, D.R. Weise. Effects of Season on Ignition of Three Species of Live Wildland Fuels using the FIST apparatus. Spring Technical Meeting of the Western States Section of the Combustion Institute, Pasadena, California, USA (2014).

[1.36] M.G. Etlinger. F.C. Beall. Development of a Laboratory Protocol for Fire Performance of Landscape Plants. International Journal of Wildland Fire 13 (2004) 479-488.

[1.37] J.R. Weir, J.D. Scaska. Ignition and fire behaviour of Juniperus virginiana in response to live fuel moisture and fire temperature in the southern Great Plains. International Journal of Wildland Fire 23 (2014) 839-844.

[1.38] G. Pellizaro, P. Duce, A. Ventura, P. Zara. Seasonal Variations of Live Moisture Content and Ignitibility in Shrubs of the Mediterranean Basin. International Journal of Wildland Fire 16 (2007) 633-641.

[1.39] C. Schemel, A Simeoni, H. Biteau, J. Riviera, J.L. Torero. A Calorimetric Study of Wildland Fuels. Experimental Thermal and Fluid Science 32 (7) (2008) 1381-1389.

[1.40] C. Schemel. Transport Effects on Calorimetry of Porous Wildland Fuels. University of Edinburgh, Edinburgh, UK. 2008. Ph.D. Thesis.

[1.41] P. Bartoli, A. Simeoni, H. Biteau, J.L. Torero, P.A. Santoni. Determination of main parameters influencing forest fuel combustion dynamics. Fire Safety Journal 46 (1-2) (2011) 27-33.

[1.42] P. Bartoli, A. Simeoni, J.L. Torero, P.A. Santoni. Experimental Study on the Combustion Dynamics of Forest Floor Fuel Beds. Proceedings of the 6th International Conference on Forest Fire Research. Coimbra, Portugal (2010).

[1.43] P. Bartoli. Feux de forêt: amélioration de la connaissance du couplage combustible-flamme. Universite de Corse-Pascal Paoli. 2011. Ph.D. (in French)

[1.44] J.C. Thomas, J.N. Everett, A. Simeoni, N. Skowronski, J.L. Torero. Flammability Study of Pine Needle Beds. Proceedings of the 7th International Seminar on Fire and Explosion Hazards, Providence, RI, USA, (2013).

[1.45] J.C. Thomas, A. Simeoni, M. Gallagher, N.S. Skowronski. An Experimental Study Evaluating the Burning Dynamics of Pitch Pine Needle Beds Using the FPA. Proceedings of the 11th International Symposium on Fire Safety Science. Christchurch, New Zealand, (2014) pp. 1406-1419.

[1.46] A. Simeoni, P. Bartoli, J.L. Torero, P.A. Santoni. On the Role of Bulk Properties and Fuel Species on the Burning Dynamics of Pine Forest Litters. Proceedings of the 10th International Symposium on Fire Safety Science. University of Maryland, Maryland, USA (2011) 1401-1414.

[1.47] A. Simeoni, J.C. Thomas, P. Bartoli, P. Borowjeck, P. Reszka, F. Colella, P.A. Santoni, J.L. Torero. Flammability studies for wildland fuels using the Fire Propagation Apparatus. Fire Safety Journal 54 (2012) 203-2017.

[1.48] A. Simeoni, F. Colella, E. Martinot, P. Bartoli, J.L. Torero. Flaming Ignition of Pine Needle Beds. Proceedings of the 7th International Conference on Forest Fire Research, Coimbra, Portugal (2010).

[1.49] J.L. Torero, A. Simeoni. Heat and Mass Transfer in Fires: Scaling Laws, Ignition of Solid Fuels and Application to Forest Fires. The Open Thermodynamics Journal 4 (2010) 145-155.

[1.50] F.X. Jervis, G. Rein. Experimental study on the burning behavior of Pinus halepensis needles using small-scale fire calorimetry of live, aged and dead samples. Fire and Materials (2015)

[1.51] F.X. Jervis, Application of Fire Calorimetry to Understand Factors Affecting flammability of Cellulosic Material: Pine Needles, Tree Leaves and Chipboard. University of Edinburgh, UK, 2012. PhD.

[1.52] F. Morandini, Y. Perez-Ramirez, V. Tihay, P.A. Santoni, T. Barboni. Radiant, Convective and Heat Release Characterization of Vegetation Fire. InternationalJournal of Thermal Sciences 70 (2013) 83-91.

[1.53] P.A. Santoni, F. Morandini, T. Barboni. Determination of Fireline Intensity by Oxygen Consumption Calorimetry. Journal for Thermal Analysis and Calorimetry 104 (2011) 1005-1015.

[1.54] J.L. Dupuy. Slope and Fuel Load Effects on Fire Behavior: Laboratory Experiments in Pine Needles Fuel Beds. International Journal of Wildland Fire 5/2 (1995) 153-164.

[1.55] V. Tihay, F. Morandini, P.A. Santoni, Y. Perez-Ramirez, T. Barboni. Combustion of Forest Litters under Slope Conditions: Burning Rate, Heat Release Rate, Convection and Radiant Fractions for Different Loads. Combustion and Flames 161 (2014) 3237-3248.

[1.56] J.H. Balbi, D.X. Viegas, J.L. Rossi, C. Rossa, F.J. Chatelon, D. Cancellieri, A. Simeoni, T. Marcelli. Surface Fires: No Wind, No Slope, Marginal Burning. Journal of Environmental Science and Engineering A3 (2014) 73-86.

[1.57] B.W. Butler, W.R. Anderson, E.A. Catchpole. Influence of Slope on Fire Spread Rate. US Forest Service Proceedings RMRS-P-46CD. US Forest Service. Rocky Mountain Research Station, Missoula, MT (2007).

[1.58] X. Xie, N. Liu, D. Viegas, J.R. Raposo. Experimental Research on Upslope Fire and Jump Fire. Proceedings of the 11th International Symposium on Fire Safety Science. Christchurch, New Zealand, (2014) pp. 1430-1442.

[1.59] D.X. Viegas, M. Almeida, J. Raposo, D. Davim. Experimental Forest Fire Research. Proceedings of the 15th International Conference on Experimental Mechanics. Porto, Portugal, July 2012.

[1.60] J.M. Varner, J.M. Kane, E.M. Banwell, J.K. Kreye. Flammability of Litter from Southeastern Trees: A Preliminary Assessment. Proceedings of the 17th Biennial Southern Silvicultural Research Conference, Shreveport, Luisiana, USA (2012) 183-187.

[1.61] M.A. Finney, J.D. Cohen, J.M. Forthofer, S.S. McAllister, M.J. Gollner, D.J. Gorham, K. Saito, N.K. Akafuah, B.A. Adam, J.D. English. Role of Buoyant Flame Dynamics on Wildfire Spread. Proceedings of the National Academy of Science USA 112/32 (2015) 9833-9838.

[1.62] G. Rein. Breakthrough in the Understanding of Flaming Wildfire. Proceedings of the National Academy of Science USA 112/32 (2015) 9795-9796.

[1.63] F. Morandini, X. Silvani. Experimental Investigation of the Physical Mechanisms Governing the Spread of Wildfires. International Journal of Wildland Fire 19 (2010) 570-582.

[1.64] P.A. Santoni, A. Simeoni, J.L. Rossi, F. Bosseur, F. Morandini, X. Silvani, J.H. Balbi, D. Cancellieri, L. Rossi. Instrumentation of Wildland Fire: Characterisation of a Fire Spreading through a Mediteranean Shrub. Fire Safety Journal 41 (2006) 171-184.

[1.65] F. Morandini, X. Silvani, L. Rossi, P.A. Santoni, A. Simeoni, J.H. Balbi, J.L. Rossi, T. Marcelli. Fire Spread Experiment Across Mediterranean Shrub: Influence of Wind on Flame Front Properties. Fire Safety Journal 41 (2006) 229-235.

[1.66] X. Silvani, F. Morandini. Fire Spread Experiments in the Field: Temperature and Heat Fluxes Measurements. Fire Safety Journal 44 (2009) 279-285.

[1.67] D. Viegas, A. Simeoni. Eruptive Behavior of Fires. Fire Technology 47 (2011) 303-320.

[1.68] E.V. Mueller, et al. An Experimental Approach to the Evaluation of Proscribed Fire Behavior. Advances in Forest Fire Research. Coimbra, Portugal (2014) 41-53.

[1.69] M.E. Alexander, M.G. Cruz. Assessing the Effect of Foliar Moisture on the Spread Rate of Crown Fires. International Journal of Wildland Fires 22/4 (2012) 415-427.

[1.70] C.E. Van Wagner. Conditions for the Start and Spread of Crown Fire. Canadian Journal of Forest Research 7 (1976) 23-34.

[1.71] M.G. Cruz, M.E. Alexander. Assessing Crown Fire Potential in Coniferous Forests of Western North America: A Critique of Current Approaches and

Recent Simulation Studies. International Journal of Wildland Fire 19 (2010) 377-398.

[1.72] S.L. Manzello, E.I.D. Foote. Characterizing Firebrand Exposure from Wildland-Urban Interface (WUI) Fires: Results from the 2007 Angora Fire. Fire Technology 50 (2014) 105-124.

[1.73] M. El Houssami, E. Mueller, J.C. Thomas, A. Simeoni, A. Filkov, N. Skowronski, M.R. Gallagher, K. Clark, R. Kremens. Experimental Procedures Characterising Firebrand Generation in Wildland Fires. Fire Technology 52 (2016) 731-751.

[1.74] S. Santamaria, K. Kempna, J.C. Thomas, M. El Houssami, E. Mueller, D. Kasimov, A. Filkov, M.R. Gallagher, N. Skowronski, R. Hadden, A. Simeoni. Investigation of Structural Wood Ignition by Firebrand Accumulation. Proceedings of the 1st International Conference on Structural Safety under Fire and Blast, Glasgow, UK (2015).

[1.75] S.P. Urbanski, W.M. Hao, S. Baker. Chemical Composition of Wildland Fire Emissions. Developments in Environmental Science 8 (2009) 79-107.

[1.76] S.P. Urbanski. Combustion Efficiency and Emssion Factors for Wildfire-Season Fires in Mixed Conifer Forests of the Northern Rocky Mountains, US. Atmospheric Chemistry and Physic 13 (2013) 7241-7262.

[1.77] S.P. Urbanski. Wildland Fire Emissions, Carbon, and Climate: Emission Factors. Forest Ecology and Management 317 (2014) 51-60.

[1.78] S.R. Reitas, K.M. Longo, R. Chatfield, D. Latham, M.A.F. Silva Dias, M.O. Andreae, E.Prins, J.C. Santos, R. Gielow, J.A. Carvalho Jr. Including the Sub-Grid Scale Plume Rise of Vegetation Fires in Low Resultion Atmospheric Transport Models. Atmospherc Chemistry and Physics 7 (2007) 3385-3398.

[1.79] B. Porterie, J.L. Consalvi, A. Kaiss, J.C. Loraud. Predicting Wildland Fire Behavior and Emissions Using a Fine-Scale Physical Model. Numerical Heat Transfer, Part A: Applications: An Internation Journal of Computation and Methodology 47/6 (2005) 571-591.

[1.80] J.D. Cohen, J.E. Deeming. The National Fire Danger Rating System: Basic Equations. General Technical Report PSW-82. US Forest Service Pacific Southwest Forest and Range Experiment Station, May 1985.

[1.81] R.E. Burgan. 1988 Revisions to the 1978 National Fire Danger Rating System. Researc Paper SE-273. US Forest Service, Southeastern Forest Experiment Station, USA (1988).

[1.82] W. Mell, M.A. Jenkins, J. Gould, P. Cheney. A Physics-based Approach to Modelling Grassland Fires. International Journal of Wildland Fire 16 (2007) 1-22.

[1.83] D. Morvan. Physical Phenomena and Length Scales Governing the Behavior of Wildfire: A Case for Physical Modelling. Fire Technology 47 (2011) 437-460.

[1.84] W. Mell, D. McNamara, A. Maranghides, R. McDermott, G. Forney, C. Hoffman, M. Ginder. Computer Modelling of Wildland-Urban Interface Fires. Fire and Materials. San Francisco, CA, USA (2011).

[1.85] M.A. Mortiz, M. E. Morais, L.A. Summerell, J.M. Carlson, J. Doyle. Wildfires, Complexity, and Highly Optimized Tolerance. Proceedings of the National Academy of Science 102/50 (2005) 17912-17917.

[1.86] ASTM E 1354-16a. Standard Test Method for Heat and Visible Smoke Release Rates for Materials and Products Using an Oxygen Consumption Calorimeter. ASTM International, West Conshohocken, PA, 2016.

[1.87] ASTM E 2058-13a. Standard Test Methods for Measurement of Material Flammability Using a Fire Propagation Apparatus (FPA), ASTM International, West Conshohocken, PA, 2013.

[1.88] ASTM E 1321-13. Standard Test Method for Determining Material Ignition and Flame Spread Properties, ASTM International, West Conshohocken, PA, 2013

[1.89] J.L. Torero. SFPE Handbook – Flaming Ignition of Solid Fuels. 5th ed. Society of Fire Protection Engineers, London, UK (2016).

[1.90] R.T. Long Jr, J.L. Torero, J.G. Quintiere, Scale and Transport Considerations on Piloted Ignition of PMMA, Proc. 6th Int. Symposium of Fire Safety Science (1999) 567-578.

[1.91] J.G. Quintiere. The Application of Flame Spread Theory to Predict Material Performance, Journal of Research of the National Bureau of Standards, 93:1 (1988) 61-70.

[1.92] M. Janssens, A thermal Model for Piloted Ignition of Wood Including Variable Thermalophysical Properties, Proc. 3rd Int. Symposium of Fire Safety Science (1991) 167-176.

[1.93] V. Babrauskas. Ignition Handbook. Fire Science Publishers, Issaquah, WA, 2003.

[1.94] D. Drysdale. An Introduction to Fire Dynamics (3rd edn). John Wiley and Sons: Chichester, UK, 2011.

[1.95] J.G. Quintiere, Fundamentals of Fire Phenomena, John Wiley and Son, West Sussex, UK, 2006.

[1.96] V. Babrauskas. SFPE Handbook of Fire Protection Engineering – Heat Release Rate. 3rd ed. National Fire Protection Association, Quincy, MA, USA (2002).

[1.97] G.C. Vaz, J.C.S. André, D.X. Viegas. Estimation of the Radiation Extinction Coefficient of Natural Fuel Beds. Internation Journal of Wildland Fire 13 (2004) 65-71.

[1.98] Firewise (webpage). Peak Fire Season. National Fire Protection Association. 1 Batterymarch Park, Quincy, MA, USA. Accessed: Aug. 26, 2016. http://www.firewise.org/wildfire-preparedness/teaching-tools/interactive-modules-and-quizzes/peak-fire-seasons.aspx.

[1.99] C.A. Polgar, R.B. Primarck. Leaf-out Phenology of Temperate Wood Plants: From Trees to Ecosystem. New Phytologist 191 (2011) 926-941.

[1.100] J. Aalto, P. Kolari, P. Hari, V.-M. Kerminen, P. Schiestl-Aalto, H. Aaltonen, J. Levula, E. Siivola, M. Kulmala, and J. Bäck. New foliage growth is a significant, unaccounted source for volatiles in boreal evergreen forests. Biogeosciences 11 (2014) 1331-1344.

[1.101] K. Didan, et al. Multi Sensor Vegetation Index and Phenology Earth Science Data Records: Algorithm Theoretical Base Document and User Guide. Vegetation Index and Phenology Lab, University of Arizona, USA (2015).

[1.102] US Department of Interior, Geological Survey. Land Remote Sensing Program. < http://remotesensing.usgs.gov/index.php>

[1.103] Oak Ridge National Laboratory Distributed Active Archive Center for Biogeochemical Dynamics. <http://daac.ornl.gov/>

[1.104] ORNL DAAC. 2015. FLUXNET Web Page. ORNL DAAC, Oak Ridge, Tennessee, USA. Accessed April 26, 2016. http://fluxnet.ornl.gov/site/999.

[1.105] G.A. Alessio, J. Penuelas, J. Llusia, R. Ogaya, M. Estiarte, M. De Lillis. Influence of Water and Terpenes on Flammability in some Dominant Mediterranean Species. International Journal of Wildland Fire 17 (2008) 274-286.

[1.106] New Jersey Office of Emergency Management. State of New Jersey 2014 Hazard Mitigation Plan Section 5.12 Wildfire. Tetra Tech, Inc. Morris Plains, NJ, USA (2014).

[1.107] N. Skowronski, K. Clark, M. Gallagher. On the Occurrence of Wildfire in the NJ Pine Barrens in the Fall Season. Personal Communication. US Forest Service, Northeastern Research Station, New Lisbon, NJ, USA (2016).

[1.108] R.T.T. Forman, R.E. Boerner. Fire Frequency and the Pine Barrens of New Jersey. Bulletin of the Torrey Botanical Club 108/1 (1981) 34-50.

[1.109] WeatherSpark, Cedar Lake Ventures, Inc. San Francisco, CA, USA. Accessed: May 5, 2016. https://weatherspark.com.

[1.110] A. Tewarson, S.D. Ogden. Fire Behavior of Polymethylmethacrylate. Combustion and Flames 89 (1992) 237-259

[1.111] P. Ellis. The likelihood of ignition of dry-eucalypt forest litter by firebrands. International Journal of Wildland Fire. 24, 225-235. 2015.

[1.112] R. Hadden, S. Scott, C. Lautenberger, C. Fernandez-Pello. Ignition of combustible fuel beds by hot particles: An experimental and theoretical study. Fire Technology. 47, 341-355. 2011.

[1.113] S. Manzello, S. Suzuki, Y. Hayashi. Enabling the study of structure vulnerabilities to ignition from wind driven firebrand showers: A summary of experimental results. Fire Safety Journal. 54, 181-196. 2012.

[1.114] C. Huggett. Estimation of Rate of Heat Release by Means of Oxygen Consumption Measurements. Fire and Material 4/2 (1980) 61-65

[1.115] V. Babrauskas, R.D. Peacock. Heat Release Rate: The Single Most Important Variable in Fire Hazard. Fire Safety Journal 18 (1992) 255-272.

[1.116] W.J. Parker. Calculations of the heat release rate by oxygen consumption for various applications, Report No. NBSIR 81-2427-1, US Department of Commerce, 1982.

[1.117] M.L. Janssens. Measuring rate of heat release by oxygen consumption. Fire Technology, 27(3), 1991, p.234-249

[1.118] S. Brohez, G. Marlair, C. Delvosalle. Fire Calorimetry Relying on the Use of the Fire Propagation Apparatus. Part 1: Early Earning from Use in Europe. Fire and Materials 30 (2006) 131-149.

[1.119] S. Brohez, G. Marlair, C. Delevosalle. Fire Calorimetry Relying on the Use of the Fire Propagation Apparatus. Part 2: Burning Characteristics of Selected Chemical Substances Under Fuel Rich Conditions. Fire and Materials 30 (2006) 35-50.

[1.120] S. Brohez. Uncertainty Analysis of Heat Release Rate Measurement from Oxygen Consumption Calorimetry. Fire and Materials 29 (2005) 383-394.

[1.121] H. Biteau, et al. Calculation Methods for the Heat Release Rate of Materials of Unknown Composition. Proceedings of the 9th International Symposium of Fire Safety Science. Karlsruhe, Germany (2008) 1165-1176.

[1.122] H. Biteau, et al. Ability of the Fire Propagation Apparatus to Characterize the Heat Release Rate of Energetic Materials. Journal of Hazardous Materials 166 (2009) 916-924.

[1.123] M. McLaggen. Novel Fire Testing Frameworks for Phase Change Materials and Hemp-lime insulation. University of Edinburgh, Edinburgh, UK. 2016. Ph.D. Thesis.

[1.124] J.P. Hildago-Medina. Performance-Based Methodology for the Fire Safe Design of Insulation Materials in Energy Efficient Buildings. University of Edinburgh, Edinburgh, UK. 2015. Ph.D. Thesis.

[1.125] G.M. Byram. Combustion of Forest Fuels. Forest Fire Control and Use, K.P. Davis (ed.). McGraw-Hill Book Company, New York,USA (1959) 61-89.

[1.126] US Department of Agriculture. Welcome to the PLANTS Database | USDA PLANTS. <Plants.usda.gov>.

[1.127] P.A. Croce, Y. Xin. Scale Modeling of Quasi-Steady Wood Crib Fires in Enclosures. Fire Safety Journal 40 (2005) 245-266.

[1.128] S. McAllister, M. Finney. Effect of Crib Dimensions on Burning Rate. Proceedings of the 7th International Seminar on Fire and Explosion Hazards. Maryland, USA (2013).

[1.129] S. McAllister, M. Finney. The Effect of Wind on the Burning Rate of Wood Cribs. Fire Technology 52/4 (2016) 1035-1050.

[1.130] S. McAllister, M. Finney. Burning of Wood Cribs with Implications for Wildland Fires. Fire Technology (2015) (online only).

[1.131] A. Fuentes, J.L. Consalvi. Experimental Study of the Burning Rate of Small-Scale Forest Fuel Layers. Proceedings of the 7th Mediterranean Combustion Symposium. Chia Laguna, Cagliari, Sardinia, Italy (2011).

[1.132] R.M. Nelson, Jr. Prediction of Diurnal Change in 10-h Fuel Stick Moisture Content. Canadian Journal of Forest Research 30 (2000) 1071-1087.

[1.133] J.D. Carlson, L.S. Bradshaw, R.M. Nelson Jr., R.R. Bensch, R. Jabrzemski. Application of the Nelson Model to Four Timelag Fuel Classes Using Oklahoma Fiel Observations: Model Evaluation and Comparison with National Fire Danger Rating System Algorithms. International Journal of Wildland Fire 16 (2007) 204-216.

[1.134] S. Lopes, D.X. Viegas, L.T. de Lemos, M.T. Viegas. Equilibrium Moisture Content and Timelag of Dead Pinus Pinaster Needles. International Journal of Wildland Fire 23 (2014) 721-732.

[1.135] US Department of Agriculture, Forest Service. Seasonal Fluctuation in Moisture Content of Pine Foliage. Research Note NC-11. North Central Forest Experiment Station. Minnesota, USA (1966).

[1.136] P.P. Grima. Determination of springtime foliar moisture content in pitch pine (*Pinus rigida*). University of Massachusetts, Amherst, Massachusetts (2009) Professional Master's Project Report. 21 p.

[1.137] W.M. Jolly. A.M. Hadlow. K. Huguet. De-coupling seasonal changes in water content and dry matter to predict live conifer foliar moisture content. International Journal of Wildland Fire 23 (2014) 480-489.

[1.138] Z. Chrosciewicz. Foliar moisture content variations in four coniferous tree species of central Alberta. Canadian Journal of Forest Research 16 (1986) 157-162.

[1.139] C.R. Keyes. Foliar moisture contents of North American conifers. USDA Forest Service Proceedings RMRS-P-41 (2006) 395-399

[1.140] K. Clark, M. Gallagher. Live Fuel Moisture Content of Pitch Pine Needle (*P. rigida*) collected in the NJ Pine Barrens Between 2009 and 2013. Personal Communication. US Forest Service, Northeastern Research Station, New Lisbon, NJ, USA (2016).

[1.141] F.P. Incropera, D.P DeWitt, T.L. Bergman, A.S. Lavine, Principles of Heat and Mass Transfer, John Wiley and Sons Ltd., Singapore, Singapore, 2013.

[1.142] M. Chaos. Spectral Aspects of Bench-Scale Flammability Testing: Application to Hardwood Pyrolysis. Proceedings of the 11th International Symposium on Fire Safety Science, Christchurch, New Zealand, (2014) pp. 165-178

[1.143] B. Monod, A. Collin, G. Parent, P. Boulet. Infrared Radiative Properties of Vegetation involved in Forest Fires, Fire Safety Journal, 44 (2009) 88-95.

[1.144] Z. Acem, G. Parent, B. Monod, G. Jeandel, P. Boulet. Experimental Study in the Infrared of the Radiative Properties of Pine Needles, Experimental Thermal and Fluid Science, 34 (2010) 893-899.

[1.145] P. Girods, N. Bal, H. Biteau, G. Rein, J.L. Torero. Comparison of Pyrolysis Behaviour Results Between the Cone Calorimeter and the Fire Propagation Apparatus Heat source. Proceedings of the 10th International Symposium of Fire Safety Science. College Park, MD, USA, (2011)

[1.146] E.C. Beder, C.D. Bass, W.L. Shackleford. Transmissivity and Absorptivity of Fused Quartz Glass Between 0.22 μm and 3.5 μm from Room Temperature to 1500℃. plied Optics 10/10 (1971) 2263-2268.

[1.147] J.R. Howell. R. Siegel, MengüÇ. Thermal Radiation Heat Transfer 6th Ed.. Taylor and Francis Group.

[1.148] A. Tewarson, J.L. Lee, R.F. Pion. The Influence of Oxygen Concentration on Fuel Parameters for Fire Modeling. Proceedings of the 8th International Symposium on Combustion (1981) 563-570.

[1.149] G. Santo, F. Tamanini. Influence of Oxygen Depletion on the Radiative Properties of PMMA Flames. Proceedings of the 8th International Symposium on Combustion (1981) 619-631.

[1.150] G. Marlair, J.P. Bertrand, S. Brohez. Use of ASTM E 2058 Fire Propagation Apparatus for the Evaluation of Underventilated Fires. Fire and Material Conference (2001) 301-313.

[1.151] G. Mulholland, M. Janssens, S. Yusa, W. Twilley, V. Babrauskas. The effect of Oxygen Concentration on CO and Smoke Produced by Flames. Proceedings of the 3rd International Symposium of Fire Safety Science (1991) 585-594.

[1.152] J.R. Lloyd, W. R. Moran. Natural Convection Adjacent to Horizontal Surface of Various Planforms. Journal of Heat Transfer 96/4 (1974) p.443.

[1.153] A. Zukauskas. Heat Transfer from Tubes in Crossflow. Advances in Heat Transfer 8 (1972) 93-160.

[1.154] F. Kreith, R.M. Manglik, M.S. Bohn. Principles of Heat Transfer (7th ed.). Cengage Learning, Inc., Stamford, CT, USA, 2011.

[1.155] S.W. Churchill, H.H.S. Chu. Correlating Equations for Laminar and Turbulent Free Convection from a Horizontal Cylinder. International Journal of Heat and Mass Transfer, 18 (1975) 1049.

[1.156] P.N. Dwivedi, S.N. Upadhyay. Particle-Fluid Mass Transfer in Fixed and Fluidized Beds. Industrial and Engineering Chemistry Process Design and Development. 16/2 (1977) 157-165.

[1.157] B. Benkoussas, J.-L. Consalvi, B. Porterie, N. Sardoy, J.-C. Loraud. Modelling thermal degradation of woody fuel particles. International Journal of Thermal Science 46 (2007) 319-327.

[1.158] J.M. Cholin. Fire Protection Handbook – Wood and Wood-Based Products. 20th ed. National Fire Protection Association, Quincy, MA (2008).

[1.159] Forest Products Laboratory. Wood Handbook: Wood as an Engineering Material. General Technical Report FPL-GTR-190. Madison, WI: U.S. Department of Agriculture, Forest Service, Forest Products Laboratory. (2010).

[1.160] D. Taoukil, A. El Bouardi, F. Sick, A. Mimet, H, Ezbakhe, T. Ajzoul. Moisture content influence on the thermal conductivity and diffusivity of wood-concrete composite. Construction and Building Materials 48(2013)104-115.

[1.161] J.G. Pausas, G.A. Alessio, B. Moreira, J.G. Segarra-Moragues. Secondary Compounds Enhance Flammability in a Mediterranean Plant. Oecologia 180/1 (2016) 103-110.

[1.162] E.S. Baker. Burning characteristics of individual Douglas-Fir trees in the Wildland/Urban Interface. Worcester Polytechnic Institute, Worcester, MA, USA (2011). MS Thesis.

[1.163] M. Possell, T.L. Bell. The Influence of Fuel Moisture Content on the Combustion of Eucalyptus foliage. International Journal of Wildland Fire 22 (2013) 343-352.

[1.164] M. Amutio, G. Lopez, R. Aguado, M. Artetxe, J. Bilbao, M. Olazar. Kinetic Study of Lignocellulosic Biomass Oxidative Pyrolysis. Fuel 95 (2012) 305-311.

[1.165] T. Kashiwagi, T. Ohlemiller. A Study of Oxygen Effects on Nonflaming Transient Gasification of PMMA and PE During Thermal Irradiation.

Proceedings of the 9th International Symposium on Combustion (1982) 815-823.

[1.166] C. Lautenberger, C. Fernandez-Pello. A Model for the Oxidative Pyrolysis of Wood. Combustion and Flames 156/8 (2009) 1503-1513.

[1.167] O. Senneca, R. Chirone, P. Salatino. Oxidative Pyrolysis of Sold Fuels. Journal of Analytical and Applied Pyrolysis 71 (2004) 959-970.

[1.168] Y. Su, Y. Luo, W. Wu, Y. Zhang, S. Zhao. Characteristics of Pine Wood Oxidative Pyrolysis: Degradation Behavior, Carbon Oxide Production and Heat Properties. Journal of Analytical and Applied Pyrolysis 98 (2012) 137-143.

[1.169] S. Zhao, Y. Luo, Y. Su, Y. Zhang, Y. Long. Experimental Investigation of the Oxidative Pyrolysis Mechanism of Pinewood on a Fixed-Bed Reactor. Energy and Fuels 28 (2014) 5049-5056.

[1.170] R.F. Simmons, H.G. Wolfhard. Some Limiting Oxygen Concentrations for Diffusion Flames in Air Diluted with Nitrogen. Royal Aircraft Establishment (1956).

[1.171] D.M. Marquis, E. Guillaume, A. Camillo. Effects of Oxygen Availability on the Combustion Behavior of Materials in a Controlled Atmosphere Cone Calorimeter. Proceedings of the 11th International Symposium of Fire Safety Science (2014) 138-151.

[1.172] H. Biteau, A. Fuentes, G. Marlair, J.L. Torero. The Influence of Oxygen Concentration on the Combustion of a Fuel/Oxidizer Mixture. Experimental Thermal and Fluid Science. 34 (2010) 282-289.

[1.173] S. Ishizuka, H. Tsuji. An Experimental Study of Effecti of Inert Gases on Extinction of Laminar Diffusion Flames. Proceedings of the 8th International Symposium on Combustion (1981) 695-703.

[1.174] V. Babrauskas. Chapter 10: Effect of Environmental Variables. In Heat Release in Fires. E and FN Spon. London, UK (1995)

[1.175] A. Tewarson, J. Steciak. Fire Ventilation. Combustion and Flames 53 (1983) 123-134.

[1.176] C.L. Beyler. Major Species Production by Solid Fuels in a Two Layer Compartment Fire Environment. Proceedings of the 1st International Symposium of Fire Safety Science (1986) 431-440.

[1.177] W.M. Pitts. The Global Equivalence Ratio Concept and the Formation Mechanisms of Carbon Monoxide in Enclosure Fires. Progress in Energy and Combustion Science 21 (1995) 197-237.

[1.178] D. Gross, A.F. Robertson. Experimental Fires in Enclosures. Proceedings of the 10th International Symposium on Combustion (1965) 931-942.

[1.179] A. Tewarson. Some Observation in Experimental Fires in Enclosure. Part 1: Cellulosic Material. Combustion and Flames 19 (1972) 101-111.

[1.180] A. Tewarson. Some Observation in Experimental Fires in Enclosure. Part 2: Ethyl Alcohol and Paraffin Oil. Combustion and Flames 19 (1972) 363-371.

[1.181] A. Tewarson, J.L. Lee, R.F. Pion. The Influence of Oxygen Concentration on Fuel Parameters for Fire Modeling. Proceedings of the 8th International Symposium on Combustion (1981) 563-570.

[1.182] B.Y. Lattimer, U. Vandsburger, R.J. Roby. Carbon Monoxide Levels in Structural Fires: Effects of Wood in the Upper Layer of a Post-Flashover Compartment Fire. Fire Technology 34/4 (1998) 325-355.

[1.183] B. Karlsson, J.G. Quintiere. Enclosure Fire Dynamics. CRC Press LLC. London, UK (2000).

[1.184] Y. Saso, H. Gotoda, Y. Ogawa. Effect of Oxygen Concentration on the Carbon Monoxide Yields from Methane and Methanol Flames. Proceedings of the 8th International Symposium of Fire Safety Science (2005) 1013-1022.

[1.185] W.M. Pitts. Application of Thermodynamic and Detailed Chemical Kinetic Modeling to Understand Combustion Product Generation in Enclosure Fires. Fire Safety Journal 23 (1994) 271-303.

[1.186] A.A. Stec, T.R. Hull. Assessment of the Fire Toxicity of Building Insulation Material. Energy and Buildings 43 (2011) 498-506.

*This page is intensionally left blank.*

# Chapter 2

## *Fuel/Sample Characterization, Description of Experimental Apparatus, Protocols and Calculations*

## *2.1. Introduction*

This chapter is the basis for all topics related to the determination of fuel and sample properties, experimental apparatus, test protocols and conditions, and calculations of the heat release rate. In subsequent chapters, various fuel/sample properties and experimental protocols that relate to the specific topic at hand will be reviewed; however, all experimentation is based on the principle equations and explanation given here.

The first two sections will describe the fuel particle and sample properties (Section 2.2 and 2.3). Then, the test apparatus and its modifications are explained in Section 2.4. Experimental protocols and data analysis techniques are outlined in Section 0 and 2.6. Section 2.7 discussed the experimental conditions used in each Chapter. Finally, Section 2.8 provides a summary of the test conditions and analysis explored in each chapter.

## *2.2. Fuel particle properties*

Throughout this thesis, three pine species common to the Northeastern regions of the United States and parts of Canada were studied. The three species of interest are: White pine (*Pinus strobus*, PS; Fig. 2.1.g.), Red pine (*Pinus resinosa*, PR; Fig. 2.1.e.), and Pitch pine (*Pinus rigida*, PRI; Fig. 2.1.f.).

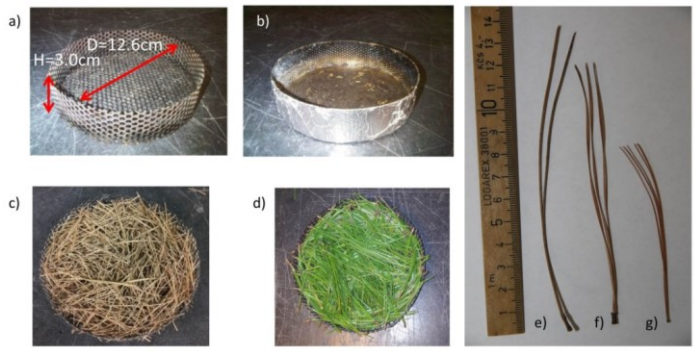


**Fig. 2.1. Open (a) and closed (b) sample holder; Dead (c) and live (d) pine needle sample; dead PR (e), PRI (f) and PS (g) needles.**

Photographs in Fig. 2.1 also show the two sample holder, open (a) and closed (b), and an example of a sample of dead fuel (c) and unconditioned live fuel (d). These species were chosen as fuel source for their availability and dominace in their respective ecosystems. Initial experimentation was conducted with PS and PR species. Later on, a transition was made to PRI, due to parralelle work being conducted on studying wildfire behavior in PRI dominated ecosystems (e.g. [2.1, 2.2]).

### *2.2.1. White, Red and Pitch pine species*

Pine needles have been selected for this study as they are among the most flammable fuels in a forest; they are present throughout the entire year and their properties can be (relatively) well characterized as will be discussed throughout this chapter. They represent a first level of complexity of porous fuels that allow small scale testing in a well-controlled environment. Studies on various species of pine needles are available in the literature; however these mainly represent species common around the Mediterranean area and western United States (See Chapter 1). The maps shown in Fig. 2.2 indicate where the used species are commonly found.

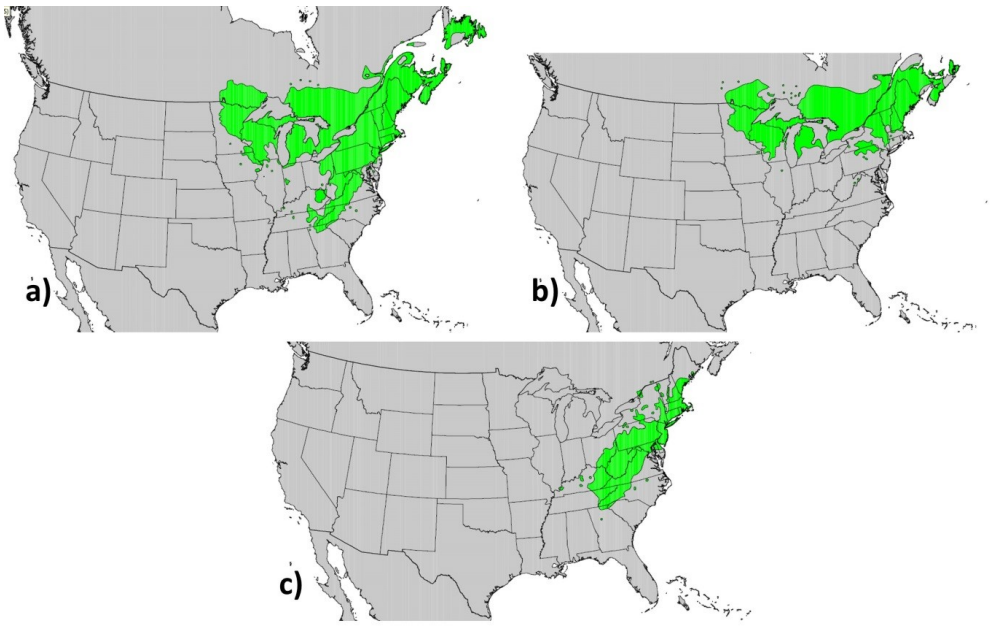


**Fig. 2.2. Map of occurrence of (a) Eastern White Pine, (b) Eastern Red Pine, and (c) Pitch Pine[2.3].**

Some of the important parameters required for the characterization of the fuel are the particle density ($\rho$), surface-area to volume ratio ($SVR$), specific heat ($c_p$) and fuel moisture content ($FMC$, % dry weight). These properties are discussed in the following sections and a summary of values is given at in Table 2.1.

Table 2.1. Summary of dead needle particle properties (PR, PS and PRI); (N/st.dev.).

| Species | PS | PR | PRI |
|---|---|---|---|
| $\rho$ [kg/m³] | 621.1 | 776.6 | 607.5 |
| | (10/39.1) | (8/49.0) | (6/17.5) |
| $SVR$ [$m^{-1}$] | 14,173 | 7,024 | 4,776 |
| | (50/1,615) | (50/805) | (20/497) |
| $c_p$ [$kJ.kg^{-1}.K^{-1}$][a] [2.4, 2.5] | 2.0904 | 1.7023 | 2.0697 |
| | (-/0.658) | (-/0.397) | (-/0.551) |
| $d_{needle}$ [mm] | 0.50 | 0.94 | 1.39 |
| | (50/0.06) | (50/0.10) | (20/0.12) |
| $FMC$ [% d.w.] | 7.0-10.0 → | | |

a) Averaged from 25 to 200℃

### 2.2.2. *Particle density*

The needle density refers to the apparent (or effective) density of the needle, because the needle itself has an inherent porosity. It was determined by immersing a known mass of needles in a known volume of liquid and reading the displaced volume (using graduated cylinder). Water is a poor choice of liquid for this, because air pockets are visible at the surface of the needles. This is due to the inferior wetting properties of water over other liquids, for example alcohols. For this reason, ethanol or alternatively methanol was used as working fluid. Both, ethanol and methanol have similar surface tension at ambient temperature (~22.0 $mN.m^{-1}$) and is much lower than for water (~72.0 $mN.m^{-1}$) [2.6, 2.7], which explains the air pockets.

The volume displaced by the needles was recorded and the density calculated by

$$\rho = \frac{m_{needle}}{V_{needle}} \quad \textbf{Eq. 2.1}$$

where

$$V_{needle} = V_{total} - V_{liquid} \quad \textbf{Eq. 2.2}$$

The impact of air pockets when using water can be illustrated by the comparison of density measurement (Table 2.2).

Table 2.2. Averaged density measurements of dead PR needles using submersion in water and ethanol.

| Working fluid | Density [kg.m$^{-3}$] (N/st.dev.) |
|---|---|
| Water | 592.0 (10/56.3) |
| Ethanol | 776.6 (8/49.0) |

The values for water submersion are significantly lower than ethanol submersion, by 24%, which highlights that water is not an appropriate fluid to use. When air pockets are present the volume displacement is larger ($V_{total}$), causing the under-estimation of the density (Eq. 2.1).

The same technique was used for dead and live (dry and wet) foliage. Dry foliage density can be relative constant (Table 2.3). Variations between species are observable (Table 2.1). PR needles had the highest density, PS and PRI had similar values.

Table 2.3. Average particle density measurements of dead PRI needles made in two different years.

| Year of measurement | Density [kg.m$^{-3}$] (N/st.dev.) |
|---|---|
| 2012 | 607.5 (7/17.5) |
| 2014 | 621.9 (3/4.2) |

Live fuel showed significant seasonal trends. Generally, dry live needle density was found to be greater than dead needle density. Growing needle density was also significantly higher than mature needles. This can, in part, be attributed to the state of growth/decay as discussed by [2.8]. Furthermore, live needle density showed a strong

relation to *FMC*. Further discussion on this topic will be provided in the relevant chapter where live fuels are investigated (Chapter 5 and 6).

### *2.2.3. Surface area-to-volume ratio (SVR)*

The *SVR* was determined by close geometric inspection, as described hereafter, of the needles and is calculated by

$$SVR = \frac{Surface\ area_{needle}}{Volume_{needle}} = \frac{Perimeter_{needle}}{Cross-secional\ area_{needle}} \quad \text{Eq. 2.3}$$

The *SVR* is a particle characteristic that is used to compare the needle geometry of different species. Large values mean that the fuel is fine, smaller values means thicker needles. Geometric features of needles vary from species to species. For example two images of the cross-sectional area taken through a microscope of PS and PR needles are shown in Fig. 2.3. PS needles have a triangular-like cross-sectional area, whereas, PR needle have a sickle-like shape. PRI, needles are similar to PR needles.

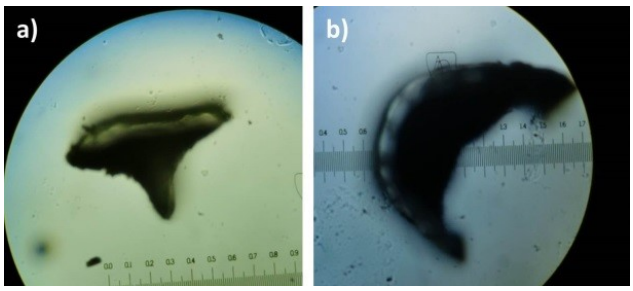


**Fig. 2.3. Cross-sectional area of (a) PS and (b) PR needles under the microscope.**

Needles can be found in pairs (PR), triplets (PRI) or quintuplets (PS). The needle cross-sectional shape varies depending on the grouping [2.3] as in Fig. 2.3. The grouping refers to the number of needles that grow out of one fascicle (see Fig. 2.1.e-f.). PR needles are paired, long and thick, PS are grouped in quintuplets, short and thin. PRI

needles grow in triplets, long and thick. A schematic of the cross-section area (as seen in the microscope images, Fig. 2.3) and the way needles are arranged in fascicles for PS and PR is given in Fig. 2.4.

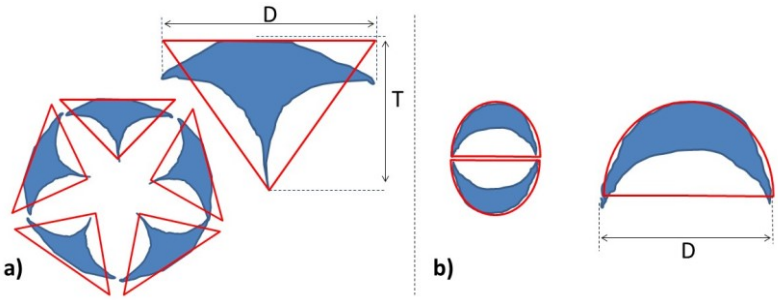


**Fig. 2.4. Schematic of growth arrangement and cross-section area of (a) PS and (b) PR needles. The red outline indicates the assumed geometric shape used for calculation of the SVR.**

The geometric features outlined in red (half cylinder and equilateral prism) are used in the determination of the *SVR*. When calculating the *SVR*, several assumptions were made: for pairs (PR) and triplets (PRI), one needle has roughly the *SVR* of half a cylinder (Fig. 2.4.b.).

$$SVR_{half\ cylinder} = \frac{\frac{1}{2}\pi d + \mathrm{d}}{\frac{1}{8}\pi d^2} = \frac{4}{d} + \frac{8}{\pi d} \qquad \textbf{Eq. 2.4}$$

For quintuplets (PS), one needle has roughly the *SVR* of an equilateral prism (Fig. 2.4.a.)

$$SVR_{prism} = \frac{3d}{\frac{\sqrt{3}}{4}d^2}\left(\frac{L}{L}\right) = \frac{12}{\sqrt{3}d} \qquad \textbf{Eq. 2.5}$$

Caliper measurements of the needle diameter (or side), *d*, were recorded and the *SVR* calculated. These calculations are very simple and diameter measurements are quickly obtained. A summary of the *SVR* is given in Table 2.4 with a comparison to a second

technique, an image analysis. From the species studied here, PS needles are the thinnest ones, followed by PR needles. PRI needles are the thickest ones. The values for the *SVR* are 14,173, 7,024, and 4,776 $m^{-1}$, respectively.

For the image analysis, cross-sectional area and perimeter are estimated with the pixel size. This requires additional equipment such as a camera and microscope. The comparison was made to evaluate if a simple calculation based on one measurement is accurate. The technique based on the geometrical features has high measurement errors, as is shown by the standard deviation of the *SVR* (Table 2.4).

Image analysis was performed on several photographs (6-7) taken through a microscope (see Fig. 2.3). Only PS and PR needles were analyzed. The conversion from pixel to length scale was 1.0 mm = 1439 pixel. Results of the analysis are also shown in Table 2.4. The comparison of the two methods shows that, the simple geometric analysis is acceptable, since it compares well with the values found from the image analysis.

Table 2.4. Comparison of *SVR* values of geometrical method with image analysis method (dead needles)

| | Surface-area-to-volume ratio (*SVR*) [$m^{-1}$] | | |
|---|---|---|---|
| | PS | PR | PRI |
| Geometric analysis (average) | 14,173 | 7,024 | 4,776 |
| (N/st.dev.) | 50/1615 | 50/805 | 10/497 |
| Image analysis (average) | 12,861 | 7,376 | - |
| (N/st.dev.) | 7/1,241 | 6/1,140 | - |

Both techniques show high variability (standard deviation). This variability is likely due to natural variation of the needle size. The uncertainty of the geometric analysis is consistent for each species, independent of diameter. For PS, PR, and PRI needles, the standard deviation is 11.4, 11.5 and 10.4%, respectively. If measurement uncertainty (caliper) was an issue, it would be visible in a trend of the standard deviation (increasing with decreasing size). The uncertainty (standard deviation) for the image analysis is 9.6 and 15.5 % for PS and PR needles, respectively, which is no

improvement over the simple analysis. Furthermore, the uncertainty is not consistent. The reason for this is likely the number of images that were analyzed and the image quality, because it is difficult to obtain acceptable images through a microscope.

Uncertainty may be reduced with more measurements, but only marginally. An additional set of measurements of 120 needles (PRI) had a standard deviation of 7.3%. These were not included in Table 2.4, because the needles were live ones. *SVR* between dried live and dead PRI needles is however equivalent, 4,661 +/- 339 $m^{-1}$ and 4,776 +/- 497 $m^{-1}$, respectively.

Common Mediterranean species [2.9] are given in Table 2.5 for a comparison to the species used in this work. PR needles compare to *P. laricio* in size, whereas, PRI needles compare to *P. halepensis*. PS on the other hand are significantly smaller than typical Mediterranean species.

Table 2.5. SVR of come common Mediterranean pine species [2.9].

| Species | *SVR* [$m^{-1}$] |
|---|---|
| P. halepensis | 7,377 |
| P. pinaster | 3.057 |
| P. laricio | 4,360 |

### *2.2.4. Fuel moisture content (FMC)*

The *FMC* was determined by conditioning needles at 60 °C for a period of 24 hours. It is calculated on a dry weight basis using:

$$\%FMC\ (d.w.) = \frac{(m_{wet} - m_{dry})}{m_{dry}} \times 100. \qquad \textbf{Eq. 2.6}$$

The wet mass, $m_{wet}$, and dry mass, $m_{dry}$, are measured before and after the 24 hours conditioning period, respectively. Values for dead needles varied slightly between 7 and 10%, depending on the ambient condition in the laboratory.

The *FMC* of unconditioned live foliage is not constant over the year. It is also significantly different for growing and mature needles [2.10, 2.11]. This has been attributed to the calculation method, and the fact that needles don't only change water content but also the amount of dry mass, which inherently impacts the *FMC* calculation. Further discussion on this topic will be provided in the relevant chapters (Chapter 5 and 6). The following section will now discuss sample preparation and bulk properties for dead and live (dried) fuel beds.

## *2.3. Sample properties and preparation*

### *2.3.1. Dead needle samples*

Experimental campaigns mainly explored impact of external factors (airflow, heating rate, oxygen concentration, and others) on the ignition and combustion behavior of needle beds. Therefore, it was crucial to minimize any other factors that might also influence the behavior. The preparation of the fuel bed was conducted with care to maximize consistency. The aim of sample preparation was to reproduce conditions typically found in pine needle layers in the field. The porosity is a sample property calculated as

$$\alpha_g = 1 - \alpha_s \qquad \textbf{Eq. 2.7}$$

Where, $\alpha_g$ is the gaseous volume fraction, and $\alpha_s$ is the solid volume fraction. The solid volume fraction can be further evaluated as

$$\alpha_s = \frac{\rho^*}{\rho} \qquad \textbf{Eq. 2.8}$$

Where, $\rho$ is the particle density and $\rho^*$ is the bulk density. The equation for porosity the becomes,

$$\alpha_g = 1 - \frac{\rho^*}{\rho} \qquad \textbf{Eq. 2.9}$$

The bulk density is calculated by knowing the mass of fuel packed into the sample basket

$$\rho^* = \frac{m_{sample}}{V_{sample}} \qquad \textbf{Eq. 2.10}$$

The nominal sample weight is 15.0 +/- 0.15 g and resulted in a bulk density of 40 +/- 0.4 kg.m$^{-3}$ for dead unconditioned pine needle samples (13.9 g dry mass at 7% *FMC*).

Table 2.6. Summary of dead pine needle sample bulk properties.

| Species | PS | PR | PRI |
|---|---|---|---|
| $\alpha_g$ [%] | 93.5 | 94.8 | 93.5 |
| (N/st.dev.) | (10/0.42) | (8/0.32) | (6/0.19) |
| $m_{sample,wet}$ [g] | 15.0 | 15.0 | 15.0 |
| (st.dev.) | (0.15) | (0.15) | (0.15) |
| $\rho$*[kg/m³] | 40.0 | 40.0 | 40.0 |
| *H* [mm] | 30.0 | 30.0 | 30.0 |
| $D_{sample}$ [mm] | 126.0 | 126.0 | 126.0 |

### *2.3.2. Live needle samples*

When using live needles, the same test procedure was followed; however, the sample mass was modified. Live needle samples were tested conditioned and unconditioned. It was desired to keep the porosity of the sample constant with changing *FMC*. In order to do this, the sample mass had to be changed, depending on the needles *FMC*. Keeping the porosity constant allowed the study of the influence of the *FMC* without changing fuel bed properties. Additionally, this meant that, effectively the same amount of combustible material is in the sample matrix with changing fuel moisture. The following equivalent mass relationship, $m_{equiv}$, was used for live PRI needle samples:

$$m_{equiv} = m_{dry}(1 + FMC) \quad \textbf{Eq. 2.11}$$

The dry mass, $m_{dry}$, is selected to reflect the dry mass of dead needles (13.9 g) used elsewhere in this thesis, whereas the *FMC* was determined for the current test sample. Table 2.7 illustrates the change of initial sample mass used when preparing live needle samples.

Shrinkage of needles was considered for live needles. It was investigated by measuring the diameter of unconditioned needles, then conditioning them for 24 hours and measuring them again. For live needles the reduction in diameter was approximately 5% as shown in Table 2.8 below (before and after conditioning). It is assumed that, this small reduction will have only a minor impact on the *SVR* and porosity of the sample.

Table 2.7. Equivalent mass for samples in the range of *FMC* under consideration.

| FMC | $m_{dry}$ [g] | $m_{eq}$ [g] |
|---|---|---|
| 0% | 13.9 | 13.9 |
| 30% | 13.9 | 18.06 |
| 60% | 13.9 | 22.22 |
| 90% | 13.9 | 26.39 |
| 120% | 13.9 | 30.56 |
| 150% | 13.9 | 34.73 |
| 180% | 13.9 | 38.89 |
| 210% | 13.9 | 43.06 |

Table 2.8. Averaged diameter of live PRI needles (wet and dry).

| Condition | Diameter [mm] (N/st.dev.) |
|---|---|
| Wet | 1.47 (40/0.10) |
| Dry | 1.39 (40/0.09) |
| % reduction | 5.2 |

After discussion of the fuel and sample characterization, the following section will now describe the test apparatus used for conducting combustion experiments.

## *2.4. FM Global Fire Propagation Apparatus (FPA)*

The FPA (Fig. 2.5) is a bench scale calorimeter developed by FM Global to perform material flammability assessments in a standardized environment [2.12]. The procedure employed here is based on ASTM E2058-13 [2.12] with certain modifications in order to accommodate wildfire research needs. These modifications are presented in Section 2.4.2. Previous studies [2.9, 2.13-2.19] have demonstrated the applicability of this apparatus to understand forest fuel burning dynamics. The versatility of this apparatus allows the study of all critical factors that influence the burning dynamics, such as bed properties, external heat flux, airflow velocity and temperature, as well as ambient oxygen concentration.

**Fig. 2.5. Photograph of the FPA at the University of Edinburgh.**

### *2.4.1. Description of set-up*

A schematic of the FPA is outlined in Fig. 2.6. The sample is placed into the combustion chamber. An incident heat flux at the sample surface is produced by four near infrared heating units, which are located, atop and around the sample. An airflow

(referred to as the inlet airflow), can be introduced into the bottom of the combustion chamber. The airflow velocity, temperature and oxygen concentration can be varied as required (see Section 2.4.2).

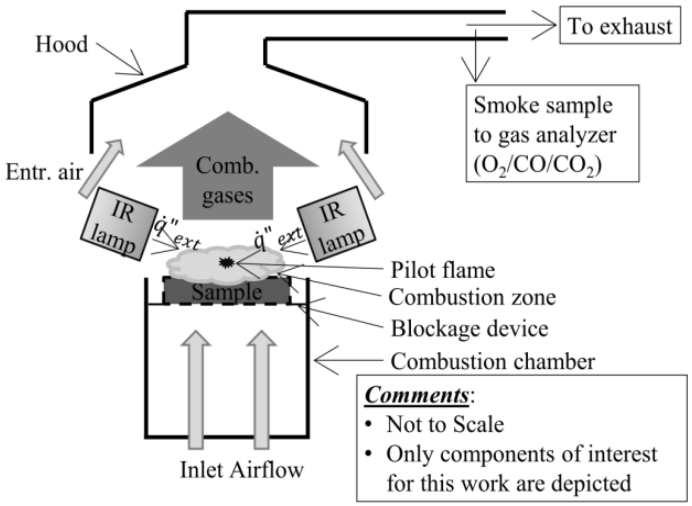


**Fig. 2.6. Schematic of the FPA.**

When changing the condition of the airflow from ambient, the operator uses a quartz tube (also referred to as "tube") to contain the environment around the sample. An illustration of the use of the quartz tube is shown in Fig. 2.7. The tube is made of a main section, sitting on the combustion chamber. A smaller extension can be added, which is held in place on the main section with a stainless steel connection. It should be noted that the transmissivity of quartz glass has a spectral dependence [2.20]; above approximately 2 μm, the transmissivity decreases. This can act as a filter and should be taken into account when setting the heat flux. Therefore, when the tube is used, the heat flux is calibrated with the tube in place. Chaos has discussed this topic (in the FPA) in more detail [2.21].

The combustion gases are drawn into the exhaust hood with an exhaust fan located downstream of the gas sampling probe. The dilution of combustion products (by entrainment air) is driven by the flow rate of the exhaust fan and is set to the suggested value of 150 lps [2.12].

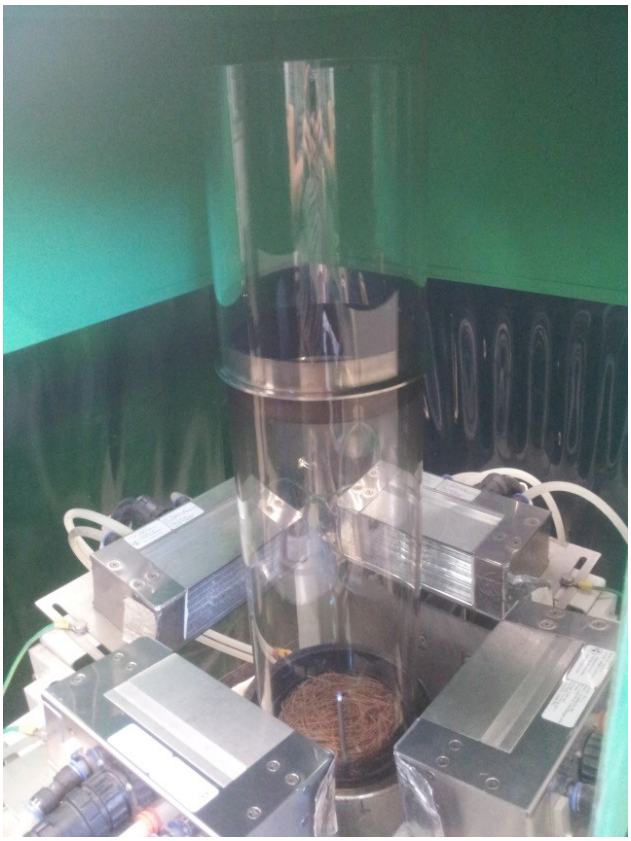

**Fig. 2.7. Photograph of the FPA test chamber with the quartz tube. In this picture the sample is with dead PS needles.**

A sample of the gas mixture is drawn from the exhaust duct via a stainless steel probe that spans the diameter of the duct. The probe has multiple holes to draw an averaged gas sample across the width of the duct. The sample gas is supplied to $O_2$, CO, and $CO_2$ analyzer (Servomex 4100). This is done with an extraction pump in the sampling line. Gas analyzers are susceptible to pressure changes, temperature and moisture. Therefore, the sample extraction was controlled and monitored with pressure gauges. The pressure in the sample lines was kept constant at 5 psi (0.345 bar; operating pressure for analyzer). Pressure fluctuations or variation of pressure between calibration and testing results in incorrect gas readings. Furthermore, over-pressure will damage the analyzer. Moisture in the sample line will also cause damage to the units. Typically, a drift in oxygen readings (< ambient, 20.95% by vol.) indicates that the gas sample is not sufficiently dehydrated (see also Section 2.4.3).

Conditioning of the gas sample is done on a number of stages. It is filtered to reduce contaminant particles (soot), condensed to reduce the temperature and moisture content with a cold trap, and finally desiccated with drying agent (Drierite [2.22]) to further reduce the moisture content. Measurements of temperature and pressure are obtained in the duct for use in calculating the mass flow rate in the duct.

### *2.4.2. Modifications*

Several modifications are made to suit wildfire research and accommodate the porous nature of wildfire fuels.

#### Sample basket and airflow blockage

The first modification to the FPA set-up specific to wildland fuels was the use of porous sample baskets to allow modification of the flow conditions through the fuel bed. Schemel [2.16] showed that baskets made of perforated steel with 63% porosity allow sufficient airflow to enter the fuel matrix thereby reducing the influence of the sample holder on the burning behavior. This is important because it is desired to reduce any impact of ventilation control (oxygen availability) on the burning dynamics.

Schemel [2.16] performed experiments in the FPA with samples placed onto a pedestal connected to a load cell in order to measure the mass of the sample in real time (a standard configuration in the FPA). This setup resulted in a gap between the sample edge and combustion chamber wall as illustrated in Fig. 2.8.

In order to characterize the flow field, when inlet airflow is forced into the combustion chamber, he conducted a particle image velocimetry (PIV) study [2.16]. It was concluded that a large amount of the total flow escapes around the sample, rather than entering it. Only 15-35% of the flow entered the sample [2.9]. This has the effect that, convective cooling of particles in the fuel bed is lower than what is expected.

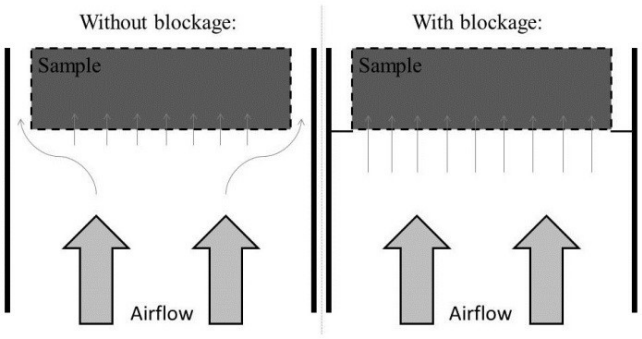


**Fig. 2.8. Schematic of flow behavior with (right) and without (left) blockage.**

The impact of this flow behavior on the ignition is highlighted in Table 2.9. In this table the percent difference is calculated between the ignition time of tests with no airflow and test with airflow, without and with blockage, at four external heat flux magnitudes. It identifies that, ignition time is longer when airflow is present (negative percentage), which can be mainly attributed to the convective cooling mechanism introduced by the airflow. More so, one can observe that this is most significant at low external heat flux.

Table 2.9. Percent difference in ignition time (flow/no flow) for tests with and without blockage at various heat flux. Negative indicates longer ignition time.

| Heat flux [kW.m$^{-2}$] | % Difference | |
|---|---|---|
| | No blockage | Blockage |
| 20 | -59 | -∞ |
| 30 | -25 | -230 |
| 40 | 8 | -3 |
| 50 | -14 | -14 |

What is important here is the increase in the percent difference when the airflow is prevented from escaping around the sample (blockage). At 20 kW.m$^{-2}$, no ignition is observed at all, which is indicated by the infinity symbol. At 30 kW.m$^{-2}$, the ignition time is nine times longer for tests with the blockage. Above 40 kW.m$^{-2}$, the variation is equivalent and low, indicating that the radiant heating is dominating the convective cooling heat transfer. The exact phenomenon will be discussed in Chapter 4. It is desired to quantify the impact of airflow, and thus it is critical to understand what the

magnitude of the airflow going through the fuel bed is. The result of this brief comparison is grounds for including a blockage in the experimental setup.

The blockage (see Fig. 2.9) was a stainless steel retaining ring wedged into the chamber. A circular thin sheet of stainless steel with a hole slightly larger than the sample basket is placed on top of the retaining ring. Finally, fiber-glass paper (3.0 mm thick) is place on top to insulate the contact to the basket (Fig. 2.9). This forces the inlet air to pass through the sample allowing better quantification of the flow through the fuel bed (Fig. 2.8). When using the blockage, it was assumed that nearly all of the forced flow enters the sample matrix.

**Fig. 2.9. Photograph of the blockage (white ring) in the FPA combustion chamber without sample basket. Also visible in this image is a thermocouple used to monitor the test chamber temperature just underneath the sample.**

When using the blockage, it is not possible to obtain mass loss data, because the basket is in contact with the blockage device which is in contact with the test chamber. This presents a limitation in the current study and should be addressed in future developments of the test set-up.

### Flow controller for inlet flow magnitude and oxygen concentration

Modifications were made to improve control of the magnitude and composition of the inlet flow supply. The modifications discussed here were inspired after consulting with scientists at FM Global who continue to improve the FPA for use as a standardized test apparatus, and also as a scientific research tool.

Mass flow control valves (Chell HFC 203) were installed in the inlet air and nitrogen supply lines. This allowed specification of the amount of air and nitrogen in the inlet flow, therefore allowing experiments to be undertaken at sub-ambient oxygen concentrations. Alternative, nitrogen could be substituted with pure oxygen and mixed with air to produce above-ambient oxygen concentrations in the test chamber.

Components of this system are illustrated in Fig. 2.10. A user-friendly software package (Fig. 2.10(b); Chell DisplayX vers. 1V0.6) was used to communicate with the digital control unit (Fig. 2.11.a; Chell CMD100). This allowed varying either the mass flow of air or nitrogen to change the oxygen condition in the test chamber. The oxygen concentration was monitored with the integrated inlet oxygen analyzer in the FPA.


**Fig. 2.10. System for inlet flow oxygen control; (a) Digital control unit, (b) Computer software interface, and (c) Mass flow control units for compressed air and nitrogen stream.**

### Heating system for varying inlet flow temperature

A heating system was installed in the inlet flow supply lines. This system was inserting into the supply line just upstream from the FPA combustion chamber, as illustrated in Fig. 2.11.

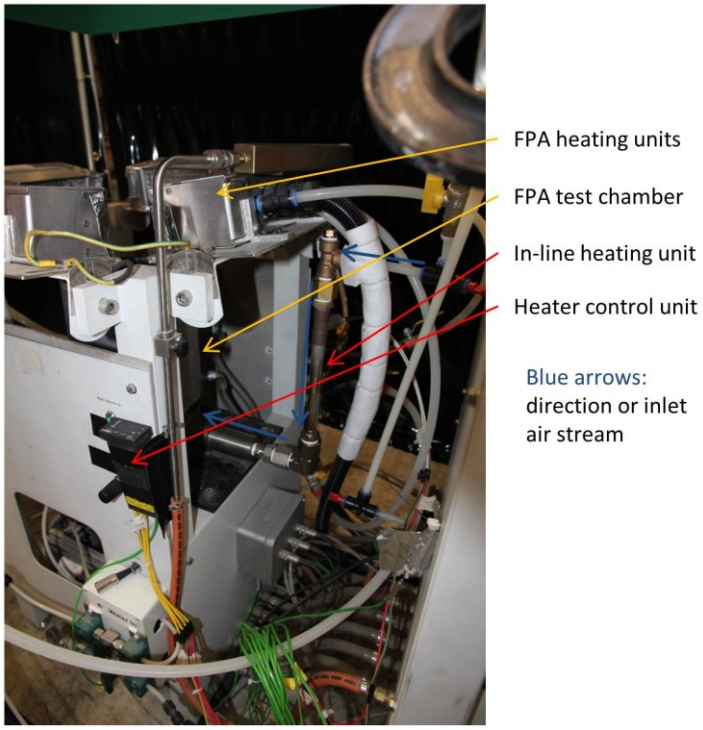


**Fig. 2.11. Illustration of the inlet airflow heating system installed in the FPA.**

The in-line heating unit (Omega Engineering AHP-7562) was operated by a digital control unit (Omega Engineering CN79000), where a desired set-point temperature could be specified. A K-type thermocouple was placed into the test chamber (see Fig. 2.9), just underneath the sample, to monitor and regulate the heater output. The schematic in Fig. 2.12 depicts a graphical representation of the system, including air flow direction and wiring schematics. With this set-up (and an airflow rate of 50-100 lpm), a maximum steady temperature at the location of the sample of 75$^{o}$C was possible.

Higher temperatures may be achieved with higher airflow rates. However, a limitation is the cooling of the combustion chamber. The chamber is cooled with chilled water to prevent damage from the high heat insult, and also to prevent premature and unquantifiable heat exposure to the fuel. Therefore, competing mechanism of heating and cooling will limit peak temperature.

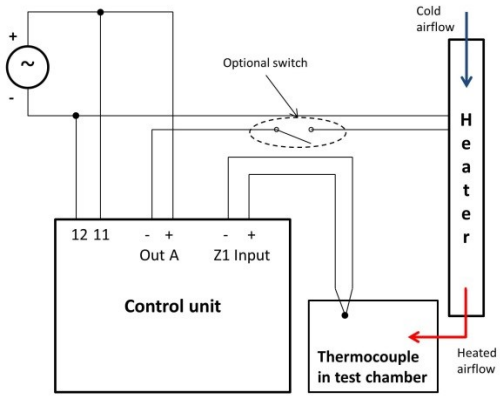


**Fig. 2.12. Wiring schematic of inlet airflow heating system.**

### *2.4.3. Influence of the desiccant on $O_2$ and $CO_2$ measurements*

The following discussion will outline the influence of the drying agent on $O_2$ and $CO_2$ measurements. This was also discussed in [2.23, 2.24].

When the desiccant is free of moisture (freshly conditioned in an oven; typically at 220℃ for two days), it captures $CO_2$ more than it releases. Thus $CO_2$ data collected downstream with the analyzer can be misrepresentative of what is actually occurring during the combustion process.

A typical example is given in Fig. 2.13 for unconditioned live needle samples. Four tests show distinctly different $CO_2$ curves.

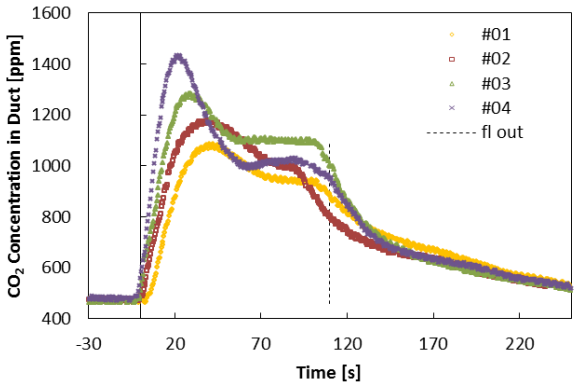


**Fig. 2.13. $CO_2$ evolution of four consecutive tests done with unconditioned OG samples (November), illustrating the influence of drying agent saturation conditions. Time interval between tests is 15 to 20 minutes. Ignition occurs for all tests at t=0s. Average flame out is represented by the dashed line.**

The main differences are the initial rise and peak (value and time) in $CO_2$ concentration. The tests were done in order (1-4) with approximately 15 to 20 minutes between each test. For test #01 the drying agent was fresh (fully dehydrated) and absorbed a large portion of the $CO_2$. This is why the rise and the peak are delayed. At test #04, the drying agent is saturated with moisture and $CO_2$ give more accurate results of the actual combustion behavior.

The drawback is that when the drying agent is not performing satisfactory, i.e. it does not absorb moisture, it can cause damage to the analyzer cells, which are sensitive to moisture in the sampling stream. The presence of moisture in the sample stream can be identified from anomalies in the $O_2$ data. When sampling $O_2$ data ambient conditions start to show a drift, it is usually an indication that the sampling stream is not sufficiently dehydrated. At this point, no further testing should continue because it can irreversibly damage the analyzers. An example of drifting oxygen data is shown in Fig. 2.14. In this graph, a drift (negative) can be seen before ignition (t=0s). After flame out, the concentration does not resume to ambient conditions (20.95%).

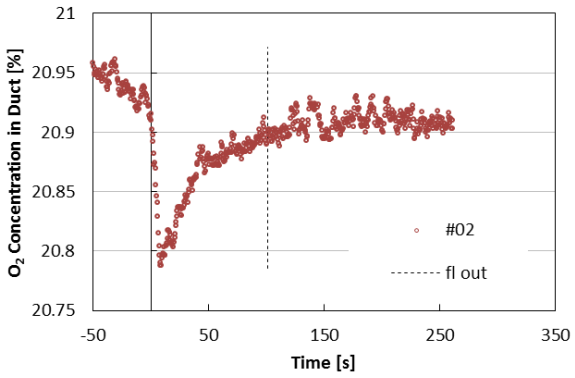


**Fig. 2.14. $O_2$ evolution of unconditioned OG needle sample (June), illustrating the influence of drying agent saturation conditions. Drift starts 30 seconds before ignition (t=0s) and measurements after flame out (fl out) do not return to ambient conditions (20.95 % by vol.).**

In order to obtain the most accurate results, the drying agent should not be used fresh. Ambient air should be passed through the drying columns in order to "cure" the agent. However, it should not be cured too long because only a short period for testing will

be granted before the agent no longer performs satisfactorily. At this point it has to be changed and cured again. For this study, care was taken to ensure good dryness of the drying agent, however inevitable variations exist. Although CO and $CO_2$ data was used here to correct for incomplete combustion in the calculation of heat release rates, it was assumed that small variations do not significantly impact the final heat release rate calculations. It should be noted that CO measurements are not affected by the drying agent's saturation state.

## *2.5. Experimental Procedures*

### *2.5.1. Data logging*

The Fire Laboratory at the University of Edinburgh developed an in-house data acquisition program (written in Excel Visual Basics Applications). The latest developments of the program were made by Dr. Juan Hidalgo. The program allowed equipment calibration and test data collection. Data acquisition occurred at a frequency of 1 or 2 Hz using an Agilent data logger (Agilent 34970A). Important variables that are recorded by the program are listed in Table 2.10. A last feature included the documentation of important events during a test, e.g. start of test, ignition, flame out, and other relevant commentary.

Table 2.10. Recorded variables of the data logging system. (List is not exhaustive; only variables pertinent to the thesis are listed).

| Variable (measurement location) | Use |
|---|---|
| $O_2$ (duct) | Measure oxygen depletion during combustion |
| $O_2$ (inlet air supply) | Measure oxygen concentration of inlet air |
| CO (duct) | Measure CO generation during combustion |
| $CO_2$ (duct) | Measure $CO_2$ generation during combustion |
| Differential pressure (duct) | Calculation of volumetric flow rate in duct |
| Temperature (duct) | Calculation of volumetric flow rate in duct, correction of air density in the duct and convective heat release rate of combustion |
| Heater output | Monitor output of heating unit |
| Relative humidity (lab) | Monitor ambient condition |
| Absolute pressure (lab) | Monitor ambient condition |
| Ambient temperature (lab) | Monitor ambient condition |
| Cold trap temperature (gas sample line) | Monitor conditioning of sample gas |
| Addition temperature channel | Record sample surface (and in-depth) temperatures |

### *2.5.2. Calibration*

Before conducting any experimentation with the FPA, the IR heating units, and gas analyzers were calibrated. Calibration was done once a day for IR heating units (unless

multiple heat flux levels were tested on one day). The gas analyzers were calibrated twice a day.

The IR heating lamps were calibrated with a water cooled Schmidt-Boelter gauge (Medtherm, model: GTW-10SB-8-36-40-484). The accuracy of the gauge is quoted as +/-3% by the manufacturer. The surface of this gauge was place at the location of the sample surface in the combustion chamber. The voltage to the lamps was regulated to vary the lamp output until the desired heat flux was measured with the heat flux gauge.

Gas analyzer ($O_2$, CO and $CO_2$) were calibrated with a "zero/low" reference point, using nitrogen gas, and "high/span" reference point using a span gas. For $O_2$ the span was ambient oxygen, for CO and $CO_2$ it was a gas of known mixture (~400/2500 ppm $CO/CO_2$; varied from cylinder to cylinder). The first step was to sample only nitrogen through the analyzer until zero values (or near zero) were read. At this point, manual zeroing of the analyzer was done by a series of commands on the analyzer. After zeroing, a 10 point average was recorded with the data acquisition program. The second step is a repeat, just with drawing the span gas through the analyzer. This provided calibration factors for each gas that are used in the conversion of the data acquisition signal (voltage to physical unit).

### *2.5.3. Test protocol*

Two types of tests were conducted with the FPA: 1) Combustion tests, and 2) ignition tests. Ignition delay and time of flaming period were determined from visual observations. The observation was verified by examination of the duct temperature, which showed a sharp increase or decrease when flames are present. Gas evolution data ($O_2$, CO and $CO_2$) was obtained by means of the data acquisition system integrated in the FPA.

### Combustion tests

These tests are extensive and utilize the potential of the FPA as a tool to estimate heat release rate. An overview of the combustion test protocol (step-by-step) is provided in Table 2.11.

Table 2.11. Combustion test protocol for combustion test using the FPA.

| Steps | Task |
|---|---|
| 1. | Prepare sample (sample holder, species, sample mass, FMC, etc.) |
| 2. | Prepare FPA (turn on smoke extraction system, drain cold trap, turn on water cooling unit, gas supply and compressed air supply, turn on power supply to heating units) |
| 3. | Calibrate FPA equipment (heat flux, duct flow, analyser; when using quartz tube, calibration must also be conducted with the tube in place) |
| 4. | Set test conditions (inlet airflow condition and external heat flux) |
| 4.1. | Airflow velocity: adjust flow rate via control unit (monitoring is also done with a flow meter) |
| 4.2. | Airflow temperature (do not turn on the heater without airflow passing through it, it will overheat and break): set desired temperature on control unit; allow test chamber to reach set temperature and stabilize |
| 4.3. | Airflow oxygen concentration: for a given flow magnitude, adjust air and nitrogen flow rate into the system; monitor inlet air oxygen concentration via FPA gas analyser; allow stabilization at desired concentration |
| 5. | Record sample and test condition in the program (sample mass and size, sample holder, heat flux, flow condition, etc.) |
| 6. | Place sample in combustion chamber, light pilot flame, and engage heat shield (when using the quartz tube, it is placed onto the combustion chamber before engaging the heat shield) |
| 7. | Check gas analyser readings (re-calibrate if required) |
| 8. | Start data logging |
| 9. | Collect 30 seconds of ambient condition (baseline) |
| 10. | After 30 seconds engage heating lamps |
| 11. | After 60 seconds, start test by dropping heat shield and exposing sample to heat flux |
| 12. | Record any relevant events (e.g. start of smoldering, flaming ignition, flame out, etc.) |
| 13. | Keep lamps engaged throughout the entire test |
| 14. | Termination of test: when $O_2$, CO and $CO_2$ analyser have reached near ambient conditions |
| 15. | Disengage lamps and continue data collection for additional 60 seconds (baseline) |
| 16. | Stop data logging and save test data |
| 17. | Allow cooling of system before removing sample and starting a next test |

### Ignition tests

These tests utilize a shorter protocol as described for the combustion tests, since no calorimetry is performed. The critical parameter is the time to ignition. Table 2.12 summarizes the protocol for conducting a typical ignition test.

Table 2.12. Ignition test protocol for combustion test using the FPA.

| Steps | Task |
|---|---|
| 1. | Prepare sample (sample holder, species, sample mass, FMC, etc.) |
| 2. | Prepare FPA (turn on smoke extraction system, drain cold trap, turn on water cooling unit, gas supply and compressed air supply, turn on power supply to heating units) |
| 3. | Calibrate FPA equipment (heat flux, duct flow; when using quartz tube, calibration must also be conducted with the tube in place) |
| 4. | Set test conditions (inlet airflow condition and external heat flux) |
| 5. | Record sample and test condition in the program (sample mass and size, sample holder, heat flux, flow condition, etc.) |
| 6. | Place sample in combustion chamber, light pilot flame, and engage heat shield (when using the quartz tube, it is place onto the combustion chamber before engaging the heat shield) |
| 7. | Start data logging |
| 8. | Collect 30 seconds of ambient condition |
| 9. | After 30 seconds engage heating lamps |
| 10. | After 60 seconds, start test by dropping heat shield and exposing sample to heat flux |
| 11. | Record any relevant events (e.g. start of smoldering, flaming ignition, flame out, etc.) |
| 12. | Termination of test: any time after flaming ignition (no post-test ambient condition sampling is required) |
| 13. | Stop data logging and save test data |
| 14. | Allow cooling of system before removing sample and starting a next test |

Timing of the protocol (step 7. through 10.) is kept identical between tests in order to preserve consistency and reduce any unquantifiable influence from environment and test apparatus. Furthermore, it simplified later data analysis if the timing of the start of the test was the same between tests.

## *2.6. Data analysis (flammability parameter)*

As was discussed in Chapter 1, material flammability can be described by a long list of parameters (e.g. various time parameters, flame height, mass loss, heat release, and others). Analyzing each one will present insightful characteristics of the combustion dynamics of a material. The most characteristic one is the time to ignition, because it is easily obtained and gives a quantifiable definition of flammability that can be used in fuel classification. However, Huggett [2.25] and later Babrauskas and Peacock [2.26] have also explained that, the heat release rate is "the single most important variable in fire hazard". This statement was made in the context of the build environment (building material, interior finishing, and furniture that provide the fuel load for a possible fire scenario), rather than the wildland fire environment. However, it can be translated directly, since it must be understood not only how well vegetation might ignite but also how well or intense it burns.

It was concluded to base the majority of the data analysis from FPA combustion tests with forest fuels on (1) time to ignition and (2) heat release rate, specifically the peak heat release rate. In Chapter 3, analyses also include duration of flaming period, CO and $CO_2$ generation rates and combustion efficiency.

### *2.6.1. Time to ignition*

It is defined as the time from first incident radiative heat flux exposure to flaming ignition. Piloted ignition conditions are desired for the tests with the assumption that in forest fires, the flame front (or glowing particles) act as the ignition source for an advancing fire. Time to ignition ($t_{ig}$) is given as the sum of the pyrolysis time ($t_p$), mixing time ($t_m$) and induction time ($t_i$) [2.27-2.32]:

$$t_{ig} = t_p + t_i + t_m \approx t_p \qquad \textbf{Eq. 2.12}$$

Mixing and induction time are assumed negligible in case for piloted ignition as discussed in Chapter 1. This is further assessed in Chapter 3, where the oxygen concentration is varied.

### *2.6.2. Heat release rate (OC)*

When combustion tests are evaluated (Chapter 3, 5 and 6), calorimetry calculations are performed in order to determine the heat release rate (HRR) from a burning fuel. This was first discussed in Chapter 1. Additional details are discussed here. The HRR estimations used here are based on the principle of oxygen consumption calorimetry (OC) [2.25, 2.33, 2.34].

Huggett [2.25] has determined that, when typical hydrocarbon fuels combust in air (assuming complete combustion), the energy released per unit mass of oxygen is relatively constant ($E_{O2}$). A mean value of 13.1 +/- 0.7 $kJ.g^{-1}$ (oxygen) was proposed [2.25], and is widely applied today. The advantage is that detailed knowledge of chemistry of the material is not required to estimate the energy release rate, although estimations are improved if it is known [2.35-2.37].

The applicability of this to forest fuel was shown by Bartoli [2.38] for typical Mediterranean forest fuels. She concluded that a value of 14.15 $kJ.g^{-1}$ (oxygen) is more accurate when conducting tests with forest fuel. For pine needles, she found that the standard value will results in under-estimation of the HRR of approximately 6.7%. Only a brief summary of the governing equations is given here. An abundance of studies are available (e.g. [2.23, 2.35-2.38]) that have reviewed the principle of OC and have illustrated the derivation in detail. This also includes comparison to the principle of carbon dioxide generation calorimetry (CDG) (e.g. [1.122]). A recent work done by Hidalgo [2.23] applied the technique to building insulation material and includes a comprehensive set of equation and comparison of the two principles, OC

and CDG. The HRR ($\dot{Q}_{OC}$; in [kW]) of a material burning in air can be estimated by the amount of oxygen consumed in the combustion [2.34] and can be formulated as

$$\dot{Q}_{OC} = E_{O_2} \Delta \dot{m}_{O_2} \quad \textbf{Eq. 2.13}$$

Where $E_{O_2}$ the oxygen consumption energy coefficient [kJ.g$^{-1}$(oxygen)], and $\Delta \dot{m}_{O_2}$ is the mass of oxygen consumed [g] in the combustion. It is commonly formulated in terms of the oxygen depletion factor, $\phi$:

$$\dot{Q}_{\mathrm{OC}} = \left( E_{O_2}\phi - \left(\mathrm{E_{CO \rightarrow CO_2}} - E_{O_2}\right)\left(\frac{1-\phi}{2}\right)\left(\frac{X_{CO}}{X_{O_2}}\right)\right) \cdot \left(\frac{\dot{m}_e}{1+\phi(\alpha-1)}\right)\left(\frac{M_{O_2}}{M_{air}}\right) X_{O_2}^0 \quad \textbf{Eq. 2.14}$$

where, $\phi$, is the oxygen depletion coefficient defined by

$$\phi = \frac{\left(X_{O_2}^o\left(1 - X_{CO} - X_{CO_2}\right) - X_{O_2}\left(1 - \mathrm{X_{CO_2}^0}\right)\right)}{X_{O_2}^o\left(1 - X_{CO} - X_{CO_2} - X_{O_2}\right)} \quad \textbf{Eq. 2.15}$$

This formulation (Eq. 2.14) includes a correction for incomplete combustion; accounting for the generation of CO. Table 2.13 summarizes the variables in the above formulation.

Table 2.13. Variables used in the formulation of oxygen consumption calorimetry (corrected for incomplete combustion).

| Variable | Description |
|---|---|
| $\dot{Q}_{OC}$ | Heat release rate [kW] from oxygen consumption calorimetry |
| $E_{O_2}$ | Energy released per unit mass of oxygen consumed (complete); for typical hydrocarbon fuel, 13.1 kJ.g$^{-1}$ (oxygen) [2.25]; for forest fuel, 14.15 kJ.g$^{-1}$ (oxygen) [2.38] |
| $E_{CO \rightarrow CO_2}$ | Energy released per unit mass of oxygen consumed (CO → $CO_2$; incomplete combustion); typical value, 17.6 kJ.g$^{-1}$ (oxygen) [2.34] |
| $\phi$ | Oxygen depletion factor |
| $X_{O_2}^o$ | Mole fraction of oxygen before test (baseline); same for CO and $CO_2$ |
| $X_{O_2}$ | Mole fraction of oxygen during test; same for CO and $CO_2$ |
| $\dot{m}_e$ | Mass flow rate in the duct; calculated based on known geometry of the duct, differential pressure measurements, and duct temperature |
| $M_{O_2}$ | Molar mass of oxygen |
| $M_{air}$ | Molar mass of air |
| $\alpha$ | Expansion factor due to the combustion (constant=1.105) [2.34] |

The following are important assumptions related to the estimation of heat release rate by oxygen consumption calorimetry:

- All gases follow the ideal gas law.
- Energy constant for complete combustion of the tested pine needles is similar to the value obtained by Bartoli [2.38], $E_{O2}$ = 14.15 kJ.g$^{-1}$ (oxygen) and for incomplete combustion, $E_{CO \rightarrow CO2}$ = 17.6 kJ.g$^{-1}$ (oxygen) obtained by Janssens [2.34].
- Entrainment air is considered of $O_2$, $CO_2$, $N_2$, and $H_2O$. All other gases are lumped into $N_2$ and considered inert.
- Vapor formed by combustion is small compared to vapor in atmosphere
- Sample gases are free of moisture (condensed and desiccated)

### Uncertainty of oxygen consumption calorimetry

The uncertainties of heat release rate calculations have multiple origins, such as unknown material properties (resulting in estimation of energy constant, *E*), heat flux calibration, duct flow and gas measurements. Detailed analysis of several aspects can be found in [2.35, 2.40]. For unknown material and using an estimated value for E (e.g. values from Huggett or Bartoli as discussed above) the uncertainty can be estimated at 5% [2.35]. Accuracy of the heat flux gauge is quoted as 3% by the manufacturer (Medtherm, model: GTW-10SB-8-36-40-484). Pitts et al [2.39] and Janssens [2.40] have illustrated (round robin in 5 different laboratories) that this is a slight underestimation but still a satisfactory level of accuracy. Furthermore, a horizontal and vertical spatial variation around the location of the sample surface of the heat flux is also likely. This variability should stay within 5% uncertainty as per [2.12] and should be tested frequently. In the laboratory, this was tested bi-annually and adjustments were made (lamp angular position) in order to conform to this level of accuracy.

Brohez [2.35] showed that the total relative error of heat release rate estimation via oxygen consumption calorimetry (estimation of *E*, duct flow measurement, expansion factor, and $O_2$ measurement) is at least 12%. He concluded that one of the largest sources of uncertainty is the oxygen depletion measurement. This is because the FPA (or the Cone) have an open system (entrainment from ambient) and generally result in low values of oxygen depletion; the uncertainty increase significantly with decreasing oxygen depletion. However, is also dependent on the accuracy of the analyzer. The accuracy of the $O_2$ analyzer used here is < 0.02% $O_2$ (< 200 ppm). For such analyzer, Brohez [2.35] suggests that the accuracy is less than 5% only when the oxygen in the duct is less than 20.55%. In this work, the lowest peak oxygen depletion was found for wet foliage (FMC ~ 140%) at around 20.85%. According to Brohez [2.35] at this level of depletion the uncertainty of heat release rate via oxygen consumption calorimetry is greater than 20%. This should be kept in mind when comparing the data to other sets

obtained in different experimental set-ups. Future work should continue in reducing the uncertainty, by for example testing at reduced duct flow rate.

## *2.7. Test conditions*

The following sections describe the fuel and test conditions used throughout the thesis. A summary of all conditions is provided in Table 2.14. The reader is reminder that, the sample mass of dead and dried live needle samples were kept constant throughout the experimentation. Only live needle samples had varying wet mass, according to their *FMC*.

### *2.7.1. Sample holder*

In all chapters (3-6) tests were performed with open baskets (63% perforation). Closed baskets (0% perforation) were only used in Chapter 3 and 4 (see Fig. 2.1 for image of baskets).

### *2.7.2. Species*

The three species discussed in Section 2.2 were used throughout this thesis. However not every species was used in every chapter. Combustion and ignition tests in Chapter 3 and 4 were performed with PS and PR needles. Combustion tests in Chapter 5 and 6 utilized PRI needles.

### *2.7.3. External heat flux*

For each test, the external heat flux was always constant, although different magnitudes were tested. A whole range of heat flux levels was tested in Chapter 3 and 4. This range included the critical heat flux required for ignition of the fuel bed, approximately 10 $kW.m^{-2}$, depending on the species, up to 60 $kW.m^{-2}$. The

experimental campaign in Chapter 5 and 6 is mainly conducted with 25 kW.m$^{-2}$ heat flux. A few tests are presented at 50 kW.m$^{-2}$ in Chapter 6.

### *2.7.4. Airflow magnitude*

The flow rates used throughout the presented studies are natural (NF) and forced convection with 50 (LF) and 100 lpm (HF). Tests with 200 lpm (HHF), as used in [2.9, 2.13] were limited, because the convection cooling from such an airflow was too high to allow ignition of samples below 45 kW.m$^{-2}$. This made such a flow rate impractical for the purpose of the studies. Although, Bartoli et al [2.9] and Schemel et al [2.13] prescribed a 200 lpm flow, the actual flow rate through the sample can be estimated to 30-75 lpm (based on 15-35% of the flow entering).

Although the exact local flow velocities above the sample are unknown, a mean flow velocity can be estimated base on the cross-section area of the sample, 0.0125 m$^2$, through which the flow passes. Converting the volumetric flow rate to mean airflow velocity resulted in 6.7 and 13.4 cm·s$^{-1}$, for 50 and 100 lpm flow rates, respectively. Porosities of the fuel beds are only marginally different from species to species and are very high (Table 2.1); therefore, it is assumed that it is not affecting the flow velocity.

Schemel found that the basket holder can influence the flow velocity depending on the size of the particles in the fuel bed [2.16]. He found an influence for *Pinus pinaster* needles (*SVR* = 3,057 m$^{-1}$) but not for *Pinus halepensis* (*SVR* = 7,377 m$^{-1}$). PS and PR needles have significantly larger *SVR* compared to *Pinus pinaster* (Table 2.1). Thus it is assumed, that samples with this type needles are not influenced by the basket. The *SVR* of PRI needles (4,776 m$^{-1}$) is only slightly larger than *Pinus pinaster*. Therefore, the sample basket may influence flow velocities for this species. However, they were only tested at natural convection.

### *2.7.1. Airflow oxygen concentration*

Most experimental campaigns were conducted at ambient oxygen concentration (20.95% by vol.). Changing the oxygen concentration has significant effects on the combustion dynamics, since it changes the oxygen availability and thus the ventilation condition. In a realistic wildfire scenario most combustion can be assumed to be well-ventilated conditions. However, in certain conditions (within the flame front, in the smoke plume, and others) this may not be fully true. Therefore, tests were performed at varying oxygen concentration, ranging from 14-23% (Chapter 3). This is done to not only to illustrate that reduced oxygen concentration will impact the combustion dynamics but also to illustrate the importance of ventilation condition.

### *2.7.2. Airflow temperature*

Typical ambient temperatures in the laboratory were 16-18 °C . Changing the ambient temperature in the test chamber provided a means to reduce the convective heat transfer (cooling) once the sample was heated via radiation. Tests were conducted at ambient, 50 and 75 °C (Chapter 3). Higher temperature were not possible and also undesirable, because it may cause premature degradation of the fuel.

## ***2.8. Chapter summary***

In this chapter, relevant aspects to experimentation were described. This included characterization of the fuel particles, sample preparation, description of the FPA and testing protocols. Results used in the data analysis are outlined. Furthermore, test conditions explored in each chapter are explained. The table below (Table 2.14) gives a summary of experimentation conducted in each chapter.

Table 2.14. Summary of test conditions and results explored in each chapter (dry sample load was constant throughout).

| Ch. | Flow conditions | | | Specie | Sample holder | Heat flux [kW.m$^{-2}$] | Results |
|---|---|---|---|---|---|---|---|
| | Magnitude | $O_2$ conc. | Temperature | | | | |
| 3. | Natural and forced convection (6.7, 13.3 and 26.7 cm.s$^{-1}$) | 14-23% at 13.3 cm.s$^{-1}$ | Ambient, 50 and 75 °C at 13.3 cm.s$^{-1}$ | PS, PR (dead) | Open Closed | 10-60 | $t_{ign}$/HRR |
| 4. | Natural and forced convection (6.7, 13.3 and 26.7 cm.s$^{-1}$) | Ambient | Ambient | PS, PR (dead) | Open Closed | 20-60 | Temp. |
| 5. | Natural convection | Ambient | Ambient | PRI (live) | Open | 25 | $t_{ign}$/HRR |
| 6. | Natural convection | Ambient | Ambient | PRI (live) | Open | 25, 50 | $t_{ign}$/HRR |

## *2.9. References*


[2.1] E.V. Mueller, N. Skowronski, K. Clark, M. Gallagher, R. Kremens, J.C. Thomas, M. El Houssami, A. Filkov, R. Hadden, W. Mell, A. Simeoni. Fire Behavior in Two Pine Stands. Proceedings of the 12th International Symposium on Fire Safety Science. Lund, Sweden, (2017). (accepted).

[2.2] J.C. Thomas, E.V. Mueller, S. Santamaria, M. Gallagher, M. El Houssami, A. Filkov, K. Clark, N. Skowronski, R. Hadden, W. Mell, A. Simeoni. Investigation of Firebrand Generation from and Experimental Fire: Development of a Reliable Data Collection Methodology. Proceedings of the 12th International Symposium on Fire Safety Science. Lund, Sweden, (2017). (accepted)

[2.3] US Department of Agriculture. Welcome to the PLANTS Database | USDA PLANTS. <Plants.usda.gov>.

[2.4] E 1269-11, Standard Test Method for Determining Specific Heat Capacity by Differential Scanning Calorimetry, ASTM.

[2.5] R. Larsen, K. Trombley. Specific Heat of Three Pine Needles; A Report to Worcester Polytechnic Institute. Report Nr. TPRL-4992. Thermophysical Properties Research Laboratory. West Lafayette, IL, USA (2012) (unpublished).

[2.6] Y.S. Won, D.K. Chung, A.F. Mills. Density, Viscosity, Surface Tension, and Carbon Dioxide Solubility and Diffusivity of Methanol, Ethanol, Aqueous Propanol, and Aqueous Ethylene Glycol at 25℃. Journal of Chemical and Engineering Data 26 (1981) 140-141.

[2.7] G. Vazquz, E. Alvarez, J.M. Navaza. Surface Tension of Alcohol + Water from 20 to 50℃. Journal of Chemical and Engineering Data 40 (1995) 611-614.

[2.8] W.M. Jolly, J. Hintz, R.C. Kropp, E. Conrad. Physiological drivers of the live foliar moisture content 'spring dip' in Pinus resinosa and Pinus banksiana and their relationship to foliar flammability. Proceedings of the 7th International Conference on Forest Fire Research. Coimbra, Portugal (2014).

[2.9] P. Bartoli, A. Simeoni, H. Biteau, J.L. Torero, P.A. Santoni. Determination of main parameters influencing forest fuel combustion dynamics. Fire Safety Journal 46 (1-2) (2011) 27-33.

[2.10] Chrosciewicz, Z. Foliar moisture content variations in four coniferous tree species of central Alberta. Canadian Journal of Forest Research 16 (1986) 157-162.

[2.11] C.R. Keyes. Foliar moisture contents of North American conifers. USDA Forest Service Proceedings RMRS-P-41 (2006) 395-399

[2.12] ASTM E 2058-13a. Standard Test Methods for Measurement of Material Flammability Using a Fire Propagation Apparatus (FPA), ASTM International, West Conshohocken, PA, 2013.

[2.13] C. Schemel, A Simeoni, H. Biteau, J. Riviera, J.L. Torero. A Calorimetric Study of Wildland Fuels. Experimental Thermal and Fluid Science 32 (7) (2008) 1381-1389.

[2.14] F. Jervis, G. Rein, J.L. Torero, A. Simeoni, The Role of Moisture in the Burning of Live and Dead Pine Needles International Seminar on Fire and Explosion Hazard, Leeds, 2010.

[2.15] A. Simeoni, J.C. Thomas, P. Bartoli, P. Borowjeck, P. Reszka, F. Colella, P.A. Santoni, J.L. Torero, Flammability studies for wildland fuels using the Fire Propagation Apparatus. Fire Safety Journal 54 (2012) 203-2017.

[2.16] C. Schemel. Transport Effects on Calorimetry of Porous Wildland Fuels. University of Edinburgh, Edinburgh, UK. 2008. Ph.D. Thesis.

[2.17] J.C. Thomas, A. Simeoni, M. Gallagher, N.S. Skowronski. An Experimental Study Evaluating the Burning Dynamics of Pitch Pine Needle Beds Using the FPA. Proceedings of the 11th International Symposium on Fire Safety Science, Christchurch, New Zealand, (2014) pp. 1406-1419.

[2.18] J.C. Thomas, J.N. Everett, A. Simeoni, N. Skowronski, J.L. Torero. Flammability Study of Pine Needle Beds. Proceedings of the 7th International Seminar on Fire and Explosion Hazards, Providence, RI, USA, (2013).

[2.19] F.X. Jervis, G. Rein. Experimental study on the burning behavior of Pinus halepensis needles using small-scale fire calorimetry of live, aged and dead samples. Fire and Materials (2015).

[2.20] E.C. Beder, C.D. Bass, W.L. Shackleford. Transmissivity and Absorptivity of Fused Quartz Glass Between 0.22 μm and 3.5 μm from Room Temperature to 1500℃. plied Optics 10/10 (1971) 2263-2268.

[2.21] M. Chaos. Spectral Aspects of Bench-Scale Flammability Testing: Application to Hardwood Pyrolysis. Proceedings of the 11th International Symposium on Fire Safety Science, Christchurch, New Zealand, (2014) pp. 165-178.

[2.22] Regular Drierite, non-indicating. W.A. Hammond Drierite CO., LTD. Xenis, OH, USA. < https://www.drierite.com>.

[2.23] J.P. Hidalgo-Medina. Performance-Based Methodology for the Fire Safe Design of Insulation Materials in Energy Efficient Buildings. University of Edinburgh, Edinburgh, UK. 2015. Ph.D. Thesis.

[2.24] M. McLaggen. Novel Fire Testing Frameworks for Phase Change Materials and Hemp-lime insulation. University of Edinburgh, Edinburgh, UK. 2016. Ph.D. Thesis.

[2.25] C. Huggett. Estimation of Rate of Heat Release by Means of Oxygen Consumption Measurements. Fire and Material 4/2 (1980) 61-65

[2.26] V. Babrauskas, R.D. Peacock. Heat Release Rate: The Single Most Important Variable in Fire Hazard. Fire Safety Journal 18 (1992) 255-272.

[2.27] J.G. Quintiere, Fundamentals of Fire Phenomena, John Wiley and Son, West Sussex, UK, 2006.

[2.28] V. Babrauskas. Ignition Handbook. Fire Science Publishers, Issaquah, WA, 2003.

[2.29] J.L. Torero. SFPE Handbook – Flaming Ignition of Solid Fuels. 5th ed. Society of Fire Protection Engineers, London, UK (2016).

[2.30] R.T. Long Jr, J.L. Torero, J.G. Quintiere, Scale and Transport Considerations on Piloted Ignition of PMMA, Proc. 6th Int. Symposium of Fire Safety Science (1999) 567-578.

[2.31] J.G. Quintiere, The Application of Flame Spread Theory to Predict Material Performance, Journal of Research of the National Bureau of Standards, 93:1 (1988) 61-70.

[2.32] M. Janssens, A thermal Model for Piloted Ignition of Wood Including Variable Thermalophysical Properties, Proc. 3rd Int. Symposium of Fire Safety Science (1991) 167-176.

[2.33] W.J. Parker. Calculations of the heat release rate by oxygen consumption for various applications, Report No. NBSIR 81-2427-1, US Department of Commerce, 1982.

[2.34] M.L. Janssens. Measuring rate of heat release by oxygen consumption. Fire Technology, 27(3), 1991, p.234-249

[2.35] S. Brohez. Uncertainty Analysis of Heat Release Rate Measurement from Oxygen Consumption Calorimetry. Fire and Materials 29 (2005) 383-394.

[2.36] H. Biteau, T. Steinhaus, C. Schemel, A. Simeoni, G. Marlair, N Bal, J.L. Torero. Calculation Methods for the Heat Release Rate of Materials of Unknown Composition. Proceedings of the 9th International Symposium of Fire Safety Science. Karlsruhe, Germany (2008) 1165-1176.

[2.37] H. Biteau, et al. Ability of the Fire Propagation Apparatus to Characterize the Heat Release Rate of Energetic Materials. Journal of Hazardous Materials 166 (2009) 916-924.

[2.38] P. Bartoli. Feux de forêt: amélioration de la connaissance du couplage combustible-flamme. Université de Corse-Pascal Paoli, Corsica, France. 2011. Ph.D. Thesis.

[2.39] W. Pitts, A. Murphy, J. de Ris, J.R. Filtz, K. Nygard, D. Smith, I. Wetterlund. Round Robin Study of Total Heat Flux Gauge Calibration at Fire Laboratories. NIST Special Publication 1031. National Institute of Standard and Technology. Washington, DC, USA (2004).

[2.40] M. Janssens. Uncertainty of Fire Test Results. Proceedings of the 11th Interflam Conference (2007).

*This page is intensionally left blank.*

# Chapter 3

## *Experimental Investigation of the Impact of Forced Convection on the Ignition and Burning Behavior of Forest Fuel Beds*

### *3.1. Introduction*

As was discussed in Chapter 1, ignition and burning dynamics of forest fuel beds are a function of many parameters, such as particle and bulk properties, but also ventilation condition. The experimental studies presented here are a continuation of previous works [3.1-3.8] that have investigated several aspects of forest fuel flammability. These have been discussed in Chapter 1 and Simeoni et al [3.9] have presented a comprehensive summary of previous research in this topic. Only a brief discussion is given here.

The first factor (fuel properties) is commonly evaluated with fuel flammability characterization to understand how fuel thermo-physical properties (thermal conductivity, particle density, or specific heat) impact the ignition and burning dynamics. Typically, this is done in a standardized test apparatus such as the Cone [3.10] or FPA [3.11]. Such evaluation should be made under conditions where all other (external) factors are controlled.

Bulk properties (e.g. bulk density) may be neglected for solid fuels, but are important for wildland fuel, because these are considered porous fuel packages. Porosity, which changes with bulk density, also affects flammability. For example Jervis [3.3] has shown that the ignition behavior changes when the porosity is altered. He showed that there are limits to the impact of porosity on ignition and heat release rate. Bartoli [3.2] has shown similar results. Importance of loading may be attributed to the amount of fuel present (and involved in pyrolysis and combustion process). But also to changes in heat and mass transfer in the porous medium. For example, in-depth radiation penetration decreases with increasing loading (see discussion in Chapter 1). Therefore, when conducting a flammability assessment with porous vegetative fuel beds, it is important to have consistency in sample preparation. In this work, fuel loading is kept constant throughout, in order to minimize any variability.

The latter factor, ventilation, can critically impact ignition and burning dynamics, by way of controlling heat and mass transfer mechanisms (Fig. 3.1) [3.4, 3.5, 3.7-3.9]. Therefore, these may also impact flammability characterization, if not controlled or quantified adequately. Ventilation conditions are governed by the specific environment and airflow properties, but also the sample orientation or bulk properties (not shown in Fig. 3.1 because this is not explicitly explored in this work). This is not only true in the case for wildland fuels, but is a generalization of the problem. Changing the ventilation in any fire scenario will affect burning dynamics [3.12, 3.13]. The analysis presented in this chapter, focuses on the ventilation aspect and will explore the impact of ventilation on the ignition and burning dynamics of forest fuel beds.

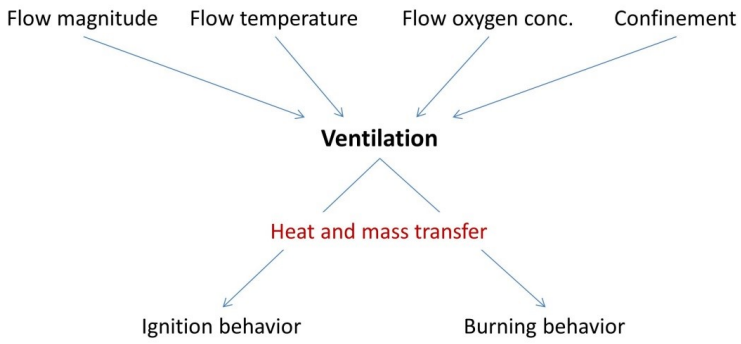


**Fig. 3.1. Explored factors governing the ventilation and impact of ventilation on ignition and burning behavior.**

As was discussed in Chapter 1 (Fig. 1.1), fuel flammability (ignition and burning behavior) is an integral part in understanding wildfire behavior. In this work, the ignition behavior (time to ignition) may be associated to flame spread over a fuel bed, because flame spread may be described as a succession of ignition of adjacent unburned fuel particles [3.14]. Combustion behavior is mainly described by the peak heat release rate (pHRR), which may be associated to peak fireline intensity of a wildfire [3.15]. Where necessary to support discussions on the burning behavior, other parameters, such as the duration of flaming, CO and $CO_2$ generation, combustion efficiency, and HRR evolution are also analyzed.

### *3.1.1. Goals and objectives*

It is the goal of this study to analyze the heat and mass transfer (Stage 1 and 2) that govern ignition and burning behavior of forest fuel beds, and assess the impact of changing ventilation condition. Changing ventilation conditions here are: ventilation area, flow magnitude, flow temperature and flow oxygen concentration.

More in detail, it is of interest to investigate: (1) the convective cooling mechanism, (2) the dilution mechanism and (3) the impact on the combustion dynamics, of a forced convection through a porous litter layer that is heated via radiation. The assessment is made with an experimental apparatus (FPA) and small scale fuel beds (12.6 cm in diameter and 3.0 cm deep). With this apparatus the user is able to control external factors that impact the ignition and burning behavior of a fuel sample, such as heating rate, cooling rate, oxygen concentration, and others. Effects related to particle and bulk properties are minimized by careful sample preparation and characterization of the fuel particles (see Chapter 2).

### *3.1.2. Chapter layout*

Before going into details with the data analysis, Section 3.2 explains the experimental protocols and methodologies. The data analysis is divided in two categories (see Chapter 1, Fig. 1.4), ignition behavior (stage 1) and burning behavior (stage 2). The ignition behavior is discussed in Section 3.3 (varying $\dot{q}''_{ext}$ and $\dot{V}$), Section 3.4 (varying $T_\infty$), and Section 3.5 (varying $y_{O_2}$). The burning behavior is explored in Section 3.4 (varying $T_\infty$) and Section 3.6 (varying $\dot{V}$ and $y_{O_2}$). Finally, the chapter is summarized in Section 3.7.

### *3.2. Experimental descriptions and methodologies*

In this chapter, four distinct conditions were tested with pine needle beds in the FPA (Fig. 3.2) in order to evaluate the ignition and burning dynamics for various ventilation scenarios. Tests were conducted in the open at natural convection with closed (a) and open baskets (b), in the open with natural and forced convection (c) and in a confinement (tube) with forced convection and changing airflow oxygen concentration (d). In the open, combustion was well-ventilated, whereas, a ventilation controlled condition was created by using the tube. Tests with changing airflow temperature utilized the configuration (c).

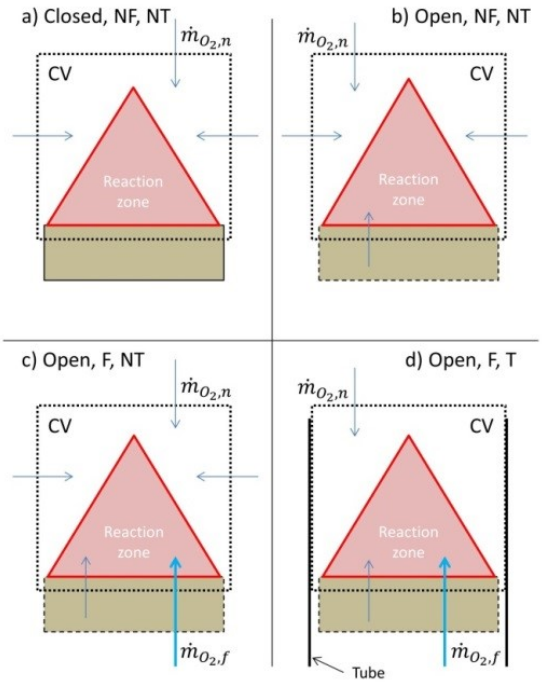


**Fig. 3.2. Schematic of flow conditions (2 dimensional): a) closed basket with no forced flow and no tube; b) open basket with no forced flow and no tube; c) open basket with forced flow and no tube; and d) open basket with forced flow and tube.**

In each case described in Fig. 3.2, oxygen flow rate is a critical parameter that impacts the burning dynamics. However, the delivery of the oxygen to the combustion zone

has different pathways depending on the condition tested. It is either due to diffusion from the atmosphere, $\dot{m}_{O_2,n}$, or due to a prescribed forced flow rate, $\dot{m}_{O_2,f}$.

The illustration of the pathways of oxygen flow to the combustion zone (Fig. 3.2) shows that, conducting tests in an unconfined, well-ventilated environment with forced convection ($\dot{m}_{O_2,f}$) still has the contribution of natural convection ($\dot{m}_{O_2,n}$). When the tube is used, condition (d) in Fig. 3.2 exists, in which the oxygen mass flux from ambient ($\dot{m}_{O_2,n}$) due to natural entrainment is minimized. Because a forced flow is used, $\dot{m}_{O_2,n}$ through the bottom surface due to buoyancy may be considered negligible.

Studying these four conditions and comparing results, provides a comprehensive evaluation of the impact of forced convection on the burning dynamics of forest fuel beds. The following section provides information on the experimental protocol, fuel used and test conditions explored.

The main fuel is PS needle beds; however, some data for other species (PR) is discussed. In cases where multiple species are discussed simultaneously, data is labeled accordingly. In all other cases, the data is for tests with PS needle beds.

The analysis of these tests is performed with the time to ignition, duration of flaming, CO and $CO_2$ generation rates, combustion efficiency, and HRR. Time parameters (ignition and flame out) are determined from visual cues. Combustion efficiency is assessed with calculation of the ratio $CO/CO_2$. Ideally, complete combustion results in $CO/CO_2 = 0$. A rise in this ratio indicates a reduction in the combustion efficiency. Here, a mean ratio for the flaming phase is used. HRR calculations are based on oxygen consumption calorimetry as outlined in Chapter 2.

Goals (1) and (2) will be evaluated with varying a forced airflow magnitude. Changing the flow magnitude has the coupled effect of impacting the heat transfer, by cooling the solid phase, and mass transfer, by diluting the gas phase. It is attempted to decouple these effects and assess the importance of each mechanism on the overall phenomenon.

The airflow temperature is increased (constant flow and oxygen concentration), which will reduce the cooling phenomenon, but not the dilution. This will allow the study of the cooling mechanism (1), in the absence of changing the dilution phenomenon.

The airflow oxygen concentration is varied (with constant flow), which will impact the dilution phenomenon, but not the cooling mechanism. This will allow the study of the dilution mechanism (2), in the absence of changing the cooling (convective heat transfer).

Altering the flow magnitude, temperature or oxygen concentration will also change the burning behavior of the samples (3), by either impacting the heat or mass transfer mechanisms (heat flux feedback, smoldering rate, pyrolysis rate). These will be evaluated with an analysis of the combustion gases, HRR calculations, and length of flaming period.

### *3.2.1. Ventilation conditions in the FPA*

Well-ventilated conditions exist when no quartz tube ("tube"; see Fig. 2.7 in Chapter 2) is used; the fuel bed burns in the open. When the tube is placed onto the combustion chamber it creates an oxygen limited scenario, because entrainment air can only reach the combustion zone through a limited area. This area refers to the exit of the tube. Furthermore, the condition with the tube allows control of the ventilation conditions by imposing a forced airflow into the combustion chamber ($\dot{V}$) or by altering the oxygen concentration ($y_{O_2}$) in the airflow. This control is required if one attempts to study the sole impact of forced convection on the ignition and burning behavior.

It should be noted that, the total oxygen mass flow into the combustion zone ($\dot{m}_{O_2,tot}$) for tests with tube was considered controlled by the imposed forced airflow. However, a small oxygen mass flow reaches the reaction zone through the tube exit. This occurs, because (1) cold air may be transported into the combustion chamber along the inner wall of the quartz tube (hot gases travel upwards near the center of the tube); and (2)

flames may reach the exit of the tube and burn in the open, i.e. in well-ventilated conditions.

Brohez et al [3.16] have discussed this experimental issue, when testing PMMA in the FPA with the quartz tube. They concluded that, an orifice plate placed on top of the tube exit is sufficient to prevent oxygen from entering the combustion region (1) [3.16]. Such a device was not used in the work presented here, because it does not prevent flames from burning in the open above the tube, which was predominantly observed here. At this point, this is assumed negligible for the purpose of this analysis. A later discussion of experimental results will go into more detail about this influence.

The influence of the tube is examined with tests done at ambient condition, with and without the tube. The external heat flux was set at 30 $kW.m^{-2}$ with an inlet flow rate of 100 lpm (13.4 $cm.s^{-1}$). Only open sample baskets were used with PS needles. Results obtained from these tests were used as the baseline for the analysis of the impact of changing forced flow oxygen concentration ($y_{O_2}$).

### *3.2.2. Controlling heat transfer (heating and cooling rate)*

In terms of heat transfer, it is more suitable to discuss forced convection with respect to flow velocity. This is because convection heat transfer effects can be related to a flow velocity via non-dimensional numbers (velocity → Reynolds number → Nusselt number → convective heat transfer coefficient). Such a non-dimensional analysis is presented in Chapter 4, where it is attempted to model the impact of a forced airflow on the ignition behavior.

As mentioned in the introduction the forced flow increases the convective cooling of particles in the fuel matrix. This changes the net energy received by the sample and will alter the ignition and burning behavior. A cooling of the sample means that, during the heating process, the particle surface temperature increases slower; therefore resulting in a longer ignition time.

The convection heat transfer was evaluated by varying the inlet flow magnitude, as well as the flow temperature. Increasing the inlet flow rate increases the heat losses by increasing the heat transfer coefficient ($h_c$). Raising the temperature will (1) increase the initial temperature of the particle; and (2) reduce the convective heat losses by reducing the temperature differential between solid and gas phase ($T_s$ - $T_g$) when the particle is heated via radiation. After ignition, the raised flow temperature will also reduce convective heat losses of the pyrolysis gases and flames, which increases their temperature.

**Flow Magnitude ($\dot{V}$)**

Conditions tested using the FPA were natural convection (NF), and forced convection (LF: 50 lpm: 6.7 cm.s$^{-1}$ and HF: 100 lpm: 13.4 cm.s$^{-1}$). The heating of the particles was achieved via a radiative external heat flux (IR lamps). The level of intensity of the heat flux was varied from 10 to 60 kW.m$^{-2}$. Two species, PS and PR, were tested. The influence of the convective transfer is evaluated by analyzing the time to piloted ignition at varying test conditions (heating and cooling). This corresponds to Stage 1 and 2 (Fig. 1.4 in Chapter 1). Convective cooling of the particle continues even after ignition.

The convective heat transfer is associated to the solid phase of the sample matrix. An increased convective heat transfer results in a slower heating of the solid particles. The time required for the particle to reach its ignition temperature is therefore increased.

Time to ignition (piloted unless otherwise stated) is presented in the form ($t_{ig}^{-0.5}$ vs. heat flux); because it is assumed that the sample behaves thermally thick at natural convection conditions [3.7, 3.9, 3.14]. Typical ignition theory of solid material dictates (assuming inert material) that, for thermally thick material, time to ignition is proportional to one over the square root of the external heat flux [3.17-3.21]. If the time to ignition is plotted in this manner, a linear relationship indicates a “solid like”

behavior. A deviation from this trend will indicate that traditional solid ignition theory does no longer apply (thermally thick). Previous work [3.22] has shown that such a behavior is reasonable up to ~60 kW.m$^{-2}$. At higher heating rates, solid material also deviates from this linear trend [3.22]. At low heating rates near the critical heat flux, deviation from this theory has also been shown (e.g. [3.18]). This is because samples start to behave thermally thin (i.e. negligible temperature distribution throughout the body). This can be attributed to the long heating period and the propagation of heat wave. Tewarson and Ogden [3.23] suggest that this is likely to occur below 25 kW.m$^{-2}$. (Remark: In Chapter 4 it will be verified that the fuel beds are in fact thermally thick under the given heating and cooling rates. It was concluded that this is acceptable when $\dot{q}''_{ext} > 20\ kW.m^{-2}$.)

**Flow Temperature ($T_\infty$)**

In order to reduce the cooling effect of the forced flow, one can change the flow temperature. The ambient temperature of the inlet flow varies from 16 to 18 $^{o}$C. Two additional temperatures, 50 and 75 $^{o}$C, were selected for investigation. In this experimental series only one needle species was tested (PS), and the flow magnitude was constant 13.4 cm.s$^{-1}$ (HF condition). This corresponds to Stage 1 and 2 (Fig. 1.4 in Chapter 1). Furthermore, gases and flames may also be affected by the changing flow temperature.

Up until ignition, the heat transfer is a balance between the applied external heat flux and the cooling of the particles (convective and radiation losses). For this test series, the behavior was evaluated with respect to one external heat flux (30 kW.m$^{-2}$).

The heat losses due to convective cooling reduce when the flow temperature is elevated. This is due to the reduced temperature difference between gas and solid phase. This has the effect of reducing the time to critical temperature for pyrolysis and ignition, because the net energy received by the particle is increased.

One aspect that needs to be considered is the fact that properties of air (density, viscosity, conductivity) change with temperature [3.24]. This has the result that $h_c$ is also affected by the change in temperature (not only by flow magnitude). An assessment of this behavior can be found in Appendix A1. It shows that the influence of raising the flow temperature is small: for the conditions under investigation the increase in $h_c$ is less than 2% when the temperature is raised from 20 to 80 °C . Therefore, it is assumed that it is negligible.

### *3.2.3. Controlling mass transfer (oxygen flow rate)*

In terms of mass transfer it is more suitable to discuss forced convection with respect to flow rate (mass or volume flow rate). This is because analysis of conservation of mass is performed on flow rates in and out of a specific control volume [3.24] (see also Fig. 3.2). For example, oxidizer and pyrolysis flow rates into and combustion gases out of the mixing/reaction zone above the fuel sample.

Oxygen availability (forced oxygen mass flow, $\dot{m}_{O_2,f}$) can be modified by two mechanisms: 1) changing the inlet flow magnitude, $\dot{V}$, and 2) by changing the inlet flow oxygen concentration, $y_{O_2}$. Tests are performed at one heat flux level (30 kW.m$^{-2}$) with one species (PS).

#### Calculation of forced $O_2$ flow rate ($\dot{m}_{O_2,f}$)

This metric is used when results from tests with changing flow magnitude ($\dot{V}$) and changing flow oxygen concentration ($y_{O_2}$) are compared in Section 3.6. This is done, because $\dot{m}_{O_2,f}$ can be changed by either variable. The oxygen flow rate can be calculated ($\dot{V}_{O_2} = y_{O_2}\dot{V}$) knowing the oxygen concentration ($y_{O_2}$) and magnitude of the volumetric air flow rate ($\dot{V}$). A detailed description of the calculation results is given in Appendix A2.

**Flow Magnitude ($\dot{V}$)**

For this test series, only ambient inlet oxygen concentrations are used ($y_{O_2} = 0.21$). A well-ventilated (no tube) condition is maintained for all cases, with varying forced convection (NF, LF: 50 lpm air: 0.210 g.s$^{-1}$ $O_2$ and HF: 100 lpm air: 0.421 g.s$^{-1}$ $O_2$). For comparison, tests done with closed sample baskets are included, in which the oxygen mass flow into the sample matrix is restricted. This test series explores impacts in Stage 2 (Fig. 1.4 in Chapter 1).

**Flow Oxygen Concentration ($y_{O_2}$)**

In order to develop oxygen reduced environment around the sample, a quartz tube is placed on top of the FPA combustion chamber (Fig.2.7 in Chapter 2). The introduction of this tube results in the development of limiting ventilation condition, even at ambient oxygen conditions with the flow rate tested (HF: 100 lpm). This test series explores impacts in Stage 1 and 2 (Fig. 1.4 in Chapter 1).

The inlet flow magnitude was kept constant at 100 lpm (13.4 cm.s$^{-1}$) for all tests. External heat flux level used was 30 kW.m$^{-2}$, with PS needle samples. Inlet oxygen concentration was varied between 14 to 23% (by vol.). The following sections will now go into discussion of the experimental results.

### *3.3. Ignition behavior with changing forced airflow magnitude and heat flux*

The ignition behavior is shown in Fig. 3.3. Ignition times decrease with increasing heat flux (increasing value $t_{ig}^{-0.5}$). PS needle samples ignite faster compared to PR, which can in part be attributed to the higher SVR. A forced airflow increases the ignition delay due to increasing convective cooling. This is shown by the changing trend lines of the data series.

Tewarson and Ogden [3.23] have shown that for black PMMA samples (0.10x0.10 m and 0.025 m thick), a forced convection (similar in magnitude to what was considered here) has no significant cooling effects on the solid samples. Therefore, it can be concluded that the porous samples used in this work experience a significant increase in convective heat transfer, which is the reason for the increase in ignition delay at low heat fluxes (reduction in $1/\sqrt{t_{ig}}$).

The closed basket, no airflow (NF) tests show a linear trend, similar to thermally thick solid materials (e.g. [3.18]). These results confirm initial findings by Torero and Simeoni [3.14] that showed a "solid like" ignition behavior of porous fuel beds with natural convection. It also shows distinct species differences.

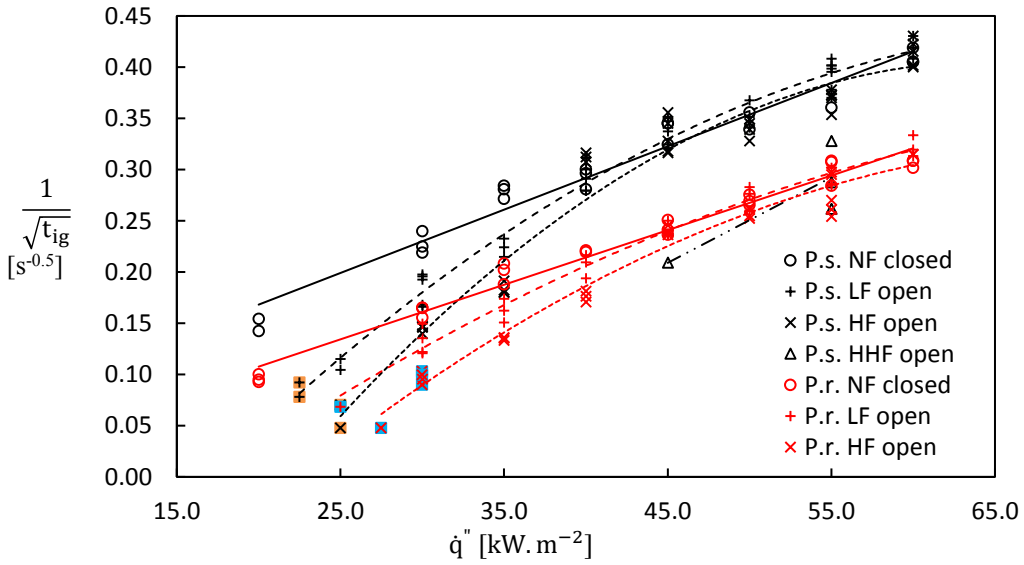


**Fig. 3.3. Ignition behavior of PS and PR needle beds in the FPA ((LF: 50 lpm or 6.67 m.s$^{-1}$, HF: 100 lpm or 13.4 m.s$^{-1}$, and HHF: 200 lpm or 26.8 m.s$^{-1}$). Solid lines: linear regression for NF/closed basket (PS and PR). Dashed lines: polynomial regression for LF/open basket (PS and PR). Dotted lines: polynomial regression for HF/open basket (PS and PR). Dash-dotted line: linear regression for HHF/open basket (PS). Orange and blue filled marker indicate smoldering ignition.**

The behavior (Fig. 3.3) changes when the baskets are open and airflow is imposed [3.7, 3.9]. The airflow introduces a convective cooling effect, which delays ignition. Furthermore, the availability of oxidizer increases, which can hinder ignition by diluting the pyrolysis gas mixture at low heat fluxes, or promote ignition by bringing

the mixture above the lower flammability limit (LFL) faster at high heat fluxes (this will be explored in Section 3.5). The latter scenario is likely the reason for some of the variability in the results above the NF conditions at high heat fluxes.

This can also be seen in Table 3.1, where the ignition time is shorter for forced convection conditions (negative % difference; PS needle samples at HF and 40 $kW.m^{-2}$, LF and 50 $kW.m^{-2}$, and PR at LF and 50 $kW.m^{-2}$). In this table, a positive percent difference means that ignition time at the forced convection condition is longer. A negative means that it is shorter.

The negative percent difference at forced convection condition can only be explained by improvement of mixing conditions opposing the impact of convective cooling. Results however, do not show a clear trend; therefore, a definite conclusion on the matter of dilution is not possible. But it should be stated that, at low heat flux and forced convection, dilution is also a factor besides convective cooling that caused some increase in the ignition time. Further experimentation is required.

Table 3.1. Percent difference between ignition time at NF and LF or HF. (+) means ignition time is longer, (-) means ignition time is shorter at the given condition (heat flux and flow magnitude).

| Heat flux [$kW.m^{-2}$] | PS [% diff.] | | PR [% diff.] | |
|---|---|---|---|---|
| | LF | HF | LF | HF |
| 30 | 55 | 147 | 54 | 180 |
| 35 | 55 | 131 | 52 | 118 |
| 40 | 0.2 | -12 | 14 | 57 |
| 45 | 1.3 | 3.8 | 1.4 | 2.4 |
| 50 | -3.2 | 3.1 | -1.9 | 9.8 |

For both species, there exists a point at which radiative heating becomes dominant over convective and re-radiative cooling. This is identified as the convergence of the data at a certain external heat flux. For PS samples this occurs at 40 $kW.m^{-2}$ and at 45 $kW.m^{-2}$ for PR (Table 3.1). These two thresholds were obtained by assessing the percent difference between the natural (NF) and forced convection (LF and HF)

condition. The convergence can be identified at the external heat flux, where the percent difference approaches zero.

The airflow only significantly influences ignition times at heat fluxes below the convergence. The data indicates that the convergence is almost independent of the airflow for the tested rates. However, it is dependent on species: PS (high SVR) convergence is at a slightly lower heat flux than PR (lower SVR). This is likely due to a balance in the convective cooling and radiation absorption, which both depend on the particle size. For PS needles, convective losses are higher, but radiation absorption is also higher. Both factors are due to the higher *SVR* of these needles.

A series of tests were conducted with 200 lpm airflow (denoted HHF in Fig. 3.3) at 45 and 55 $kW.m^{-2}$ with PS samples in order to verify the independent behavior. This was done because the convective cooling of airflow will increase with higher flow-rates and it was not believed that the convergence is independent of high flow-rates. The ignition times were over 151% longer compared to 100 lpm conditions at 45 $kW.m^{-2}$ but seemed to begin to converge, with only 70% longer times, at 55 $kW.m^{-2}$. If the tendencies are comparable to 50 or 100 lpm conditions, one can conclude that a convergence will occur above 60 $kW.m^{-2}$.

It can be concluded that, the convergence is not independent of the flow magnitude. The definition of the convergence is a balance between heat and mass transfer between the heat source, the sample and airflow. Although cooling increases with increasing flow magnitude, mixing of combustion gases with oxygen seems to also improve. The first mechanism increases ignition time, whereas, the latter mechanism decreases the time to ignition. The given experimental setup with the blockage device, did not allow collection of mass loss data, which would be beneficial in understanding the mass balance between pyrolysis and oxidizer flow rates. Future experimentation should continue investigation in this matter.

### Critical heat flux

The critical heat flux for needle samples was determined by systematically decreasing the heat flux to determine the lowest heat flux at which ignition occurred (Fig. 3.3). The critical heat flux provides insight into the ignitability and burning behavior of the fuel beds (what is the minimum energy requirement to cause ignition) and may also be used as a means to rank flammability of different fuels (and/or fuel beds). Rothermel's spread model [3.25] describes the ratio of available energy over the energy required to ignite a porous fuel bed. Therefore, a bed that requires more energy to ignite will cause a lower spread rate (under the same heating conditions).

The critical heat flux results are presented in Table 3.2. At low heat fluxes, needles tend to start smoldering before transitioning to a flaming state. Therefore, two different critical heat flux levels can be observed: (1) when purely piloted ignition is observed; and (2) when smoldering ignition is observed before transitioning to flaming. The latter one was not observed for natural convection (NF) conditions, but for forced convection (LF and HF) it is lower than (1). For subsequent analysis (Chapter 4) the latter one is more important, because considering piloted ignition simplifies physical phenomena, i.e. it ignores chemistry and mass transfer effects, which become important when assessing ignition due to smoldering and/or auto-ignition conditions.

Table 3.2. Summary for critical heat flux results.

| | Critical Heat Flux [kW/m$^2$] | | | |
|---|---|---|---|---|
| | Smoldering ignition | | Piloted ignition | |
| | PS | PR | PS | PR |
| Closed, NF (0 lpm) | 12.5 | 13.0 | 12.5 | 13.0 |
| Open, LF (50 lpm = 6.67 m.s$^{-1}$) | 22.5 | 25.0 | 25.0 | 30.0 |
| Open, HF (100 lpm = 13.4 m.s$^{-1}$) | 25.0 | 27.5 | 30.0 | 35.0 |

Results in Table 3.2 indicate that the influence of airflow is noticeable as the critical heat flux increases with increasing flow rate. Both mechanisms, convective cooling and gas dilution, contribute to delay the ignition at a low heat flux level.

*Pinus Resinosa* (PR) samples show a higher critical heat flux than PS samples. As previously mentioned, the porosities in each species samples are slightly different. However, it was concluded that porosity values were too similar to yield significant effects on the ignition time [3.2, 3.3]. Bartoli [3.2] showed that, the ignition time does not change significantly in the range of porosities considered. Therefore, the variation in critical heat flux is attributed to species properties; Surface-area-to-volume ratio being the driving factor because radiation absorption can occur on a larger surface-area for high *SVR* (14,173 $m^{-1}$ and 7,024 $m^{-1}$ for PS and PR, respectively). The higher *SVR* also allows larger convection cooling to take place. This would mean that, the critical heat flux for PS needles should be higher, because they are more effectively cooled. Overall, the balance between radiation (absorption on the needle scale and attenuation on the sample scale), convective losses (at forced convection conditions), and chemical effects (species) is such that PS needles ignite at lower heat fluxes compared to the thicker PR needles. The exact mechanisms however, cannot be explained with the given experiments; for one, because size and chemical effects are coupled by the use of two species.

Results of the ignition experiments with forced airflow suggest that, there exist two distinct ignition regimes: (1) before the convergence, ignition is driven by radiation and convection; and (2) beyond, only by radiation. The convergence represents a combination of two conditions, where radiation heating becomes much larger than heat losses, and where mass transfer in the gas phase becomes favorable to a fast ignition, i.e. $t_m$ is short.

The first regime is dependent on the forced airflow and external heat flux, the second one, on the external heat flux only. Regime (1) is likely to have some influence from dilution which challenges the assumption, $t_{ig} \approx t_p$, because the relation, $t_m << t_p$ may not be valid any more. Experimental results were not sufficient to fully understand at what threshold this occurs (Further discussion on dilution will follow in Section 3.5).

It was recently discussed that, wildfire spread is more likely to occur due to convective heat transfer rather than radiative heat transfer [3.26, 3.27]. The two ignition regimes may explain when a fire spreads via convection and when via radiation. The results also suggest that the spreading mode is strongly dependent on the radiative heat flux (from flames) and convection condition (wind). Therefore, both scenarios may occur. Future research should be conducted to further assess this behavior.

## *3.4. Ignition and burning behavior with changing forced airflow temperature*

At first, the influence of the flow temperature is evaluated with respect to the ignition time (Stage 1). Secondly, results of pHRR are discussed to explain convective cooling during the combustion phase (Stage 2).

### *3.4.1. Ignition behavior*

Results from experimentation for PS needle samples at 30 $kW.m^{-2}$, 100 lpm (13.4 $cm.s^{-1}$), and three flow temperatures are illustrated in Fig. 3.4. Time to ignition decreases (quasi-linearly) with increasing flow temperature (in the range tested). The tendency for the ignition time is due to the fact that the ambient gas and thus initial solid temperature is higher, which results in shorter time to reach pyrolysis and ignition temperatures. It is assumed that the needles are initially at equilibrium with the flow temperature. This was achieved by keeping the sample in the flow with elevated temperature typically for ten minutes before commencing the test.

Other factors that may be impacted by the rise in gas temperature are a reduction in fuel moisture content (*FMC*) or onset of degradation before starting the test. Separate baseline test, without external heat flux, showed that in this period (~10 min), no mass loss occurred (dehydration and degradation). It can be deduced that, the fuel sample was not altered when testing at different flow temperature, besides changing its temperature. It can be inferred that, the reduction in ignition time is only due to the

reduction in the differential solid temperature between initial and ignition temperature. It was explained in Section 3.2.2 that changes in the convective heat transfer coefficient ($h_c$), due to temperature effects, are marginal. It should be noted that the relationship beting ignition time and airflow temperature is not strong and the experimental error associated to ignition time is comparatively large. In order to find a more conclusive relationship, additional experimentation is required.

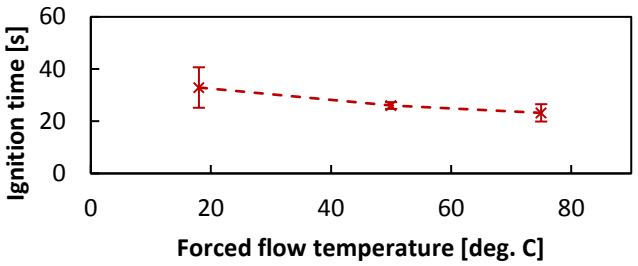


**Fig. 3.4. Time to ignition for tests at three inlet flow temperatures. Test done with PS needles at 30 kW.m$^{-2}$ and ambient oxygen. Error bars are one standard deviation.**

### *3.4.2. Burning behavior*

The convective cooling effects of the forced flow at different temperatures change the burning dynamics (Stage 2), which can be observed from a varying pHRR (Fig. 3.5). The increase of the pHRR is marginal when increasing the airflow temperature from ambient (~ 18℃) to 50 °C, resulting in a rise of pHRR of only 7.7%. When the temperature is further increased to 75 °C, the pHRR increases more significantly, 24.4% (from ambient condition). Overall, the relationship is weak and additional experimentation should be conducted to solidify the trends.

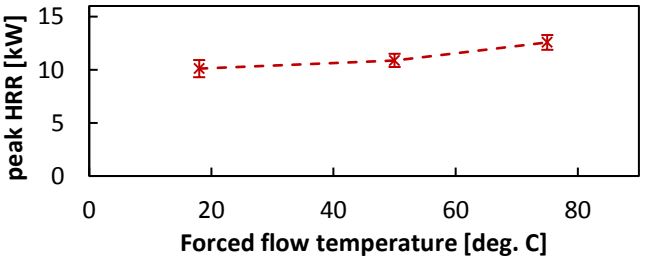


**Fig. 3.5. Peak HRR for tests at three inlet flow temperatures. Test done at 30kW/m$^2$ and ambient oxygen. Error bars are one standard deviation.**

In this part of the experimental study, one can observe well, the continuing influence of the heat transfer mechanism (Stage 2). The trends of the results are due to a reduction in the convection heat losses (solid phase), even during the burning phase. The reduced convection losses increase the pyrolysis rate, which results in a more intense combustion. Furthermore, it also reduces heat losses in the gas phase (pyrolysis gases and flames), which increase the flame temperature. This increases soot generation [3.28] producing more luminous flames, which increases the heat flux feedback to the fuel surface and thus the pyrolysis rate. Both mechanisms, reduced heat losses in the solid and gas phase, favor a more intense combustion. This can be further observed when evaluating the HRR with respect to time (Fig. 3.6).

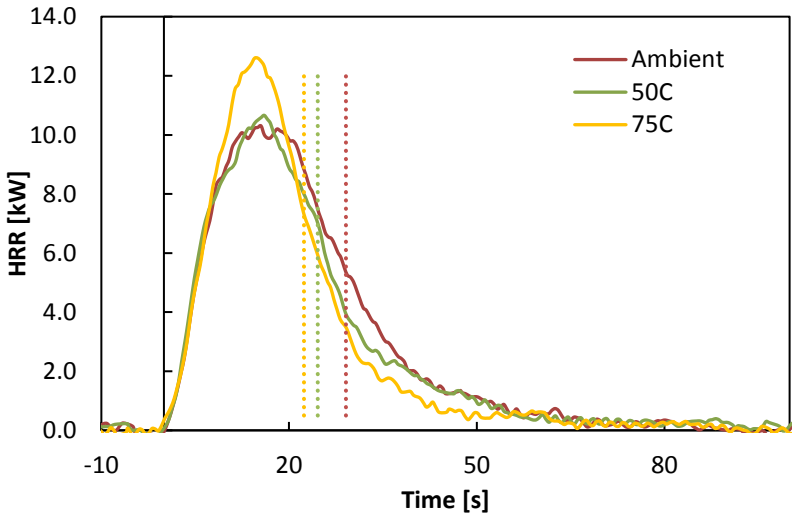


**Fig. 3.6. Typical HRR curves for PS needle samples subjected to 30 kW.m$^{-2}$, HF condition (13.4 cm.s$^{-1}$) and three airflow temperatures (ambient ~18°C, 50°C and 75°C).**

In this graph three typical HRR curves for each airflow temperature are presented. The data was adjusted so that $t$ = 0 s represents ignition for each condition. Also indicated in this graph are the times of flame extinction. It decreases slightly with increasing airflow temperature, which further highlights that combustion dynamics are intensified (sample initial mass is constant).

Averaged duration of flaming period for three repetitions are given in Table 3.3.

Table 3.3. Averaged times of flaming and mean $CO/CO_2$ ratio for tests with varying $T_\infty$. Flow condition: HF.

| | Flow temperature [°C]; (St.Dev.) | | |
|---|---|---|---|
| | 18 | 50 | 75 |
| duration of flaming [s] | 28.5 | 24.9 | 24.9 |
| | (3.5) | (0.6) | (2.6) |
| mean CO/CO2 [%] | 1.49 | 0.72 | 0.66 |
| | (0.57) | (0.22) | (0.30) |

Although, there is a small reduction, it is bordering significance, because it is just outside the experimental uncertainty (St.Dev.). Furthermore, the mean ratio of $CO/CO_2$ indicates a slight improvement of the combustion efficiency with increasing ambient temperature. This can be attributed to an enhanced oxidation of the CO to $CO_2$ in the combustion reaction (higher flame temperatures due to slightly lower convective heat losses of the flames). The improved combustion efficiency will contribute to the higher energy release with increasing ambient temperatures, because the combustion is more complete.

Results shown here indicate that the major impact of changing airflow temperature ($T_\infty$) is on the ignition behavior and only marginally on the burning behavior. This is likely due to the dominance of radiation feedback over convective heat transfer. The reduction in time to ignition when $T_\infty$ is raised is however also not large, compared to changes in ignition times when the flow magnitude is changed (Section 3.3, Table 3.1). The ignition time decrease only by approximately 29.5% when the temperature is raised by about 317%. Contrarily, the ignition time increases by 147%, when the flow velocity is increased from NF to HF (see Table 3.1). This means that either the more critical variable is $h_c$, or dilution.

The next section will now evaluate the dilution mechanism. At the end, impacts of convective heat transfer and dilution are compared to assess if one prevails over the other.

### *3.5. Ignition behavior with changing forced airflow oxygen concentration*

Test with varying flow oxygen concentration, $y_{O_2}$, (constant flow) were conducted with the tube, which created a ventilation controlled environment. The ventilation controlled environment is necessary if one desires to study the effects of oxygen mass flow on the combustion dynamics.

It has been shown in past research [3.3] that, time to ignition does not change significantly until a limiting oxygen concentration (LOC) is reached. Fuel in [3.3] was however solid material (wood particle board). This illustrates that dilution is not significantly affected for solid fuel. It is unknown if this is the case for porous vegetative fuels beds as well. For example, mixing conditions around and above solid material is likely different compared to porous fuel beds, where mixing can also occur within the fuel matrix.

The time to ignition is plotted in Fig. 3.7, with respect to the forced flow oxygen concentration. The ignition time is not influenced by a change in oxygen concentration, until a concentration of 15%, which compares well with values for LOC found in literature [3.29-3.34]. At 15 and 14% ignition occurred, but it was not piloted ignition anymore. The needles started smoldering and created a hot spot, at which the combustion process transitioned to a flaming state.

The variability (error bars: St.Dev.) is due to the ignition process, which is highly dependent on local conditions which may be impacted by the heterogeneity of the fuel bed. Overall, the averaged standard deviation for all tests is approximately 15%, with a peak experimental error for $y_{O_2} = 0.19$, 33%. Slightly lower average variability of the time to ignition (~10%) was observed for the tests with varying $\dot{V}$ and $\dot{q}''_{ext}$ in Section 3.3.

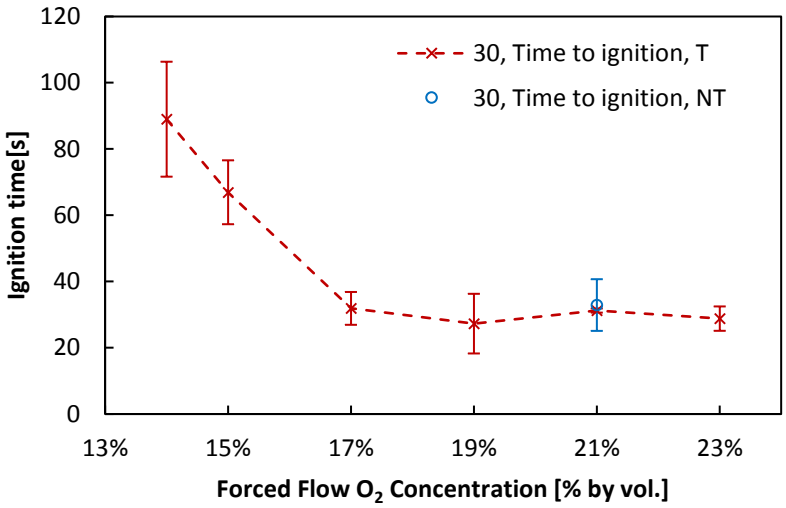


**Fig. 3.7. Time to ignition for tests at various inlet flow $O_2$ concentrations. Tests at 30 kW.m$^{-2}$, constant flow magnitude (HF) with tube (T) and without (NT).**

Vitiation of the atmosphere above the fuel bed may occur, which means that the exact local oxygen levels at the sample surface may be lower than what is measured upstream in the supply line ($y_{O_2}$). Some recirculation of smoke was observed visually near the edges of the sample. Marquis et al [3.34] have shown that vitiation may be significant if the forced flow rate is not higher enough. Major differences exist between the experimental apparatus used in [3.34] (Controlled Atmosphere Cone Calorimeter) and the FPA.

The combustion chamber and quartz tube are a continues cylindrical "chimney" which favors the fluid dynamics of hot gases and provides an unobstructed path for them to leave. However, when the hot gases (pyrolysis and/or combustion) contact the colder quartz tube, they cool and may fall along the inner wall of the tube, while hot gases escape through the center of the tube. This creates buoyancy driven turbulence that may cause the vitiation. It is assumed that this effect will be small compared to the forced flow rate of oxidizer.

It can be concluded from these results that a threshold oxygen concentration below which piloted ignition is unlikely, is between 15-17%. Above this threshold, piloted

ignition is possible and shows no influence of the forced oxygen flow ($\dot{m}_{O_2,f}$). It should be noted that the threshold (LOC) can depend on the flow rate (e.g. [3.31]). No experimentations were conducted to test this, because it is outside the scope of this work.

Results in Fig. 3.7 indicate that, the ignition time is independent of the inlet flow oxygen concentration when $y_{O_2} \geq 0.17$. Therefore, the assumption that $t_m << t_p$ is still acceptable for this range of oxygen concentrations. Below 17%, the change in ignition scenario indicates that the simplification, $t_{ig} \approx t_p$ is not applicable anymore. This is however, because $t_i \rightarrow 0$ s (only true for piloted ignition), is not acceptable any more.

Even at elevated oxygen concentration (23%) the time to ignition is the same as at ambient condition. Results show that the dilution at this flow rate and concentration is not enough to cause $t_m$ to significantly increase, because $t_{ig}$ (21%) ≈ $t_{ig}$ (23%). It can be concluded that $t_m$ is small compared to $t_p$, when $0.17 \leq y_{O_2} \leq 0.23$ and the flow rate is 100 lpm.

No significant differences were observed when comparing ignition times for test without tube to test with tube. Results for tests without tube are also included in Fig. 3.7. Therefore, using the tube has no significant adverse effects on the ignition behavior.

A number of tests were conducted at higher heat flux (60 kW.m$^{-2}$) to assess the impact of heating rate on this behavior. Tests with the tube had an ignition time of 6.17 +/- 0.71 s. The time for tests without the tube was 6.37 +/- 0.26 s. Also no significant differences are observed. Therefore, the assumption, $t_m << t_p$ is acceptable for the conditions tested (forced convection). Further experimentation is required to fully test what magnitude of $\dot{m}_{O_2,tot}$ is required to raise $t_m$ to a level where the assumption $t_{ig} \approx t_p$ becomes unacceptable. This may be achieved by further increasing $y_{O_2}$ until deviations of the ignition times are observed.

It has been shown in this section that, dilution ($t_m$) is a minor factor impacting the ignition behavior when the ventilation is controlled well. The flow magnitude tested was 100 lpm, with $0.14 \leq y_{O_2} \leq 0.23$. It was observed that piloted ignition was only possible when $y_{O_2} > 0.15$. Below this threshold, ignition is a transition from smoldering to flaming away from the pilot flame. Therefore, at this condition $t_{ig} \approx t_p$ is challenged, because $t_i \rightarrow 0$ s is not valid any more.

It can be concluded that the convection heat transfer effects (due to flow velocity and temperature) are more significant compared to the dilution effects. This suggests that the most critical parameter impacting the ignition behavior of porous fuel beds subjected to forced convection is $h_c$, and thus the velocity of the forced convection. Future research should therefore focus on determination of appropriate values of $h_c$ for porous wildland fuel beds.

### *3.6. Burning behavior with changing forced airflow magnitude and $O_2$ conc.*

In this section results of duration of flaming, mean ratio of $CO/CO_2$, and pHRR are plotted against the forced oxygen flow rate ($\dot{m}_{O_2,f}$), which was calculated according to Section 3.2.3. The first part of this section discussed the duration of flaming period. This is followed by discussion of visual observations of the combustion process and generation rates of CO and $CO_2$ (Section 3.6.2). Explanations of the gas generation rates aid in the understanding of the combustion efficiency (mean $CO/CO_2$), which is discussed in Section 3.6.3. Finally, the HRR is analyzed in Section 3.6.4.

#### *3.6.1. Duration of flaming period*

It has been shown in past research [3.28, 3.35] that the radiative power of flames increases when the ambient oxygen concentration increases (20.95-40%). This has been attributed to increasing flame temperatures, which leads to greater soot production. The increase in flame temperatures is due to the change in heat capacity

of the atmosphere, when the oxygen concentration is altered (diluted or enriched). This means that there is an inherent effect, depending on the dilution gas used (e.g. $c_{p,N2}$ = 1.04 kJ.kg$^{-1}$.K$^{-1}$ and $c_{p,CO2}$ = 0.844 kJ.kg$^{-1}$.K$^{-1}$). Such effects were observed in [3.32, 3.34], but were not assessed in this work (only $N_2$ was used as dilution gas).

The higher soot production leads to more luminous flames [3.28], which increases the radiative losses from the flame. The increased losses lower the temperature. A competition between the effects controlling the flame temperature can be observed (due to changes in gas heat capacity and soot production) [3.35]. The increased radiative power results in a larger flame heat flux feedback to the fuel surface, which drives the pyrolysis rate.

Experimentations conducted here are done at reduced ambient oxygen concentrations. It has been shown in [3.28, 3.36] that a similar relationship between the radiative power and oxygen concentration is true for reduced oxygen concentrations (< 20.95%), i.e. it reduces due to lower soot production. This results in reduced heat flux feedback and thus lower pyrolysis rates.

Besides the impact on the gas phase (flames), it is likely that the surface reaction (smoldering) is also impacted. Increasing $\dot{m}_{O_2,f}$ intensifies the smoldering due to improved availability of oxygen at the solid interface. Therefore, changes in pyrolysis rate are due to both factors: (1) heat flux feedback from the flames and (2) smoldering intensity.

Although no mass loss data was obtained here (due to experimental constraints), it was possible to infer changes in pyrolysis rate at different test conditions (varying $\dot{V}$ and $y_{O_2}$). This was achieved by analyzing the duration of flaming period, which is plotted in Fig. 3.8.

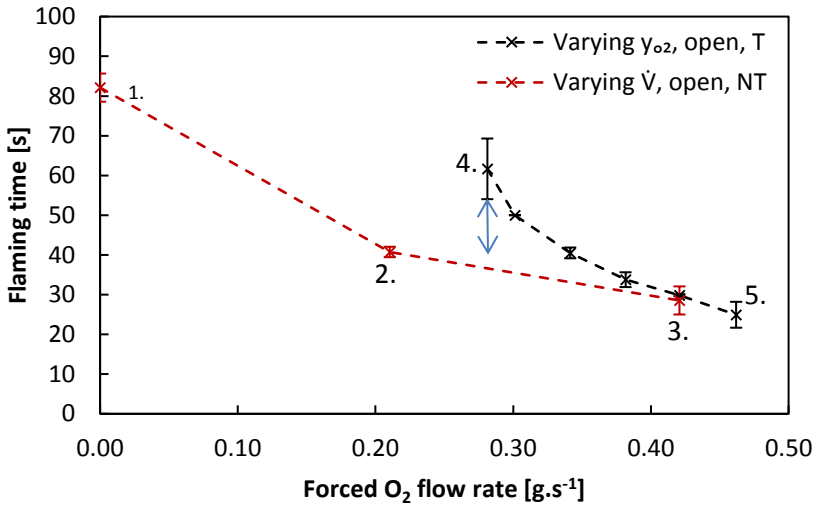


**Fig. 3.8. Duration of flaming period of tests with varying forced airflow magnitude and oxygen concentration.**

The duration of flaming can be defined as a function of the pyrolysis rate ($\dot{m}_p$). Thus, if the flaming period increases it is because the pyrolysis rate decreases, and vice versa. The pyrolysis rate increase when the heat flux to the surface and/or smoldering reaction intensifies, and vice versa. This can be assumed, because sample preparations were consistent. The pyrolysis rate may change when sample preparations changes, e.g. fuel loading. At the end of all tests, only ash remained in the sample holder.

Both test series (Fig. 3.8) indicate that, the duration of flaming decreases (1 → 3, and 4 → 5) with increasing $\dot{m}_{O_2,f}$, but at different rates. Increasing $\dot{m}_{O_2,f}$ by increasing $\dot{V}$, increases the flame heat flux and smoldering intensity, but also increases the convection cooling of the particles. However, the increase in heat flux feedback and smoldering outweigh the increase in convective cooling.

Increasing $\dot{m}_{O_2,f}$ by increasing $y_{O_2}$, increases the flame heat flux and smoldering intensity, but convection cooling of the particles is constant (constant velocity). Therefore, the deviation between the trends (blue arrow), can be associated, in part, to a change in convective cooling.

For example, consider the black marker at 0.281 g.s$^{-1}$ (4), which is the condition: $y_{O_2} = 0.14$ and $\dot{V} = 100\ lpm$. This forced oxygen flow rate would correspond to $\dot{V} = 67\ lpm$ (8.9 cm.s$^{-1}$) at ambient oxygen (red line). At this flow rate the convection cooling is lower compared to 100 lpm, which means that the pyrolysis rate is higher due to lower heat losses. This describes the longer flaming time for (4) compared to the trend of the red marker (blue arrow).

A second factor impacting the deviation (blue arrow) is the change in heat flux feedback, which changes in different oxygen atmospheres, as was described above.

It may be assumed that the smoldering intensity is only dependent on the oxygen availability at the solid surface. Thus, it can be concluded that the smoldering for each test series (black and red marker) at a given $\dot{m}_{O_2 f}$, is equivalent. This also assumes that, oxygen diffusion from the surrounding to the surface ($\dot{m}_{O_2,n}$) is small compared to $\dot{m}_{O_2,f}$.

In Fig. 3.8, the deviation (blue arrow) between black markers and the trend set by the red markers (varying $\dot{V}$), shows the combined effect of convective cooling and reduction in heat flux feedback, with constant smoldering.

When $\dot{m}_{O_2,f}$ is raised (from data point (4) and corresponding point on the red trend line), either by increasing $y_{O_2}$(black marker), or by increasing $\dot{V}$ (red marker), the deviation reduces and the duration of flaming converge. This may be attributed to: (1) heat flux feedback in both cases increases, but it increases more drastically by increasing $y_{O_2}$; and (2) convective cooling increases when increasing $\dot{V}$, but not when increasing $y_{O_2}$. In both cases the smoldering intensifies when $\dot{m}_{O_2,f}$ is increased.

In the next section, the combustion dynamics will be discussed in terms of the CO and $CO_2$ generation rates. Analyzing the generation rates of these two gases provides evidence for changing combustion behaviors, e.g. the distinction between complete

and incomplete combustion. Furthermore, it also shows evidence of changing pyrolysis behavior before ignition. Knowledge of the generation of CO and $CO_2$ will be used in Section 3.6.3 and 3.6.4 to discuss the combustion efficiency and combustion intensity, respectively.

### *3.6.2. CO and $CO_2$ generation rates*

Before going into the data analysis of the generation rates, some visual observations are discussed, which are important to understand the combustion dynamics.

*Visual observations of changes in flaming regime (diffusive and premixed)*

Varying the oxygen mass flow rate affected the flaming regime in the FPA tests (diffusion or premixed). As was discussed in Chapter 1, this is a known phenomenon. Visually, the change in flame regime can be observed in Fig. 3.9 and 3.10. In ambient environment (well-ventilated) the flame is dominantly a diffusion type (Fig. 3.9.b), whereas, in reduced oxygen concentration (< 19%), the flame is better characterized as a premixed type (Fig. 3.10.b). A mixed state (premixed and diffusion) occurs for tests with the tube and oxygen concentration ≥ 19% (Fig. 3.9.a).

At ambient and 23% oxygen concentrations, flames were clearly visible for the duration of the flaming period. This is shown in Fig. 3.9.a and b. When the tube is used at 23% inlet oxygen, flaming occurs above the exit of the tube (Fig. 3.9.a). This is also the case for 21%. At 19%, intermittent flaming occurs above the tube, only in a few seconds after ignition. The majority of the flaming occurs inside the tube.


**Fig. 3.9. Flaming state after ignition at a) 23% oxygen concentration with tube and b) 21% oxygen concentration without tube.**

For 17% and lower oxygen concentrations no flaming is observed above the tube exit. At these concentrations it also became difficult to see the flames when the heating lamps are engaged. An illustration of this scenario is shown in Fig. 3.10.a. Flames are, however, still present, which become visible when the lamps are turned off (Fig. 3.10.b). In this case, flame extinction (to determine duration of flaming period) was determined by analyzing the exhaust duct temperature. Details to this procedure are discussed in Appendix A3. The picture in Fig. 3.10.b also illustrates the intensity of the smoldering combustion, well.

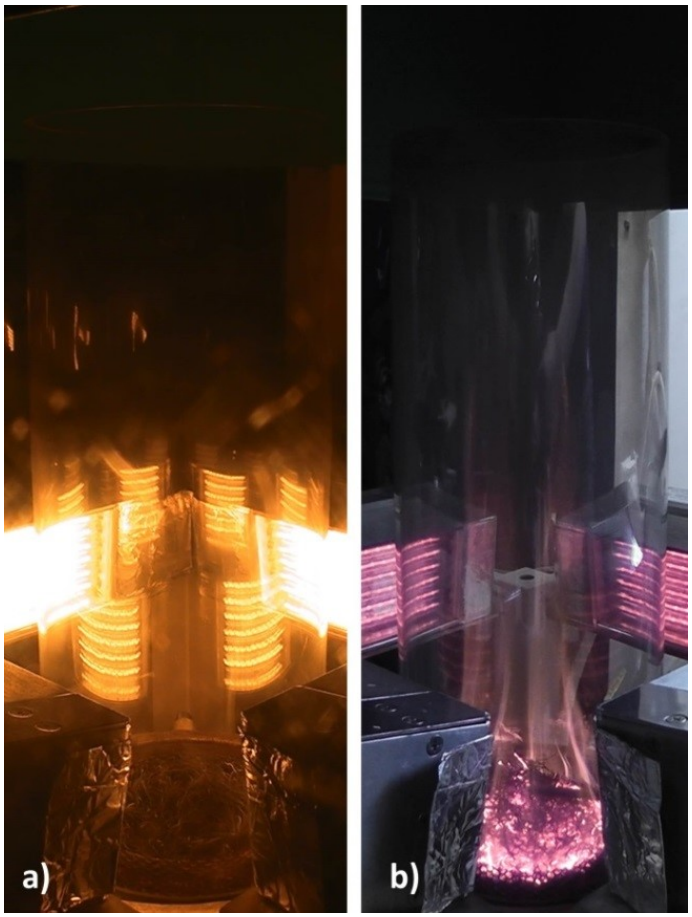


**Fig. 3.10. Flaming state after ignition at a) 14% oxygen concentration with tube and b) 15% oxygen concentration with tube (lamps turned off and filter removed).**

It can be concluded that, a threshold for transition is at approximately 19%. Therefore, two flame regimes can be described: 1) a premixed dominated, laminar type flame, which exists at concentrations < 19%; and 2) a diffusion dominated, turbulent type flame, which exists at concentrations ≥ 19%. This threshold compares well with the one obtained by Biteau et al [3.33], 18%. In the current work, no further intermediate values of $y_{O_2}$ were tested. It was also not the intent of this study to determine the exact transition point.

In [3.33] it was concluded that, below the threshold, only oxidizer contained in the fuel was utilized in the combustion process (potassium nitrate), i.e. a single premixed flame

occurred with oxidizer and combustible gases originating from within the fuel matrix. No oxygen from the atmosphere was used.

In the case for the porous fuel beds in this study, a similar scenario may be considered; only oxidizer mixing with combustible gases in the porous fuel bed is used in the combustion process. In this case, the oxidizer is prescribed and forced into the bottom of the sample. This creates a similar scenario compared to what was observed by Biteau et al [3.33]. The main difference for the porous fuel beds being that, as the oxygen concentration is lowered further below the threshold, an extinction event of the flames occurs. With the given tests, such level of oxygen concentration was not reached, since premixed flaming still occurs at 14%. These observations concur with what was observed by Simmons and Wolfhard [3.31] – the LOC of diffusion flames is higher than premixed flames.

For the study with pine needle beds, a LOC for premixed flaming was not reached. At this limit, the fuel gas and oxygen mixture will not reach a LFL because it is too diluted. Results suggest that this value is not much lower than 14%, although the exact level was not determined. Jervis [3.3] reported a value of 14% in his work with the FPA. Marquis et al [3.34] reported a value as low as 10% in a study with the Controlled Atmosphere Cone Calorimeter. Simmons and Wolfhard [3.31] discussed that the LOC is different for diffusion and premixed flaming, which was also illustrated here. The LOC for diffusion type flaming was found to be between 17-19% in this work, which agrees with literature. It should be note that, the LOC also depends on the flow magnitude [3.31]. This makes comparison to other tests difficult.

*CO and $CO_2$ generation rates*

The data is shown in the graphs in Fig. 3.11, for oxygen concentration 21-15% (a comparison for NF/closed basket and HF/open basket is shown in Appendix A4). In these graphs, the dashed lines are $CO_2$ generation rates and solid lines are CO generation rates. Each color represents one repetition at the test condition. They

indicate excellent repeatability. The same color dashed and solid lines correspond to the same test. The data was adjusted so that $t$ = 0 s represents the time of flaming ignition for each test. Times of flame extinction can be extracted from Fig. 3.8. As a reminder, all tests are done at constant external heat flux (30 kW.m$^{-2}$). General remark: $CO_2$ generation rates are non-zero when no pyrolysis or combustion occurs, because of the naturally occurring $CO_2$ in the atmosphere (~400 ppm). This is captured in the measurements, and should be interpreted as the baseline.

Table 3.4 below summarizes the major findings from the analysis of the CO and $CO_2$ generation rates at varying oxygen concentrations ($y_{O_2}$).

Table 3.4. Summary of peak CO and $CO_2$ generation rates, significant remarks and visual observations, for tests with varying forced airflow oxygen concentration.

| Oxygen concentration | Peak $CO_2$ gen. rate [g.s$^{-1}$] | Peak CO gen. rate [g.s$^{-1}$] | Comments | Visual observation of flaming type: |
|---|---|---|---|---|
| 21%, no tube | 0.7-0.9 | 0.012-0.016 | Peak CO after peak combustion; corresponding to smoldering phase | Turbulent diffusion |
| 21%, tube | 0.55-0.70 | 0.06-0.08 | Peak CO before peak combustion; afterburning above tube exit | Turbulent diffusion |
| 19%, tube | 0.42-0.50 | 0.062-0.074 | Peak CO at ignition | Mixed laminar and turbulent diffusion |
| 17%, tube | 0.43-0.52 | 0.049-0.61 | Peak CO before peak combustion | Laminar premixed |
| 15%, tube | 0.38-0.49 | 0.029-0.045 | Peak CO before peak combustion | Laminar premixed |

In the open, pyrolysis favors the generation of hydrocarbons as opposed to CO. Because of the little amount of CO produced during pyrolysis phase (pre-ignition), there is only little $CO_2$ generated from CO oxidation. During the flaming phase, $CO_2$ generation rates increase until peak combustion. At the same time CO generation rate also increase until the peak rate is reached at or shortly after flame extinction.

The HF condition with open baskets is compared to NF condition with closed baskets in Appendix A4. The forced condition has significantly higher production rates

compared to the NF condition. The peak $CO_2$ production for HF conditions is about three times that of NF condition; the peak CO generation rate approximately 5 times. The occurrence of the peak during the smoldering phase is more evident for closed baskets.

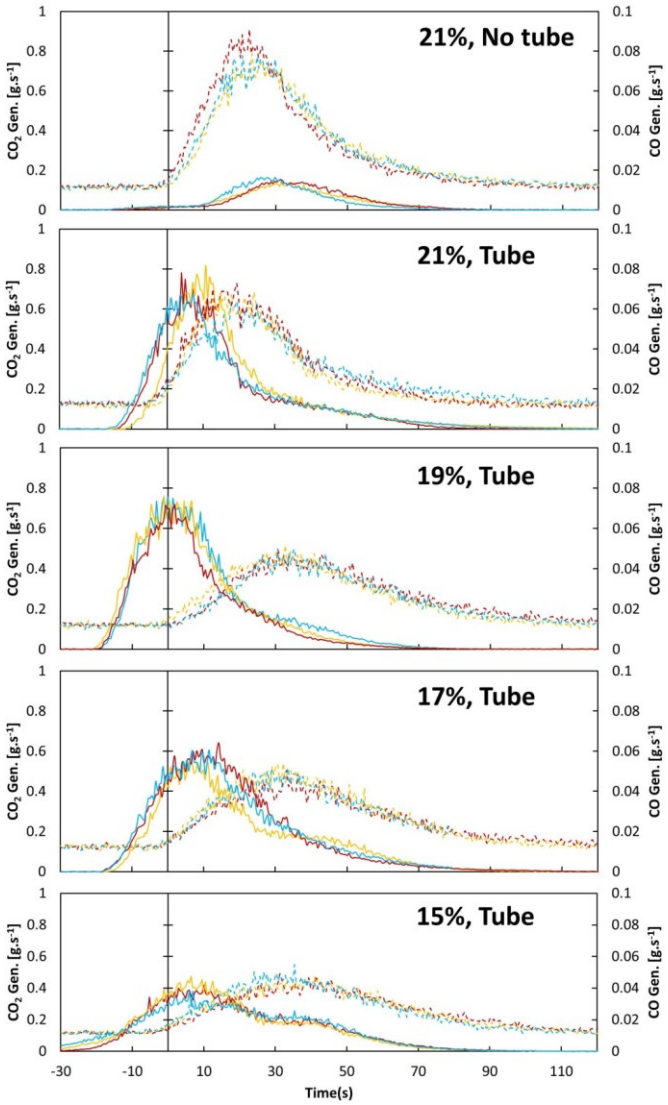


**Fig. 3.11. CO and $CO_2$ generation rates for tests with varying forced airflow oxygen concentration. Dashed lines are $CO_2$ and solid lines are CO generation rates. Each color is one repetition.**

In the confinement of the tube, oxygen is limited (even with 100 lpm forced airflow). The atmosphere around the sample is vitiated. Pyrolysis in this environment favors CO

generation [3.37-3.42]. Because a large amount of CO is generated and oxygen is still available it may oxidize to form $CO_2$ (with sufficiently high temperature). This behavior is weakened when the oxygen concentration is reduced, obviously due to the lack of oxygen available.

Peak $CO_2$ production rate always corresponds to peak combustion intensity; but peak CO production may not be associated to a single distinct event. In the open it corresponds to the flame extinction event. In the confinement of the tube, it occurs before peak combustion intensity (or ignition as was observed for 19% oxygen condition).

Peak $CO_2$ generation is highest for no tube tests ($y_{O_2} = 0.21$). It reduced when the tube is added and oxygen is reduced to 19%. Further reduction in $y_{O_2}$ does not reduce the peak $CO_2$ generation rate.

Peak CO generation is lowest for the no tube tests ($y_{O_2} = 0.21$). It increase and reaches a maximum when the tube is added ($y_{O_2} = 0.21$). Reducing $y_{O_2}$, results in lower CO generation rates.

The 19% condition seems a special condition were CO generation during the pyrolysis phases was most pronounced. This condition has the highest peak CO generation with low peak $CO_2$ generation. Therefore, it may be deduced that the combustion efficiency at this condition is a worst case scenario. Lower oxygen concentration produces the same amounts of $CO_2$ but less CO; higher concentrations produced more $CO_2$ and less CO. This trend seems to be linked with the threshold between flame regimes (19%), which was discussed in the previous subsection (visual observations).

Overall, the results presented here, CO and $CO_2$ generation rates at various ventilation conditions, agree with the understanding of pyrolysis and combustion in reduced oxygen environments [3.28-3.34, 3.37-3.42]. It shows that large amounts of CO are produced when the oxygen availability is limited. This understanding has been

extensively applied to enclosure fire dynamics in the past [3.37-3.42], because CO is a toxic gases and one of the main reason leading to deaths in fires [3.43].

The knowledge is however, less well applied to the wildfire context. Mainly, because wildfire burn in the open, where oxygen is unlimited. As was shown with the data, such a condition leads to minor generation of CO, because the combustion allows the oxidation to $CO_2$. Peak CO generation rates can be attributed to the smoldering state after flame out (most obvious when observing samples with closed baskets in Appendix A4).

The importance in the wildfire scenario is not necessarily life safety, as is the case for the build environment, but it is aimed at understanding the emissions of large wildfire [3.44-3.47]. It is well understood that smoldering produces higher levels of CO compared to well-ventilated combustion [3.47, 3.48]; as it was also shown in this work. However, it was also shown that CO generation is enhanced in conditions were the oxygen availability is limited. Pyrolysis and combustion in such an environment generate much greater amounts of CO compared to smoldering, approximately four times as much (see Table 3.4; 21% no tube and tube peak CO generation rate).

Therefore, a question that arises is: do oxygen limited combustion scenarios occur in wildfires? This is not a simple question to answer, but results presented here suggest that a large fraction of wildfire emission may be attributed to oxygen limited combustion. At this point, there is no direct answer to this question contained in this work. Three scenarios may however be described that can result in limited oxygen environment: (1) the interior of a large fire front; oxygen is consumed mainly along the borders of the fire front (wind may bring oxygen into the center or oxygen may diffuse from above). Nonetheless, it is likely that combustion at reduced oxygen concentration can occur inside a large flame front. (2) Combustion of live fuel in the canopy that are inside the plume of a passing surface fire. The oxygen concentration may be reduced due to the presence of combustion products that vitiate the atmosphere.

This might be further enhanced by the release of water vapor from live foliage, which displaces oxygen. (3) A last case may be a full active crown fire. In the build environment, under-ventilation combustion and the danger of toxic gas production is often associated to a "post-flashover" condition (e.g. [3.13]). In such a scenario, the entire room in which the fire originated is involved in the fire dynamics. In a wildfire context, the analogous condition would be the active crown fire.

Future investigations of the sources of emission of wildfire should include the possibility of oxygen limited combustion, as results presented here indicate that it might be a significant factor.

The HRR is another important metric describing the combustion dynamics (besides duration of flaming and emissions). Before discussing the combustion intensity, the combustion efficiency is explored. Here, the mean ratio for the flaming period is used to describe the combustion efficiency.

### *3.6.3. Combustion efficiency*

In the previous section it was illustrated that under well-ventilated condition, $CO_2$ generation is large and CO generation is low, compared to the ventilation limited condition (with tube). In the ventilation limited condition, CO generation is high due to the reduced oxygen availability. In such atmosphere, oxygenated fuels (e.g. wood or vegetative fuels) generate large amounts of CO compared to unburned hydrocarbon or $CO_2$. This is in agreement with literature (e.g. [3.41, 3.42]). The reduced oxygen availability prevents further oxidation of CO to $CO_2$. This can now be evaluated with respect to the ratio of $CO/CO_2$. Results of the mean $CO/CO_2$ ratios are summarized in Fig. 3.12. It is evident that it is significantly higher for tests with tube compared to tests without it.

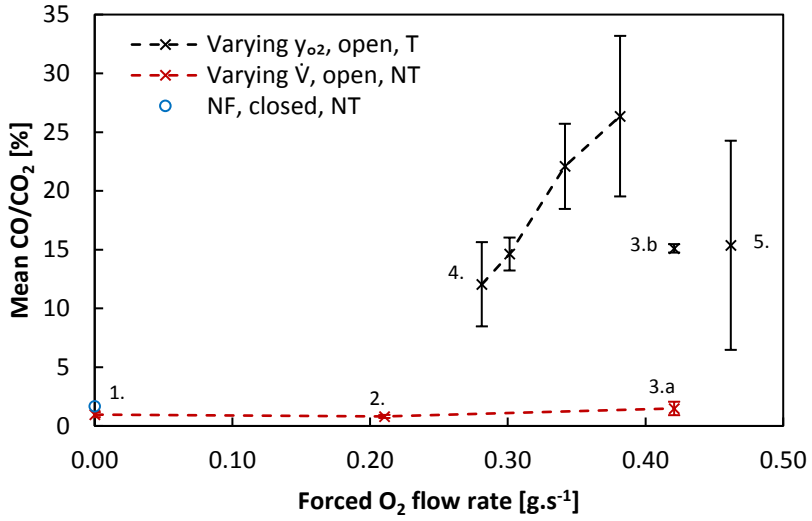


**Fig. 3.12. Mean CO/CO₂ ratio during flaming for tests with varying forced airflow magnitude and oxygen concentration.**

The discussion will first focus on the test series with varying flow magnitude ($\dot{V}$; red marker), with constant oxygen concentrations ($y_{O_2} = 0.21$). Labeling of the data points in Fig. 3.12 was kept consistent with the labeling in Fig. 3.8 (duration of flaming period).

### Varying forced airflow magnitude

When the ventilation condition is slightly improved, from closed to open baskets at natural convection (1), the combustion efficiency is impacted. The mean ratio during flaming is presented in Fig. 3.12 for each ventilation condition. The mean $CO/CO_2$ ratio for closed baskets and NF (0.0 $g.s^{-1}$) has the highest value, 1.70%. With open baskets it is 0.97% and 0.81% for NF and LF (0.210 $g.s^{-1}$), respectively. When the forced flow rate is increased to HF (0.421 $g.s^{-1}$), the ratio increases to 1.5%. These conditions refer to data points (1), (2) and (3.a), respectively.

Low generation of CO compared to $CO_2$ (low $CO/CO_2$ ratio), indicates a combustion with high efficiency, and represents a well-ventilated condition. Such condition can be assumed for all tests with varying flow magnitude. The slight increase or $CO/CO_2$ for

HF condition (3.a) is likely due to minor smoldering prior to flaming ignition. Although the smoldering was not clearly visible at this heating rate (ash formation), evaluation of the $CO/CO_2$ ratio provides a suitable tool to assess this behavior. (Remark: even though it seems that smoldering combustion starts before flaming, the tests at this heat flux are still considered piloted, because ignition occurred at the pilot flame. When the heat flux is reduced, smoldering became more obvious and transition to flaming occurred away from the pilot. See critical heat flux discussion in Section 3.3.)

This smoldering behavior can also be observed in Fig. 3.13 (”HF, open”), where the $CO/CO_2$ ratio is plotted against time for typical tests with varying flow magnitude. The $CO/CO_2$ ratio increases before flaming ignition ($t$ = 0 s). At ignition, the ratio drops sharply due to the oxidation of CO to $CO_2$. When flames start to extinguish, the ratio increases again and reaches its peak shortly after flame out.

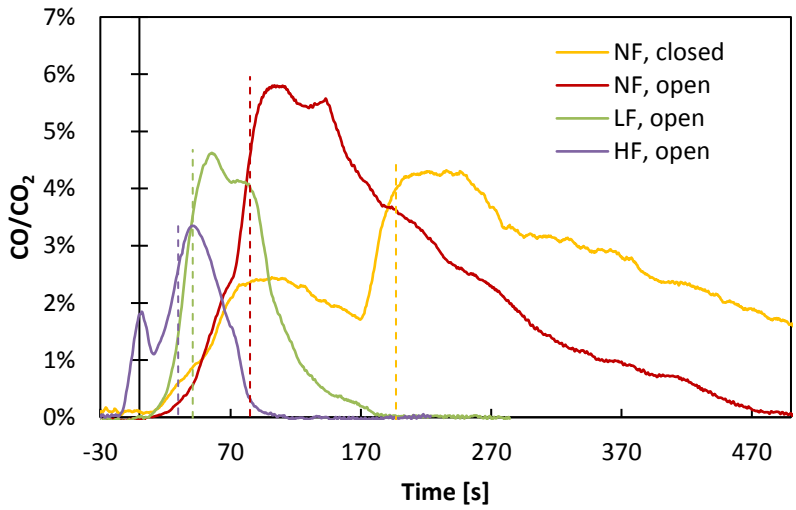


**Fig. 3.13. Typical $CO/CO_2$ evolution for tests with varying forced airflow magnitude. t=0s indicates flaming ignition for all tests; dashed lines indicate flame extinction.**

The peak value of $CO/CO_2$ is lower for closed baskets compared to open baskets (Fig. 3.13), which indicates a less intense surface reaction (smoldering). For all conditions tested (in this well-ventilated scenario), the peak value corresponds to a time after

flame extinction, i.e. a residual smoldering period. This is different to the ventilation limited conditions, where the peak corresponded to the flaming period (as will be discussed in next subsection).

The peak $CO/CO_2$ ratio decreases with increasing flow rate (Fig. 3.13). This is peculiar, because it was observed visually that, the smoldering is more energetic when a forced flow is present (stronger glow of the smoldering). Several reasons may cause the reduction in $CO/CO_2$ ratios with increasing flow magnitude: (1) more CO is oxidized to $CO_2$ due to higher surface temperatures; or (2) peak smoldering period (where $CO/CO_2$ is largest) occurs during flaming period.

In the case of forced flow condition, flaming and smoldering combustion occur simultaneously [3.9]. When the forced flow is blocked (closed sample baskets) the two types of combustion occur more separated, with little overlap (see also CO and $CO_2$ generation rates in Appendix A4). The peak smoldering period may occur during the flaming state. In this case, CO produced from the surface reaction has to pass through the flame front, at which point it is oxidized to $CO_2$, resulting in lower $CO/CO_2$ ratio. Therefore, the actual production of CO from smoldering is not captured in these experiments.

**Varying forced airflow oxygen concentration**

Overall, the $CO/CO_2$ increases significantly when the tube is used due to increase in CO generation during pyrolysis and combustion in vitiated atmosphere (Fig. 3.12). It indicates a drastic change in combustion efficiency. The process was first explained with the generation rates in Section 3.6.2. The lowest value of $CO/CO_2$ was observed when $y_{O_2} = 0.14$ ($\dot{m}_{O_2,f} = 0.281\ g.s^{-1}$), the highest at $y_{O_2} = 0.19$ ($\dot{m}_{O_2,f} = 0.381\ g.s^{-1}$). The values are 12.1 and 26.4%, respectively. The reduced values for $y_{O_2} = 0.21$ ($\dot{m}_{O_2,f} = 0.421\ g.s^{-1}$) and $y_{O_2} = 0.23$ ($\dot{m}_{O_2,f} = 0.462\ g.s^{-1}$) are due to afterburning above the tube exit.

Reducing $y_{O_2}$ to 0.19 increases CO generation during pyrolysis, but less oxidation of CO to $CO_2$ is observed during the pre-ignition phase, due to the reduced oxygen availability. This results in very high $CO/CO_2$ ratios. Reducing $y_{O_2}$ further reduces CO generation during pyrolysis. Little oxidation occurs before ignition. Therefore, $CO/CO_2$ ratio reduces because of less CO generation.

Typical mean $CO/CO_2$ ratio evolutions during the test phase are plotted in Fig. 3.14.

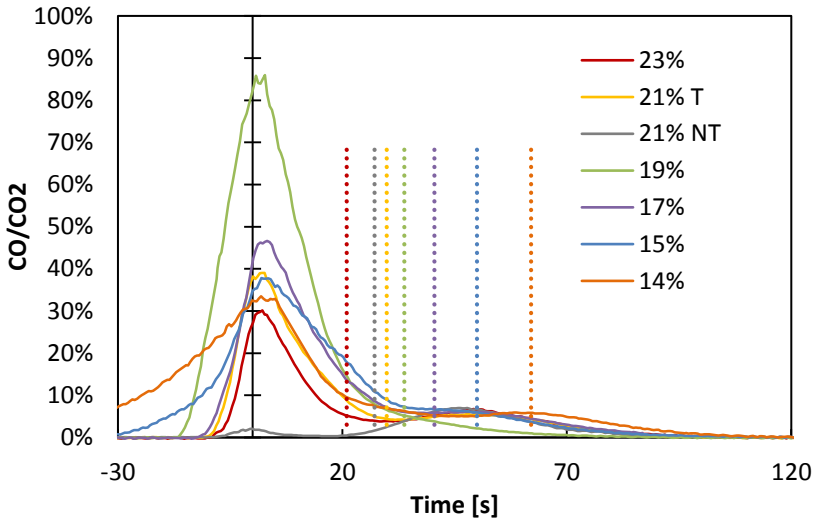


**Fig. 3.14. Typical $CO/CO_2$ evolution for tests at varying forced airflow oxygen concentration. t=0s indicates flaming ignition for all tests. T: tube. NT: no tube. Dotted lines represent flame extinction (color coded)**

Several observations can be made: (1) Pyrolysis is affected by the changing in confinement (Tube) and oxygen concentration. The rise of the $CO/CO_2$ ratio begins earlier. Tests are piloted ignition when $y_{O_2} \geq 0.17$ with the similar ignition times (29.8 +/- 2.14 s), yet the rise of $CO/CO_2$ begins at different times. A trend can be observed: the rise starts closest to ignition for tests without tube. Tests at 23% have the highest $\dot{m}_{O_2,f}$ but utilize the tube. The rise begins slightly early compared to the no tube test. Reducing the concentration to 21%, results in an earlier rise. Reducing the concentration further to 19%, results in an even earlier rise. After this, a reduction to 17% resulted in a later rise, which was attributed to $CO_2$ generation during this phase.

15 and 14% have a much earlier rise, because they have a much longer preheating time (ignition is delayed); (2) the ratios are much higher compared to the open burning condition (21% NT); (3) the ratio is highest for 19% oxygen concentration, which was discussed to be a threshold below which flaming regime changes (above 19% afterburning above the tube is the reason why the $CO/CO_2$ ratio decreases); (4) the residual smoldering phase can be identified by a plateau, which corresponds roughly to peak $CO/CO_2$ for tests without tube (5-7%); and (5) the evolution of $CO/CO_2$ is distinctly different for tests that are piloted ignition (≥ 17%) compared to tests that are transitioning from smoldering to flaming (≤ 15%). This is because of the longer pre-heating time, which results in extended pyrolysis and smoldering. For comparison, the ignition times are 67 +/- 10 s and 89 +/- 17 s for 15 and 14% oxygen concentration, respectively.

The analysis of the $CO/CO_2$ ratio proved to be a good tool to assess the combustion efficiency in these tests. The following section discusses the combustion intensity. The importance of the combustion efficiency will be highlighted.

### *3.6.4. Combustion intensity*

The understanding obtained from analyzing the length of the flaming period and combustion efficiency now allows the analysis of the HRR. In context of pHRR, the behavior should be such that, it increases with (1) increasing $\dot{V}$, and (2) increasing oxygen concentration, because it was discussed that the pyrolysis rate increases in both cases. Results of the pHRR calculations (via oxygen consumption calorimetry) of the current study with pine needle beds are shown in Fig. 3.15.

Labeling of the data points in Fig. 3.15 was kept consistent with the labeling in Fig. 3.12 (mean $CO/CO_2$). In the graph, 0.0 $g.s^{-1}$ forced oxygen flow rate corresponds to natural convection. The discussion will first focus on the test series with varying flow magnitude ($\dot{V}$; red marker), with constant oxygen concentrations ($y_{O_2} = 0.21$).

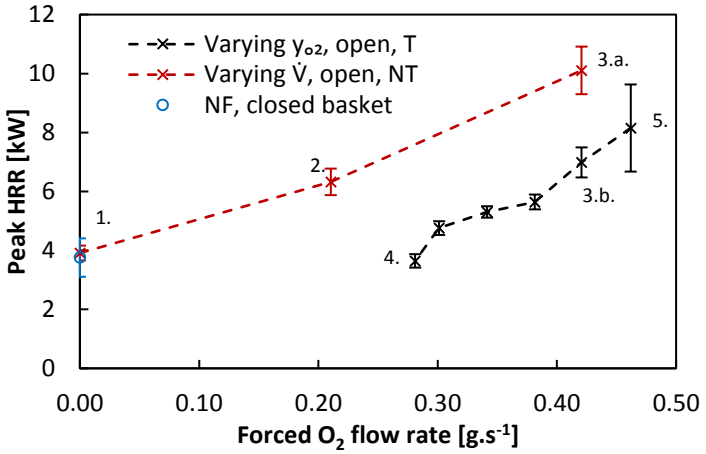


**Fig. 3.15. Peak HRR for tests with varying forced airflow magnitude and oxygen concentration.**

### Varying forced airflow magnitude

The pHRR results (Fig. 3.15) indicate that a more intense combustion took place when the forced convection flow rate is increased (1 → 3), which supports the discussion that the flame heat flux to the surface and smoldering increases and thus drives the pyrolysis rate. For pine needle beds, similar behavior was first shown by Schemel et al [3.4] and Bartoli et al [3.8]. A linear relationship between pHRR and $\dot{m}_{O_2,f}$ was found here.

For comparison, tests done with closed sample baskets and natural convection are also included in Fig. 3.15 (blue marker at 0.0 g.s$^{-1}$). No difference is found in the pHRR for natural convection, closed and open baskets (PS needles). The combustion efficiency only reduced marginally compared to tests with the tube.

For both samples, pHRR occurs shortly after ignition (Fig. 3.16), and corresponds to the time when the entire surface of the fuel is involved in the combustion. Once the flames cover the entire surface of the sample, oxygen availability becomes limited in the sample matrix (for closed baskets), which limits heterogeneous surface combustion. Oxygen can only diffuse through the flame sheet. In contrast, when the

sample basket is open, it may still reach the interior of the fuel matrix and flaming region. Therefore, oxygen supply is less limited.

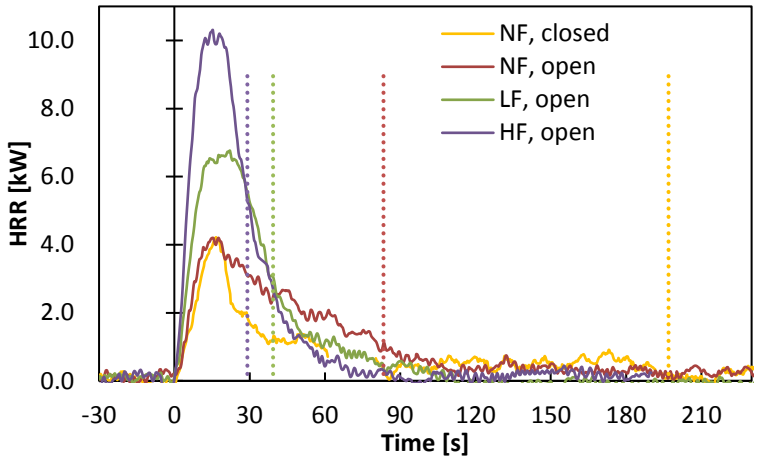


**Fig. 3.16. Typical HRR (OC) curves for tests with varying forced airflow magnitude. t = 0 s represents flaming ignition for each test. dotted lines are flame extinction (color coded).**

The differences between these two combustion dynamics can be observed from the drop in HRR after the peak has been reached (Fig. 3.16). The drop is more sudden for samples with closed baskets (yellow line), which indicates that the intensity of the combustion reduces faster for this condition. The flaming period is however much longer than the time for open baskets (compare dotted lines). For closed basket the flaming period is long, but the flaming intensity is low. The flaming state can be best described as a flashing state, with little flamelets.

These results (Fig. 3.16) are slightly different to what was discussed in [3.5, 3.7, 3.8] for different pine needle species. Authors showed that pHRR increases for natural convection when open baskets are used instead of closed baskets. Bartoli et al [3.5] showed this behavior for three Mediterranean species and Thomas et al [3.7] showed this behavior for two North American species (PR and PRI).

Each one of these species has a significantly lower *SVR* compared to PS needles. PS has a *SVR* that is almost twice as large as the largest one for species tested in [3.5] or [3.7] (also see Chapter 2). Even though the sample porosities are similar, Simeoni et

al [3.8] established that permeability is a critical parameter that governs the combustion dynamics of fuel beds.

According to the empirical correlation for permeability [3.8], PS needle beds studied here (bulk loading is 1.2 kg.m$^{-2}$), have a permeability, $K$, of $0.491 \cdot 10^{-7}$ m$^2$ (values for calculations are taken from Chapter 2; thickness of the needle is required for the calculation of $K$. This was assumed equivalent to diameter). Under the same loading, needles tested in [3.5] and [3.8] have a permeability between 0.96-$1.45 \cdot 10^{-7}$ m$^2$. Data presented by in [3.8] indicates that, the influence of airflow on the combustion intensity reduces with decreasing permeability. The lower permeability of PS needle beds compared to beds with Mediterranean species tested, can be attributed to the behavior observed in Fig. 3.15, i.e. the pHRR is little influenced by the sample basket.

This is only true for natural convection. When airflow is forced into the fuel bed, pHRRs are significantly higher and flaming periods are shorter (see also Fig. 3.8, flaming time).

Next it is explored how the combustion intensity changes when $\dot{m}_{O_2,f}$ is varied by changing $y_{O_2}$. Results of the pHRR are provided in Fig. 3.15.

**Varying forced airflow oxygen concentration**

In these tests, only the prescribed forced oxygen flow rate ($\dot{m}_{O_2,f}$) impacts the combustion (exception at 21 and 23%). Convective cooling of the solid phase, which can impact the pyrolysis rate, is constant, because the flow magnitude is constant. It can be observed in Fig. 3.15 that, the pHRR is increased with increasing oxygen flow rate, from (4) to (3.b) to (5). This increase in pHRR can be associated with an increase in pyrolysis rate ($\dot{m}_p$). As was described earlier (Section 3.6.1) this is because of the increase of the heat flux feedback from the flames to the fuel surface and smoldering intensity with increasing $y_{O_2}$.

The pHRR values are much lower compared to values for tests done with varying $\dot{V}$ (red marker). This is because of several factors. It was concluded in Section 3.6.1 that, the pyrolysis rate is different for the two test series at the same value of $\dot{m}_{O_2,f}$ (due to deviation of duration of flaming period at the same $\dot{m}_{O_2,f}$). On the one hand, for a given $\dot{m}_{O_2,f}$ the convection cooling is higher for the test series with varying $y_{O_2}$. On the other hand, it was described that, the flame heat flux feedback reduces in reduced oxygen environment (changing flame properties due to changing atmosphere heat capacity), which only impacts the test series of varying $y_{O_2}$ and not where $\dot{V}$ is varied. For a given $\dot{m}_{O_2,f}$ it was assumed that, the smoldering reaction is similar for both test series.

Another factor impacting variation in pHRR is the limiting of the total oxygen flow ($\dot{m}_{O_2,tot}$) by preventing natural entrainment ($\dot{m}_{O_2,n}$) due to the use of the tube. This resulted in significant reduction in the combustion efficiency ($\chi$), which was described in the previous section with CO/$CO_2$. The forced oxygen flow rate ($\dot{m}_{O_2,f}$) was not sufficiently high to make up the amount of $\dot{m}_{O_2,n}$ that was blocked. The highest efficiency was observed at $\dot{m}_{O_2,f} = 0.281$ (CO/$CO_2$ = 12.1%), the lowest at $\dot{m}_{O_2,f} = 0.382\ g.s^{-1}$ (CO/$CO_2$ = 26.4%). At $\dot{m}_{O_2,f} = 0.421\ g.s^{-1}$, combustion efficiency improved again, because of afterburning above the tube.

The increase in $\dot{m}_p$ and variability of the $\chi$ with increasing $y_{O_2}$ cause the non-linear trend in the result of the pHRR (Fig. 3.15). For example, as pyrolysis rate increases, from $\dot{m}_{O_2,f} = 0.281\ to\ 0.382\ g.s^{-1}$, combustion efficiency decreases. These are competing effects on the pHRR, that cause the non-linear trend in this range of $\dot{m}_{O_2,f}$. The deviation from this trend at 0.421 g,$s^{-1}$ (data point 3.b; $y_{O_2} = 0.21$) and 0.462 g.$s^{-1}$ is due to the afterburning above the tube exit.

The HRR of a burning item in the open can be generally estimated as (e.g. [3.12]):

$$\dot{q} = \chi \Delta h_c \dot{m}_p \quad \textbf{Eq. 3.1}$$

Where $\Delta h_c$ is the heat of combustion. From Eq. 3.1, one can deduce that the HRR depends on the fuel ($\Delta h_c$). The pyrolysis rate is impacted by many factors on the scale of the particle and sample, as well as external factors, as was discussed throughout the chapter. It was not possible to apply the Eq. 3.1, directly, because no mass loss data was obtained (due to experimental constraints). This also did not allow the quantification of $\chi$. Thus, it can only be evaluated qualitatively.

Results for tests with and without tube at $y_{O_2} = 0.21$ and $\dot{V} = 100\ lpm$ ($\dot{m}_{O_2,f} = 0.421\ g.s^{-1}$) can be compared (point 3.a and 3.b in Fig. 3.15). Because the flow rate is the same for both test conditions, convection cooling can be considered equivalent. Furthermore, the smoldering intensity can be considered equivalent because it depends on $\dot{m}_{O_2,f}$. It was found in Fig. 3.8 that the duration of flaming and thus the pyrolysis rate is the same for both conditions. Therefore, according to Eq. 3.1, the reason for the difference in pHRR (~31%) must be the combustion efficiency. This was shown to be the case in Section 3.6.3 (higher $CO/CO_2$ ratio for tests with tube).

At 14% (0.281 $g.s^{-1}$ oxygen), the condition reaches a LOC. Lower concentrations were not tested, but it can be deduced that, pHRR will continue to decrease rapidly until a "no flaming" condition is reached. This point marks the condition where a LFL is not reached. The mass loss during a "no flaming" condition is only a function of the applied heat flux from the lamps as was described by Marquis et al [3.34], and describes the pyrolysis rate, in the absence of smoldering.

The graph in Fig. 3.17 shows typical HRR curves for tests where the oxygen flow rate was changed (either by changing $\dot{V}$ or $y_{O_2}$). Dotted vertical lines indicate the time of flame out for the corresponding condition (color coded). Grey curves (solid, dashed and dashed/dotted) correspond to test without tube, open baskets, constant $y_{O_2}$ and

varying $\dot{V}$. All other tests are done with the tube, open baskets, constant $\dot{V}$ and varying $y_{O_2}$.

This graph shows well how the combustion dynamics change when $y_{O_2}$ is reduced. Not only does the magnitude of the pHRR decrease when $y_{O_2}$ is reduced, it also shows that, the time to reach the peak increases. This behavior is different when comparing it to the dynamics of the combustion of tests in which $\dot{V}$ was altered (grey curves). For these tests, the peak occurs more or less at the same time. The difference in the behavior explains a flame spread mechanism.

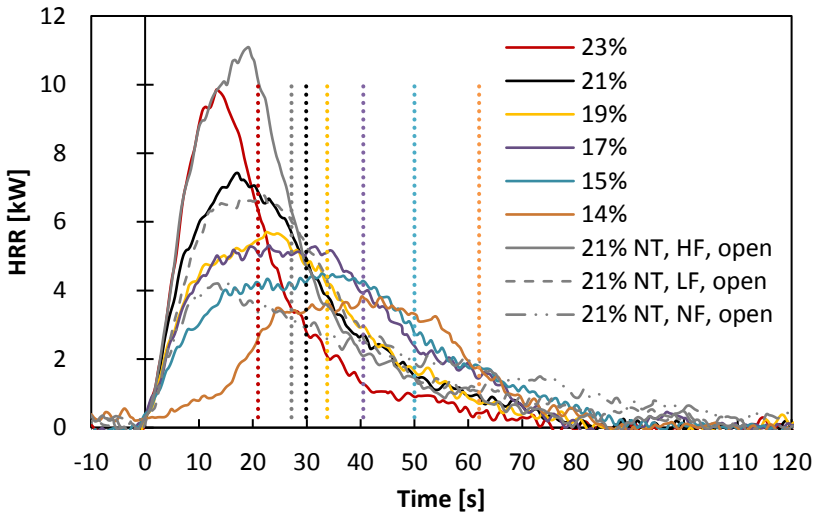


**Fig. 3.17. Typical HRR (OC) curves for tests with varying forced airflow oxygen concentration. t = 0 s represents flaming ignition for each test. Dotted lines are flame extinction (color coded). Flame extinction for LF and NF tests is not shown.**

For tests with forced flow and in the open, the entire sample is almost instantly involved in the combustion process. At reduced oxygen concentration, the combustion initiates at the pilot flame (or smoldering hot spot when $y_{O_2} \leq 0.15$), and spreads over the sample more slowly, until the entire sample is involved. This behavior may also be associated to changing heat flux feedback from the flames. It is significantly greater for well-ventilated conditions, and reduces for tests with constant $\dot{V}$ and reducing $y_{O_2}$ (due to convection cooling and flame properties).

An interesting observation can be made from tests at 21% $O_2$ with tube at HF (black curve) and without tube at LF (grey dashed curve). These have similar shapes (comparable pHRR in Fig. 3.15), even though the forced convection condition is significantly different. This is because $\chi$ and $\dot{m}_p$ are balanced specifically to result in this behavior. It can be deduced from the duration of flaming period (Fig. 3.8) that tests with the tube have a greater $\dot{m}_p$ compared to tests without tube and lower flow rate. This means the HRR should be higher. However, these also have lower combustion efficiency (Fig. 3.12), which dampens the combustion intensity. Thus they are balanced.

### *3.7. Chapter summary and conclusions*

In this chapter the impact of forced ventilation on the ignition and burning behavior of forest fuel beds is explored. Forced ventilation changes the heat and mass transfer, which govern combustion dynamics. Experimental test series with the FPA were designed to assess variation in ignition and burning dynamics, by controlling critical heat and mass transfer mechanisms; these are, forced airflow magnitude ($\dot{V}$), temperature ($T_\infty$) and oxygen concentration ($y_{O_2}$).

When $\dot{V}$ was varied, $y_{O_2}$ was constant. When $y_{O_2}$ was varied, $\dot{V}$ was constant. Test where $y_{O_2}$ was varied the quartz tube was used to create an adequate control of the atmosphere around the sample. A common test metric was identified for both test series (varying $\dot{V}$ or $y_{O_2}$). This was the forced oxygen flow rate ($\dot{m}_{O_2,f}$).

The ignition behavior was analyzed with the time to ignition (piloted). The burning dynamics was analyzed with the duration of flaming period, CO and $CO_2$ generation rates, combustion efficiency ($CO/CO_2$ ratio), and combustion intensity (HRR). Mass loss data was not obtained due to experimental constraints. It was illustrated that heat and mass transfer are closely linked and are the mechanism by which wildfire spread. Because forced ventilation conditions (e.g. wind) cause significant variations in these

mechanisms it is paramount to understand them. It was discussed that forced ventilation impacts a wildfire in two stages: ignition (1) and burning behavior (2).

**Ignition behavior**

*Stage 1 – Heat transfer*

In Stage (1), a flammable mixture needs to be developed in order to allow ignition. This stage is impacted by heat transfer (radiant heating and convective/re-radiative cooling), which governs the mass transfer (pyrolysis rate) originated from the solid phase. The ventilation condition governs the flow of $O_2$ available to mix with pyrolysis products (mass transfer). Stage (1) is best assessed with the ignition behavior. One critical assumption that is tested in this work is, $t_{ig} \approx t_p$. This is acceptable only if the induction time ($t_i$) and mixing time ($t_m$) are short compared to the pyrolysis time ($t_p$).

When the heating rate is increased with a higher external heat flux, ignition time decreases, because critical ignition temperatures (solid phase) are reached faster. Results indicate a strong dependence on the fuel, which was mainly attributed to the particle size. PS needles are much thinner (larger *SVR*) than PR needles and ignited faster. It was concluded, that under natural convection condition, needle bed samples have an ignition behavior comparable to solid material ($< 60$ kW.m$^{-2}$). This is however, not the case when a forced flow is imposed. The forced flow increased the convective cooling of the particle.

When such a convective cooling is added to the heat transfer, it was found that two ignition regimes exist: (1) convection-radiation driven, and (2) radiation only driven. The threshold is dependent on the fuel and bulk properties, but also on the flow velocity and marks the transition at which radiation heat transfer becomes dominant over convective heat transfer. Critical heat flux levels were determined. When convection cooling increases, higher critical heat fluxes are required for ignition to

occur. Furthermore, critical heat fluxes for smoldering are lower than for pure piloted ignition.

The effects of convective cooling were reduced by conducting tests at increased forced flow temperature. The reduced convection effects at 75 °C caused a reduction in ignition time of approximately 29.5%. The reduction was attributed to the reduced differential between initial and ignition temperature. It is small compared to the increase in ignition time when the flow velocity is increased.

*Stage 1 – Mass transfer*

It was concluded that dilution causes no significant delay in the ignition for forced convection ($0.17 \geq y_{O_2} \geq 0.23$). For the flow rate tested, these findings suggest that the assumption, $t_{ig} \approx t_p$ is still valid for forced convection (in the range tested) with radiative heating. Below this concentration, ignition was not piloted any more, which means that $t_i \rightarrow 0$ s is no longer valid. Tests are also conducted at 23% oxygen, which showed no effect on the ignition behavior.

For experimentation at 30 kW.m$^{-2}$, the percent difference in ignition time (between no flow and forced flow, HF) was 147%. Comparing this to findings from the test series with changing gas temperature, results in the conclusion that the most critical parameter is $h_c$ and thus the flow velocity.

**Burning behavior**

*Stage 2 – Heat transfer*

After ignition, cooling of the solid phase continues to be important. Furthermore, increased flow can cool gases and flames, which impacts the heat flux feedback to the fuel. It was discussed that, after ignition, pyrolysis rates are driven by the heat flux feedback from the flames, convective cooling and the rate of smoldering. The pyrolysis

rate drives the HRR (besides the fuel/bulk properties and combustion efficiency). The HRR was impacted by changing convective heat transfer. This was assessed from experiments conducted with varying flow magnitude and ambient temperature. When the flow magnitude increased the pHRR increased, which can be attributed to a higher pyrolysis rate due to higher heat flux feedback and smoldering intensity. When the gas temperature is raised from 18 to 75 °C the pHRR increased by 24.4%.

*Stage 2 – Mass transfer*

The mass transfer was assessed experimentally where the $\dot{V}$ and $y_{O_2}$ were varied. It was concluded that, the duration of flaming is a function of the pyrolysis rate. Therefore, even without mass loss data, it was possible to infer tendencies in the pyrolysis rates ($\dot{m}_p$). For both test series, duration of flaming decreases with increasing $\dot{m}_{O_2,f}$, but at different rates. It was discussed that the pyrolysis rate is a function of (1) the heat flux feedback from the flame to the sample surface, (2) the smoldering intensity, and (3) the convection cooling (at constant external heat flux). Increasing $\dot{m}_{O_2,f}$ in both test series altered these phenomena. It was concluded that the deviation of the duration of flaming between the two test series (at a given $\dot{m}_{O_2,f}$) is due to a differences in $\dot{m}_p$. Heat flux feedback and convective cooling were identified to be the causes for the difference in $\dot{m}_p$.

Visual observation indicated a change in flaming regime from turbulent diffusion to laminar premixed, for tests with varying $y_{O_2}$. This agrees with observation made in other works. The threshold (at constant $\dot{V}$) was found to be between 17 and 19% $O_2$. No intermediate values of $y_{O_2}$ were tested. At 14% flames are still present, but it can be assumed that a "no flaming" regime is not far below this concentration.

The CO and $CO_2$ generation rates were analyzed to understand the effects of limited oxygen availability on pyrolysis processes and combustion efficiency. Results agree

with literature. It was observed that generation rates are impacted by varying $y_{O_2}$ in both phases: pyrolysis pre-ignition and combustion post-ignition.

The combustion efficiency is evaluated with the mean ratio of $CO/CO_2$ during the flaming phase. It is low when combustion occurs in the open for all flow magnitudes (< 2%). In ventilation limited conditions and varying $y_{O_2}$ it is significantly higher: the lowest value was found at $y_{O_2} = 0.14$, 12.1%, the highest at $y_{O_2} = 0.19$, 26.4%. Tests with the tube at 21 and 23% $O_2$ had increased efficiency, because afterburning above the tube exit was observed.

Finally, the combustion intensity (HRR) was analyzed and results between the two test series were compared. It was explained that the HRR is impacted by the fuel (heat of combustion), combustion efficiency, and pyrolysis rate ($\dot{m}_p$). Here, only one type of fuel was used with constant sample preparation and heat flux. Changes in bulk properties as well as external heat flux may also impact $\dot{m}_p$. Therefore, changes in HRR observed are either due to changes in combustion efficiency (see previous paragraph), or $\dot{m}_p$ (see discussion on duration of flaming).

Results obtained in this work, agree with literature, i.e. HRR increases with increasing $\dot{m}_{O_2,f}$. Peak HRR for tests without tube and varying $\dot{V}$ increased linearly with increasing $\dot{m}_{O_2,f}$. This can be attributed mainly to increasing $\dot{m}_p$, because the combustion efficiency only varies marginally.

Peak HRR for tests with tube and varying $y_{O_2}$ increased non-linearly with increasing $\dot{m}_{O_2,f}$. This can be attributed not only to increasing $\dot{m}_p$, but also varying combustion efficiency. When $y_{O_2}$ is increased, $\dot{m}_p$ increases, but the combustion efficiency decreases (until $y_{O_2} = 0.19$). Results from tests at 21 and 23% $O_2$ are slightly different, because afterburning occurs above the tube exit. At $y = 0.14$, conditions are near the limiting oxygen concentration, below which the lower flammability limit is not reached.

The difference in pHRR between the two test series, at a given $\dot{m}_{O_2,f}$ is due to difference in pyrolysis rate and combustion efficiency. The sole impact of the combustion efficiency on pHRR can be observed when comparing tests at $y_{O_2} = 0.21$, with and without tube (at constant $\dot{V}$). It can be assumed that the convective cooling and smoldering intensity are similar in both cases. It was shown that, the duration of flaming for these tests is similar, which means that the pyrolysis rate is similar. Therefore, the difference in pHRR (31%), is due to the reduction in combustion efficiency. The reduction of the combustion efficiency is mainly due to blocking the oxygen entrainment from the surroundings.

**Concluding remarks**

The extensive experimental investigation of the impact of forced convection on the ignition and burning behavior of porous forest fuel beds provided insightful results. The application of these results has many facets. Fundamentally, it aids in the understanding of the physical processes that govern the ignition and combustion dynamics. There are many factors that impact these processes and it is paramount that these are understood adequately.

Conducting experimentation of this kind allows the development of a database that can be used for model validation exercises. Physical combustion models require such data in order to assess if the physical phenomena are properly represented by the mathematical equations.

In the wildfire research community, flammability of foliage has been assessed in many different ways (mainly via ignitibility). But there is a lack of unified methodology to assess the flammability in a rigorous, complete manner (not only one flammability parameter). Testing of vegetation in the FPA has been conducted over the past decade, and each study aids in the understanding of factors that impact the flammability of

porous wildland fuel beds. Therefore, using the FPA as a standardized test method for assessing foliar flammability is a long term goal.

It was explained in Chapter 1 that, fuel flammability (ignition and burning behavior) is an integral part of understanding wildfire behavior (Fig. 1.1). Therefore, by extension, investigations such as the one presented here can be used to advance the development of the knowledge of wildfire behavior.

Understanding which external factors (for example wind) have the greatest effect on fire behavior and on what pathways they impact the behavior is the basis for wildfire research. Conducting experimentation in bench-scale tests provides the best control. A next step is to assess any scaling laws in order to bridge the gap of the large scale differences that have to be considered in wildfire.

A last application of this work is in understanding the emission products from wildland fuels. In order to analyze emissions data, it is required to understand where the emissions originated. In the FPA, pyrolysis and combustion can be controlled well, and any impact of changing test parameters can be monitored. Therefore, this apparatus is ideal to assess the source of emissions. Work presented here indicates that for burning in the open, CO emissions is higher during the smoldering combustion phase after flame out, which is expected because less CO is oxidized to $CO_2$ in this type of combustion. More interestingly, the work also shows that, in ventilation limited conditions, flaming combustion produces significantly higher CO emissions compared to smoldering combustion (~ 4 times). This is in line with literature. Therefore, it may be hypothesized that, in a real wildfire, high CO emission factors may not necessarily be attributed to residual smoldering only, but also to high levels of incomplete combustion. This might be counter intuitive, because wildfires burn in the open, but results and discussions shown here (and in Chapter 1) present significant evidence to support a case for high CO emissions due to incomplete combustion in wildfire. Future

experimentation should investigate in this matter to fully understand the origins of emissions from wildfire.

### *3.8. References*

[3.1] C. Schemel, Transport Effects on Calorimetry of Porous Wildland Fuels, University of Edinburgh, Edinburgh, UK, 2008, Ph.D. thesis.

[3.2] P. Bartoli. Feux de forêt: amélioration de la connaissance du couplage combustible-flamme. Universite de Corse-Pascal Paoli, Corsica, France, 2011. Ph.D. thesis.

[3.3] F.X. Jervis, Application of Fire Calorimetry to Understand Factors Affecting flammability of Cellulosic Material: Pine Needles, Tree Leaves and Chipboard. University of Edinburgh, Edinburgh, UK, 2012. Ph.D. thesis.

[3.4] C. Schemel, A. Simeoni, H. Biteau, J. Riviera, J.L. Torero. A Calorimetric Study of Wildland Fuels. Experimental Thermal and Fluid Science 32 (7) (2008) 1381-1389.

[3.5] P. Bartoli, A. Simeoni, H. Biteau, J.L. Torero, P.A. Santoni. Determination of main parameters influencing forest fuel combustion dynamics. Fire Safety Journal 46 (1-2) (2011) 27-33.

[3.6] F.X. Jervis, G. Rein. Experimental study on the burning behavior of Pinus halepensis needles using small-scale fire calorimetry of live, aged and dead samples. Fire and Materials (2015)

[3.7] J.C. Thomas, J.N. Everett, A. Simeoni, N. Skowronski, J.L. Torero. Flammability Study of Pine Needle Beds. Proceedings of the 7th International Seminar on Fire and Explosion Hazards, Providence, RI, USA, (2013).

[3.8] A. Simeoni, P. Bartoli, J.L. Torero, P.A. Santoni. On the Role of Bulk Properties and Fuel Species on the Burning Dynamics of Pine Forest Litters. Proceedings of the 10$^{th}$ International Symposium on Fire Safety Science. University of Maryland, Maryland, USA (2011) 1401-1414.

[3.9] A. Simeoni, J.C. Thomas, P. Bartoli, P. Borowjeck, P. Reszka, F. Colella, P.A. Santoni, J.L. Torero, Flammability studies for wildland fuels using the Fire Propagation Apparatus. Fire Safety Journal 54 (2012) 203-2017.

[3.10] ASTM E 1354-16a. Standard Test Method for Heat and Visible Smoke Release Rates for Materials and Products Using an Oxygen Consumption Calorimeter. ASTM International, West Conshohocken, PA, 2016.

[3.11] ASTM E 2058-13a. Standard Test Methods for Measurement of Material Flammability Using a Fire Propagation Apparatus (FPA), ASTM International, West Conshohocken, PA, 2013.

[3.12] D. Drysdale. An Introduction to Fire Dynamics (3rd edn). John Wiley and Sons: Chichester, UK, 2011.

[3.13] B. Karlsson, J.G. Quintiere. Enclosure Fire Dynamics. CRC Press LLC. London, UK (2000).

[3.14] J.L. Torero, A. Simeoni. Heat and Mass Transfer in Fires: Scaling Laws, Ignition of Solid Fuels and Application to Forest Fires. The Open Thermodynamics Journal 4 (2010) 145-155.

[3.15] P.A. Santoni, F. Morandini, T. Barboni. Determination of Fireline Intensity by Oxygen Consumption Calorimetry. Journal for Thermal Analysis and Calorimetry 104 (2011) 1005-1015.

[3.16] S. Brohez, G. Marlair, C. Delvosalle. Fire Calorimetry Relying on the Use of the Fire Propagation Apparatus. Part 1: Early Earning from Use in Europe. Fire and Materials 30 (2006) 131-149.

[3.17] J.G. Quintiere. Fundamental of Fire Phenomena. John Willey and Sons, Hoboken, NJ, USA, 2006.

[3.18] J.Torero. SFPE Handbook of Fire Prevention Engineering – Flaming Ignition of Solid Fuels. 5$^{th}$ ed. Society of Fire Protection Engineers, London, UK, (2016).

[3.19] R.T. Long Jr, J.L. Torero, J.G. Quintiere, Scale and Transport Considerations on Piloted Ignition of PMMA, Proc. 6th Int. Symposium of Fire Safety Science (1999) 567-578.

[3.20] J.G. Quintiere. The Application of Flame Spread Theory to Predict Material Performance, Journal of Research of the National Bureau of Standards, 93:1 (1988) 61-70.

[3.21] M. Janssens. A thermal Model for Piloted Ignition of Wood Including Variable Thermalophysical Properties, Proc. 3rd Int. Symposium of Fire Safety Science (1991) 167-176.

[3.22] P.A. Beaulieu, N. Dempsey. Flammability Characteristics at Applied Heat Flux Levels up to 200 kW.m$^{-2}$. Fire and Materials 32 (2008) 61-86.

[3.23] A. Tewarson, S.D. Ogden. Fire Behavior of Polymethylmethacrylate. Combustion and Flames 89 (1992) 237-259

[3.24] F.P. Incropera, D.P DeWitt, T.L. Bergman, A.S. Lavine, Principles of Heat and Mass Transfer, John Wiley and Sons Ltd., Singapore, Singapore, 2013.

[3.25] R.C. Rothermel. A Mathematical Model for Predicting Fire Spread in Wildland Fuels. INT-115. USDA, Forest Service, Ogden, UT, USA (1972).

[3.26] M.A. Finney, J.D. Cohen, J.M. Forthofer, S.S. McAllister, M.J. Gollner, D.J. Gorham, K. Saito, N.K. Akafuah, B.A. Adam, J.D. English. Role of Buoyant Flame Dynamics on Wildfire Spread. Proceedings of the National Academy of Science USA 112/32 (2015) 9833-9838.

[3.27] G. Rein. Breakthrough in the Understanding of Flaming Wildfire. Proceedings of the National Academy of Science USA 112/32 (2015) 9795-9796.

[3.28] A. Tewarson, J.L. Lee, R.F. Pion. The Influence of Oxygen Concentration on Fuel Parameters for Fire Modeling. Proceedings of the 8th International Symposium on Combustion (1981) 563-570.

[3.29] A. Tewarson, J. Steciak. Fire Ventilation. Combustion and Flames 53 (1983) 123-134.

[3.30] G. Marlair, J.P. Bertrand, S. Brohez. Use of ASTM E 2058 Fire Propagation Apparatus for the Evaluation of Underventilated Fires. Fire and Material Conference (2001) 301-313.

[3.31] R.F. Simmons, H.G. Wolfhard. Some Limiting Oxygen Concentrations for Diffusion Flames in Air Diluted with Nitrogen. Royal Aircraft Establishment (1956).

[3.32] G. Mulholland, M. Janssens, S. Yusa, W. Twilley, V. Babrauskas. The effect of Oxygen Concentration on CO and Smoke Produced by Flames. Proceedings of the 3rd International Symposium of Fire Safety Science (1991) 585-594.

[3.33] H. Biteau, A. Fuentes, G. Marlair, J.L. Torero. The Influence of Oxygen Concentration on the Combustion of a Fuel/Oxidizer Mixture. Experimental Thermal and Fluid Science. 34 (2010) 282-289.

[3.34] D.M. Marquis, E. Guillaume, A. Camillo. Effects of Oxygen Availability on the Combustion Behavior of Materials in a Controlled Atmosphere Cone Calorimeter. Proceedings of the 11th International Symposium of Fire Safety Science (2014) 138-151.

[3.35] P. Beaulieu. Flammability Characteristics at Heat Flux Levels up to 200 $kW.m^{-2}$ and the Effect of Oxygen Concentration on Flame Heat Flux. Worcester Polytechnic Institute, Worcester, MA, USA. 2005. Ph.D. thesis.

[3.36] G. Santo, F. Tamanini. Influence of Oxygen Depletion on the Radiative Properties of PMMA Flames. Proceedings of the 8th International Symposium on Combustion (1981) 619-631.

[3.37] D. Gross, A.F. Robertson. Experimental Fires in Enclosures. Proceedings of the 10th International Symposium on Combustion (1965) 931-942.

[3.38] A. Tewarson. Some Observation in Experimental Fires in Enclosure. Part 1: Cellulosic Material. Combustion and Flames 19 (1972) 101-111.

[3.39] A. Tewarson. Some Observation in Experimental Fires in Enclosure. Part 2: Ethyl Alcohol and Paraffin Oil. Combustion and Flames 19 (1972) 363-371.

[3.40] C.L. Beyler. Major Species Production by Solid Fuels in a Two Layer Compartment Fire Environment. Proceedings of the 1st International Symposium of Fire Safety Science (1986) 431-440.

[3.41] B.Y. Lattimer, U. Vandsburger, R.J. Roby. Carbon Monoxide Levels in Structural Fires: Effects of Wood in the Upper Layer of a Post-Flashover Compartment Fire. Fire Technology 34/4 (1998) 325-355.

[3.42] W.M. Pitts. The Global Equivalence Ratio Concept and the Formation Mechanisms of Carbon Monoxide in Enclosure Fires. Progress in Energy and Combustion Science 21 (1995) 197-237.

[3.43] A.A. Stec, T.R. Hull. Assessment of the Fire Toxicity of Building Insulation Material. Energy and Buildings 43 (2011) 498-506.

[3.44] S.P. Ubanski, W.M. Hao, S. Baker. Chemical Composition of Wildland Fire Emissions. Developments in Environmental Science 8 (2009) 79-107.

[3.45] S.P. Urbanski. Combustion Efficiency and Emssion Factors for Wildfire-Season Fires in Mixed Conifer Forests of the Northern Rocky Mountains, US. Atmospheric Chemistry and Physic 13 (2013) 7241-7262.

[3.46] S. Urbanski. Wildland Fire Emissions, Carbon, and Climate: Emission Factors. Forest Ecology and Management 317 (2014) 51-60.

[3.47] R.J. Yokelson, R. Susott, D.E. Ward, J. Reardon, D.W.T. Griffith. Emissions from Smoldering Combustion of Biomass Measured by Open-Path Fourier Transform Infrared Spectroscopy. Journal of Geophysical Research 102/D15 (1997) 18865-18877.

[3.48] R. Hadden. Smouldering and Self-sustaining Reactions in Solids: An Experimental Approach. University of Edinburgh, Edinburgh, UK. 2011. Ph.D. thesis.

*This page is intensionally left blank.*

# Chapter 4

## *Modeling the Impact of Forced Convection on the Ignition Behavior of Porous Forest Fuel Beds*

## *4.1. Introduction*

In the previous chapter, the influence of airflow on the ignition and burning behavior of pine needles was explored in terms of heat and mass transfer. It was concluded that the effects of airflow are, in part, due to the changing net heat flux that is experienced by the solid particle in a porous medium. This was evaluated by looking at the ignition behavior at various flow velocities over a wide range of incident heat flux levels. Furthermore, it was concluded that dilution has no significant effects at the given flow rates. The ambient temperature also had little effects on the convection heat transfer. Therefore, the convection heat transfer coefficient is the most critical parameter in the convective heat transfer.

### *4.1.1. One-dimensional porous model*

The purpose of the analysis presented herein, is the validation of a porous ignition model that was developed by Simeoni et al [4.1, 4.2]. It is described in detail in Chapter 1. This model is based on the energy conservation equation for a porous medium. It is simplified to a one-dimensional, two phase formulation, with thermal equilibrium between solid and gas phase. The fuel package is considered as a semi-infinite solid with the energy balance performed at the surface.

The partial differential equation (PDE) has been numerically integrated on a uniform grid by using a finite volume approach [4.3]. Diffusive fluxes and convective fluxes have been approximated at the volume interfaces by using central difference and up-wind schemes, respectively. Time advancing has been implemented by using a fully implicit scheme because of its unconditional stability for any time step size. The non-linearity introduced by the Rosseland approximation of the diffusive transfer has been treated implicitly; in particular, for each time step, inner iterations are performed until the convergence of the computed temperature field is observed.

The porous model described above (and in Chapter 1) was applied with the total heat transfer coefficient for natural convection found from the thermal analysis in Section 4.3. Other input parameters are given in Table 4.1. No parameter was fitted. The program used to solve the porous model (PDE) was developed by Dr. Francesco Colella.

Table 4.1. Porous model input parameters.

| Species | PS | PR | Origin |
|---|---|---|---|
| $T_{ambient}$ [K] | 291 | 291 | Measured (ambient condition) |
| $T_{ig}$ [K] | 553 | 613 | Experimental (Section 4.2.1) |
| $a$ [-] | 0.64 | 0.64 | Estimated (from[4.11]) |
| $\delta_{rad}$ [mm] | 5.20 | 7.40 | Experimental (Section 4.2.2) |
| $c_p$ [kJ.g$^{-1}$.K$^{-1}$] | 2,090 | 1,702 | Experimental (TGA/DSC analysis [4.4]) |
| $\rho$ [kg.m$^{-3}$] | 621 | 777 | Experimental (Chapter 2) |
| $\alpha_g$ [%] | 93.6 | 95.0 | Calculated (based on ρ and ρ*) |
| $h_T$ [W.m$^{-2}$.K$^{-1}$] | 21 | 24 | Calculated (Section 4.3) |
| Velocities, $v$ [cm.s$^{-1}$] | | | |
| No flow (NF) | 0.0 | 0.0 | |
| Low flow (LF) | 6.67 | 6.67 | Estimated (based on known volumetric flow rate) |
| High flow (HF) | 13.3 | 13.3 | Estimated (based on known volumetric flow rate) |

The time-step and cell size selections were evaluated with respect to the ignition time to evaluate the error associated to the section. Secondly, the size of the computation domain also needs to be evaluated to assess influences of the back face boundary condition. The discretization and associated error as well as the domain size consideration are summarized in Appendix B1.

A time-step of 0.05 s was found to be sufficiently small for the range of heat flux levels considered to produce errors less than 1%. The cell size has to be on the order of 0.025 mm, to produce computation error within the acceptable range (1%). A computation domain of at least 5.0 cm was required in order to reduce error due to domain boundary conditions (fixed temperature).

### *4.1.2. Goals and objectives*

The goal is to assess, to what extent a simplified two phase physical model (energy conservation) [4.2] can be used to predict the ignition behavior of a porous forest fuel bed. Experimental results developed in Chapter 3 are used to validate the performance of this model. The model is validated with experimental results for in-depth temperature distribution, critical heat flux, and ignition times for two species. Current limitations of the model are described. Thermal analyses are performed on the scale of the sample and needle to (1) estimate a convective heat transfer coefficient and (2) assess the thermal behavior of the sample and particle. This analysis is based on non-dimensional numbers for fuel beds and particles heated radiatively and cooled convectively. A comparison is provided to assess, when heat losses (convective and radiative) may be ignored in the assessment of the thermal behavior or the particles.

### *4.1.3. Chapter layout*

Before going into details about this porous model and concluding validation (Section 4.4) several supporting experiments are discussed (Section 4.2), such as critical heat flux, ignition temperature and in-depth temperature distributions. The thermal analyses are performed on the scale of the sample and needle in Section 4.3.

## ***4.2. Supporting experimentation***

Experimentation presented here is based on FPA ignition tests with PS and PR needles. Heat flux levels ranged up to 60 $kW.m^{-2}$. Natural and forced convection was tested. Critical heat flux and ignition data developed in Chapter 3 is used in this analysis. Because the ignition criterion for the model is the ignition temperature, measurements were obtained for varying heat flux, and flow condition. Finally, the in-depth temperature measurements used for the validation of the model performance are discussed below.

### *4.2.1. Ignition temperature*

The ignition temperature is an important criterion for modeling purposes. It is used as the onset of flaming combustion and hence dictates if a material will ignite or not. The ignition temperature was measured with a K-type thermocouple (250 µm wire gauge) located at the sample surface (Fig. 4.1).

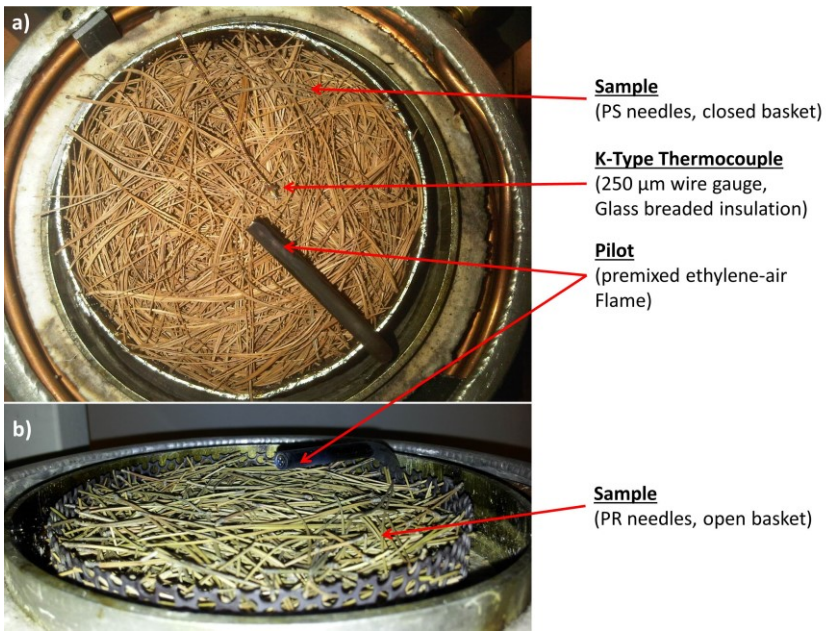


**Fig. 4.1. Illustration of surface thermocouple location. Also shows location of pilot flame. a) PS needle sample with closed sample basket; b) PR needle sample with open sample basket (no thermocouple).**

As can be seen in Fig. 4.1.b, the needles do not form a smooth even surface. Furthermore, it was extremely challenging (physically) to attach a thermocouple to the actual surface of a needle. Therefore, the temperature measurements are estimations of the actual needle temperature. The sampling frequency for the temperature measurement was 1 Hz. This frequency is adequate for solid phase temperature measurements, but not necessarily for gas phase temperature. Air has a very lower thermal inertia ($kpc$) compared to the solid needles, which means that it (referring to an infinitesimal volume of either gas or solid) does not store energy well, causing high and frequent temperature fluctuations. The thermal inertia dampens the change in temperature, storing and transferring energy depending on thermo-physical properties,

which means that a material (solid, liquid or gaseous) with a low value of thermal inertia heats up quickly but also cools down fast. A material with high thermal inertia heats up slowly and retains the heat (temperature) longer. Therefore, to capture actual gas phase temperatures, one must sample at very high frequencies in order to observe temperature fluctuations. Additionally, the size of the thermocouple wire and measuring junction (also commonly called bead) become critical. The physical size of the thermocouple elements also dampen the measurements due to the response time, which increases with wire size (and bead diameter). The response time for the thermocouples used in this work is approximately one second (provided by manufacture, Omega Engineering Inc., and obtained under standard test conditions). For this particular thermocouple it would not improve the measurements significantly if the sampling frequency is increased (above 1 Hz) because the response time is on the same order of magnitude.

Gases (air in this case) are transparent (low emissivity); hence do not absorb radiation effectively compared to solids. The air above the sample surface (in which the thermocouple is submerged) is heated by convection from the hotter surface of the needles, which heat up via radiation provided by the external heat flux. The thermocouple measures the temperature of the gas, but depending on the size, will also experiences heat transfer (losses and gains) by radiation and conduction along the wires. This causes uncertainty in the actual gas phase measurements. Furthermore, the conduction heat transfer (losses or gains due to temperature differential) along the length of the thermocouple can also increase the uncertainty of the measurements. For the purpose of this work it is assumed that these uncertainties are small compared to the measurement error (standard deviation shown in Fig. 4.2).

Ignition temperature measurements in Fig. 4.2 are averaged values for three repetitions at four heat flux levels. Table 4.2 shows averaged values over the range of heat flux levels and standard deviation of the measurements showed a spread between 7 and 17%.

Table 4.2. Average ignition temperature measurements [℃] (st.dev. [%]) for three flow conditions. Measurements are averaged for three repetitions at four heat flux levels each.

| Species | Flow condition | | | Averaged |
|---|---|---|---|---|
| | NF | LF | HF | |
| PR | 353.3 (9.7) | 341.2 (12.6) | 329.0 (11.5) | 341.2 (11.2) |
| PS | 251.0 (7.6) | 276.5 (17.0) | 301.4 (8.1) | 276.3 (10.9) |

The discussion provided above shows that, the temperature measurements are neither the actual needle surface temperatures, nor the actual gas temperature. Realistically, it is the temperature of the thermocouple bead, which we assume to be an estimation of needle temperature. It is part of this work to explore the validity of this assumption. An ignition temperature of 300 °C is often assumed for pine needles [4.5-4.7]. Results presented herein globally agree with this estimation with some noticeable variations.

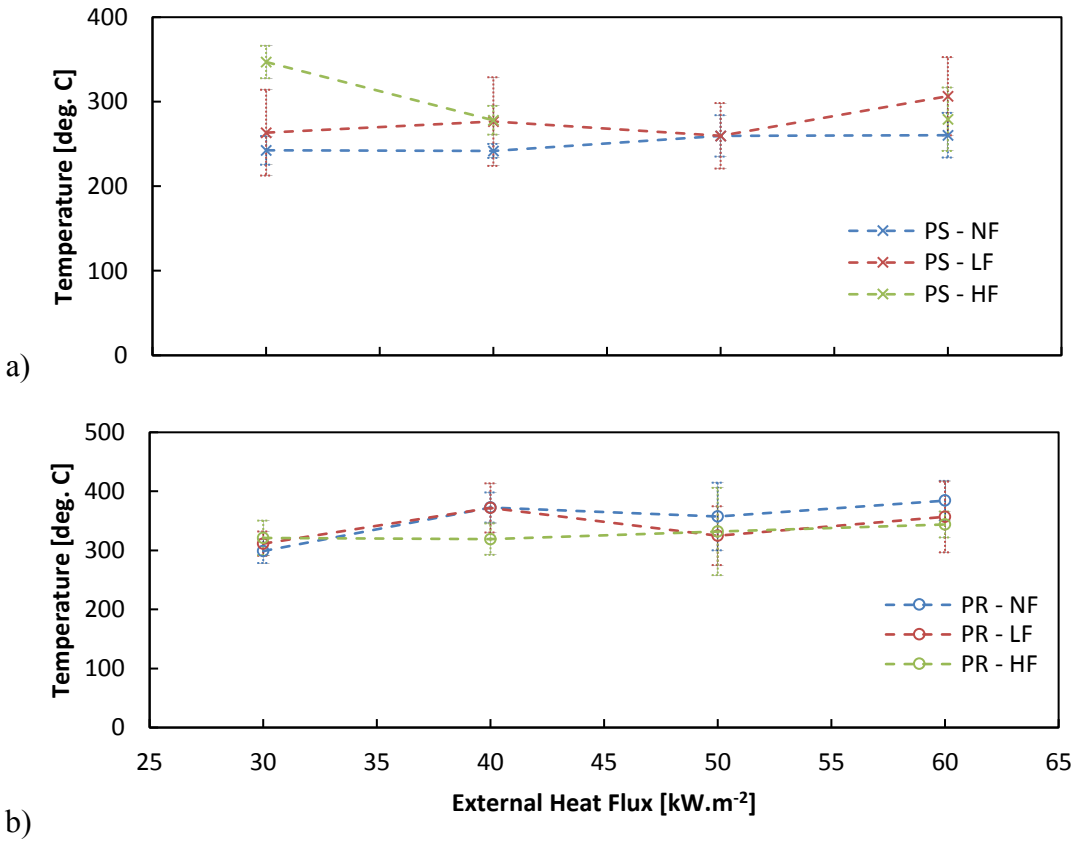


**Fig. 4.2. Ignition temperature of a) PS and b) PR sample beds at various external heat flux and flow conditions. Error bars indicate one standard deviation.**

*Species*

The results for PS and PR are plotted in Fig. 4.2.a. and b, respectively. On average, a large difference in ignition temperature between these two species can be observed (Table 4.2). PR needles, the thicker once (smaller *SVR*) have a much higher ignition temperature; generally above 300 °C. PS needles have an ignition temperature below 300 °C, for most conditions. At low heat flux and strong forced convection (HF) the ignition temperature is above 300 °C

. The overall difference in ignition temperature between the two species can be attributed to chemical differences, i.e. decomposition of volatiles occurs at different temperatures for each species.

*Airflow*

Airflow has varying degrees of influence on ignition temperature, depending on the heat flux. For PS samples (Fig. 4.2.a.) at lower heat flux (30 $kW.m^{-2}$) an increase in convection increases the ignition temperature. This is however, not observed at higher heat flux levels. At elevated radiation (> 40 $kW.m^{-2}$) the average temperatures for each flow condition tested fall within the error bars of the others. This is also true for PR samples (Fig. 4.2.b.). No clear dependence on airflow rate can be determined. By changing the magnitude of the airflow, transport and mixing mechanisms can be influenced causing a change in development of a flammable mixture. This can result in overestimation of the ignition temperature due to dilution of the flammable mixture (i.e. the time it takes to form a flammable mixture is increased at higher airflow rates). For the flow rates tested, it does not seem to be a major factor due to the lack of clear deviation of the measured values between flow conditions. An exception where the dilution caused an overestimation of the ignition temperature is the strong forced flow (HF) condition for PS needles at 30 $kW.m^{-2}$. It can be explained, that the pyrolysis rate at this heating condition is low compared to the airflow rate, resulting in a significant dilution of the flammable mixture. Such tendency is not observed under any other

condition which concludes that the dilution (at the given conditions) is not influencing the temperature measurements. This is important to know for modeling purpose, where the ignition temperature is used as the ignition criterion for simulations of these samples at varying airflow conditions.

*Heat flux*

For PS needle samples (Fig. 4.2.a.) at no airflow (NF) and low airflow (LF) a slight increase of the ignition temperature with increasing heat flux is observed. This tendency is however, masked by the larger standard deviation of the measurements. Furthermore, it was also not observed for high airflow (HF) condition, masked due to reasons said in the previous paragraph. For PR samples (Fig. 4.2.b.), ignition temperatures also slightly increase with the heat flux. However, the high standard deviation for this species again does not allow a definite conclusion but gives insightful information, that a weak dependence could exist. Throughout the rest of this study an average ignition temperature for each species ($T_{PS,average}$=280 °C and $T_{PR,average}$=340 °C ) is used independent of airflow rate or external heat flux. The above discussion and the results given in Fig. 4.2 substantiate this selection.

### *4.2.2. In-depth temperature distribution*

In-depth temperature measurements, obtained as illustrated in Fig. 4.3, are useful in two ways: (1) to evaluate the sample thermal behavior (thermally thick or thin and semi-infinite); and (2) to validate the porous model. The fuel bed was fitted with thermocouples to measure the vertical temperature distribution along the centerline of the sample. The measurements were obtained by constructing a probe including two thermocouples (mid-depth and back face) that was inserted into the sample from the bottom. Additionally, one thermocouple was placed at the surface as described in the previous section. Thermocouples, uncertainties and assumptions outlined in Section 4.2.1 also apply here.

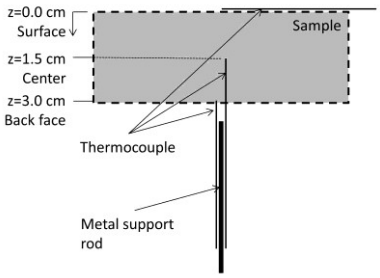


**Fig. 4.3. Schematic of in-depth temperature measurements.**

Fig. 4.4 illustrates a typical graph of the temperature evolution of PR samples for strong convection (HF) conditions with open baskets at 55 kW/m2. The rapid increase in the surface thermocouple measurement (solid line) is indicative of ignition. It was of interest to determine if the back face temperature would rise significantly above room temperature at the time of ignition; therefore to investigate whether ignition could be influenced by the heat loss at the back face of the sample. If not, the sample could be modeled as a semi-infinite medium [4.8].

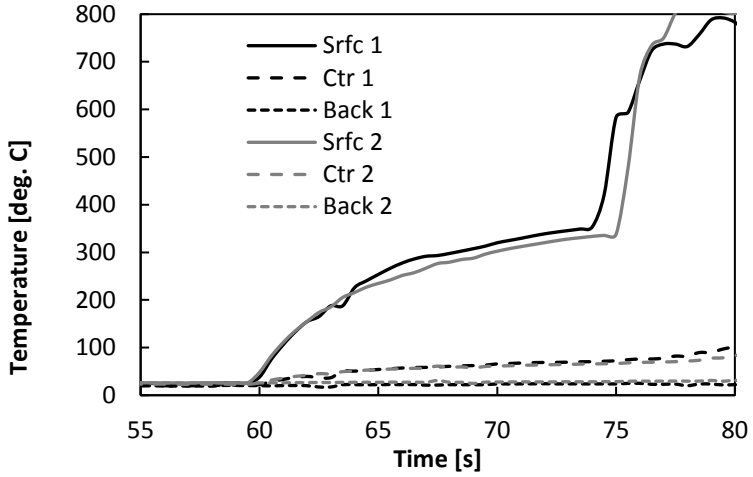


**Fig. 4.4. Temperature evolution of PR samples for HF with open baskets at 55 kWm$^{-2}$; solid lines are surface temperature, dotted lines are at mid-depth, and dashed lines are at the bottom of the sample; black and grey indicate two repetitions. First heat exposure begins at t=59-60s.**

Instead of using the thermal penetration depth ($\delta << 4(\alpha t)^{0.5}$) [4.8] as used for solid opaque material, the mean free path of radiation, $\delta_{rad}$ is used in porous fuel beds [4.9]. The reason for this is due to the lack of conduction heat transfer within the sample

matrix (high porosity). Heat transfer within the porous medium is due to convection and radiation.

The mean free path of radiation marks the depth at which the radiation intensity has decreased by 63%, as was discussed in Chapter 1. Theoretical and experimental values for two species are compared to in Table 4.3.

Table 4.3. Theoretical and experimental mean free path of radiation.

| | PS | PR |
|---|---|---|
| $\delta_{rad,th}$ [mm] | 4.41 | 11.4 |
| $\delta_{rad,ex}$ [mm] | 5.20 | 7.40 |

Interestingly, radiation attenuation for the very fine PS needles is actually overestimated by the theoretical calculation. Theoretical and experimental values are relatively close compared to values for PR. The theory underestimates the mean free path of radiation by 15% and overestimates it by 54% for PS and PR, respectively.

The underestimation of $\delta_{rad,th}$ for PS needles can be attributed to two factors: (1) experimental uncertainty due to sample heterogeneity and needle arrangement in the fuel bed and (2) uncertainty in the calculation of $\alpha_s$ and *SVR*. Uncertainty of the *SVR* calculation is 11.4% (Chapter 2). Therefore, the 15% difference between theoretical and experimental mean free path of radiation may be considered small, in comparison to the larger difference for PR needles. The larger overestimation for PR needles can be attributed to non-isotropic particles.

It can be concluded that, the isotropic assumption is more appropriate for the very fine needles (PS). Observations of the samples agree with this hypothesis. Indeed, samples with PS needles seem to have a more homogenous arrangement than PR samples. For both needle species, the parameter indicates semi-infinite samples, because $\delta_{rad} << 3.0$ cm (sample thickness).

In the following figures this is verified with in-depth temperature profiles. All temperature values provided are at the time of ignition for the corresponding test. The

thermal distribution for PR experiments with open baskets and HF condition are plotted in Fig. 4.5. Average temperatures decrease by 250-290 °C from the surface to the mid-depth and only 27-43 °C from the center to the back face. The back face temperature was roughly at room temperature (20-30 °C). The mid-depth thermocouple does not lie within the radiation penetration depth which is verified by a temperature measurement of around 50 °C.

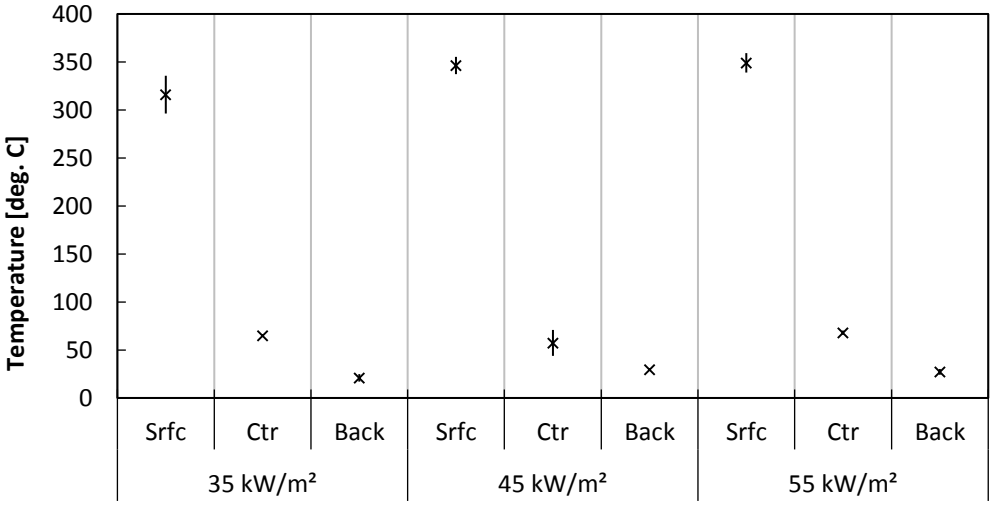


**Fig. 4.5. Temperature distribution at ignition for PR samples with open baskets and HF condition. Error bars indicate one standard deviation. (Srfc: Surface, Ctr: Center, and Back: Back face)**

The worst-case scenario from these experiments in which the semi-infinite assumption is most questionable is the closed basket case. Convection is minimized by blocking it from entering the fuel matrix. Additionally under natural convection it is considered small compared to forced convection conditions. This assumption is evaluated in the non-dimensional analysis in order to determine its validity. In this scenario, the heat losses are minimized which would result in faster heating of the sample. The temperature distribution for PS experiments with closed basket and no flow are displayed in Fig. 4.6.

Average temperatures decrease by 202-221 °C from the surface to the center and only 16-50 °C from the center to the back face. The back face temperature was

approximately at room temperature (17-35 °C), confirming the validity of the semi-infinite solid assumption. Data shows elevated temperatures at mid-depth for low heat fluxes, approximately 100 °C at 20 kW.m$^{-2}$, which are due to long heating times before ignition.

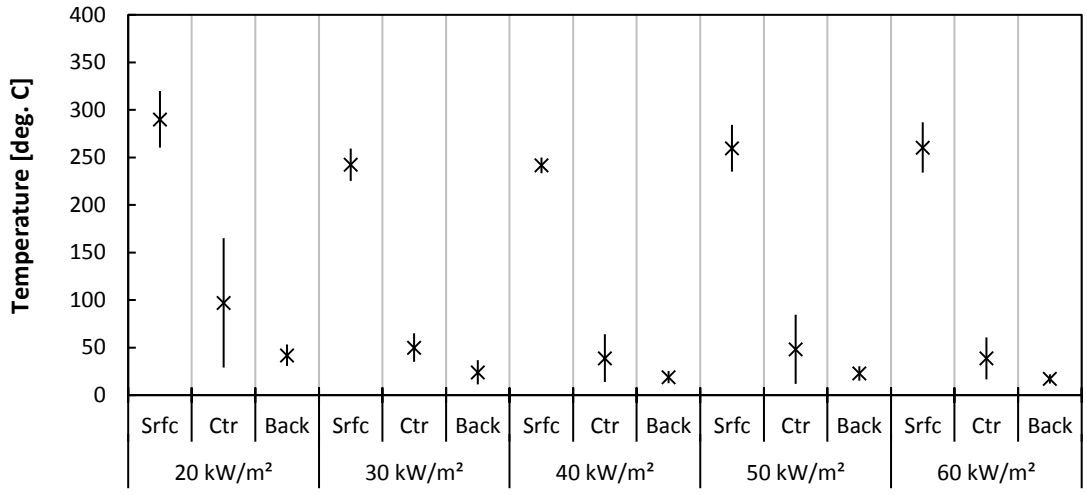


**Fig. 4.6. Temperature distribution at ignition for PS samples with closed baskets and NF condition. Error bars indicate one standard deviation. (Srfc: Surface, Ctr: Center, and Back: Back face)**

The long times can affect the depth of the combustion zone and allow the propagation of the heat wave. The propagation of the heat wave in the porous medium is less due to conduction, but more so due to needles heating up and re-radiating more energy as their surface temperature increases. Radiant energy that is released from needles in top layers is received by needles below and thus causing the heat wave to propagate. The heat transfer in a porous medium is a complex process involving radiation attenuation, re-radiation (from particle to particle and to the ambient), and convection. Conduction is negligible due to the high porosity (> 90%). Convective losses are either due to buoyancy or forced airflow. Therefore, it should be noted that, despite the fact that the samples can be considered as being a semi-infinite solid, the processes of heat transfer are different in many ways compared to solid materials, for which conduction is the main mode of heat transfer. In-depth radiation can exist for transparent materials with convection losses existing only at the surface of the material [4.10].

### *4.3. Thermal analysis of the sample and needle*

In this analysis various dimensionless numbers are applied to the given problem: pine needle beds in natural or forced convection flow fields with radiant heating. These were first discussed in Chapter 1.

Variables in these equations are: $\rho_{air}$ is the density of the air (1.2 kg.m$^{-3}$), $g$ is the gravity acceleration (9.81 m.s$^{-2}$), $\beta$ is the coefficient of thermal expansion (3.43x10$^{-3}$ K$^{-1}$), $\Delta T_{ig}$ the temperature differential between ambient and ignition temperature (Table 4.5), $L$ the characteristic length (Table 4.4), $\mu_{air}$ the viscosity of air (1.98x10$^{-5}$ kg.m$^{-1}$.s$^{-1}$), $c_{p,air}$ the specific heat of air (1.005 kJ.kg$^{-1}$.K$^{-1}$), and $k_{air}$ the thermal conductivity of air (0.0257 W.m$^{-1}$.K$^{-1}$), $v$ is the free stream velocity (Table 4.5), $\alpha_g$ is the gas volume fraction (Chapter 2), $h_c$ the convective heat transfer coefficient (Table 4.5), $a$ is the absorptivity of the needle at the source temperature (~ 0.64 for the FPA lamps [4.11]), $\dot{Q}"_{ext}$ is the external heat flux, $k_p$ is the thermal conductivity of the needle (0.112 W.m$^{-1}$.K$^{-1}$ [4.12]), and $\sigma_p$ is the *SVR* of the needle (Chapter 2).

Table 4.4. Characteristic lengths for the sample and needle scale.

| Scale | Characteristic Length, L [mm] | |
|---|---|---|
| | PS | PR |
| Sample (natural convection) | 31.5 | 31.5 |
| Sample (forced convection) | 0.5 | 0.95 |
| Needle | 7.056x10$^{-2}$ | 1.424x10$^{-1}$ |

The non-dimensional analysis was done at two scales: (1) evaluating the thermal behavior of the sample and (2) evaluating the thermal behavior of the needle. The purpose is to understand the physical phenomenon that best describes the heat transfer for pine needle beds and eventually to determine appropriate heat transfer coefficients that can be applied to the porous model. Finally, it can be used to establish limitations of such a simplified model by evaluating the thermal behavior on the scale of the needle. Because heat transfer in a porous medium is mainly due to radiation and convection, it is critical to understand the fundamental mechanisms driving it. These

were first described in Chapter 1. Therein, it was described that the convective boundary condition for the given fuel samples (needle beds) changes depending on the scale that is considered: from a single needle, to a bundle of needles (needle bed) in cross flow. Under natural convection the latter scenario can be idealized into a simple horizontally oriented flat plate. For each scenario, the corresponding correlation of the Nusselt number is used to calculate the convective heat transfer coefficient.

The characteristic length, $L$, also depends on the scenario under consideration (sample or needle scale). On the scale of the sample for natural convection, it is the ratio of the sample cross sectional area to perimeter [4.13], which is equal to $D/4$ for a cylindrical sample, where $D$ is the diameter of the sample. On the scale of the sample at forced convection, it is the needle diameter. On the scale of the needle, the characteristic length is the $SVR^{-1}$. A summary of these parameters is given in Table 4.4.

Finally, the total heat transfer coefficient ($h_T$) was calculated as the sum of both, radiative and convective heat transfer coefficients. Radiative and convective (only under natural convection) heat transfer coefficient are in reality transient parameters depending on the solid and gas temperature, respectively. In the present study, the coefficients are evaluated at the ignition temperature (Section 4.2.1) and the transient state leading to the time of ignition was omitted. This is reasonable as a first approximation, because it marks the conservative condition where both modes of heat transfer are maximized. In the case of forced convection, the radiative heat transfer coefficient is still transient. However, the convective coefficient is now depending on the velocity of the airflow and therefore, is constant (assuming the velocity is constant). A transition period exists where both, natural and forced convection must be considered, which is assessed with the convective Froude number.

The discussion that follows is separated into two sections. The first one, Section 4.3.1, will discuss the thermal behavior of the fuel bed under natural and forced convection conditions. Findings obtained from this section are then used in Section 4.3.2 going

into more detail and evaluate the thermal behavior of a single needle within the fuel bed.

### *4.3.1. Thermal behavior on the scale of the sample*

Determining the thermal behavior of the sample is important in order to verify that the modeling conducted in this work is applicable and where the limitations lie.

#### Natural convection

Samples with closed baskets (no airflow) and with open baskets (airflow) show a distinctively different thermo-physical behavior when heated. For the closed basket, convection occurs (due to buoyancy effects) over the surface and only limited (assumed negligible) within the sample matrix. Therefore, the convective heat transfer condition can be idealized by evaluating the Nusselt number over a heated flat plate.

The suitability of this idealization is tested with ignition experiments with closed and open baskets at natural convection and compared to forced convection. Results of these tests are shown in Fig. 4.7. In these tests it was desired to identify if the ignition time changes when closed or open baskets are used when the flow condition is the same. If buoyancy forces increase when the sample basket is open, causing the convection cooling inside and at the surface of the fuel matrix to increase, it will be shown by longer ignition times.

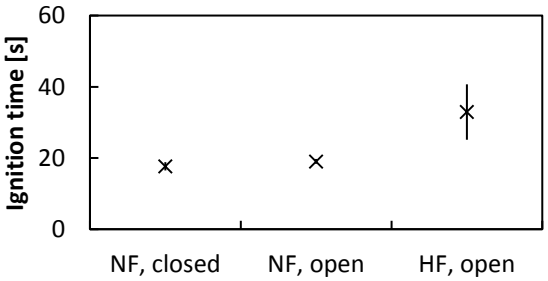


**Fig. 4.7. Time to ignition of PS samples at 30 kW.m$^{-2}$ external heat flux, for different basket and flow condition. Error bars indicate one standard deviation.**

The results given in Fig. 4.7 do not support this hypothesis; therefore, indicating that the convective heat transfers inside and at the surface of the fuel matrix is the same in both, open and closed baskets. Only when airflow is forced through the sample does the ignition time become much longer. Hence, it is concluded that such an idealization is appropriate and that the convection boundary layer is not an artifact forced by the closed sample basket. A similar behavior was found for Mediterranean species by Bartoli et al [4.14] and Thomas et al [4.15].

Table 4.5 summarizes the results of the analysis of the sample thermal behavior at natural convection. For comparison it also contains results of the analysis at forced convection, which will be discussed in the next subsection. Results are shown for two species (PS and PR), which are used in the modeling activity in Section 4.4.

Table 4.5. Evaluation of sample thermal behavior, flow regime and heat transfer coefficients at 4 airflow conditions for PS and PR needles. The (*) indicates corrected coefficient for mixed convection condition. The percent difference of $h_c$ is between the uncorrected and corrected value at the same flow condition.

| | PS | | | | PR | | | |
|---|---|---|---|---|---|---|---|---|
| | Natural Convection | Forced Convection | | | Natural Convection | Forced Convection | | |
| | NF | LF | HF | HHF | NF | LF | HF | HHF |
| $L_{ch}$ [m] | 0.0315 | 0.0005 | | | 0.0315 | 0.00094 | | |
| $v$ [m.s$^{-1}$] | | 0.0667 | 0.133 | 0.267 | | 0.0667 | 0.133 | 0.267 |
| $\Delta T_{ig}$ [K] | 533 | | | | 593 | | | |
| $Gr_L$ | 1.01x10$^6$ | | | | 1.24x10$^6$ | | | |
| Pr | 0.78 | | | | 0.78 | | | |
| $Ra_L$ | 7.83x10$^5$ | | | | 9.64x10$^5$ | | | |
| $Nu_n$ or $Nu_f$ | 16.06 | 1.09 | 1.44 | 1.90 | 16.92 | 1.40 | 1.85 | 2.44 |
| $Re_L$ | | 2.03 | 4.04 | 8.11 | | 3.81 | 7.60 | 15.25 |
| $h_c$ [W.m$^{-2}$.K$^{-1}$] | 13.11 | 56.00 | 73.80 | 97.52 | 13.80 | 38.34 | 50.53 | 66.77 |
| $h_c$* [W.m$^{-2}$.K$^{-1}$] | | 63/58 | 77.55 | 99.23 | | 44.54 | 53.66 | 68.22 |
| $h_r$ [W.m$^{-2}$.K$^{-1}$] | 7.73 | | | | 10.64 | | | |
| $h_T$ [W.m$^{-2}$.K$^{-1}$] | 20.83 | 63.72 | 81.52 | 105.25 | 24.44 | 48.98 | 61.17 | 77.42 |
| $h_T$* [W.m$^{-2}$.K$^{-1}$] | | 71.30 | 85.27 | 106.96 | | 55.18 | 64.30 | 78.86 |
| %Diff. in $h_c$ | | 13.54 | 5.08 | 1.75 | | 16.16 | 6.20 | 2.16 |
| $Fr_L$ | | 0.91 | 3.61 | 14.53 | | 0.48 | 1.92 | 7.73 |

Results for the Grashof number indicate that the correlation for the Nusselt number is applicable [4.13] for the given scenario and both species. The convective heat transfer coefficient, $h_c$, is slightly higher for PR needles, because the differential temperature term between ambient and ignition temperature is slightly higher, resulting in slightly larger buoyancy forces. The same applies for the radiative heat transfer coefficient, $h_r$. Therefore, the total heat transfer coefficient is higher for this species. For both species, convective heat transfer coefficients are higher than radiative ones.

In Section 4.2.2, in-depth temperature measurements and evaluation of the radiation penetration depth, $\delta$, indicated a thermally thick, semi-infinite medium. Theoretical assessment of this behavior can be made by evaluating the Biot number. Considerations for the Biot number were discussed in Chapter 1. It was concluded that, the radiative Biot number defined by Benkoussas et al [4.16] is an adequate representation if convection cooling can be ignored. A development of this definition, including heat losses is proposed. Results in Table 4.5 indicate that total heat losses ($h_T$) are significant and should be included even for natural convection conditions. Furthermore, it was also discussed that, for a porous medium the internal heat transfer is due to radiation and convection. Therefore, the Biot number analysis has to reflect this accordingly. It is proposed that the Rosseland approximation [4.2] can be a suitable representation of the radiative heat transfer in the porous bed. Table 4.6 below shows the averaged values for fuel beds with PS and PR needles. Averaging was done on the temperature range from ambient up to ignition temperature.

Table 4.6. Summary of averaged Rosseland approximation for radiative heat transfer in the needle beds.

| Species | Rosseland Approx. [$W.m^{-1}.K^{-1}$] |
|---|---|
| PS | 0.131 |
| PR | 0.236 |

The averaged Rosseland approximation is higher for PR needle samples. This is because PS needles are the thinner needles and therefore, the radiation extinction coefficient, $K$, is larger, i.e. radiant energy is absorbed closer to the surface. In terms

of the thermal behavior, this means that for fuel beds with the thinner needles (PS), a thermally thick behavior is favorable compared to beds with thicker needles (PR).

It was discussed that the approximation depends strongly on the bulk density of the samples. For the given fuel beds, the solid volume fractions for both species samples are similar (Chapter 2), and correspond to typical values that can be found in reality for needle litter. This is the only condition that is evaluated in this work. Therefore, the difference in the Rosseland approximation (and ultimately the Biot number) for the two species is due to the particle size. Future experimentation should continue exploring the Rosseland approximation with respect to changing sample bulk density.

Results from the Biot number calculations, with heat losses and without heat losses are given in Table 4.7. The Biot number is calculated for three heat flux levels which represent the range of the experimental heat fluxes, which the samples were subjected to.

When the heat losses are ignored, the Biot number is overestimated, because the net energy received by the solid phase is over-estimated. The Biot number increases with external heat flux, which was first discussed by Benkoussas et al [4.16] on the scale of a fine forest fuel particle. This relates to the heating process, which is faster at elevated heat flux levels. Species differences are due to variation in particle size and ignition temperature, which is reflected in a larger value for $k_R$.

Table 4.7. Calculation of the Biot number on the scale of the sample at natural convection, with and without heat losses for three heat flux levels.

| Species | Heat losses | Biot number @ heat flux [kW.m$^{-2}$] | | |
|---|---|---|---|---|
| | | 20 | 40 | 60 |
| PS | without | 11.83 | 23.65 | 35.48 |
| | with | 6.82 | 18.65 | 30.48 |
| PR | without | 5.35 | 10.70 | 16.04 |
| | with | 2.56 | 7.91 | 12.78 |

At low heat flux, the Biot number approaches the threshold to thermally intermediate conditions (< 1). This correlates well to in-depth temperature measurements found in Section 4.2.2. In Fig. 4.6 results for PS needles at 20 kW.m$^{-2}$ indicated elevated temperatures in the center and back face of the sample, which was attributed to the progression of the heat wave.

This means, that the sample thermal behavior diverges from a semi-infinite one. A semi-infinite assumption is accurate when $Fo < 0.2$ [4.13]. The thermal diffusivity here is calculated with the sample bulk density ($\rho^*$), Rosseland approximation ($k_R$) and specific heat ($c_p$) for the two needles. Calculated times corresponding to the threshold, $Fo = 0.2$, are 115 and 52 s for PS and PR needles respectively. At these times, the heat wave propagated through the sample. For a given external heating condition, if the ignition time lies below this threshold one can assume that the heat wave has not reached the back face. Contrarily, if the time to ignition was found longer, a semi-infinite assumption will not be accurate.

At 20 kW.m$^{-2}$, experimental time to ignition was found as 45.8 +/- 5.1 s and 109.6 +/- 8.5 s for PS and PR samples, respectively. Comparison of these values to the threshold indicates that, the heat wave has not fully propagated through the PS needle beds, but it has through the PR beds. This can be partly verified with experimental temperature measurements (Section 4.2.2) for PS needles and agrees well with the assessment of the sample Biot number.

This evaluation of the Biot number does not contain any internal convection heat transfer. For the natural convection conditions, it is assumed small compared to the radiation transfer inside the sample. Results shown in Fig. 4.7 suggest that this assumption is acceptable for natural convection. It is however, challenged when forced convection conditions are present. This scenario will be discussed in the following section, where, instead of considering convection over a hot horizontal surface due to buoyancy, the scenario is better described as a bundle of cylinder in cross-flow.

Nevertheless, in terms of the sample thermal behavior, the natural convection scenario is the most conservative case, because the forced convection case (actively cooling the sample from the bottom) favors a thermally thick behavior (as was seen in Fig. 4.5).

**Forced convection**

The physical phenomenon for open basket tests, where airflow is imposed through the bottom of the sample can be more appropriately represented by cylinders in cross flow. A correlation for a bundle of cylinders is used (Eq. 1.21). Zukauskas et al [4.17] (also in [4.18]) developed a correlation for heat exchanger design that does not depend on pitch dimensions (ratios between cylinder spacing and diameter) of the bundle. Therefore, this is useful here, since these measurements are unknown for the needle beds. The correlation does depend on the number of rows of cylinders in the bundle. This is because the flow condition changes with fewer rows. When the cylinder bundle has many rows, the boundary layer can develop to a steady, fully developed state at which point no additional rows will cause any more change. It is assumed that the number of rows of needles in the sample, although unknown or variable, is large.

The correlation for the Nusselt number is based on the maximum velocity in the pore space of the bundle, which is unknown in this scenario. It is assumed that the velocity in the pore space of the sample is higher than the free stream velocity, therefore the $Re_L$ is underestimated, resulting in lower $Nu_L$ values. Results for $Re_L$ given in Table 4.5 (ranging from 2 to 15) are outside the limits of the correlation. Since lower velocities are used, it is assumed that this deviation is acceptable.

It is important to determine the conditions of the flow field around the sample or particle in order to evaluate if heat and mass transfers are dominated by natural or forced convection. This is done with the convective Froude number [4.13]. A fully forced convection driven condition in which buoyancy can be ignored is present when $Fr_L > 1.0$. On the other hand, a buoyancy only driven condition occurs when $Fr_L < 0.1$. In between these thresholds one must consider a mixed condition.

In the case of forced convection, the Reynolds number replaces the Rayleigh number in the Nusselt number correlation. Results for this Reynolds number given in Table 4.5 show that all forced convection conditions are within the laminar flow regime (transition to turbulent flow at $Re_L \approx 5 \times 10^5$).

The Reynolds number correlation has been subject to modifications, in order to accommodating the condition of a porous media (or packed beds). Dwivedi and Upadhyay [4.19] have produced a comprehensive summary of relevant works. A modified correlation ($Re_{porous}$) introduces the porosity of the fuel bed. When the Reynolds number for porous media is used, only minor differences appear because the porosity is very high. Therefore, these two definitions can be used interchangeable in this scenario. Small variation exists between species, which can be attributed to the needle size and sample porosity.

Convective heat transfer coefficients ($h_c$ in Table 4.5) for forced convection are much larger compared to natural condition explaining the increasing influence of cooling of the sample, which results in delayed ignition. Between the two species, PS has higher values due to the smaller diameter of the needles. This reflects on the heat transfer between the solid and gas phase, which occurs at a larger interface (relative to its volume) for the fuel with larger *SVR*, i.e. with PS needles.

Results for the convective Froude number are given in Table 4.5. At a given flow condition, the values are higher for PS needles, because they have a smaller diameter. For both species, the evaluation of the convective Froude number indicates that a fully forced flow regime is only achieved above the HF conditions (13.3 $cm.s^1$). At the LF condition a mixed condition (buoyancy and forced convection) should be considered. When the velocity is increased to reflect HF and HHF conditions, effects of buoyancy become smaller, at which point forced convection becomes the driving mechanism. This transition was observed visually (Fig. 4.8).

Shortly after the beginning of heat exposure, the needles start to release smoke (water vapor and pyrolysis gases). Under natural convection (Fig. 4.8.a), a cloud of smoke forms above the surface of the fuel bed. This cloud is turbulent due to the buoyancy driven fluid dynamics. When a forced flow is imposed through the bottom of the sample, the smoke pattern becomes more and more streamline as the flow velocity increases.

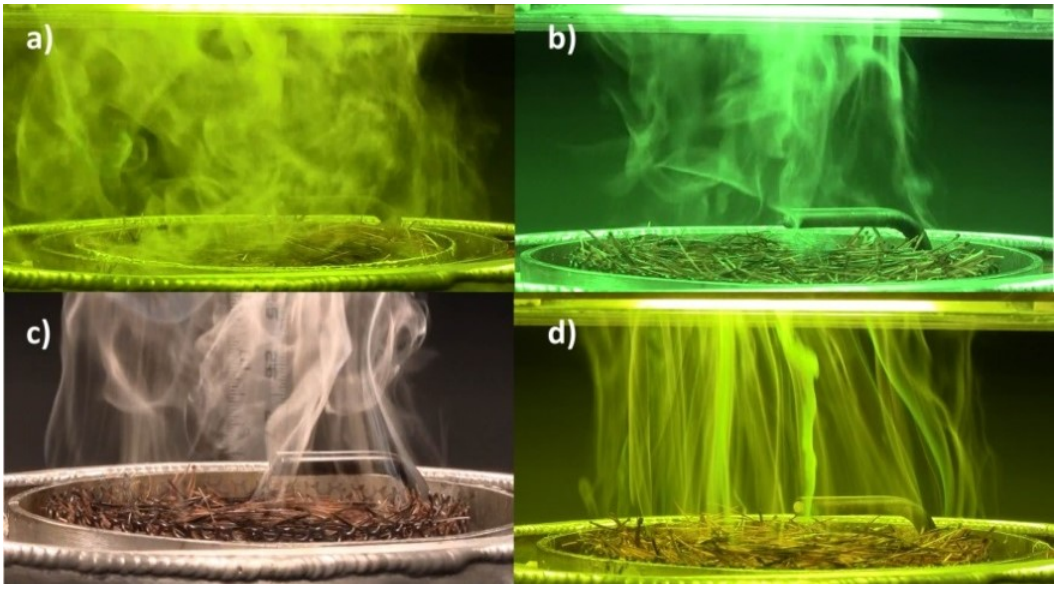


**Fig. 4.8. Smoke patterns just before ignition commences. a) Natural convection; b) forced convection (LF); c) forced convection (HF); and d) forced convection (HHF).**

At LF condition (Fig. 4.8.b), still a lot of turbulence is visible, with only very little stream lining above the sample. At HF condition (Fig. 4.8.c) the stream lining increases indicating the development of the laminar flow regime and the reseeding influence of buoyancy induced turbulence. Finally at HHF condition (Fig. 4.8.d), the flow field is fully laminar even far from the sample surface (pilot flame is 10 mm above surface). In this condition the buoyancy can be ignored for heat and mass transfer considerations but certainly should not be for LF condition.

Sample and test condition in this work represented a fuel bed on the ground and low flow conditions are expected to exist within and just above such fuel beds, compared

to flow conditions in a fuel matrix within a shrub layer or tree canopy. Therefore, convection due to buoyancy should not be ignored for this case.

When extrapolating this phenomenon to larger fires, it is clear, that in a realistic scenario, fires can involve a large amount of fuel at one instance. The released energy will create much stronger buoyancy forces than what is observed in the FPA experiments. In order to overcome the strong buoyancy forces, a much stronger airflow (wind) is required.

In order to accommodate both, natural and forced convection, one must consider a modified Nusselt number that is a composite including both phenomena, as was discussed in Chapter 1.

The Nusselt number found for natural convection conditions (hot plate) does not apply here due to the difference in definition: The flat plate configuration is not compatible with cylinder in cross-flow configuration because two different characteristic lengths are used. Churchill and Chu [4.20] developed a correlation for heated cylinder under natural convection: this correlation is useful for a large range of Rayleigh numbers ($\leq 10^{12}$) [4.20].

Using this correlation, calculated Nusselt numbers are 0.983 and 1.335 for PS and PR, respectively. If natural and forced convection are both considered, the convective heat transfer coefficient increases by 13.54% for LF and 1.75% for HHF, for PS (see percent difference in $h_c$ in Table 4.5). For PR needle samples the percent increase is 16.16% and 2.16% for LF and HHF, respectively.

These results indicate that, at low forced convection the convective heat transfer can be well under-predicted if a mixed condition is not accounted for. In the given experimentation the samples are small and production of hot pyrolysis gases (driving the plume dynamics) is limited. The buoyancy forces created by the hot gases are quickly dominated by a forced convection (with a flow velocity of approximately 27

cm.s$^{-1}$). On a larger scale, a realistic wildfire, the buoyancy forces can be much larger due to the physical size and plume development, and thus, requiring much higher flow velocities to transition from buoyancy driven to wind driven fires. It becomes clear that the increase in convective heat transfer at low flow conditions must be considered when modeling ignition of porous fuel. The relevance here lies in the modeling of fire spread, which can be described as a succession of ignition of adjacent fuel packages. If mixed convection is not considered, it can lead to an over-estimation of the spread rate.

Results of calculated Biot numbers, $Bi_{rad,losses}$, for PS and PR needle samples at various flow and heat flux conditions are given Table 4.8. Results show that $Bi_{rad,losses}$ decreases with increasing flow magnitude, due to the rise of $h_T$. This does not represent the observation of in-depth temperature measurements shown in Fig. 4.5 (PR needle samples at HF). For example, at 40 kW.m$^{-2}$ and HF condition, PR samples have a $Bi_{rad,losses}$ of 2.10, which is near the transition from thick to thin ($Bi$ = 1.0). Yet, temperature measurements for this condition (see Fig. 4.5 and compare to 35 kW.m$^{-2}$), show that the heat wave has not propagated through the sample, still showing a thermally thick behavior.

Table 4.8. Biot number calculations for PS needle samples at natural and forced convection with four heat flux levels.

| | Heat flux | PS | | | | PR | | | |
|---|---|---|---|---|---|---|---|---|---|
| | [kW.m$^{-2}$] | Nat. Conv. | Forced Convection | | | Nat. Conv. | Forced Convection | | |
| | | NF | LF | HF | HHF | NF | LF | HF | HHF |
| $v$ [m.s$^{-1}$] | | 0 | 6.67 | 13.3 | 26.7 | 0 | 6.67 | 13.3 | 26.7 |
| $h_T$ [W.m$^{-2}$.K$^{-1}$] | | 20.83 | 71.30 | 85.28 | 106.96 | 24.44 | 55.18 | 64.30 | 78.86 |
| | 30 | 12.74 | -- | -- | -- | 4.75 | -- | -- | -- |
| $Bi_{rad,losses}$ at | 40 | 18.65 | 6.52 | 3.17 | -- | 7.43 | 3.32 | 2.10 | -- |
| Heat Flux | 50 | 24.56 | 12.44 | 9.08 | 3.87 | 10.10 | 5.99 | 4.77 | 2.83 |
| | 60 | 30.48 | 18.35 | 14.99 | 9.79 | 12.78 | 8.67 | 7.45 | 5.50 |

The misrepresentation is because a crucial heat transfer mechanism is not represented in this formulation of the Biot number: the internal convection heat transfer. It only takes radiant heat transfer into account, with the application of $k_R$.

Finally, it can be concluded that, on the scale of the sample, the Biot number ($Bi_{rad,losses}$), is only applicable if buoyancy driven convection is present. Further development is required for forced convection condition, to account for increase in internal thermal resistance due to convective cooling.

The following section now explores the thermal behavior of a needle that is located in a fuel bed under the flow conditions discussed above.

### *4.3.2. Thermal behavior on the scale of the needle*

As discussed in Chapter 1, it is widely assumed that fine wildland fuel particles exhibit a thermally thin behavior [4.9, 4.21], i.e. the temperature gradient within the particle is marginal. In recent works, such as by Benkoussas et al [4.16], this assumption has been challenged. They showed that even very fine particles (on the order of 0.5 mm) can start to behave thermally intermediate, depending on the heating condition, i.e. an external heat flux. Benkoussas et al [4.16] showed that the limitation of thermal regimes depends strongly on the external heat flux. Conclusions delivered by [4.16] suggest that, significant uncertainties of current wildfire models can be associated to the misrepresentation of the solid particles in a multi phase formulation.

Results presented in this section agree with conclusions drawn by Benkoussas et al [4.16], but also illustrate the limitations of ignoring heat losses. It was shown in the previous section that, losses, specifically due to convection under forced flow regimes ($Fr > 1.0$) can become larger (Table 4.5).

Thus, the heat losses will counteract the radiant heating and reduce the net energy transfer to the particles, which has the effects of slowing down the temperature rise of

the particle. This suggests that, a radiative Biot number analysis which ignores the heat losses will be an over-estimation. Meaning that, particles predicted to have a thermally thick behavior can in fact still be in the thermally thin regime. Or alternatively, ignoring heat losses will under-predict the threshold heat flux at which a certain size particle will transition to a thermally thick behavior. The raditive Biot number inlcuding losses can be formulated as:

$$Bi_{rad,losses} = \left(\frac{a\dot{q}_e^{"}}{\Delta T_{ig}} - h_T\right)(\sigma k)^{-1} \qquad \textbf{Eq. 4.1}$$

The first two terms on the r.h.s of the equation correspond to the two heat transfer mechanisms, radiative and convective (plus re-radiation) boundary condition. The two opposing heat transfer mechanisms have two different effects that define the overall thermal behavior. Increasing the external heat flux causes the external thermal resistance to decreases, which results in the increasing value of *Bi*. On the other hand, increasing convection causes the external thermal resistance to increase, which results in the decreasing value of *Bi*.

Contrarily, if one should choose radiative and convective heating simultaneously, both mechanisms are complimentary and will both cause a decrease in the thermal resistance and thus result in a larger value of *Bi*. This would mean that such a scenario would lead to a high possibility that particles behave thermally thick.

The first term on the r.h.s can be considered as an equivalent radiation heat transfer coefficient:

$$h_{eq,rad} = \frac{a\dot{q}_e^{"}}{\Delta T_{ig}} \qquad \textbf{Eq. 4.2}$$

The definition of the Biot number now describes the ratio of external (radiant heating, re-radiation and convective cooling) to internal (conduction) heat transfer. If heat losses are considered negligible, Eq. 4.1 reduces to a "no loss" condition defined in [4.16]. Including heat losses, effectively slows down the heat transfer to the solid, i.e. the net energy received by the solid is reduced. This is described by a decreasing Biot number, $Bi_{rad,losses}$, with increasing total heat transfer coefficient (cooling). An illustration of the relationship is given in Fig. 4.9 for two species, PS and PR.

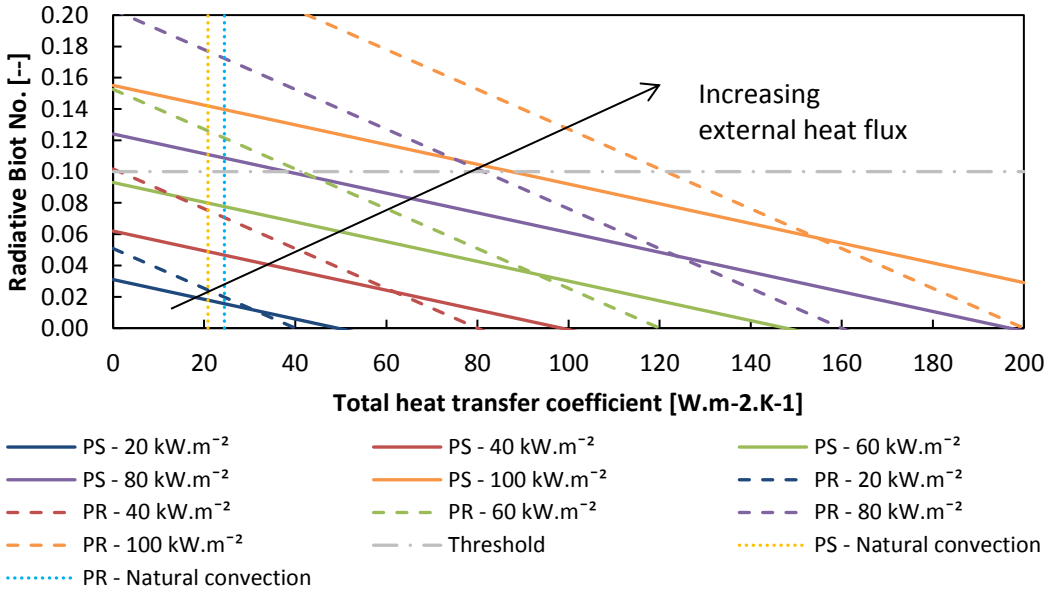


**Fig. 4.9. Relationship between corrected radiative Biot number and total heat transfer coefficient at different heat flux levels for two species, PS and PR.**

When heat losses are included, the needles behave thermally thin at higher heat fluxes as initially estimated by $Bi_{rad}$. For example, PS needles for no heat losses condition ($h_T$ = 0 W.m$^{-2}$.K$^{-1}$ in Fig. 4.9), exhibit a thermally thin behavior until an external heat flux of approximately 65 kW.m$^{-2}$ (slightly above solid green line). When the radiant exposure is below this threshold, needles will always behave thermally thin no matter what the heat losses are.

When the heat flux is above this level, the heat loss condition will govern what the thermal behavior of the fuel is. For example, PS needles behave thermally intermediate

at 100 kW.m$^{-2}$ (solid orange line) and no heat losses ($h_T$ = 0 W.m$^{-2}$.K$^{-1}$). When forced convection is introduced, for example by wind, the thermal behavior can transition to thermally thin. This transition occurs at a total heat transfer coefficient of around 85-90 W.m$^{-2}$.K$^{-1}$ (see intercept between solid orange and "threshold" line in Fig. 4.9). A similar evaluation can be made for PR needles.

Experimentation discussed was conducted with heat flux levels up to 60 kW.m$^{-2}$. Therefore, it can be concluded that, for all conditions tested, PS needles behave thermally thin. The same is true for most conditions for PR needles. The thermal behavior transitions to thermally thick only for tests with 60 kW.m$^{-2}$ and natural convection (dotted green line in Fig. 4.9).This can be evaluated more closely by observing critical conditions.

Table 4.9. Summary of critical heat flux levels, required to overcome convection losses and to transition from thermally thin to intermediate for two needle species at four airflow conditions.

| | PS | | | | PR | | | |
|---|---|---|---|---|---|---|---|---|
| | Natural Conv. | Forced Conv. | | | Natural Conv. | Forced Conv. | | |
| | NF | LF | HF | HHF | NF | LF | HF | HHF |
| Airflow velocity [cm.s$^{-1}$] | 0 | 6.67 | 13.4 | 26.8 | 0 | 6.67 | 13.4 | 26.8 |
| Total heat transfer coefficient [W.m$^{-2}$.K$^{-1}$] | 20.83 | 71.30 | 85.27 | 106.96 | 24.44 | 55.18 | 64.30 | 78.86 |
| Critical heat flux to overcome heat losses ($\dot{q}''_{cr,theory}$) [kW.m$^{-2}$] | 8.46 | 28.97 | 34.64 | 43.45 | 12.22 | 27.59 | 32.15 | 39.43 |
| Critical heat flux to transition from therm. thin to thick ($\dot{q}''_{cr,threshold}$) [kW.m$^{-2}$] | 72.95 | 93.45 | 99.13 | 107.94 | 51.56 | 66.92 | 71.49 | 78.76 |

Certain critical conditions: On the one hand, the condition at which radiation gain becomes larger than heat losses: $Bi_{rad,losses} = 0.0$. On the other hand, estimating the critical heat flux at which fuel particles transition from thermally thin to thick: $Bi_{rad,losses} = 0.1$. A summary of this assessment, for the needles and flow conditions considered in this work, is given in Table 4.9.

The total heat transfer coefficients used are the ones determined from the analysis of the fuel bed (adjusted for mixed convection, $h_T^*$) in Section 4.3.1.

*Critical heat flux for ignition*

Physically, the meaning of $h_{eq,rad}$ (Eq. 4.2) infers a critical condition, which is required to overcome heat losses imposed by convection and re-radiation ($h_T$). When the condition is such that

$$\dot{q}''_{cr,theory} < \frac{h\Delta T_{ig}}{a} \qquad \textbf{Eq. 4.3}$$

cooling (via convection and radiation losses) of the particle is more effective than the heating due to the external heat flux. Thus, can be associated to the critical condition where the particle will never reach its ignition temperature, i.e. will not ignite.

Theoretical critical heat flux levels required to overcome heat losses are shown in Table 4.9. At natural convection the value is higher for PR needles, because the total heat transfer coefficient is higher for this species. This is due to the significant influence of radiant losses, which are higher for this species, because the ignition temperature is higher (see also Table 4.5). Additionally, the larger *SVR* of PS needles means, that radiation absorption can occur on a larger surface area.

Comparing these values to experimental results for the critical heat flux (for piloted ignition) shows that the same tendency is present (Table 4.10). However, the theoretical value for both species is under-estimated; more so for PS needles (by 48%). The critical variable that leads to this larger difference for PS needles is the ignition temperature. The lower temperature value (compared to PR needles) results in lower radiative and convective losses, which accumulative is reflected in a lower $h_T$.

Table 4.10. Comparison of theoretical and experimental critical heat flux levels (piloted ignition) for two species at three flow conditions. The percent difference is between theoretical and experimental values.

| | PS | | | | PR | | | |
|---|---|---|---|---|---|---|---|---|
| | Natural Convection | Forced Convection | | | Natural Convection | Forced Convection | | |
| | NF | LF | HF | HHF | NF | LF | HF | HHF |
| $(\dot{q}''_{cr,theory})$ [kW.m$^{-2}$] | 8.46 | 28.97 | 34.64 | 43.45 | 12.22 | 27.59 | 32.15 | 39.43 |
| $(\dot{q}''_{cr,exp})$ [kW.m$^{-2}$] | 12.50 | 25.00 | 30.00 | - | 13.00 | 30.00 | 35.00 | - |
| % Difference | 47.7 | 22.3 | 27.8 | - | 6.4 | 9.4 | 14.5 | - |

For forced convection conditions, radiant losses are less significant in comparison to convection losses. Therefore, the critical heat flux values are higher for PS needles, because they experience larger convection losses compared to PR needles, which can be attributed to the larger surface area on which heat transfer can take place (i.e. *SVR* for PS needles is much larger compared to PR needles).

At HHF flow conditions (the highest airflow rate tested) only a few experiments were carried out for PS needles. These tests were done at 45 and 55 kW.m$^{-2}$. Ignition was observed for both heat flux levels. However, at 45 kW.m$^{-2}$ do the needles smolder before transitioning to a flaming state. The ignition behavior is piloted for 55 kW.m$^{-2}$. Therefore, one can assume that the critical heat flux for piloted ignition is in between 45 to 55 kW.m$^{-2}$ at this flow condition.

Overall, the theory matches the experimentation well for PR needles, but not so well for PS needles (Table 4.10). Although it is not entirely evident what the exact reason for this is, it is likely that it is due to a combination of two factors: (1) estimation of the flow velocity, and (2) measurement of the ignition temperature. However, for a first estimation these percent differences may be considered acceptable. Future work should focus on improving the estimation of the flow velocity (measuring actual pore space velocity) and temperature measurements.

*Critical heat flux at threshold between thermally thin and intermediate behavior*

This threshold heat flux level ($\dot{q}''_{cr,threshold}$) in Table 4.9 describes at what point the needle behaves thermally intermediate. When using the "no loss" definition [4.16] the threshold for PS and PR is 64.5 and 39.3 kW.m$^{-2}$, respectively. The thicker PR needles transition to an intermediate behavior at a lower external heat flux due to its physical size. This threshold is however, under-estimated, because heat losses are ignored.

Including the losses in the assessment increases the threshold by 13 and 31% for PS and PR needles at natural convection, respectively (see values at natural convection in Table 4.9). The increase for PR needles is much more significant, because the radiant losses are higher for this species (higher ignition temperature). Now, adding the losses due to forced convection will increase the threshold even further (see values at forced convection in Table 4.9). This is the case for both species, but more so for PS needles because convection cooling has a stronger impact on them. Table 4.11 summarizes the per cent difference between the "no loss" and "loss" evaluation of the threshold heat flux ($\dot{q}''_{cr,threshold}$) and shows the significant under-estimation of the "no loss" condition.

Table 4.11. Percent difference for threshold heat flux when $Bi$ > 0.1 between "no loss" and "loss" condition.

| PS | | | | PR | | | |
|---|---|---|---|---|---|---|---|
| Natural Convection | Forced Convection | | | Natural Convection | Forced Convection | | |
| NF | LF | HF | HHF | NF | LF | HF | HHF |
| 13.1 | 44.9 | 53.7 | 67.4 | 31.1 | 70.1 | 81.7 | 100.2 |

The results for the threshold calculations at forced convection, although theoretical, show that, significant external heat flux levels are required in order to cause a shift in thermal behavior. Such levels can occur, however, only in very intense fires (> 50 kW.m$^{-2}$). Alternatively, such high heat fluxes also occur in the near field and within a fire front. Once a particle is very close to the flame, the convection heat transfer mechanism can transition to a heating mode, at which point the above assessment loses its validity.

*Transient condition*

The last part of the analysis now evaluates the transient condition that combines radiant and convection heat transfer effects. This analysis is done to assess when a "no loss" condition is acceptable and when it is not. Initial discussion and equations are in Chapter 1.

The graph given below (Fig. 4.10) plots the particle temperature evolution (non-dimensional) against the Fourier number (non-dimensional time). It shows the radiant heating condition at 60 kW.m$^{-2}$ at various cooling condition.

The dotted lines in Fig. 4.10 indicate the "no loss" condition for the two species, PS (yellow) and PR (black). These two conditions should be used as a baseline for comparison of the impact of heat losses on the thermal evolution of the particle.

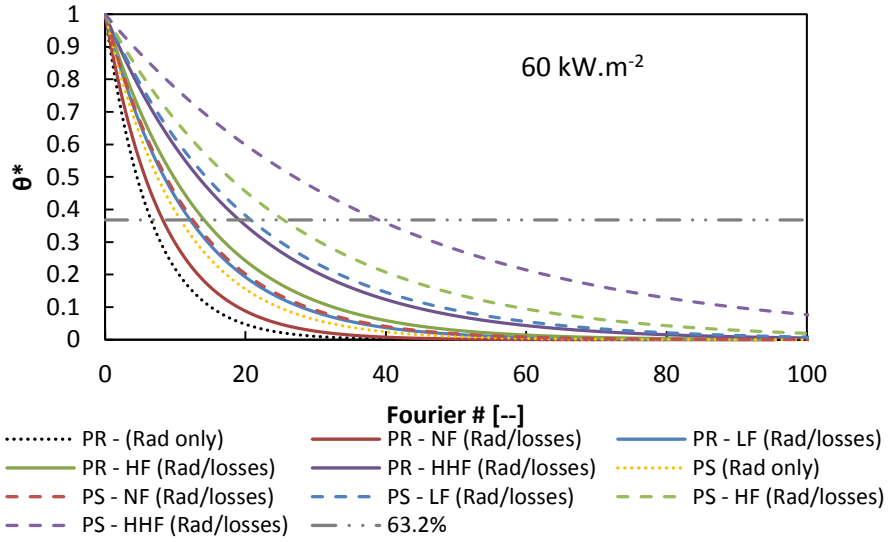


**Fig. 4.10. Thermal evolution (PS and PR) with respect to the Fourier number for the radiation-losses boundary condition.**

Consider the "no loss" condition, for either species: Under this condition, the particle reacts to the radiant heating and reaches the equilibrium temperature ($\theta^* \rightarrow 0$) in the shortest amount of time. Adding heat losses, given by conditions LF, HF, and HHF, slows down the temperature rise of the particle, as was previously postulated. The

increased convection counteracts against the heating via radiation (slowing down the temperature rise). Thus, the graphical representation of this phenomenon shows the existing physical behavior correctly.

The graph with dimensionless time does not clearly show that, PS needles respond quicker because the Fourier number depends on particle properties. A similar plot for $\theta^*$ against time can be found in Appendix B2. Additional graphs for different heat flux levels are also shown in Appendix B3 (various heating rates).

Results shown in Fig. 4.10 and Appendix B3 illustrate the departure of the assessment with heat losses from the "no loss" condition. This can be further quantified with the thermal time constant, $\tau$. Tau was calculated for several test conditions and are summarized in Appendix B3. The percent difference between the two conditions is even high for natural convection (above 16%), where heat losses are considered from buoyancy driven convection and re-radiation. This indicates that, the "no loss" assumption is only acceptable under a narrow range of conditions, i.e. high heat flux and low convection conditions. A graphical representation of this trend is given in Fig. 4.11 for PS needles (similar for PR needles). At the critical heat flux (dotted vertical lines, see Table 4.10 for values), $\tau \rightarrow \infty$, and only when the heating rate is sufficiently high does $\tau_{rad,losses} \rightarrow \tau_{rad}$ (see convergence of solid lines with dashed line at increasing heat flux).

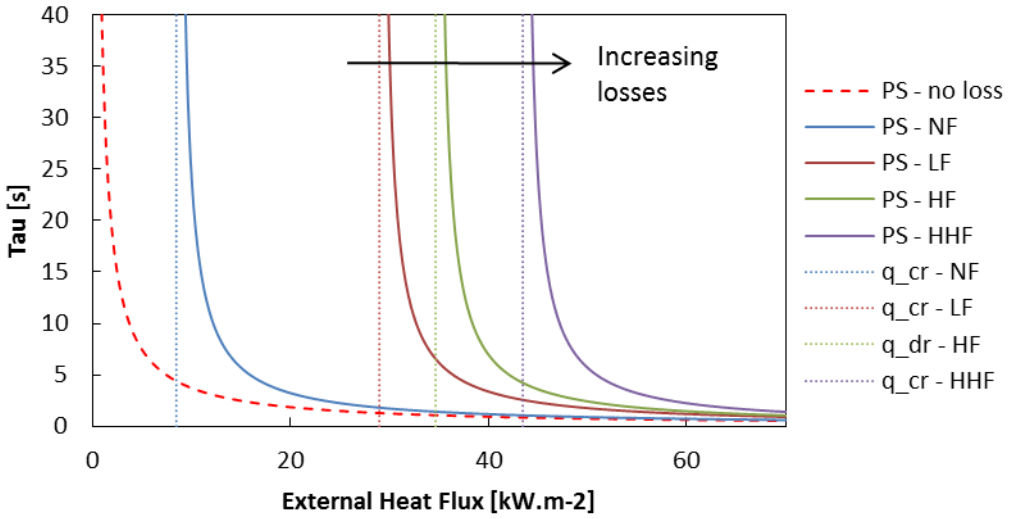


**Fig. 4.11. Thermal time constant evolution (PS) with respect to external heat flux for radiation-only and radiation-losses boundary conditions. Dotted vertical lines indicate the theoretical critical heat flux (Table 4.10).**

In order to determine a threshold level at which point the "no loss" condition becomes acceptable, the analysis has to be extended to higher heat flux levels. This is shown in Fig. 4.12, where $\tau_{rad,losses}$ is plotted against $\tau_{rad}$. Furthermore, a threshold for acceptability has to be defined. For a first approximation, this threshold was considered 15%. Thus, the "no loss" becomes acceptable when $\tau_{rad,losses}$ =1.15 $\tau_{rad}$.

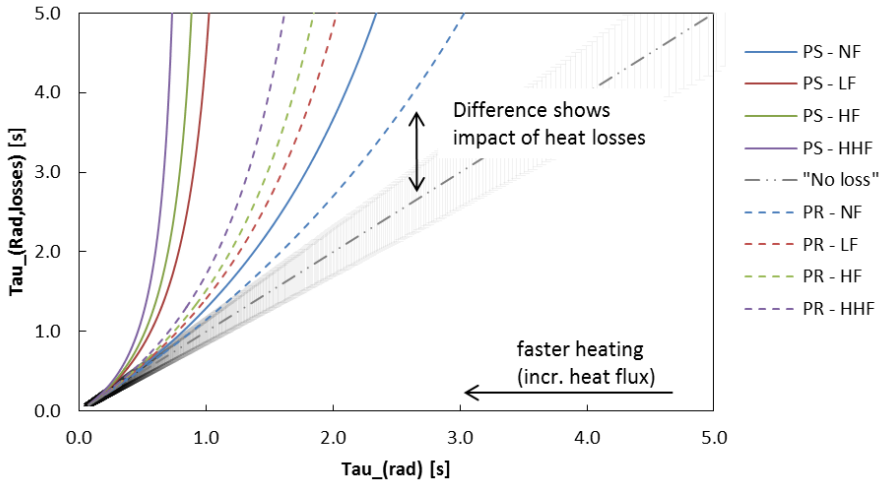


**Fig. 4.12. Evaluation of the impact of heat losses on the thermal time constant. Thermal time constant from radiation-losses boundary condition is plotted against constant from radiation-only boundary ("no-loss") condition.**

Tau increases with decreasing heat flux. Thus, $\tau \rightarrow 0$ indicates an infinitely fast heating condition. The linear (grey dashed/dotted) line shows the "no loss" condition, whereas, the colored lines show the condition with heat losses (solid: PS needles and dashed: PR needles). The deviation of the colored lines from the linear "no loss" condition illustrates the impact of cooling on the thermal behavior of the particle. This deviation also shows the inadequacy of the "no loss" consideration. Determining the heating condition at which point $\tau_{rad,losses} = 1.15\ \tau_{rad}$ is satisfied, results in the following heat flux levels (Table 4.12).

Table 4.12. Heat flux levels below which the "no-loss" boundary condition results in significant uncertainties.

| | Heat flux [kW.m$^{-2}$] corresponding to 15% deviation from "no loss" condition | | | |
|---|---|---|---|---|
| | NF | LF | HF | HHF |
| PS | 65.0 | 222 | 266 | 333 |
| PR | 94.0 | 212 | 247 | 302 |

For natural convection, the threshold is higher for PR needles compared to PS needles, because heat losses are driven by temperature differences (ignition temperature was considered), which are higher for this species. On the contrary, threshold levels are higher for PS needles compared to PR needles when forced convection is present. This is due to the physical size of the needles, i.e. PS experiences higher convection losses compared to PR needles.

When the radiation only boundary condition is used in an analysis with heat flux levels below the thresholds at the given cooling condition, the error associated to neglecting heat losses will be significant. This analysis indicates that, the "no loss" assumption is challenged even at natural convection. At forced convection conditions, it is effectively not a suitable consideration to ignore heat losses, because the thermal response of the particle, and therefore, the evaluation of the thermal behavior (thick or thin), will be over-estimate. It will only be accurate for very intense fires that produce conditions in which the fuel experiences heat flux levels well above 200 kW.m$^{-2}$ (with airflow).

**Summary**

The thermal analysis performed in the proceeding sections was done on the scale of the sample and on the scale of the needle. It was discussed that, a radiative Biot number such as defined by Benkoussas et al [4.16], although significantly more accurate in representing the physics compared to the standard convective Biot number, over-predicts the thermal behavior. In this assessment, the radiative Biot number was corrected to account for convective and radiative losses via a lumped heat transfer coefficient.

Analysis of the sample provided means to estimate appropriate heat transfer coefficients for natural and forced convection for forest fuel beds, which were then used in the analysis on the scale of the needle. Furthermore, the theoretical results of the thermal behavior of the sample (thick or thin) showed good agreement with experimental results. It was concluded that the fuel beds behaved thermally thick when the heat flux is greater than 20 $kW.m^{-2}$ (for natural convection). On the scale of the fuel bed, the modified radiative Biot number ($Bi_{rad,losses}$) is not applicable for forced convection, because internal convective heat transfer is not represented.

The thermal analysis performed on the scale of the needle was done in order to give a detailed account of the thermal behavior of fine forest fuels, such as dead pine needles. This was done because in recent works [4.16], the assumption that fine forest fuel particle behave thermally thin was challenged. Overall, the assessment outlined above, indicates that, a thermally thin assumption for fine dead forest fuel is in fact still reasonable for a large range of conditions. The corrected definition of the radiative Biot number still follows the same trend as discussed by Benkoussas et al [4.16], i.e. transition from thermally thin to thick at elevated external heat flux levels (faster heating rate). However, it shows that, this transition occurs at up to 31% higher heat flux than for the “no loss” conditions (for natural convection). When forced convection is introduced, this deviation continues to increase. Finally, it was shown, that the

radiation-only ("no loss") condition is only suitable for a very narrow range of external conditions, i.e. natural convection and high heat flux levels (see Table 4.12).

### *4.4. Modeling results*

A simplified one-dimensional, two phase model developed for porous media to predict the ignition behavior is explored here. The validation is done to explore to what extent such a simplified model can be used. Validation is done with experimental results (critical heat flux, in-depth temperature distribution, and ignition times).

The simulation outputs are twofold: predict the temperature gradient inside the porous medium and the time to ignition. The latter output is associated to an ignition temperature criterion. Therefore, the model must be validated in two ways. On the one side, physical in-depth temperature measurements are used to compare with the model simulation. On the other hand, experimental ignition times at a range of heat flux levels are used to verify the ignition behavior. A first evaluation of the model was shown by [4.2] but only with limited experimental ignition data. In-depth temperature measurements for these samples were never obtained before and therefore marking a critical evolution in the assessment of the model.

The first validation is performed with airflow velocity equal zero, which represents a natural convection condition. Finally, forced convection was considered.

#### *4.4.1. Model performance – Natural convection (NF)*

Simulations were performed with the parameters given in Table 4.1. No fitting was performed to this point. Experimental data (for PS needles) is given for low and high heat flux levels in order to validate the performance of the model. For PS samples (Fig. 4.13.a.), the model predicts the temperature distribution well in some areas, and not so well in others.

It must be noted, that the ignition criterion is the ignition temperature, which, in the case of the porous medium is reached first at some distance inside the sample and not at the surface. Physical measurements were only obtained at three locations, which did not fall into this range; therefore, this phenomenon still needs to be verified in detail.

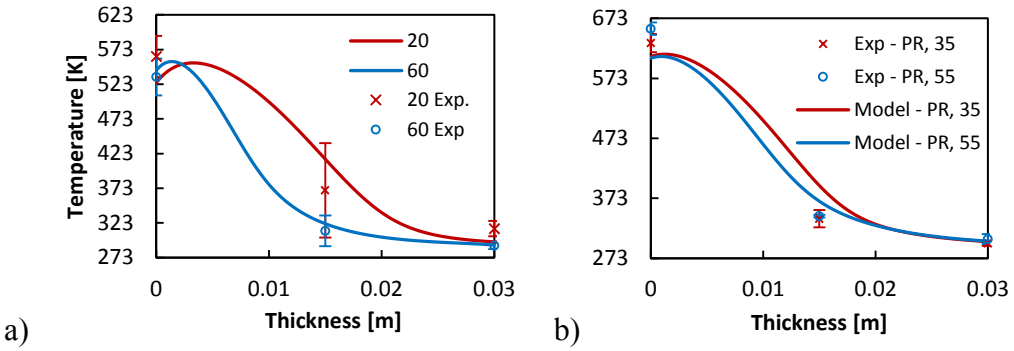


**Fig. 4.13. Simulation and experimental temperature profiles of a) PS sample at two heat flux level [kW.m$^{-2}$] and natural convection; and b) PR at two heat flux level [kW.m$^{-2}$] and forced convection (LF).**

In the given formulation of the model, convective cooling is only applied to the surface, at $x = 0.0$ m. In conjunction with the in-depth heating, i.e. not all radiant energy is absorbed at $x = 0.0$ m, but over a depth $x \approx \delta$, this produces a higher temperature underneath the sample surface ($0.0\ \text{m} \leq x < \delta$). For this reason, a limitation will be applied: the location of ignition (peak temperature in Fig. 4.13) has to be less than the radiation penetration depth, $\delta$, which was the case for all simulations presented here. This phenomenon was not physically measured, because only 3 thermocouples were used in the entire sample. With the present technique, it was not feasible to place a number of thermocouples in such a small place without significantly disturbing the sample matrix (producing flue spaces that add to creating a heterogeneous fuel layer). Future development should address this issue.

At 20 kW.m$^{-2}$, the experimental data shows a high variability at the center location (1.5 cm). The model results fall within these but are relative far from the average value. At the back face, the slight temperature rise is not captured by the model. At high heat flux levels (60 kW.m$^{-2}$), the model results are well within the experimental variability throughout the thickness of the sample.

The performance of the model can be evaluated with respect to time and is illustrated in Appendix B5. It is evident that the overall model performance is satisfactory, as it is possible to simulate the evolution of the thermal profile of the fuel bed. Furthermore, it agrees with the assumption of a semi-infinite and thermally thick behavior of the sample.

### *4.4.2. Model performance – Forced convection (LF)*

Similar to the natural convection scenario, a forced convection scenario is now evaluated in order to prove the models performance. The scenario examined is the LF condition (6.67 $cm.s^{-1}$ airflow) with PR needles at two heat flux levels, 35 and 55 $kW.m^{-2}$. A comparison of experimental in-depth temperature measurements and simulated temperature profile is given in Fig. 4.13.b. Simulations are run with the input parameters provided in Table 4.1. Results presented in this graph correspond to the time of ignition.

Overall the simulations provide satisfactory results, with minor deviations from physical measurements. It can be observed, that for the forced convection scenarios explored, the experimental ignition temperatures are slightly higher than the average value used in the simulation. A slight over-estimation of the mid-point temperature (0.015 m thickness) is visible. The simulations match the back face temperatures well.

At higher flow rates, such as HF (13.3 $cm.s^{-1}$), model performance was not adequate. Ignition was not achieved with PR needle samples, and only above 50$kW.m^{-2}$ for PS needle samples with a high deviation from experimental results (> 30%). Therefore, high flow rates are not shown. It can be concluded that, the model performs adequate at natural convection and at low forced convection condition with a flow rate, below 10.0 $cm.s^{-1}$. Within these limitations, the model will predict ignition times to an acceptable degree of uncertainty. Further limits will be established with respect to critical heat flux conditions.

### *4.4.3. Model prediction with natural convection*

The second model output, the time to ignition (Table 4.13 and 4.14) shows good predictions above 20 kW.m$^{-2}$, for both PS and PR needle samples. The simulation for PS needles slightly under-predict the critical heat flux, whereas, the simulation of PR needles over-predicts it. The failing performance of the model at low heat flux levels can be explained by the heat transfer consideration.

Table 4.13. Simulation and experimental results (time to ignition) for PS at NF condition.

| Heat flux | Time to ignition [s] | | | % Diff. |
|---|---|---|---|---|
| [kW.m$^{-2}$] | Model | Exp. Avg. | Exp. St. dev. | |
| 12.5 | 122.82 | 490 | 10 | -74.9% |
| 20 | 37.87 | 45.8 | 5.1 | -17.3% |
| 30 | 18.41 | 19.4 | 1.8 | -5.1% |
| 40 | 11.25 | 11.7 | 0.9 | -3.8% |
| 50 | 8.0 | 8.3 | 0.6 | -3.6% |
| 60 | 6.0 | 6.0 | 0.2 | 0.0% |

At low heat flux levels, close to the critical heat flux the semi-infinite assumption for the sample is challenged (also see discussion in Section 4.3.1), because the exposure time is very long, and the heat wave can propagate through the sample.

Table 4.14. Simulation and experimental results (time to ignition) for PR at NF condition. (NI: no ignition)

| Heat Flux | Time to ignition [s] | | | % Diff. |
|---|---|---|---|---|
| [kW.m$^{-2}$] | Model | Exp. Avg | Exp. Stdev | |
| 13 | NI | 450 | 10 | -- |
| 20 | 89.3 | 110.0 | 8.5 | -18.8% |
| 30 | 34.57 | 38.3 | 2.7 | -9.7% |
| 40 | 20.64 | 20.7 | 0.2 | -0.3% |
| 50 | 14.0 | 13.7 | 0.5 | 2.2% |
| 60 | 11.0 | 10.7 | 0.3 | 2.8% |

For further analysis of the ignition behavior, experimental and simulated times to ignition are plotted with respect to the external heat flux for PS and PR needle samples in Fig. 4.14 below.

In the graph (Fig. 4.14), the data is portrayed in typical format (one over the square root of ignition time against external heat flux) to reflect ignition theory for thermally thick samples (e.g. [4.22]). Simulation results match the experimental data well for the PS samples for heat flux levels > 20 kW.m$^{-2}$. Below this level, the sample's thermal behavior starts to deviate from a semi-infinite behavior, meaning, that it starts to experience additional heat losses at the back face, which are not formulated in the model.

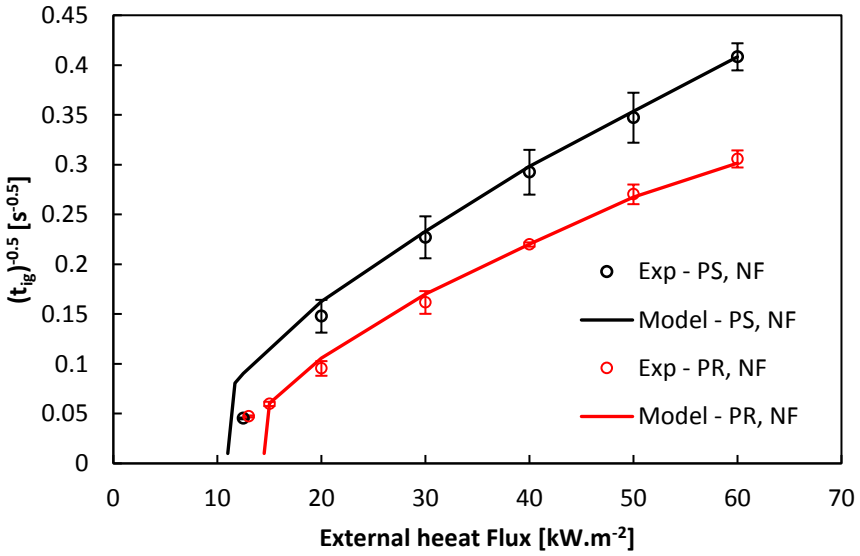


**Fig. 4.14. Simulation and experimental results for PS and PR at no flow condition (NF). Ignition time in the range of critical heat flux to 60 kW.m$^{-2}$.**

This can be observed from the in-depth temperature measurements shown in Fig. 4.6: The back face temperatures are already around 50 °C at 20 kW.m$^{-2}$, which is at the time of ignition. At heat flux levels below 20 kW.m$^{-2}$, the model significantly under-predicts the ignition time and slightly under-predicts the critical heat flux for PS needle samples ($\dot{q}''_{cr,model} = 11.0 - 11.5\, kW.m^{-2}$). Results from the thermal analysis ($Bi_{rad,losses}$) in Table 4.7 also suggests that the fuel bed approaches a thermally thin behavior below 20 kW.m$^{-2}$. Ignition time results are included for PR samples (Fig. 4.14), and simulation results indicate a good agreement with experimental results. The

critical heat flux is slightly over-predicted by the model ($\dot{q}''_{cr,model} = 14.5 - 15.0\ kW.m^{-2}$).

### *4.4.4. Model prediction with forced convection*

Before comparing ignition results with forced convection conditions, a brief discussion on the importance of gas phase properties is presented. This is pertinent, because simulating incorrect gas phase properties (specifically density), will result in incorrect results.

**Importance of gas phase properties (density)**

Using a constant air density is a poor assumption because (1) the gas inside the sample matrix will be a mixture of air and combustion gases and (2) it will be heated significantly above ambient. The first point can be considered negligible if one assumes that the dilution is high due to the imposed airflow. The second point on the other hand, should not be ignored, because the density of air reduces with increasing temperature (assuming constant pressure). This can be evaluated with the ideal gas law:

$$\rho_g = \frac{P}{RT} \qquad \textbf{Eq. 4.4}$$

where $P$ is the pressure (101.4 kPa), $R$ the universal gas constant (286.99 $J.K^{-1}.kg^{-1}$) and $T$ the temperature. When the porous sample (PS as an example) has reach ignition temperature, the density of the air is almost halved, from 1.21 to 0.64 $kg.m^{-3}$. Because the porosity of these samples is on the order of 95%, this change in density will have a significant impact on the heat transfer, which must not be ignored. To account for this change, a first approximation of was done with a mean density, calculated between ambient (20 °C) and ignition temperature (280 °C for PS needles and 340 °C for PR

needles; see Table 4.2). This resulted in mean densities: $\rho_{g,mean,PS}$ = 0.87 kg.m$^{-3}$ and $\rho_{g,mean,PR}$ = 0.82 kg.m$^{-3}$, for PS and PR needles, respectively. These values were used in simulations with forced convection discussed below. Averaging the density over this range is justifiable, because on the one hand the density changes with time, from first exposure to ignition, and on the other hand, spatially due to a temperature gradient within the sample.

**Model predictions**

Simulations were performed with PS and PR needle properties with the addition of the velocity parameter. Comparison of simulation and experimental results are presented in Fig. 4.15.a. for PS needle samples and Fig. 4.15.b. for PR needles samples. Because now, the advection term is non-zero, the air properties are important. Although specific heat changes with temperature, it is assumed that this change is small compared to the change of density.

The flow velocity term in the spatial temperature gradient term (advection) impacts the simulation by changing the distribution of the temperature (or equivalently energy). Diffusion and advection of heat occur in opposite directions. The direction of diffusion is top to bottom, because the top surface of the sample is heated via the external radiation. Advection of heat is acting from the bottom to the top, because the airflow is forced through the bottom of the sample. This “negative” advection (acting against diffusion) describes a cooling mechanism.

Specifically in this case, because the ambient temperature is lower than the needle temperature. In the model formulation, a total heat transfer coefficient (convection and radiation) was initially prescribed to the surface of the porous sample (surface boundary conditions). Such formulation is acceptable for natural convection, because convection heat transfer within the sample is considered negligible compared to radiative transfer. This is however, not valid for forced convection conditions any longer.

If such a boundary condition is included, it effectively over-estimates convective cooling, because it is imposed by advection and additionally prescribed at the surface. This over-estimation of convection can cause over-prediction (longer time) of the ignition time. To reduce this uncertainty, the simulations are run without the prescribed convection cooling at the surface, which means, that the surface boundary heat losses become only dependent on the radiation losses (Table 4.5). Simulation results are plotted against experimental results in Fig. 4.15.

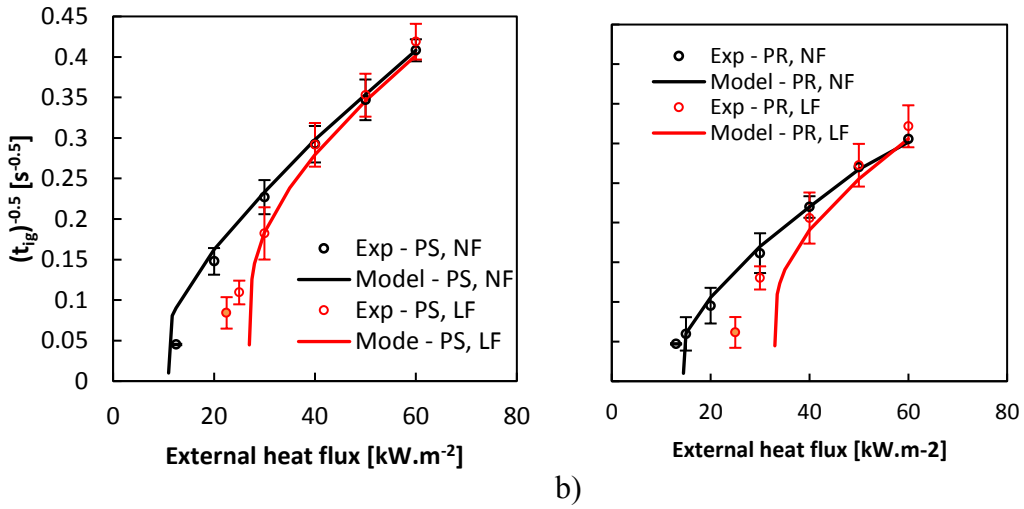


**Fig. 4.15. Experimental and simulation results for low flow (LF) conditions for a) PS and b) PR. NF condition is presented for comparison. The solid marker (LF) corresponds to smoldering ignition conditions.**

Simulation results for PS samples agree well with experimental data, above an external heat flux of 30 kW.m$^{-2}$. The critical heat flux predicted by the simulation, 27 kW.m$^{-2}$, compares reasonably well with the experimental value for pure piloted ignition, 25 kW.m$^{-2}$ (Table 4.10).

Simulation results (Fig. 4.15.b.) for PR samples agree well with the experimental results, above a heat flux of 40 kW.m$^{-2}$. The critical heat flux predicted by the simulation for PR samples is 33 kW.m$^{-2}$. Even though the ignition times are well over-predicted, the prediction for critical heat flux compares reasonably well with the experimental one (30 kW.m$^{-2}$; Table 4.10).

For both species, the predictions of the simulations compare well with the critical heat flux estimated in Section 4.3.2 ($\dot{q}''_{cr,theory}$ in Table 4.10), 32 and 31 kW.m$^{-2}$ for PS and PR, respectively.

When simulations are performed with flow velocity of 13.3 cm.s$^{-2}$ (HF conditions), results diverge significantly from experimental data, for both needle species. The model is no longer able to predict the ignition times of the needle beds. The reason for this is the over-estimation of the convection heat transfer, which prevents the surface temperature to reach the critical ignition temperature. This over-estimation can occur due to several factors: (1) radiant heat transfer within the sample is not represented properly, i.e. under-estimated; (2) deviation from thermal equilibrium between solid and gas phase; (3) deviation from a thermally thin behavior of the particles; or (4) the flow velocity used does not represent the actual flow velocity through the sample. These factors are now explored.

**Representation of in-depth radiant heat transfer**

The preceding discussion and comparison of the simulation and experimental results are sufficient evidence that (1) is not a valid factor. The linearization of the radiant heat transfer with the Rosseland approximation is considered appropriate. If this was not the case, deviations between experimental results and simulations at natural convection would have been significant.

**Deviation from a thermal equilibrium condition**

A major assumption that is required for this model to be appropriate is the thermal equilibrium between solid and gas phase, i.e. only one temperature variable represents the thermal profile of the porous medium.

A local thermal equilibrium (LTE) in a two phase system (solid and gas phase) exists when $T_{solid} = T_{gas}$ [4.23]. Contrarily, a local thermal non-equilibrium (LTNE) condition

exists when $T_{solid} \neq T_{gas}$. For the case of a LTNE condition, a simplified model depending on only a single temperature, should not be used, because it will have a large degree of uncertainty [4.23].

If the thermal equilibrium assumption is not satisfied, temperatures of each phase need to be represented separately. Minkowycz et al demonstrated in [4.23] that the heating condition is critical to the state of thermal equilibrium. When a porous media undergoes rapid heating, the deviation from a LTE increases [4.23]. In the current work, this is reflected by an increasing external heat flux. Thus, the thermal equilibrium assumption is most valid at the critical external heat flux, where particles heat up slowly. This is true independently of the convection condition. At a given heat flux, the heating rate (of the needle surface) reduces with increasing forced convection. This means that, a LTE condition is prevailing at higher airflow rates. Thus, this factor is likely not an indicator why the model is unable to predict ignition times at high flow rates.

**Impact of the thermal behavior of the needle**

Complementing the assumption from the previous subsection that a single temperature variable to describe both phases may be inappropriate, is the particle's transition from a thermally thin to a thermally thick behavior at elevated external heat flux. The LTE condition does not depend on the thermal behavior of the particle. But if particles stop behaving thermally thin, using a single temperature to describe the porous medium has high uncertainties, because temperature gradients within the particle are ignored. It was shown in Section 4.3.2 that this is the case at high heating rates. For the examined species, only PR needles at 60 $kW.m^{-2}$ and natural convection exhibit a thermally intermediate behavior. Thus, this is also an unlikely factor why the model does not predict ignition with higher flow rates well. Furthermore, needles with higher flow rates will favor a thermally thin behavior as discussed in Section 4.3.2.

**Flow velocity consideration**

The flow velocity consideration is an estimation based on the cross-sectional area of the sample, and prescribing a volumetric flow rate. This assumes that all flow enters the fuel matrix through the bottom and exits through the top. It may be the case that significant flow escapes through the sides of the basket rather than traversing through the entire sample and exiting out the top surface. If that is the case, flow velocities considered for the simulations are over-estimation, which may cause the over-estimation of the convection cooling.

Thus far, this is a likely factor causing the model not to predict ignition for HF condition. Additional experimentation is required to fully verify this. Drawbacks of the current experimental design should be addressed in the future

### *4.4.5. Current limitations of the porous model*

Validation of the porous model indicated that, it is acceptable to be used, with limitations, for predicting ignition behavior of dead forest fuel beds. The limitations are for natural convection and low forced convection conditions, only. Uncertainty of the time to ignition prediction increases as the external heat flux approaches the critical heat flux condition. For both species tested acceptable accuracy, below 10% was achieved at heat flux levels above 30 $kW.m^{-2}$. Similar considerations should be made for forced convection conditions, in which the critical heat flux required for piloted ignition increases. For the two needle species tested, the flow conditions where such that $Fr < 1.0$. Therefore, this may be considered as a limitation of the model.

Particles evaluated behaved thermally thin ($Bi_{rad,losses} < 0.1$), except for one condition, PR needles at 60 $kW.m^{-2}$ and natural convection, which indicated a thermally intermediate behavior. 60 $kW.m^{-2}$, was the maximum external heat flux tested. Thus, it is not possible to conclusively identify if this model is only applicable to thermally thin particles. Additional validation at higher external heat flux levels, where particles

start to behavior thermally intermediate, is required to formulate a conclusion in this matter.

### *4.5. Chapter summary and conclusions*

In this chapter, the impact of convection cooling on forest fuel beds heated with an external radiant heat flux was explored. The purpose of the analysis was the validation of a simplified one-dimensional heat transfer model for porous fuel media. Such validation was achieved with experimental results for (1) critical heat flux required for piloted ignition, (2) in-depth temperature measurements, and (3) piloted ignition times at a range of external heat flux and convection flow conditions. The test apparatus was the FPA, and two species were used for this validation, dead PS and PR needle.

The model is a two phase representation of the energy conservation (solid and gas) with in-depth absorption of radiation. Interior heat transfer was considered by radiation and convection. Conduction was considered negligible due to the high porosity of the fuel bed. Heat losses are due to re-radiation and convection and are prescribed at the sample surface. At forced convection conditions, advection provided means to characterize the interior heat transfer associate with convective flows. For this scenario, surface boundary conditions were reduced to only account for radiant losses. In-depth radiant heat transfer was linearized with the Rosseland approximation, which proved an acceptable simplification.

Limitations of the porous model are discussed: (1) It can predict ignition times of forest fuel beds to an acceptable accuracy for natural and forced convection when $Fr < 1.0$; (2) accuracy improves at heat flux levels sufficiently far from critical heat flux, > 20 $kW.m^{-2}$, for natural convection. This is attributed to the deviation from a semi-infinite medium when heating rates are slow. At forced convection conditions, the threshold increases, since also the critical heat flux increases; (3) a maximum heat flux level of 60 $kW.m^{-2}$ was tested experimentally; therefore, extrapolation beyond this limit are

not advised. Only a single packing ratio was tested, thus, the model still requires validation for a range of porosities. This should be part of future explorations.

To support the model validation, a detailed thermal analysis was performed on the scale of the sample and needle. The analysis provides a development of a radiative Biot number including heat losses (re-radiation and convection). In the novel definition of the Biot number, the Rosseland approximation is employed instead of the thermal conductivity to account for the radiant heat transfer mechanism in the highly porous fuel bed.

Heat transfer coefficients determined in the sample-scale analysis were employed in the simulations. For most conditions, the samples behaved thermally thick ($Bi_{rad,losses}$ > 1.0). Values of the Biot number found for natural convection supported the limitation (2); below 20 kW.m$^{-2}$ values approached the threshold of 1.0. The definition of $Bi_{rad,losses}$ does however, only apply to natural convection (sample scale). When forced convection is present, radiant heat transfer (defined by the Rosseland approximation) is not the only heat transfer mechanism that needs to be accounted for. Ignoring the convection portion significantly over-estimates the heat transfer resulting in low values for $Bi_{rad,losses}$. This conclusion was supported by physical in-depth temperature measurements.

Heat transfer coefficients developed for the fuel bed are used in the analysis on the needle-scale. It was assumed that the developed convective boundary layer is based on the entire fuel bed, rather than an individual needle. The analysis shows that, the thermal behavior of the needle is best described with a boundary condition accounting for radiant heating and heat losses due to convection and re-radiation. With such a definition of the boundary layer, it was concluded that, all test conditions but one, resulted in thermally thin behavior for PS and PR needles. The one exception was for PR needles at the highest heating rate (60 kW.m$^{-2}$) with natural convection.

Ignoring heat losses results in significant over-estimation of the external thermal resistance (i.e. heating rate) compared to the internal thermal resistance, which results in over-estimation of Biot numbers. This over-estimation results in an under-estimation of the threshold heat flux at which transition from thermally thin to intermediate ($Bi > 0.1$) occurs. The under-estimation was as much as 31% for PR needles at natural convection. The under-estimation increase with increasing forced convection. This is because the convection cooling effectively reduces the net energy transfer to the particle, and thus, particles heat slower, more uniformly.

The acceptability of a "no loss" conditions was illustrated with a transient analysis. For this analysis, it was assumed that a 15% deviation is acceptable. It was concluded that, it is acceptable to ignore heat losses only for a narrow range of heating conditions. For natural convection the "no loss" condition is acceptable for heat flux levels above 65.0 and 94.0 $kW.m^{-2}$ for PS and PR needles, respectively. However, for forced convection, the threshold increases to above 200 $kW.m^{-2}$, depending on the magnitude of the airflow.

The thermal behavior is an important characteristic of fine forest fuel that will drive how accurate fire spread is predicted by models. The common assumption of a thermally thin behavior of fine forest fuel particles was challenged in recent works, illustrating that at elevated heating rate even fine particles can exhibit a thermally intermediate or thick behavior. Although the analysis presented in this work agrees with this, it also concluded that a thermally thin assumption is still valid for a large range of conditions. More so where particles are subjected to forced convective cooling conditions. Such conditions are likely to exist in reality ahead of a moving wildfire.

### *4.6. References*

[4.1] A. Simeoni, J.C. Thomas, P. Bartoli, P. Borowjeck, P. Reszka, F. Colella, P.A. Santoni, J.L. Torero. Flammability Studies for Wildland and Wildland-Urban

Interface Fires Applied to Pine Needles and Solid Polymers. Fire Safety Journal 54 (2012) 203-2017.

[4.2] A. Simeoni, F. Colella, E. Martinot, P. Bartoli, J.L. Torero. Flaming Ignition of Pine Needle Beds. Proceedings of the 7th International Conference on Forest Fire Research, Coimbra, Protugal (2010).

[4.3] J.H. Ferziger, M. Peric, Computational Methods for Fluid Dynamics, 3rd ed., Springer, Berlin, Germany, 2002, p. 59.

[4.4] R. Larsen, K. Trombley. Specific Heat of Three Pine Needles; A Report to Worcester Polytechnic Institute. Report Nr. TPRL-4992. Thermophysical Properties Research Laboratory. West Lafayette, IL, USA (2012) (unpublished).

[4.5] A.M. Grishin. Mathematical Modeling Forest Fire and New Methods Fighting Them. Publishing House of Tomsk University, Tomsk, Russia, 1997.

[4.6] H.E. Anderson. Forest Fuel Ignitibility. Fire Technology 6/4 (1970) 312-319.

[4.7] S. McAllister, I. Grenfell, A. Hadlow, W.M. Jolly, M. Finney, J. Cohen. Piloted ignition of live forest fuels. Fire Safety Journal, 51 (2012) 133-142.

[4.8] J.G. Quintiere. Fundamental of Fire Phenomena. John Willey and Sons, Hoboken, NJ, USA, 2006.

[4.9] N.J. de Mestre, E.A. Catchpole, D.H. Anderson, R.C. Rothermel, Uniform Propagation of a Plana Fire Front Without Wind. Combustion Science and Technology 65 (1989) 231-244.

[4.10] N. Bal, J. Raynard, G. Rein, J.L. Torero, M. Försth, P. Boulet, G. Parent, Z. Acem, G. Linteris. Experimental Study of Radiative Heat Transfer in a Translucent Fuel Sample Exposed to Different Spectral Sources. International Journal of Heat and Mass Transfer. 61 (2013) 742-748.

[4.11] M. El Houssami, J.C. Thomas, A. Larmorlette, D. Morvan, M. Chaos, R. Hadden, A. Simeoni. Experimental and Numerical Studies Characterizing the Burning Dynamics of Wildland Fuels. Combustion and Flames 168 (2016) 113-126.

[4.12] V. Tihay, A. Simeoni, P.A. Santoni, L. Rossi, J.P. Garo, J.P. Vantelon. Experimental Study of Laminar Flames Obtained by the homogenization of Three Forest Fuels. International Journal of Thermal Science 48 (2009) 488-501.

[4.13] F.P. Incropera, D.P DeWitt, T.L. Bergman, A.S. Lavine, Principles of Heat and Mass Transfer, John Wiley and Sons Ltd., Singapore, Singapore, 2013.

[4.14] P. Bartoli, A. Simeoni, J.L. Torero, P.A. Santoni. Experimental Study on the Combustion Dynamics of Forest Floor Fuel Beds. Proceedings of the 7th Interational Conference on Forest Fire Research. Coimbra, Portugal (2010).

[4.15] J.C. Thomas, J.N. Everett, A. Simeoni, N. Skowronski, J.L. Torero. Flammability Study of Pine Needle Beds. Proceedings of the 7th International Seminar on Fire and Explosion Hazards, Providence, RI, USA, (2013).

[4.16] B. Benkoussas, J.-L. Consalvi, B. Porterie, N. Sardoy, J.-C. Loraud. Modelling thermal degradation of woody fuel particles. International Journal of Thermal Science 46 (2007) 319-327.

[4.17] A. Zukauskas. Heat Transfer from Tubes in Crossflow. Advances in Heat Transfer 8 (1972) 93-160.

[4.18] F. Kreith, R.M. Manglik, M.S. Bohn. Principles of Heat Transfer (7th ed.). Cengage Learning, Inc., Stamford, CT, USA, 2011.

[4.19] P.N. Dwivedi, S.N. Upadhyay. Particle-Fluid Mass Transfer in Fixed and Fluidized Beds. Industrial and Engineering Chemistry Process Design and Development. 16/2 (1977) 157-165.

[4.20] S.W. Churchill, H.H.S. Chu. Correlating Equations for Laminar and Turbulent Free Convection from a Horizontal Cylinder. International Journal of Heat and Mass Transfer, 18 (1975) 1049.

[4.21] F.A. Albini. Wildland Fire Spread by Radiation – a Model Including Fuel Cooling by Natural Convection. Combustion Science and Technology 45 (1986) 101-113.

[4.22] J.Torero. SFPE Handbook of Fire Prevention Engineering – Flaming Ignition of Solid Fuels. 5th ed. Society of Fire Protection Engineers, London, UK, (2016).

[4.23] W.J. Minkowycz, A. Haji-Sheikh, K. Vafai. On the Departure from Local Thermal Equilibrium in Porous Media due to a Rapidly Changing Heat Source: the Sparrow Number. Internation Journal of Heat and Mass Transfer 42 (1999) 3373-3385.

*This page is intensionally left blank.*

# Chapter 5

## *Flammability Assessment of Conditioned Live Foliage – Seasonal Trends of Ignition and Burning Behavior*

## *5.1. Introduction*

The previous two chapters discussed in length various factors influencing the flammability (ignition and burning behavior) of dead pine needles. In the following two chapters, focus is directed to live foliage, that is present in the forest canopy, rather than on the ground (dead fuel). As outlined in Chapter 1, the ecosystem of interest is the New Jersey Pine Barrens, USA. Foliage studied herein (and Chapter 6) is Pitch pine (*Pinus rigida*). It was discussed in Chapter 1, that the state of growth/decay of foliage can be associated to seasonality of the chemical composition, on the account that it is living organisms. This has inherent effects on the properties of the particles which impact the ignition and burning behavior (e.g. [5.1-5.3]).

Later, Chapter 6, explores the impact of fuel moisture content (*FMC*) on the flammability, which also varies with season [5.1, 5.4-5.8]. However, in this chapter, all experimentations were conducted at 0% *FMC*. It is assumed that, seasonal trends are best investigated in the absence of water, because it has inherent effects on fuel properties, as well as fundamental mechanisms that drive ignition and burning behavior (heat and mass transfer).

### *5.1.1. Live fuel flammability assessment*

Flammability in solid material, specifically for polymers, can be considered constant (with time) because the material is stable and will not degrade significantly over time. But for wildfire fuel, this is not necessarily the case, as was discussed in Chapter 1. The flammability assessment discussed in this work has two significant implications: (1) it explores the possibility of an accumulative live fuel flammability factor (for one or multiple foliage generations) and (2) tracks the evolution of the flammability throughout a typical growth cycle. The former, is a novel methodology for quantifying and comparing flammability of individual plant species. The latter will allow the correlation of live fuel flammability to typical fire seasons for a given region (NJ Pine Barrens in this case).

The following formulation of a total live fuel flammability factor, $F_{total}$, is proposed:

Herein, the notation "OG" refers to old generation needles that grew in 2013 (or earlier) and "NG" refers to new generation needles that grew in 2014. The variables $t_{ign}$, $t_{ign,min}$, $\dot{q}''$ and $\dot{q}''_{max}$ are obtained experimentally from FPA combustion experiments. Scaling of two flammability parameters (ignitibility: $F_{ign}$ and combustibility: $F_{comb}$) allows the direct comparison of each one and quantification of a total flammability, on the scale of zero to one; unity refers to the highest level of flammability, zero to not flammable at all.

The total flammability of live foliage is the weighted average of individual flammability components of each foliage generation currently present, here, $F_{og}$ and $F_{ng}$; individual flammability is in turn defined by a number of flammability parameters, which in this work are, ignitibility and combustibility. Thus,

$$F_{total} = w_{og}F_{og} + w_{ng}F_{ng} \quad \textbf{Eq. 5.1}$$

where

$$0 \leq w_{og} \leq 1 \quad \textbf{Eq. 5.2}$$

$$1 = w_{og} + w_{ng} \quad \textbf{Eq. 5.3}$$

$$F_{og} = \frac{1}{2}\left(F_{ign} + F_{comb}\right)_{og} \quad \textbf{Eq. 5.4}$$

$$F_{ng} = \frac{1}{2}\left(F_{ign} + F_{comb}\right)_{ng} \quad \textbf{Eq. 5.5}$$

Flammability parameter, $F_{ign}$ and $F_{comb}$, are defined as the normalized ignition time (piloted) and peak heat release rate (pHRR):

$$F_{ign} = t_{norm} = \left( \frac{t_{ign}}{t_{ign,\min}} \right)^{-1} \quad \textbf{Eq. 5.6}$$

$$F_{comb} = \dot{q}''_{norm} = \frac{\dot{q}''}{\dot{q}''_{max}} \quad \textbf{Eq. 5.7}$$

Weighting coefficients, $w$, represents the distribution of OG and NG foliage in the total fuel loading and requires appropriate determination, for example by physical measurements of the canopy fuel loading. In the winter and early spring only OG needles are present, thus, $w_{og} = 1$. When OG and NG needles coexist, $w_{og} < 1$. At the end of the year, OG needles disappear and only NG needles remain, $w_{og} = 0$. Remark: the discussion assumes that all OG needles will disappear and not remain on the tree. It is possible that multiple generations stay on the tree [5.9, 5.10].

### *5.1.2. Goals and objectives*

The goal in this chapter is to assess the flammability in terms of ignition and burning behavior of live, fully dehydrated foliage and determine any seasonal trend. It was desired to determine if live fuel flammability correlates with the occurrence of a typical fire season. A novel framework for live fuel flammability assessment is developed, which can also be used for fuel classification. This is achieved by conducting combustion tests over the period of one year. Variations in flammability are linked to ignition time and heat release rate results from combustion tests, and were obtained for two needle generations (young growing and mature). Finally, the monthly live fuel flammability assessment is compared to historic fire data to evaluate any correlation.

### *5.1.3. Chapter layout*

To achieve this, combustion experiments are carried out using the FPA over the period of one year. Specifications of test set-up, methodologies, fuel/sample properties, and critical parameters are discussed in Section 5.2. Results of the experimentation are analyzed in Section 5.3, which is divided into the relevant flammability parameters, ignitibility and combustibility. Finally, the live fuel flammability assessment, as proposed by Eq. 5.1-5.7, is evaluated in Section 5.4. In this section, the total live fuel flammability evolution is then compared to NJ's fire history (from Chapter 1) in order to determine any correlation between live fuel flammability and the timing of the fire season.

## ***5.2. Experimental description and critical parameter***

The study was conducted over a time period from April 2014 to April 2015. Pine needles were collected in New Jersey (NJ), USA (39°57'38.6"N 74°37'37.0"W) on a monthly basis. The needles were collected in sealed zip lock bags, placed in coolers with sufficient ice packs to keep them cold for the duration of the shipping to the University of Edinburgh, Edinburgh, UK. This time period was between 2 and 5 days. After arrival, the needles were visually inspected. For all shipments, no significant degradation was visible and the cooling packs were still cold. A sample of needles was taken for *FMC* measurements immediately after arrival. The remaining stock was stored in a refrigerator that was kept at 6-9 °C until further testing was conducted.

Coniferous plants can carry a number of generations of foliage [5.9, 5.10], depending on species, climate, geographic factors, and stress levels (disease or drought). In this study only distinction was made between two generations (OG and NG). New needles (NG) start to emerge in spring (June) and grow throughout the summer months (July-August) and mature in the fall. Aalto et al. [5.11] suggested that the time period of new needle growth is about 100 days, which agreed with visual observation (main growth

period was from June to August). In the following year they are fully mature and become that years old generation (OG) when that year's new generation needles emerge. The OG needles degrade in the fall months. For the case studied here, OG needles started to show extensive degradation (yellowing) in October. November collection included a large fraction of dead (yellow) OG needles. For the purpose of this study, only green needles were considered as "live" foliage. Needles with extensive decays where not used in order to minimize unquantifiable variability.

Experimentation was carried out using the FPA, with the same protocol as outlined in Chapter 2. Some critical aspects that were not addressed in Chapter 2 are now discussed. This include a more detailed explanation of the needle density, a spectral analysis, and a thermal analysis according to findings from Chapter 4.

### *5.2.1. Fuel/Sample properties and test conditions*

The fuel used was live Pitch pine needles (*Pinus rigida*, PRI). All samples were oven dried at 60 °C for 24 hours to reduce the *FMC* to 0%. PRI needles were found to have a *SVR* of 4,776 $m^{-1}$. This was the case for growing NG needle as well. Although the length of the needle varied as they grew. The apparent needle density was closely monitored over the test period. A detailed analysis of this property is given in Section 5.2.2.

Only open sample baskets (12.5 cm diameter, 3.0 cm deep) were used in order to reduce any influence that arises from a ventilation controlled scenario (See Chapter 3 for discussion on ventilation controlled scenario). Fuel and sample properties are summarized in Table 5.1.

Sample mass was kept constant at 13.9 g, which was chosen because it reflects similar loading conditions than samples tested in previous chapters. This resulted in a fuel loading of 1.11 $kg.m^{-2}$ (bulk density: 37 $kg.m^{-3}$) and a porosity between 95-96% depending on the particle density. It is critical that this is kept constant, because the

fuel loading has an effect on the heat and mass transfer mechanisms inside the fuel matrix, which influence the combustion dynamics [5.12-5.15]. It has less of an effect on the ignition behavior in the range of porosities tested, as was concluded by both Bartoli [5.13] and Jervis [5.12].

Table 5.1. Summary of fuel and sample properties (PRI needles).

| Type | Collection Data | FMC | Dry Density | Sample Mass | Bulk Density | Porosity |
|---|---|---|---|---|---|---|
| | | [%] | [kg.m$^{-3}$] | [g] | [kg.m$^{-2}$] | [%] |
| OG | 17/04/2014 | 111 | 744.6 | 13.9 | 1.11 | 95.02 |
| | 07/05/2014 | 97 | 763.5 | | | 95.14 |
| | 02/06/2014 | 119 | 778.8 | | | 95.24 |
| | 07/07/2014 | 119 | 802.6 | | | 95.38 |
| | 04/08/2014 | 112 | 787.3 | | | 95.29 |
| | 27/08/2014 | 112 | 767.2 | | | 95.17 |
| | 05/10/2014 | 108 | 835.5 | | | 95.56 |
| | 29/10/2014 | 98 | 815.8 | | | 95.46 |
| NG | 07/07/2014 | 191 | 974.3 | 13.9 | 1.11 | 96.20 |
| | 04/08/2014 | 162 | 979.0 | | | 96.21 |
| | 27/08/2014 | 144 | 1036.9 | | | 96.43 |
| | 05/10/2014 | 127 | 953.8 | | | 96.11 |
| | 29/10/2014 | 113 | 884.8 | | | 95.81 |
| | 04/12/2014 | 114 | 817.7 | | | 95.47 |
| | 17/04/2015 | 103 | 779.1 | | | 95.24 |

The flow condition was always natural convection. A forced flow condition improves the ventilation condition, but it also increases influences of convection cooling (See Chapter 4 for discussion on convection cooling). It was desired to keep these minimal.

The heat flux was kept constant at 25 kW.m$^{-2}$. At high heat flux levels, approximately > 50 kW.m$^{-2}$, ignition occurs fast, ~ 10 s [5.2, 5.16] (see also Chapter 3). This is not ideal, because it might not be possible to observe any flammability variation due to changing chemical composition, as was the case in [5.2] (small variability of ignition

time for dried needles). The ambient oxygen concentration was normal at 20.95% by vol., and no quartz tube was used.

### *5.2.2. Particle density*

Analysis of this property deserved a detailed discussion, because it was monitored over the test period. Intensions were to explore if it can be used as an indicator for changes in chemical composition and correlate it to flammability parameters (ignition time and heat release rate). Furthermore, density is monitored, because it is often an important input parameter for physical models (e.g. [5.17-5.20]). These usually assume a constant value, and understanding of the dynamics of this parameter will improve accuracy of such models in the future. Measurements were done for each stock (shipment) upon arrival. It was obtained as outlined in Chapter 2 (liquid submersion technique).

#### Influence of conditioning technique

It is acknowledged [5.21] that conditioning vegetative fuel can change the chemical composition, because some essential oils contained in the needle can evaporate at low temperatures [5.22, 5.23]. For some insight of the impact of the conditioning process, samples from June (OG) were conditioned in ambient air for several days until they reached a *FMC* of approx. 7%. This point was chosen because they did not lose any further mass. Also, dead pine needles kept in ambient air in the lab (condition in the lab: 15-25 $^{o}$C and 15-40% relative humidity) typically had a *FMC* of around 7%. At this point the density was measured (unconditioned "air-dried"). A subset of these "air-dried" needles was conditioned in the oven. At the same time, density was measured from unconditioned "as is" and immediately conditioned "as is" needles. The results of this comparison are given in Fig. 5.1.

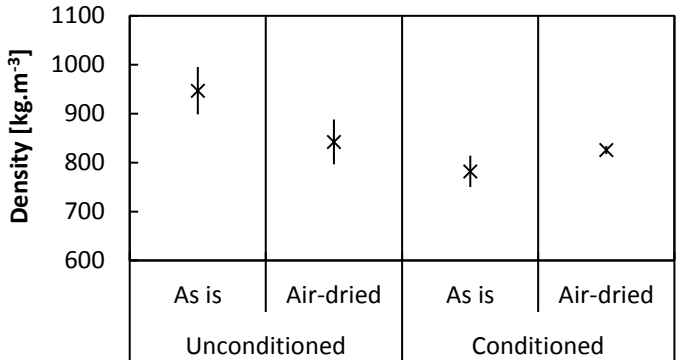


**Fig. 5.1. Comparison of density measurements of June needles (OG) at various conditioning.**

Unconditioned "as is" needles show the highest density. This is due to the *FMC*, which was between 108 and 118% for this stock. It should be noted, that the density is almost 1,000 kg.m$^{-3}$, which corresponds to the density of water. The conditioned "as is" needles show the lowest density (780 kg.m$^{-3}$). The "air-dried" density is similar for conditioned and unconditioned (825 to 842 kg.m$^{-3}$).

If one considers that the conditioning at elevated temperatures evaporates essential oils in the needle it is logical that the unconditioned "air-dried" needles have higher densities than the conditioned "as is" needles: transpiration of water at ambient temperature, with minor evaporation of extractives (e.g. essential oils); contrarily, at elevated temperatures, evaporation of extractives is increased.

It was surprising to see that the density did not reduce when the unconditioned "air-dried" needles are also conditioned. It is likely, that certain chemical compounds (e.g. resin) harden during the air-drying period, and therefore changing their molecular structure. Once hardened, these components will not evaporate when dried in the oven, which could explain the difference in apparent density of conditioned "as is" and "air-dried" needles. The hardened compounds are still present in conditioned "air-dried" needles but were evaporated in the conditioned "as is" needles.

Whatever the reason for this variation in density, it is assumed, that the apparent density measurements for conditioned "as is" needles is an under-estimation. These

are the measurements used throughout this chapter. Because the conditioning is done in the same manner throughout the entire study this has little influence on the trends, but Jervis and Rein [5.21] have shown that drying induces a degree of thermal degradation that affects the combustion dynamics of pine needles.

### Apparent dry needle density history

Overall, it was observed that, live oven dried NG needles can have significantly higher density than OG needles. Although there is some variation for OG needles, it is small compared to the variation of NG needle density. The evolution of ρ over the test period is plotted in Fig. 5.2 (*FMC* history is given as reference). A summary of some averaged values and standard deviations is provided in Appendix C1, including a measurement of dead needles, which was found to be the lowest value.

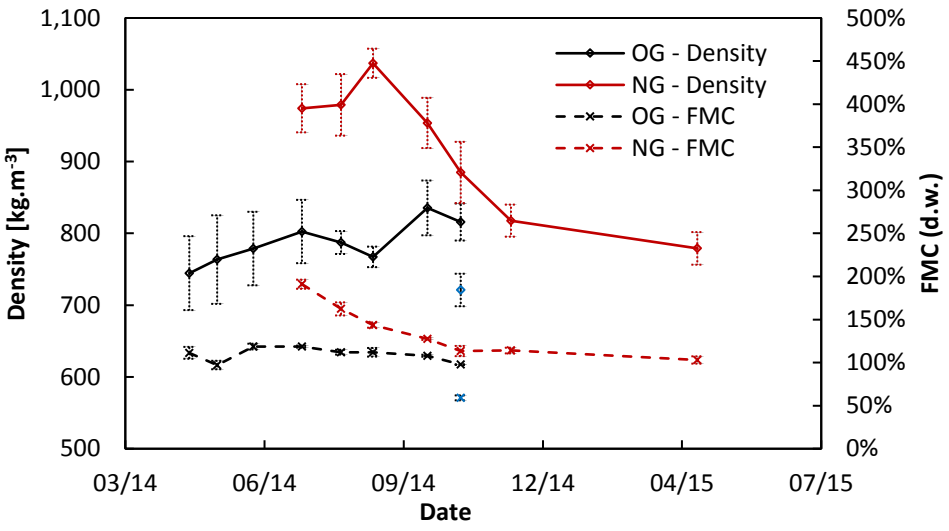


**Fig. 5.2. Seasonality of apparent density and live *FMC* of OG and NG needles (live oven dried). Blue markers in November refer to density/*FMC* measurements of just dead OG needles (from tree). Dead PRI needles (collected from ground) have a dry density of 610 +/- 10 kg.m$^{-3}$.**

#### *OG needles*

The lowest value for OG occurs in April 2014 and increases until July, which marks the beginning of significant NG needle growth. At this point, the density reduces until

September. The reasoning for this reduction in density is likely the allocation of plant resources that are required for the growth of the NG needles, which has been described by Jolly et al [5.1].

Jolly et al. [5.1] (and others [5.4-5.7]) explained that the spring dip (SD) is identified by a minimum *FMC* of live foliage, occurring after the break of dormancy. It is explained that this is not only due to low water content, but also due to an increase of the solid mass. This has the same effect as a reduction of water mass.

This conclusion is not fully supported by the results found here. The density of dried OG needles (Fig. 5.2) continuously increases from April till July. If the conclusion of [5.1] was accepted, a peak density of OG needles should be visible during the SD, which occurred in May of that year (See "OG – FMC" in Fig. 5.2). The current results do agree with the conclusion that OG needles gain mass due to the storing of plant resources, before the start and during the initial growth period of NG needle. This correlates to the slight increase in density during this phase (assuming OG needles will not grow in size). At the same time, the *FMC* (Fig. 5.2) is relatively constant, except in May when the SD takes place. It can be concluded, that the SD is due to the combined effects of water loss and gain of dry mass, although the exact mechanism cannot be explained with this data.

OG needles show a reduction in dry density during NG growth period (July-September). But after September, OG needle density increases to a maximum recorded value of 835 $kg.m^{-3}$ (mean value) in October. It is not certain why this occurs. Further fuel characterization would be required to identify the reason for the sudden increase. Such rise was not observed by Jolly et al [5.1], which suggests that, chemical composition is not the cause. After this time, significant decay of the needles becomes visible by the change in pigmentation (yellowing). Yellowing of the needles is common until November, when a large percentage of the needle stock is fully yellow (dead). Distinction between still live and dead needles is made for the density

measurements. It can be seen, that the density of dead needles (November: lower value) is significantly lower than live needles (November: high value)

*NG needles*

NG needles start to grow in June (first sample collected in early July) and have a high density compared to OG needles. Throughout the summer, the density increases even further before reducing in the fall. In the fall and winter, the needles complete their maturing process, during which the density decreases to converge with the density of mature OG needles.

Aalto et al [5.11] collected data on NG needle growth of Scots pine (*Pinus sylvestris L.*) from 2009 until 2011. The purpose of their study was to evaluate seasonal variation and the contribution of new generation needles to VOC (volatile organic compound) emissions. Interestingly, this study also monitored shoot and needle elongation rates. They observed that needle growth rate (length) is not constant. Elongation rates (millimeter per day) increase from early growth stage until a peak rate of around 2 $mm.d^{-1}$. After this peak, the rate decreases until the needles reach their final size.

A growth rate for the mass is not available for obvious reasons; however, it may be assumed that it will follow a trend similar to the elongation rate. Theoretically, a constant needle density through the growing phase can be achieved with proportional mass and elongation growth rates. The variable NG needle density in Fig. 5.2, suggest that this is not granted at all times.

In the early stage of growth (July to August) rates can be assumed proportional, resulting in constant density. During the months of August and September, the elongation rate slows down. At the same time, needles still gain mass, but at a faster rate than growing in size; which forces a disproportionality of the two rates, and thus causes the density to change (increase). This concurs with a high NG needle density in September (maximum: 1,037 $kg.m^{-3}$). In the fall, no more elongation takes place,

and it is likely that at the same time the needle experience a mass loss rate, which again results in a change (decreasing) in density. A comparison of the NG needle density to OG needle density in this time suggests that, the mass loss experienced by NG needles is a mass gain for OG needles, because their density increases in this time period. This shift suggests an allocation of plant resources in preparation of the upcoming dormancy period. However, this is not supported by observations of chemical composition found by Jolly et al [5.1] and their respective species. Further investigation is required to fully understand the tendencies of the density.

NG needle density tendency is significantly different to what Jolly et al [5.1] reported for Jack (*Pinus banksiana*) and Red (*Pinus resinosa*) pine needles. They found that young NG needles have lower densities than OG needles. As they grow, density increases until the needles are matured at which point the density matches the one from OG needles. Slight differences due to density calculations between this work and [5.1] can be expected. Here, the density is calculated for the dry mass and dry volume, whereas in [5.1] the density was calculated for the dry mass over the wet volume. It can be assumed that some shrinkage will cause the volume of the needle to reduce, resulting in higher density values when the dry volume is used. In either case, the density is more appropriately interpreted as an "apparent" density, because the needle itself is porous. The reason for the differences in tendencies are yet unknown. Further investigation is required to fully understand the seasonality of the density.

*Visual observations*

The experiments done to measure the density were performed with methanol, which has a density of approximately 782-801 $kg.m^{-3}$ (at temperatures, 30 and 10℃, respectively) [5.24]. When submerging OG needles it was observed that they float. Young NG needles, on the other hand, sink. When NG needles are matured they also start to float. This observation alone, depicted in Fig. 5.3, verifies that the results of

density measurements given here are in a physically reasonable range (Table 5.1 and Fig. 5.2).

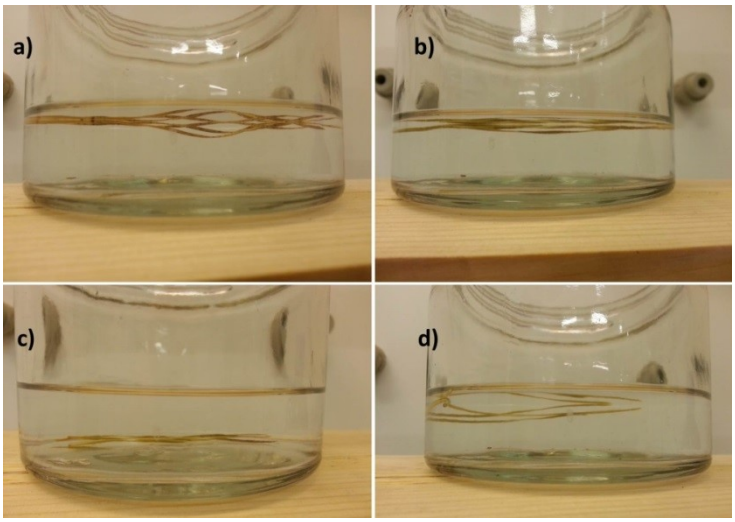


**Fig. 5.3. PRI needles submerged in Ethanol (~789 kg.m$^{-3}$). a) dead, b) August OG, c) August NG, and d) April '15 NG; Young live needles sink, mature and dead needles float.**

### Influence of needle porosity and composition

*Influence of needle porosity*

Needle porosity is a likely mechanism that causes the NG needle density to decrease during the maturing period in the fall. A relationship between apparent density and porosity of various plant fibers was illustrated by Mwaikambo et al [5.25], who illustrated a significant difference between absolute and apparent density.

Both densities were determined by the Archimedes method. The absolute density measurements used gas (Helium) submersion, and the apparent density was determined by submersion in Benzene [5.25]. The difference being that, Helium penetrates into the pore space of the fibers, whereas, Benzene does not (or only limited). Therefore, the apparent density measurements will vary depending on the porosity of the material. If the porosity is high, the apparent density will be

significantly lower than the absolute density. This suggests that, NG needle porosity is initially low and increases as they mature.

*Composition of the needles*

The following discussion is an illustration of the needles as a composite material. A needle can be considered a composite material made up from cellulose, lignin, hemicellulose, resin, tars, and extractives (for example, essential oils and waxes). Each component has an individual mass fraction of the total mass of the needle, which is unknown in the present work. This principle can be extended to the density of each component and a total equivalent density can be estimated (weighted with appropriate mass fraction). For the above mentioned components, densities are given in Table 5.2.

Table 5.2. Some major chemical compounds found in pine needles.

| Component | Density [g.cm$^{-3}$] |
|---|---|
| Cellulose [5.25] | 1.5 |
| Hemicellulose [5.26] | 1.5 |
| Lignin [5.26] | 1.3 |
| Resin [5.27] | 1.1 |
| Tar [5.27] | 1.0 |
| Paraffin wax [5.27] | 0.9 |

Without knowing the mass fraction of each of these components, one can see that the equivalent density has to be between 0.9 and 1.5 g.cm$^{-3}$, without considering porosity. The porosity of the needle causes some reduction of density (thus the use of 'apparent') in comparison to the actual density. This needle porosity is a function of maturity and species (porosity increases with maturity). Therefore, it can be concluded that apparent densities given here are under-estimations of the true density.

### *5.2.3. Spectral behavior of dead and live PRI needles*

The absorptivity of the needles is one important parameter that was evaluated in detail, because the test apparatus heating lamps operate on a very specific spectral band. The

importance is associated to the ability of the foliage to absorb the radiant energy, which must be quantified. Various authors [5.28-5.30] have highlighted the importance of knowing the spectral regime of the radiant source in conjunction with dead and live vegetative fuels, because the absorptivity of such fuels is highly dependent on wavelength. These studies, however, did not capture the full range in which the FPA operates (mainly below 2 μm).

A full spectral analysis was performed on dead and live needles (OG) to obtain the absorptivity as a function of temperature as was first done by Chaos et al for wood [5.31]. A similar analysis was performed by Dr. Chaos at FM Global for PRI needles. The full report is given in Appendix C2 and only the results are shown in Fig. 5.4. El Houssami et al discussed the spectral analysis of dead needles in [5.20] with the same methodology, where a numerical investigation of the combustion dynamics of forest fuel beds is compared to experimentation done with the FPA.

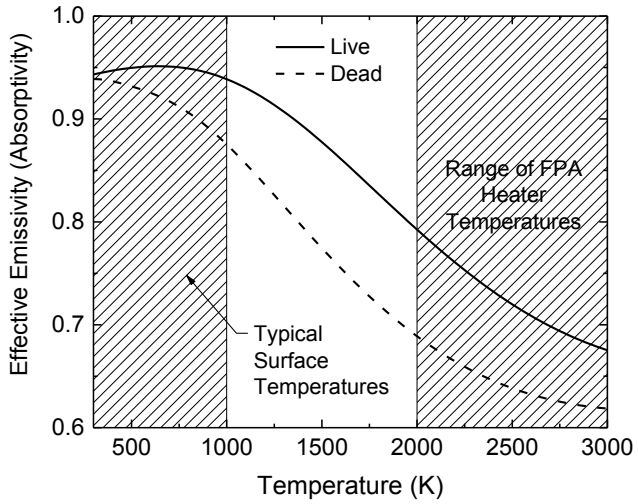


**Fig. 5.4. Dead and live PRI needle absorptivity/effective emissivity as a function of temperature (see Appendix C2 for detailed analysis).**

In the range of FPA operating temperature, live needles have a mean absorptivity of 0.72 and dead needles 0.64. The graph in Fig. 5.4 also shows that the effective emissivity of dead and live needles at typical surface temperatures varies slightly. For live needles the mean effective emissivity is 0.95 and dead needles 0.92. From a heat

transfer perspective, this means that, live foliage absorbs radiant energy more efficiently compared to dead foliage. But also has higher heat losses due to re-radiation. These results suggest (ignoring other effects) that, if external radiation is sufficiently high to overcome heat losses (re-radiation and convective), live needle ignite faster than dead needles (0% *FMC*).

### *5.2.4. Thermal behavior of dead and live PRI needles*

In Chapter 4 the thermal behavior of pine needles was discussed in detail. It was concluded, that a thermal boundary layer that describes both radiant and convective heat transfer will provide the best estimation of the thermal behavior of the needle.

The thermal response of a material to heat depends on the thermal mass ($\rho c_p$). Density measurements summarized in Table 5.1 and discussion in Section 5.2.2 illustrate that, this property is not constant, most likely due to changes in composition over the year (another factor is the porosity of the needle). Specific heat was not monitored over the test period, but it is likely that it also change over the year. In the calculations below, thermal conductivity and specific heat were estimated with constant values found for dead needles.

The initial step is to determine the thermal behavior, thin or thick, of PRI needles by calculating the Biot number (Bi). The calculation follows the methodology of Chapter 4, considering radiant heating with convective and reradiative cooling ($Bi_{rad,losses}$). The flow regime is a buoyancy driven one assuming the convective Froude number ($Fr$) is less than 0.1. Therefore, one can approximate the convective heat transfer coefficient ($h_c$) as the one from a hot horizontal plate (See Chapter 4 “Natural Convection”). A total heat transfer coefficient can be calculated from convective ($h_c$) and radiative ($h_r$) coefficients, $h_T = h_c + h_r$. Results from the analysis are summarized in Table 5.3.

Table 5.3. Particle properties and thermal analysis of dry PRI needles.

| | PRI (dry) |
|---|---|
| $a$ [--] | 0.72 |
| $T_{ig}$ [°C] | 300 |
| $\sigma$ [$m^{-1}$] | 4776 |
| $\rho$ (OG dry) [$kg.m^{-3}$] | 787 |
| $c_p$ (dead)[$kJ.kg^{-1}.K^{-1}$] [5.32] | 2.07 |
| $h_T$ [$W.m^{-2}.K^{-1}$] | 23.2 |
| $k$ (dead) [$W.m^{-1}.K^{-1}$] [5.34] | 0.112 |
| $\alpha$ ($x10^{-8}$) [$m^2.s^{-1}$] | 6.88 |
| $\dot{q}''_{ext}$ [$kW.m^{-2}$] | 25 |
| $Bi_{rad,losses}$ [--] | 0.077 |
| $Fr$ [--] | < 0.1 |

Ignition temperature was estimated as 300 °C, which is a common temperature used in literature [5.57] and measurements for two species (see Chapter 4) suggested that this is a realistic value; although species differences do exist. The surface-to-volume ratio ($\sigma$) and $\rho$ were found as outlined in Chapter 2. Specific heat was determined according to ASTM E1269 [5.33] by an external laboratory (Thermophysical Properties Research Laboratory, Inc) [5.32] and is an averaged value between ambient and 200 °C. Thermal conductivity is estimated as the value determined by Tihay [5.34] for dead pine needles (*Pinus halepensis*).

Calculation of $Bi_{rad,losses}$ indicate that these needles have a thermally thin behavior under the given heating and cooling conditions ($Bi_{rad,losses}$ < 0.1). A semi-infinite assumption is appropriate if the Fourier number ($Fo$) is less than 0.2 [5.35, 5.36]. This threshold corresponds to a time of 0.13 s; effectively, a constant internal thermal profile can be considered instantly.

Thus, a *lumped capacitance method* [5.35] (single temperature for particles) will provide an accurate estimation of the thermal evolutions under the given heating rate. The procedure is outlined in Chapter 4, to which the reader is referred. Four values for particle densities were evaluated to illustrate impact on the needle temperature

evolutions. The four densities are: (1) a value for dead OG needles, (2) an average value for all OG needles, (3) an average value for all NG needles, and (4) the highest value measured for NG needles. These are summarized in Table 5.4. Additionally, the thermal mass is reported.

Table 5.4. Selected apparent densities and thermal diffusivities of PRI needles used in the analysis of the thermal behavior.

| | OG, dead | OG, live, avg. | NG, live, avg. | NG, live, high |
|---|---|---|---|---|
| $\rho$ [kg.m$^{-3}$] | 721 | 787 | 918 | 1,036 |
| ($\rho c_p$) [kJ.m$^{-3}$.K$^{-1}$] (x10$^3$) | 1.49 | 1.63 | 1.90 | 2.14 |

The normalized solid temperature evolution ($\theta$*) of the particle is plotted in Fig. 5.5 (1: initial temperature, 0: equilibrium temperature). The analysis shows that, needles with higher densities heat up slower when subjected to a heat source, because the thermal mass of these particles is higher. This is traditionally described as the solid ignition theory for thermally thin material ($t_{ig} \propto \rho$) [5.37-5.39].

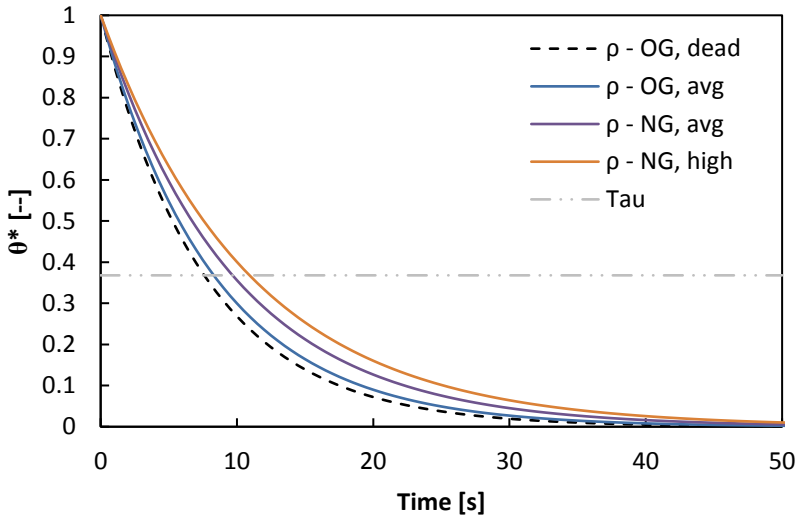


**Fig. 5.5. Thermal evolution of PRI needles with varying apparent density under given heating condition. Tau is the thermal time constant (See Chapter 4).**

The analysis suggests two things: (1) live OG needles should ignite slower than dead needles; (2) that overall, NG needles should ignite slower than OG needles, because

their density is higher; and (3) it preludes that, ignitibility of both OG and NG will have seasonality, based on the changing density (Table 5.4).

Jolly et al. [5.1] concluded that, ignition of live foliage (unconditioned) is inversely proportional to the density, which contradicts typical solid ignition theory. It will be evaluated if results obtained from this study follow a similar trend. If this is true, other properties ($k$ or $c_p$) will be the driving factors in the heat transfer mechanisms, rather than the particle density. Suggestion (1) of the thermal analysis is competing against the suggestion from the spectral analysis (faster ignition of live needles compared to dead). Therefore, a definite trend of the ignition behavior cannot be assumed at this point.

## *5.3. Seasonal trends of the ignitibility and combustibility*

The following section now discusses results of the combustion experiments. Results discussed in this section are the time to ignition and pHRR and are plotted against the collection date of the fuel.

### *5.3.1. Ignitability*

Conditioned samples are best used for the evaluation of chemical composition, because the *FMC* is reduced to 0%. The time to ignition results are plotted in Fig. 5.6, in which density is also given as a reference. Overall, significant seasonality of the ignitibility was observed for both, OG and NG needles, which was suggested by the spectral and thermal analysis of the needles. However, it is not evident that, live OG needles ignite slower than dead needles (ignition time: 39.2 +/- 6.5 s). Neither is it evident that, NG needles ignite slower than OG needles. Both behaviors were suggested by ignition theory. The results indicate the competing effects that were described from the spectral and thermal analysis of the needles.

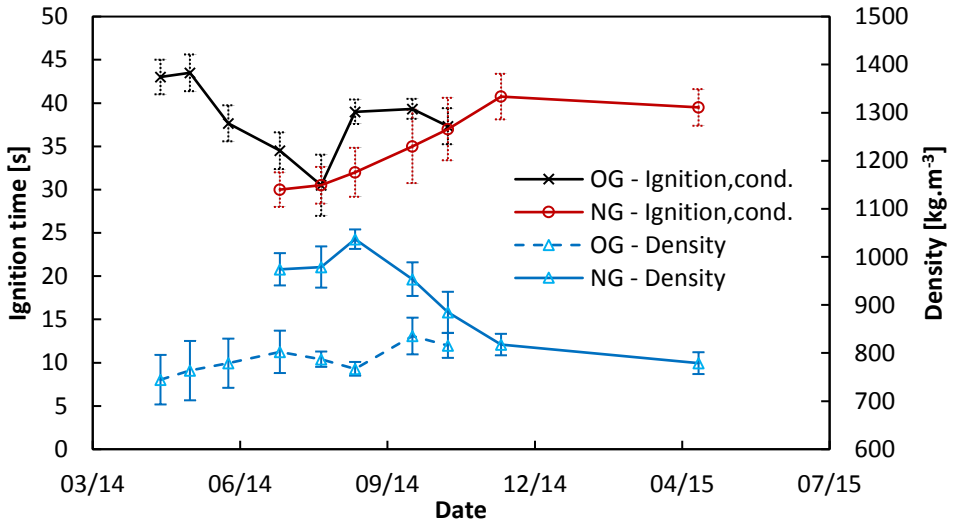


**Fig. 5.6. Seasonality of time to ignition of 0% *FMC* samples from April 2014 to April 2015. Density data is included for reference. Ignition time of dead needles (November): 39.2 +/- 6.5 s.**

### OG needles

OG samples in April and May 2014 show a similar ignition time. After May (which corresponds to the time of the spring dip) the ignition time starts to decrease until August, followed by an increase in September through November. The initial decrease indicates that the needles become more flammable, from an ignitability perspective, in this period.

It was suggested that in this period significant chemical changes can cause variation in the flammability [5.1], due to plant resource allocation. The ignition behavior certainly indicates a trend. However, this cannot be solely explained by the particle density, because NG needle emerge in June and time to ignition still reduces until August. Also, the change in density (increasing) is low.

Ignition times for OG needles in September through November are significantly higher than in August. This does not correspond directly to the change in density. However, the chemical composition might not be the only factor that influences the ignition at this point, because the density variations are relatively low.

At this time (September), needle absorptivity might start to become a significant factor. It was shown in Fig. 5.4 that, the absorptivity of dead and live needles varies significantly (in the spectrum of the FPA, dead needle absorptivity is lower than for live needle). Starting in late summer and fall, OG needles degrade while still attached to the branch. Although it was ensured that only green needles were used in the experimentation (due to the fact that absorptivity of dead yellow/brown and live green needles is different), degradation effects which are not visible to the naked eye are likely to occur.

The spectral analysis (Fig. 5.4) was done on live needles collected on (August 2014) and dead needles collected from the ground at the same time. Therefore, the exact dependence of the absorptivity as a function of the state of degradation is unknown. The only conclusion that can be made at this point is that the results shown in Fig. 5.4 can be described as the maximum (for live needle) and minimum (for dead needles) possible absorptivity.

The results suggest that the mechanism driving the change in ignition behavior after August is due to a combination of two effects: change in chemical composition, which alters particle properties (for example increased density), and change in surface absorptivity (lower absorptivity). It was however not possible to distinguish individual contributions with the current results.

**NG needles**

Young NG needles ignite fastest (July, Fig. 5.6). As they grow and mature, the ignition time increases until they are fully mature. The ignition behavior also does not follow the trends set by the particle density. Furthermore, it is contradicting the notion of solid ignition theory (e.g. [5.37]); time to ignition is proportional to the particle density. Similar observations were made from ignition tests conducted by Jolly et al [5.1]. According to the thermal analysis (Fig. 5.5) and the trends of the density, ignition times should increase in the period, July to September, and decrease after that. It also

indicates that young NG needles should ignite slower than mature OG needles. Results do not confirm either of these behaviors. Hence, it can be concluded that, apparent density is not governing the seasonality of the ignitibility. At first sight the results suggest that bulk properties might therefore be more important than particle properties. However, the bulk properties where kept constant in this test series, therefore, it must be particle properties.

Other parameters that might govern the seasonality are: (1) other fuel properties, such as specific heat, and absorptivity, but also (2) the ability of the needle to release gases, such as pyrolysis gases.

Spectral analyses of NG needles were not performed. It is likely that, young NG needles have lower absorptivity values compared to mature (OG or NG) needles, because they have a lighter shade of green, thus, reflecting/transmitting more of the radiation. A lower absorptivity increases the ignition time, because less energy is absorbed. This does not reflect the given tendency of the ignition time. It is however, assumed to be a small factor, because NG needles tested during the main growing phase, July-August, have indifferent ignition time: 30.0 +/- 2.0 s and 30.5 +/- 2.1 s, respectively.

A mechanism that can explain some of the ignition behavior of NG needles (and likely also for OG needles) is the ease at which gases can escape from the interior of the needle. As the needles evolve, structural changes (beyond the obvious elongation) occur and depend on environmental conditions [5.40]. Gas transport (mainly $O_2$ and $CO_2$) into and out of the needles (or any leaf) occurs through stomata (waxy layer prevents diffusion through cell wall), which are openings in the epidermis [5.9]. The plant regulates the time at which the stomata are open and closed in order to minimize the loss of excessive amounts of water [5.9]. Kouwenberg et al. [5.41] have illustrated that, the stomata density per unit area of the stomatal region (area of the needle where stomata are located), is highest in very young needles and decreases until fully mature.

This might suggest that the gas exchange (normally at ambient) can occur at an elevated rate when the stomata density is higher. This would also be the case under heating conditions where pyrolysis gases can escape the interior more freely. Finally, this would result in faster times to reach a flammable mixture and thus faster ignition.

An analogy can be made here to the orientation in which a piece of wood is heated up. When heated up along the grain, ignition times and critical heat flux were found to be lower (due to lower ignition temperature) compared to across the grain heating [5.38]. This is attributed to the less restricted transport of pyrolysis gases from the interior of the wood along the grain compared to across (also conductive heat transfer is different in each orientation).

Ideally, a comparison of mass loss rates of OG and young NG samples at the given heating conditions would be able to substantiate this hypothesis. Unfortunately, such data was not obtained from the combustion experiments. As a first approximation, this can, however, be substantiated from drying curves, which were obtained for several needle types. Such curves are given in Fig. 5.7 for August (a) and October (b) needles.

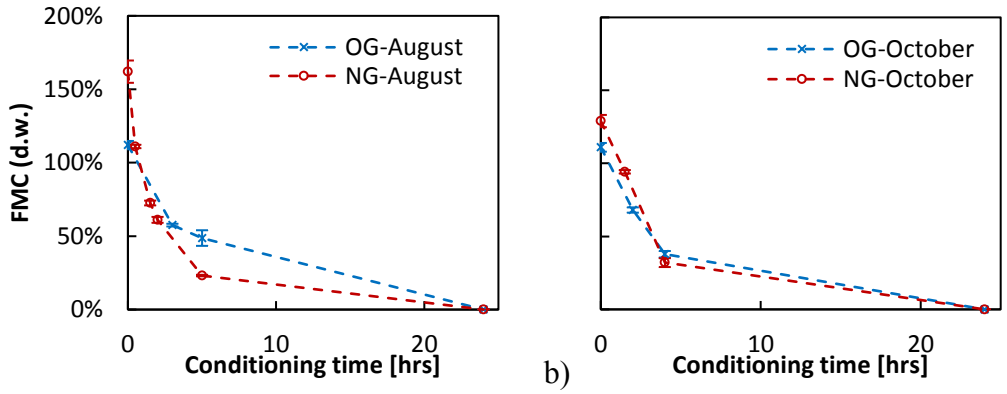


**Fig. 5.7. *FMC* after varying conditioning periods for needles collected in (a) August (b) and October. NG needles are immature.**

Young NG needles (Fig. 5.7.a) dehydrate faster than OG needles, which supports the notion that these needles may also release pyrolysis products at a faster rate. When NG needles mature (Fig. 5.7.b), the dehydration rate is similar to the one of OG needles.

Therefore, the hypothesis that young NG needles ignite faster due to a lower resistance to gas transport (release of pyrolysis products), can be accepted.

**Influence of heating rate**

A brief discussion on the heating rate is given here, because the ignition time is highly dependent on it (see Chapter 3 and 4). This discussion will evaluate the justification for conducting the tests at the given external heat flux.

McAllister et al [5.2] described a correlation between ignition time and FMC. However, they also tested fully conditioned live needles over a long time period. In their experimentation, dried needle samples did not indicate a significant influence of seasonality. Tests conducted in [5.2] were done with a similar heating system than tests done in this work (infrared heating lamps). But the external heat flux condition in [5.2] was 50 $kW.m^{-2}$, which was twice the intensity used to this work. It was shown in Chapter 3 and 4 that the ignition time is significantly influenced by the external heat flux. Therefore, the differences between the current work and results shown in [5.2] indicate that, seasonality of the ignition behavior of dry fuel can be suppressed by a high external heat flux. This is likely due to the rate at which pyrolysis gases are produced. When the heating rate is low, the pyrolysis rate is low and chemical composition of the pyrolysis gas mixture is important. Contrarily, at high heating rates, pyrolysis rates are high and the composition of the gas mixture becomes irrelevant.

This justifies the use of a lower heating rate when evaluating flammability characteristics, because the purpose of this work is to identify seasonality. Ideally, experimentation should be conducted for a range of heating rates in order to capture how the ignition behavior changes. During the test period, limitations of available resources (e.g. fuel) prevented this.

### Concluding remarks

Seasonal variation in the ignitibility was identified for both, OG and NG needles. However, the apparent needle density is not an appropriate descriptor of the variation (also see Appendix C3 where ignition time is plotted against apparent density). Although it is likely that a change in chemical composition is a factor as was determined by others [5.1-5.3], the results here indicated another mechanism might also play a role. That is the needles ability to release vapor from its interior. Furthermore, competing effects of thermo-physical properties on the solid particle temperature evolution are likely.

A summary of the experimental error is presented in Appendix C4. Density measurements have an uncertainty below 5% (standard deviation). Uncertainty in April, May and June (OG) are slightly elevated, which is attributed to human error (measurement technique). 5% is however an acceptable error for the particle density, considering the fuel is biomass.

Time to ignition measurements have a relatively high uncertainty, between 5-12%, which can be mainly attributed to the complexity of the ignition process of porous beds. A similar level of uncertainty was shown for the ignition of dead pine needle beds in Chapter 3. Some operator error is certain, but it is assumed to be low ($<< 1\%$) compared to the error associated to the ignition process. Minor uncertainty can be attributed to the porosity of the bed, because Bartoli [5.13] and Jervis [5.12] have demonstrated little influence in the tested range.

Detailed chemical analysis such as outlined in [5.1, 5.2] and evaluation of other fuel properties such as specific heat, thermal conductivity, or absorptivity could provide better understanding of the seasonality of the ignition behavior and should be included in future studies.

Furthermore, the true density of the material (excluding effect of needle porosity), measured by submersion in gas [5.25], is likely a more appropriate parameter to use. This parameter will likely reveal trends that are otherwise masked by the porosity of the needles. Such measurement technique requires additional equipment that was not available but is recommended for future evaluation.

### *5.3.2. Combustibility*

In this section, peak heat release rate (pHRR) obtained from oxygen calorimetry, as outlined in Chapter 2, is evaluated over the experimental period. Results were obtained for conditioned OG and NG needle samples (0% FMC) and are presented in Fig. 5.8. As was the case for ignitibility, significant seasonal trends of the combustibility for both needle generations were observed.

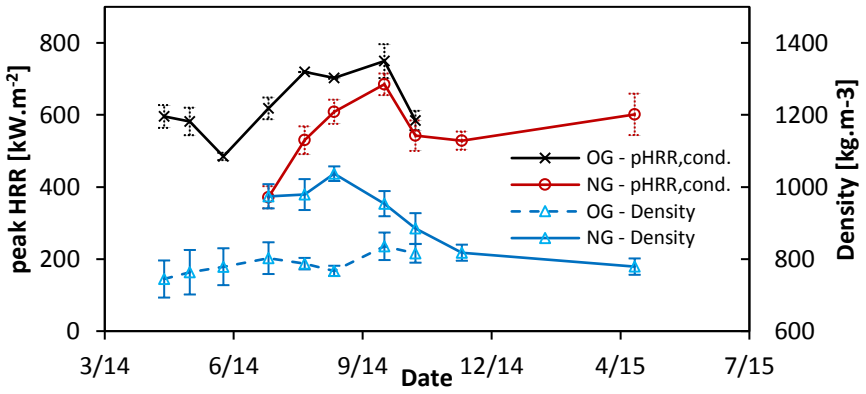


**Fig. 5.8. Seasonality of pHRR of 0% *FMC* samples from April 2014 to April 2015. Density data is included for reference. Peak HRR of dead needles (November): 604 +/- 22 kW.m$^{-2}$.**

#### OG needles

In the spring (April – May) the combustibility is moderate, followed by a reduction in later spring (June). The pHRR increases from June to August, followed by a relatively constant period over the summer and early fall months (until October). The highest value for pHRR was found in October. Finally, the pHRR decreases again in November as the needles decay.

**NG needles**

The lowest value for the pHRR was observed for young needles in July. Followed by a rise until October, where these needles reach a maximum. A sharp drop in the pHRR value occurs in November, followed by a slight rise until April 2015.

Neither trend from OG or NG follows the seasonal trend of the needle density, as was also observed with the ignition time. In the case of the pHRR, this is not a surprise, because the combustion reaction is a gas phase phenomenon. As was discussed in Chapter 3, it depends on several factors (predominantly the pyrolysis rate), but also the chemical composition. The results in Fig. 5.8 indicate a cyclical behavior linked to the growing season. The driving mechanism behind the cyclical behavior (seasonality) of the combustibility seems to be the chemical composition varying from spring to summer to fall. The combustion intensity is varied due to the change in flammability of the pyrolysis gas mixture, which originated from the fuel.

Experimental results obtained by Aalto et al. [5.11], can be interpreted to support this conclusion, in the absence of detailed chemical analysis of the fuel. Aalto et al [5.11] have linked significant rises in flammable volatile organic compounds (VOC) emissions to the growth season (for Scots pine). The release of VOCs depends on the chemical make up in the needles and thus hints that live foliage is more flammable during the time of increased VOC emissions. VOC emissions were measured at ambient temperature. At elevated temperature, created by a heat insult it can be assumed that, emissions of flammable VOCs intensify with the release of other combustible gases due to the degradation of the material. The elevated release of VOCs from the canopy fuel during the growing season can therefore be considered a relevant driver to the elevated combustibility of the fuel during this period. In fact, this might also be a factor that drives the faster ignition during the growing season.

Finally, it can be concluded that, in terms of combustibility, apparent density is not a suitable predictor of chemical variation in the fuel. This concurs with the discussion in

the previous section on ignitibility. As with ignitibility, comparing the density history to pHRR history does not indicate significant correlation (see also Appendix C3). Values of the uncertainty for the pHRR are listed in Appendix C4 and are below 10%. Such a level of uncertainty is acceptable, because of the overall complexity of the combustion experiments with the FPA (homogeneity of sample preparation, consistency of test conditions, measurements of various variables) and calculation technique (oxygen consumption calorimetry), as was discussed in Chapter 2 (e.g. see [5.42]).

### *5.3.3. Evolution of NG needles to OG needles*

It was shown in the previous sections that, mature NG needles (April 2015) are equivalent to OG needles in April 2014. A summary of the results, ignition delay and pHRR, of these two months is given in Table 5.5. Minor variation can be observed, and can be attributed to the fact that the fuel is biomass, and more so to the fact that seasonality (weather condition) has some variability in itself. In other words, the start of the spring is not always exactly on the same day of the year.

Table 5.5. Comparison of density, ignition time and pHRR results from April 2014 and 2015.

| | April | |
|---|---|---|
| | 2014 – OG data | 2015 – NG data |
| Ignition (st.dev) [s] | 43.0 (2.0) | 39.5 (2.1) |
| pHRR (st.dev.) [kW.m$^{-2}$] | 595.7 (32) | 601.6 (57) |
| Density (st.dev.) [kg.m$^{-2}$] | 744.6 (52) | 779.1 (23) |

The values for the flammability parameter and density allow the deduction of a full lifecycle of a needle from the data sets. In the following section, the data sets of OG and NG needles are coupled and a live fuel flammability assessment is formulated. Ignition time and pHRR are normalized such that a representation on a common scale is possible (Section 5.1.1).

## *5.4. Live fuel flammability assessment*

It was proposed in the introduction (Section 5.1.1) that, a total fuel flammability factor, including multiple flammability parameters, is most suitable to characterize the overall flammability of live foliage in order to capture varying seasonal trends from each parameter.

Furthermore, such a factor can be used to develop an improved fuel flammability classification system. The following analysis utilizes Eq. 5.1-5.7, given in Section 5.1.1 and is done in three stages: (1) each individual flammability parameter is compared for each generation (Section 5.4.1). (2) Individual parameters for one generation are combined to a single flammability factor for each generation (Section 5.4.2). (3) The flammability factors from each generation are combined to characterize a total flammability of the live foliage (Section 5.4.3). This is then related to historical fire data for the NJ Pine Barrens in order to evaluate, if live fuel flammability is a significant driver of the typical fire season (Section 5.4.4).

### *5.4.1. Individual flammability parameter ($F_{ign}$ and $F_{comb}$)*

This was achieved by normalizing the time to ignition and the peak heat release rate, as outlined by Eq. 5.6 and 5.7. A fastest ignition time ($t_{ign,min}$) was found for NG needles in July, 30.0 +/- 2.0 s, and highest peak heat release rate ($pHRR_{max}$) for OG needles in October, 749.4 +/- 47.1 $kW.m^{-2}$.

The normalization allows a direct comparison of the flammability parameters, ignitibility and combustibility, on a single scale (Fig. 5.9). A normalized value of unity refers to most flammable; zero refers to not flammable at all.

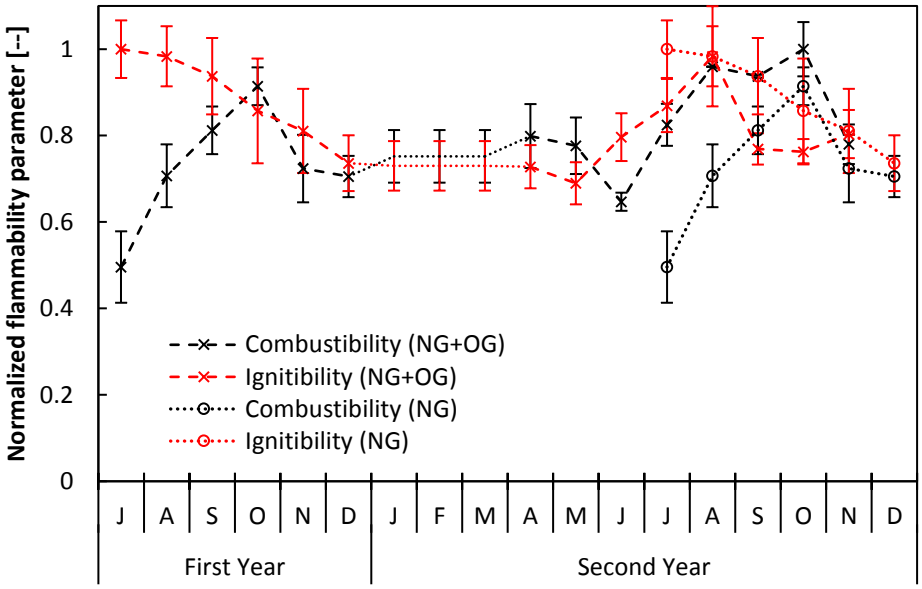


**Fig. 5.9. Seasonality of individual flammability parameter for OG and NG needles ("Dotted" section from January to March of curves mean that no tests were conducted in this period and data is interpolated between Dec. and Apr.).**

In the growth cycle of the needles (x-marker), initial hazard is due to high ignition potential, but with little risk for intense fires (First year, June-August). As they grow, ignition potential decrease but risk for more intense fires increases (First year, August-October). From then, the overall hazard condition is low to moderate until the late spring of the following year (Second year, June). A minor peak in combustibility can be identified in April. In the early summer of the second year, the overall hazard is highest, because the fuel has a moderate/high ignition potential and a moderate/high level of risk for intense fires (Second year, July-August). Although the hazard for extreme fires stays high (even reaches its peak combustibility) in late summer and fall, ignition potential reduces to moderate/low. Thus, the likelihood of fires occurring is low, but when they do occur, they can be intense. In the final months of the year, the overall risk is moderate.

Critical observation from Fig. 5.9:

- Ignitibility and Combustibility do not follow the same trends; but globally elevated flammability may be associated to the growing season.
- Seasonal trends are different for growing and mature needles.
- Combustibility: August, September and October (second year) are the dangerous months.
- Combustibility: Winter and spring months correspond to low combustibility levels, even until July.
- Ignitibility: Very young needles have overall highest ignition potential.
- Ignitibility: Mature needles have highest ignition potential in August.

It is evident, that the time period denoted "First year" in Fig. 5.9 is only a hypothetical state where only one generation of foliage exists (For evergreen plants such as conifers; deciduous plants will only have a single generation). In reality, there will almost always be a condition shown as in the "Second year", where two (or more) generations are present at the same time. Although a single generation condition may occur after a fire has passed through, consuming all canopy fuels. If the tree stand survives, the first subsequent foliage generation will be the only one.

To account for this in the assessment, a state of superposition needs to be considered when the new foliage emerges in June/July. This is indicated in Fig. 5.9 by the addition of the circular markers. The high ignition potential of very young needles increases the overall risk in this time (Second year, July-August) even further. The higher hazard, due to ignition potential of young needles, can produce a segue for ignition of old needles, which than provide the hazard for intense fire conditions at this time of the year.

The combination of very high combustibility of both, NG and OG needles in October, makes this month very dangerous for extreme fire conditions. In the balance between risk from ignition and intensity, it is suggested that the most dangerous time of the year is August, because ignition potential and intensity are moderate/high. This will be quantifiable with the total flammability factor.

### *5.4.2. Flammability factor for each needle generation ($F_{og}$ and $F_{ng}$)*

An accumulative flammability, including ignitibility and combustibility, for each generation can be calculated according to Eq. 5.4 and 5.5. This allows the side by side comparison of the overall flammability of each generation, which is presented in Fig. 5.10. In this graph the blue marker represent the flammability of OG needles and the red marker represent NG needles. Both generations indicate significant seasonality in flammability, as was already discussed in the previous section.

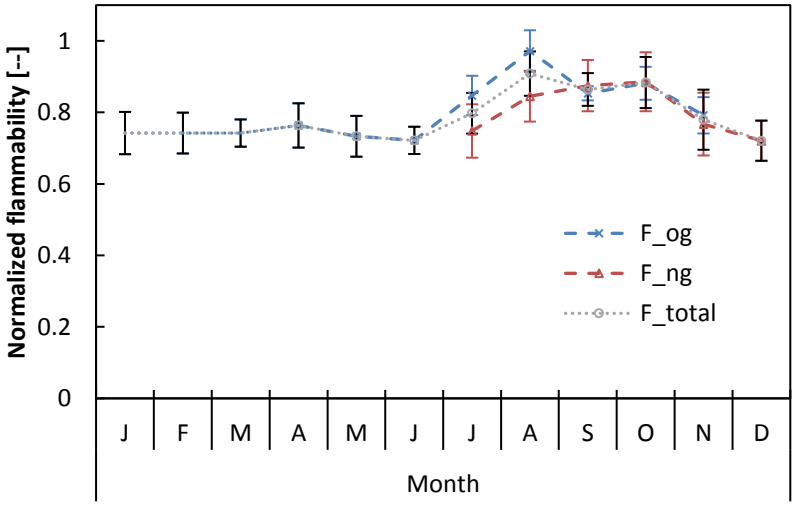


**Fig. 5.10. Seasonality of (1) flammability of OG (blue) and NG (red) needles (incl. ignitibility and combustibility parameter), and (2) total flammability factor (grey) of PRI foliage (incl. OG and NG needles). ("Dotted" section of curve means that no tests were conducted in this period and data is interpolated between Dec. and Apr).**

The accumulative flammability of OG needle is low for the first half of the year, with a minor rise in April (due to combustibility). At the end of the spring flammability

rises and reaches a peak in August followed by a decrease and plateau in late summer and early fall (until October). After October, the flammability decreases further.

The accumulative flammability of NG needles starts relatively low in July and increases until reaching a peak in October. As was the case for OG needles, the flammability of NG needles also decreases after October, to its lowest calculated value, in December.

When both generations coexist, they have similar trends in flammability, with some differences in July and August, which is the main growth period of NG needles. In the later part of the year, September and onwards, flammability of both generations is at the same level. This concurs with the notion that, NG needles mature and become equivalent to OG needles.

Overall, OG needles are more flammable than NG needles, because of the higher values in the early month of the summer. From the above graph it is still not possible to define a single most hazardous time, because the peak flammability of each generation occurs at different times. The final part of the analysis includes the combination of the flammability of each generation into the total flammability factor, $F_{total}$.

### *5.4.3. Total flammability factor including both generations ($F_{total}$)*

The total flammability factor, $F_{total}$, given by Eq. 5.1 is presented in Fig. 5.10 (grey marker). The fuel distribution between OG and NG is considered balanced equally ($w_{og}$ = 0.5) when both generations exist. With such a weighting, the highest live fuel flammability is calculated in August, with $F_{total}$ = 0.908. Therefore, it can be concluded that this correlates to the most dangerous month, from a live fuel flammability perspective.

One may question a balanced fuel distribution between OG and NG. In fact, this coefficient is certainly not a constant value, but should be considered as a function of the NG needle state of growth and OG needle state of decay.

**Importance of fuel load distribution**

This coefficient can be evaluated quantitatively with physical sampling of the canopy fuels. Although this is not done here, future development should incorporate a more sophisticated weighting function (fuel sampling). Such data becomes valuable because it attributes physical meaning to *w*. In the current work, a simple logical function is used to illustrate the application of w. This was chosen, because individual flammability factors ($F_{og}$ and $F_{ng}$) were not significantly different.

When NG needles grow, $w_{og}$ deceases (spring to summer). In the fall, OG needles decay and fall off the tree, which further reduces $w_{og}$ until eventually it becomes zero in late fall and early winter. It should be noted here that the discussion assumes that all OG needles will disappear and not remain on the tree. It is possible that multiple generations stay on the tree, at which point one could go into further detail and extent the assessment to a third (and even fourth) needle generation. This becomes increasingly more complex, because one must ensure that only an individual generation is tested without contamination from another generation. Distinction between second and third/fourth generation when picking needles from the tree will be almost impossible and thus is not recommended.

An example of a dynamic fuel loading is shown in Fig. 5.11, where a logical distribution was assigned to *w* (orange marker) to highlight the importance of using an appropriate fuel distribution model. With this distribution, the peak flammability is still observed in August, with $F_{total} = 0.934$.

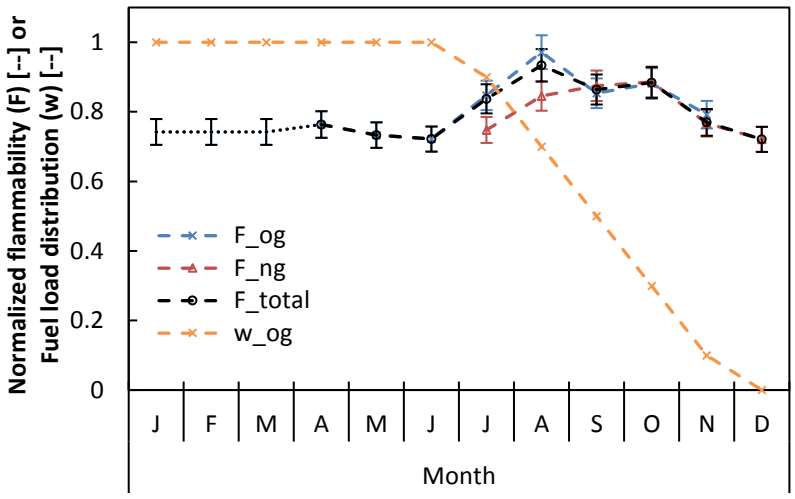


**Fig. 5.11. Influence of fuel load distribution on the total flammability factor (black). ("Dotted" section of curve means that no tests were conducted in this period and data is interpolated between Dec. and Apr)**

In this particular case (PRI needles), changing the distribution model did not change the conclusion of the flammability assessment – the most dangerous month is still August. This is because each generation's flammability is not drastically different from the other during the growing period. It needs to be evaluated with other species, if this is a general characteristic. If it is, one may disregard the fuel distribution model (weighting of $F_{total}$ in Eq. 5.1), because it does not significantly impact the results of the flammability assessment. However, for other species, flammability components might reveal significant differences, and until other species are evaluated, the weighting coefficients, $w$, should remain in Eq. 5.1. Future work should include determination of suitable fuel distribution models in order to make the weighting more robust.

### *5.4.4. Correlation of $F_{total}$ to the fire season in the NJ Pine Barrens*

Historical fire data [5.43] was first shown in Chapter 1 and is now compared to the total live fuel flammability factor. It is evident from Fig. 5.12 that the seasonality of the live fuel flammability does not correlate with the major fire season in the spring.

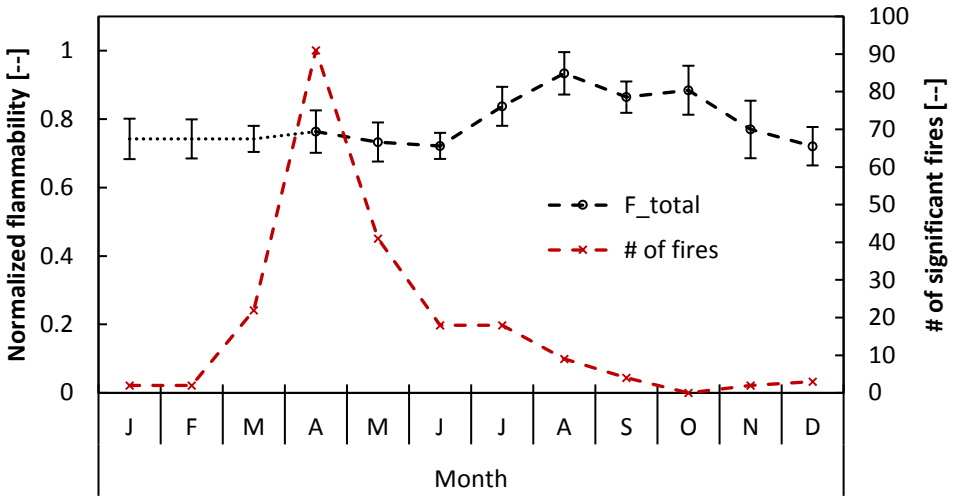


**Fig. 5.12. Total flammability factor compared to historic fire data [5.43].**

In order to discuss the relevance, one must look at the common ignition scenario of a wildfire. Initial ignition of forest fires generally occurs in dead surface fuels (forest litter), which are not included in the above assessment. Furthermore, it is understood that most fires spread on the ground and only under certain circumstances can a fire spread into the canopy [5.44-5.46]. Dead fuels are inherently linked to meteorological conditions, as was discussed in Chapter 1 (e.g. explained by the Nelson model [5.47, 5.48]). Thus, the weather (high winds, low relative humidity and high temperatures) plays the prevailing role in the occurrence of the fire season, rather than the seasonality of live fuel flammability (species dependence is still critical).

Considering the hypothetical case where the weather conditions stay constant over the year, one can say that: if a fire can ignite on the surface and spread into live fuel strata (shrub layer or canopy), most sever fires can be expected in the summer months, due to the increased fuel flammability, and not in the spring. However, in NJ, the spring, and especially March and April, mark a time with historically lower humidity and stronger winds compared to the summer months, as was discussed in Chapter 1. Thus, the risk of ignition of dead surface fuels in the summer is lower than in the spring. This

analysis indicates that, potentially devastating fires are possible in the NJ Pine Barrens in the summer, if unseasonal weather conditions develop.

Furthermore, this begs the question if applying the same assessment to a different ecosystem, for example Northwestern US, will reveal different observations? This question is posed because, weather conditions are significantly different. There, the summer months are the driest (and warmest) months of the year [5.49], which means that the highest risk of initial ignition of dead fuels can be associated to this time. The major fire season in these regions occurs in the summer months [5.50]. Assuming that common pine species (or equivalent) will exhibit comparable seasonality of live fuel flammability to Pitch pine, one can deduce that the risk of more sever fires is then not only driven by the weather condition, but also by the live fuel flammability.

A material flammability assessment, such as the one presented here, is important, because it is an inherent characteristic of the fuel and thus aids in understanding wildfire behavior (Fig. 1.1 in Chapter 1). This characteristic can be drastically different from species to species and thus will influence regional fire danger. Furthermore it is critical to consider flammability, not only from one parameter. Fundamentally, it is intuitive that, flammability changes depending on the chemical composition of the fuel, because if subjected to heat, resulting pyrolysis products will be different, as suggested by results in Fig. 5.8. The analysis provided in this study further elaborates on the dynamic nature (seasonality) of live foliar flammability as a function of growth state. However, it was shown that plant chemistry is likely not the only factor that drives this behavior.

A missing link at this point, is the flammability assessment of live unconditioned foliage. This will add another variable, the *FMC*, to the system, which was found to influence the ignitibility and combustibility [5.1-5.3, 5.12, 5.16, 5.51-5.57]. It needs to be evaluated if these flammability components are correlated to the trends set forth

by the seasonality of the *FMC*. This is addressed in the following Chapter, where unconditioned needle samples (OG and NG) are subject to the same combustion tests.

### *5.5. Chapter summary and conclusions*

Effects of seasonality on the ignitibility and combustibility of live foliage can be twofold: either as a change in chemical composition (and thermo-physical properties) related to the state of growth/decay or the *FMC*. Both are significant factors driving the ignition behavior and burning dynamics. In this chapter, the former effect was explored by conditioning the foliage to obtain 0% *FMC* before submitting to combustion experiments. This allows an analysis in the absence of effects driven by the presence of water (either in the solid or gas phase).

The purpose of this study was, to analyze the flammability of live foliage over the course of a growing period and to determine any variation that can be attributed to the state of growth/decay. Material flammability has many facets, and is commonly related to the ignition behavior only, for classification purposes; here it was defined with two parameters, ignitibility: how well does the fuel ignite (time to piloted ignition), and combustibility: how intense does it burn (peak heat release rate). Combustion intensity is a critical component of a flammability assessment, because material that ignites fast but doesn't burn very intense might be considered less hazardous than a material that takes longer to ignition, but burns very intense. The data analysis in this work led to the development of a total flammability factor, incorporating both components. The developed flammability assessment can be applied (1) to improve fuel classification systems (including a measure of combustibility) and (2) to explore any correlation between live fuel flammability and timing of the typical fire season (e.g. in the NJ Pine Barrens).

Conditioned live pine needle samples (PRI) were subjected to a standard combustion test using the FPA in order to identify the flammability parameter, ignitibility and

combustibility. The test period extended from April 2014 to April 2015 and included two generation of foliage (OG and NG). It should be noted, that no further distinction between multiple generations were made in the type OG, but should be seen as overall mature foliage. NG needles emerged in June, and first testing on these type needles was done in July. OG needles were tested until November at which point a majority of needles indicated a significant decay (yellowing).

During the experimental period, the apparent needle density was monitored to monitor changes in chemical composition. Minor variations in apparent needle density of OG were observed (3.8%). Contrarily, variations for NG needles were greater (10.2%), indicating that changes in chemical composition is more significant for this type needle. Significant differences were observed in the growing needles. Young needles have the highest density. As they grow, density reduces to match the one obtained for OG needles. Dead needles have the lowest density. This behavior was described to be due to composition of the needle, but also likely due to the internal porosity of the particle. Future studies should explore the option to obtain actual needle densities (via submersion in gas rather than liquid).

It was concluded that, apparent density cannot be used as a sole variable to evaluate the ignitibility or combustibility. Other factors that were discussed to impact the seasonal trends in ignitibility or combustibility are other fuel properties (thermal conductivity and specific heat), chemical composition, and absorptivity. It was shown that changing thermo-physical properties (density and absorptivity) have competing effects on the ignition behavior. Finally, it was also discussed that a likely factor for some of the seasonal trends of flammability is a change in the needles ability to release gases from its interior. It is recommended that future work identifies this mechanism in detail.

Significant seasonality in ignition behavior and combustion intensity over the course of the test period was observed for both NG and OG needles. Overall, young NG

needles ignite fastest, whereas, OG needles burn most intense. These two critical conditions were correlated to the months of July and October, respectively. This is evidence to the notion that both, ignitibility and combustibility are critical components of a flammability assessment, and neither one should be neglected.

The critical conditions were then used in a normalization process that allowed comparison of both flammability components on a single scale. Finally, a total flammability factor was developed with one weighting function to account for fuel distribution (OG and NG needles). This led to the conclusion that, (1) an increase of live fuel flammability can be associated to the growing period of PRI needles; and (2) live PRI needles are most flammable in August, thus signifying that, this is the most dangerous month of the year, from a live fuel flammability standpoint.

The flammability assessment was compared to historical fire data in the NJ Pine Barrens. The comparison revealed no significant correlation between the live fuel flammability and number of significant fires (nor area burned). New Jersey's major fire season is in the spring, with historically most fires occurring in April. Contrarily, the relative live fuel flammability (of PRI needles) is low in this time period. Two conclusions were drawn: (1) the occurrence of a fire season is more governed by meteorological condition, which also govern the dead *FMC*, rather than live fuel flammability. (2) The live fuel flammability assessment cannot be directly correlated to the fire season, because not every fire involves canopy fuel consumption. The danger may be interpreted as a crowning potential, because fuel discussed here are located in the forest canopy. The spring weather in NJ is generally low in relative humidity with strong winds. Adding rising ambient temperatures creates favorable wildfire conditions. Other regions, such as the Northwest of the US, have drier months during the summer, which correlates to the peak fire season. If common plant species in these regions exhibit similar seasonality of live fuel flammability compared to PRI, as per the developed assessment, it can explain why fires there are much more severe.

Future research should include assessment of foliage from different ecological regions to evaluate this.

### *5.6. References*

[5.1] W.M. Jolly, J. Hintz, R.C. Kropp, E. Conrad. Physiological drivers of the live foliar moisture content 'spring dip' in Pinus resinosa and Pinus banksiana and their relationship to foliar flammability. Proceedings of the 7th International Conference on Forest Fire Research. Coimbra, Portugal (2014).

[5.2] S. McAllister, I. Grenfell, A. Hadlow, W.M. Jolly, M. Finney, J. Cohen. Piloted ignition of live forest fuels. Fire Safety Journal, 51 (2012) 133-142.

[5.3] S. McAllister, D.R. Weise. Effects of Season on Ignition of Three Species of Live Wildland Fuels using the FIST apparatus. Spring Technical Meeting of the Western States Section of the Combustion Institute, Pasadena, California, USA (2014).

[5.4] US Department of Agriculture, Forest Service. Seasonal Fluctuation in Moisture Content of Pine Foliage. Research Note NC-11. North Central Forest Experiment Station. Minnesota, USA (1966).

[5.5] Z. Chrosciewicz. Foliar Moisture Content Variation in Four Coniferous Tree Species in Central Alberta. Canadian Journal of Forest Research 16 (1986) 157-162.

[5.6] C.R. Keyes. Foliar moisture contents of North American conifers. USDA Forest Service Proceedings RMRS-P-41 (2006) 395-399

[5.7] P.P. Grima. Determination of springtime foliar moisture content in pitch pine (*Pinus rigida*). University of Massachusetts, Amherst, Massachusetts (2009) Professional Master's Project Report. 21 p.

[5.8] W.M. Jolly. A.M. Hadlow. K. Huguet. De-coupling seasonal changes in water content and dry matter to predict live conifer foliar moisture content. International Journal of Wildland Fire 23 (2014) 480-489.

[5.9] G. Bonan. Ecological Climatology: Concepts and Applications. 2nd ed. Cambridge University Press, Cambridge, UK (2008).

[5.10] B. Ťupek, R. Mäkipää, J. Heikkinen, M. Peltoniemi, Liisa Ukonmaanaho, T. Hokkanen, P. Nöjd, S. Nevalainen, M. Lindgren, A. Lehtonen. Foliar turnover rates in Finland – comparing estimates from needle-cohort and litterfall-biomass methods. Boreal Evironment Research 20 (2015) 283-304.

[5.11] J. Aalto, P. Kolari, P. Hari, V.-M. Kerminen, P. Schiestl-Aalto, H. Aaltonen, J. Levula, E. Siivola, M. Kulmala, and J. Bäck. New foliage growth is a

significant, unaccounted source for volatiles in boreal evergreen forests. Biogeosciences 11 (2014) 1331-1344.

[5.12] F.X. Jervis, Application of Fire Calorimetry to Understand Factors Affecting flammability of Cellulosic Material: Pine Needles, Tree Leaves and Chipboard. University of Edinburgh, UK, 2012. PhD.

[5.13] P. Bartoli. Feux de forêt: amélioration de la connaissance du couplage combustible-flamme. Universite de Corse-Pascal Paoli. 2011. Ph.D. (in French)

[5.14] P. Bartoli, A. Simeoni, H. Biteau, J.L. Torero, P.A. Santoni. Determination of main parameters influencing forest fuel combustion dynamics. Fire Safety Journal 46 (1-2) (2011) 27-33.

[5.15] A. Simeoni, P. Bartoli, J.L. Torero, P.A. Santoni. On the Role of Bulk Properties and Fuel Species on the Burning Dynamics of Pine Forest Litters. Proceedings of the 10th International Symposium on Fire Safety Science. University of Maryland, Maryland, USA (2011) 1401-1414.

[5.16] J.C. Thomas, A. Simeoni, M. Gallagher, N.S. Skowronski. An Experimental Study Evaluating the Burning Dynamics of Pitch Pine Needle Beds Using the FPA. Proceedings of the 11th International Symposium on Fire Safety Science. Christchurch, New Zealand, (2014) pp. 1406-1419.

[5.17] R.C. Rothermel. A Mathematical Model for Predicting Fire Spread in Wildland Fuels. INT-115. USDA, Forest Service, Ogden, UT, USA (1972).

[5.18] F.A. Albini. Wildland Fire Spread by Radiation – A Model Including Fuel Cooling by Natural Convection. Combustion Science and Technology 45 (1986) 101-113.

[5.19] B. Porterie, D. Morvan, J.C. Loraud, M. Larini. Fire Spread Through Fuel Beds: Modeling of Wind-Aided Fires and Induced Hydrodynamics. Physics of Fluids 12/7 (2000) 1762-1782.

[5.20] M. El Houssami, J.C. Thomas, A. Larmorlette, D. Morvan, M. Chaos, R. Hadden, A. Simeoni. Experimental and Numerical Studies Characterizing the Burning Dynamics of Wildland Fuels. Combustion and Flames 168 (2016) 113-126.

[5.21] F.X. Jervis, G. Rein. Experimental study on the burning behavior of Pinus halepensis needles using small-scale fire calorimetry of live, aged and dead samples. Fire and Materials (2015)

[5.22] A.A. Pappa, N.E. Tzamtzi, M.K. Statheropoulous, G.K. Parissakis. Thermal analysis of Pinus halepensis pine-needles and their main components in the presence of (NH4)2HPO4 and (NH4)2SO4. Thermochimica Acta 261 (1995) 165-173.

[5.23] M.K. Statheropoulous, M. Liodakis, N.E. Tzamtzi, A.A. Pappa, A. Kyriakou. Thermal Degradation of Pinus Halepensis Pine-Needles Using Various Analytical Methods. Journal of Analytical and Applied Pyrolysis 43/2 (1997) 115-123.

[5.24] Methanol-Thermophysical Properties. The Engineering Toolbox. Accessed: Aug. 26, 2016. http://www.engineeringtoolbox.com/methanol-properties-d_1209.html.

[5.25] L.Y. Mwaikambo, M.P. Ansell. The determination of porosity and cellulose content of plant fibres by density methods. Journal of Materials Science Letters 20 (2001) 2095-2096.

[5.26] S. Youssefian, N. Rahbar. Melecular Origin of Strength and Stiffness of Bamboo Firbils. Nature Scientific Reports 5 (2015) 11116.

[5.27] National Physical Laboratory. Kaye and Laby Tables of Physical and Chemical Constants. http://www.kayelaby.npl.co.uk/general_physics/2_2/2_2_1.html.

[5.28] P. Girods, N. Bal, H. Biteau, G. Rein, J.L. Torero. Comparison of Pyrolysis Behaviour Results between the Cone Calorimeter and the Fire Propagation Apparatus Heat Source. Proceedings of the 10th International Symposium of Fire Safety Science. College Park, MD, USA, (2011)

[5.29] B. Monod, A. Collin, G. Parent, P. Boulet. Infrared Radiative Properties of Vegetation involved in Forest Fires, Fire Safety Journal, 44 (2009) 88-95.

[5.30] Z. Acem, G. Parent, B. Monod, G. Jeandel, P. Boulet. Experimental Study in the Infrared of the Radaitive Porperties of Pine Needles, Experimental Thermal and Fluid Science, 34 (2010) 893-899.

[5.31] M. Chaos. Spectral Aspects of Bench-Scale Flammability Testing: Application to Hardwood Pyrolysis. Proceedings of the 11th International Symposium on Fire Safety Science, Christchurch, New Zealand, (2014) pp. 165-178.

[5.32] R. Larsen, K. Trombley. Specific Heat of Three Pine Needles; A Report to Worcester Polytechnic Institute. Report Nr. TPRL-4992. Thermophysical Properties Research Laboratory. West Lafayette, IL, USA (2012) (unpublished).

[5.33] ASTM E-1269. Standard Test Method for Determining Specific Heat Capacity by Differential Scanning Calorimetry. ASTM International, West Conshohocken, PA, USA (2011).

[5.34] V. Tihay, A. Simeoni, P.A. Santoni, L. Rossi, J.P. Garo, J.P. Vantelon. Experimental Study of Laminar Flames Obtained by the Homogonization of three Forest Fuels. International Journal of Thermal Science 48 (2008) 488-501.

[5.35] F.P. Incropera, D.P. DeWitt, T.L. Bergman, A.S. Lavine, Principles of Heat and Mass Transfer, John Wiley and Sons Ltd., Singapore, Singapore, 2013.

[5.36] H.E. Anderson. Forest Fuel Ignitibility. Fire Technology 6/4 (1970) 312-319.

[5.37] D. Drysdale. An Introduction to Fire Dynamics (3rd edn). John Wiley and Sons: Chichester, UK, 2011.

[5.38] J.G. Quintiere. Fundamental of Fire Phenomena. John Willey and Sons, Hoboken, NJ, USA, 2006.

[5.39] J.Torero. SFPE Handbook of Fire Prevention Engineering – Flaming Ignition of Solid Fuels. 5th ed. Society of Fire Protection Engineers, London, UK, (2016).

[5.40] J. Lin, M.E. Jach, R. Caulemans. Stomatal Density and Needle Anatomy of Scots Pine (Pinus Sylvestris) are Affected by Elevated $CO_2$. New Phytologist 150 (2001) 665-674.

[5.41] L.L.R. Kouwenberg, W.M. Kuerschner, H. Visscher. Changes in Stomatal Frequency and Size During Elongation of Tsuga Heterophylla Needles. Annals of Botany 94 (2004) 561-569.

[5.42] S. Brohez. Uncertainty Analysis of Heat Release Rate Measurement from Oxygen Consumption Calorimetry, Fire and Materials 29 (2005) 383-394.

[5.43] New Jersey Office of Emergency Management. State of New Jersey 2014 Hazard Mitigation Plan Section 5.12 Wildfire. Tetra Tech, Inc. Morris Plains, NJ, USA (2014).

[5.44] M.E. Alexander, M.G. Cruz. Assessing the Effect of Foliar Moisture on the Spread Rate of Crown Fires. International Journal of Wildland Fires 22/4 (2012) 415-427.

[5.45] C.E. Van Wagner. Conditions for the Start and Spread of Crown Fire. Canadian Journal of Forest Research 7 (1976) 23-34.

[5.46] M.G. Cruz, M.E. Alexander. Assessing Crown Fire Potential in Coniferous Forests of Western North America: A Critique of Current Approaches and Recent Simulation Studies. International Journal of Wildland Fire 19 (2010) 377-398.

[5.47] R.M. Nelson, Jr. Prediction of Diurnal Change in 10-h Fuel Stick Moisture Content. Canadian Journal of Forest Research 30 (2000) 1071-1087.

[5.48] J.D. Carlson, L.S. Bradshaw, R.M. Nelson Jr., R.R. Bensch, R. Jabrzemski. Application of the Nelson Model to Four Timelag Fuel Classes Using Oklahoma Fiel Observations: Model Evaluation and Comparison with National Fire Danger Rating System Algorithms. International Journal of Wildland Fire 16 (2007) 204-216.

[5.49] WeatherSpark, Cedar Lake Ventures, Inc. San Francisco, CA, USA. Accessed: May 5, 2016. https://weatherspark.com.

[5.50] Firewise (webpage). Peak Fire Season. National Fire Protection Association. 1 Batterymarch Park, Quincy, MA, USA. Accessed: Aug. 26, 2016. http://www.firewise.org/wildfire-preparedness/teaching-tools/interactive-modules-and-quizzes/peak-fire-seasons.aspx.

[5.51] D.R. Weise, R.H. White, F.C. Beall, M. Etlinger. Use of the Cone Calorimeter to Detect Seasonal Differences in Selected Combustion Characteristics of Ornamental Vegetation. International Journal of Wildland Fire 14 (2005) 321-338.

[5.52] A.P. Dimitrakopoulos, K.K. Papaioannou. Flammability Assessment of Mediterranean Forest Fuels, Fire Technology, 37(2) (2001) 143-152.

[5.53] J.R. Weir, J.D. Scaska. Ignition and fire behaviour of Juniperus virginiana in response to live fuel moisture and fire temperature in the southern Great Plains. International Journal of Wildland Fire 23 (2014) 839-844.

[5.54] J.M. Varner, J.M. Kane, E.M. Banwell, J.K. Kreye. Flammability of Litter from Southeastern Trees: A Preliminary Assessment. Proceedings of the 17th Biennial Southern Silvicultural Research Conference, Shreveport, Luisiana, USA (2012) 183-187.

[5.55] M.E. Alexander. Foliar Moisture Content Input in the Canadian Forest Fire Behavior Prediction System for Areas Outside Canada. Proceedings of the 6th International Conference on Forest Fire Research. Coimbra, Portugal (2014).

[5.56] W.M. Jolly, R.A. Parsons, A.M. Hadlow, G.M. Cohn, S.S. McAllister, J.B. Popp, R.M. Hubbard, J.F. Negron. Relationships between moisture, chemistry, and ignition of Pinus contorta needles during the early stages of mountain pine beetle attack. Forest Ecology and Management 269 (2012) 52-59.

[5.57] A.M. Grishin, Mathematical Modeling Forest Fire and New Methods Fighting Them, Publishing House of Tomsk University, Tomsk, Russia, 1997.

# Chapter 6

## *Flammability Assessment of Unconditioned and Partially Conditioned Live Foliage – Influence of Fuel Moisture Content on the Ignition and Burning Behavior*

## *6.1. Introduction*

Ignition behavior and combustion dynamics of live Pitch pine needles (*Pinus rigida*; PRI) was first discussed in Chapter 5. The discussion was however limited to fully dehydrated needles, in order to explore seasonal effects due to state of growth/decay in the absence of effects driven by *FMC*. The following discussion now explores the ignition behavior and combustion dynamics of unconditioned or partially conditioned needles. A similar flammability assessment, based on ignitibility and combustibility, as developed in Chapter 5 is conducted with unconditioned needles. This is done to assess if dry and wet fuel have the same seasonal trends. Understanding the flammability of dry fuel provides insight what can occur in an extreme case (0% *FMC*), however, such conditions are not the reality. Result of the flammability assessment with wet fuel ($F_{total,wet}$) is compared to dry fuel ($F_{total,dry}$). Studying the ignition and combustion behavior of partially dried needles provided the linkage between the two boundary conditions (0% and maximum *FMC*).

### *6.1.1. Chapter 5 conclusions on dry fuel flammability*

The main conclusions in Chapter 5 were: (1) Seasonal trends of ignitibility and combustibility are best explored when fuel is dry and under low heat flux condition; (2) Seasonal trends of ignitibility and combustibility are evident and are not necessarily the same; (3) flammability of growing and mature foliage is not necessary the same; (4) a combined factor ($F_{total}$), including ignitibility and combustibility, for both type of needles (OG and NG), best describes the overall seasonal trends of flammability of canopy fuel; (5) from a dry fuel flammability stand point, August is the most dangerous month in which canopy involvement in fire behavior is at the highest risk; (6) Live foliar flammability does not correlate to the occurrence of a typical fire season (in the NJ Pine Barrens), therefore, the prevailing indicator is the weather (high temperatures, low wind and relative humidity); (7) fuel properties are likely not the only factor impacting flammability, vapor release mechanism of the needles is another.

### *6.1.2. Impact of FMC*

Fuel moisture content (*FMC*) is a factor commonly understood to drive the combustion of live vegetation. The particular mechanisms that cause the ignition behavior and burning dynamics to change when the fuel is wet are explored. Detailed description of the impact of water content was first described in Chapter 1. Impact of *FMC* on the ignition and burning behavior is twofold: (1) in the solid phase and (2) in the gas phase. In the solid phase it changes thermophysical properties and acts as a heat sink, which alters the thermal response of the particle. These impacts affect the heat transfer mechanism and can cause the ignition to be delayed, or pyrolysis rates to be altered (burning behavior).

In the gas phase, it cools pyrolysis gases and flames (heat transfer), as well as displacing oxygen from the combustion zone (mass transfer). In terms of ignition (piloted), this means that the time to reach a flammable mixture can be delayed. Explanation is given throughout this chapter alluding that, the oxygen displacement mechanism is likely a dominant factor that governs the combustion of wet vegetation. The release of water vapor controls the burning behavior, analogous to how ventilation can control the burning dynamics in a compartment fire [6.1] (see discussion in Chapter 3). When oxygen availability is limited the combustion intensity is reduced due to a reduction of the combustion efficiency.

The impact of the water release mechanism on the combustion dynamics is illustrated in Fig. 6.1. For a combustion reaction to take place, sufficient pyrolysis gases have to mix with oxygen to create a flammable mixture. This mixture has then to be raised to a critical temperature at which an uninterrupted chain reaction (combustion reaction) can take place.

The pyrolysis rate (Fig. 6.1) is driven by the energy received by the fuel. Initially this is induced with an external heat flux. After ignition, the driving mechanism is the heat flux feedback from the flames (see also Chapter 3). This feedback is governed by the

flame shape and temperature (also type of flame, laminar of turbulent). Flame temperature and geometry are governed by combustion dynamics, which are governed by the ventilation condition (see Chapter 3 for detailed discussion on ventilation condition).

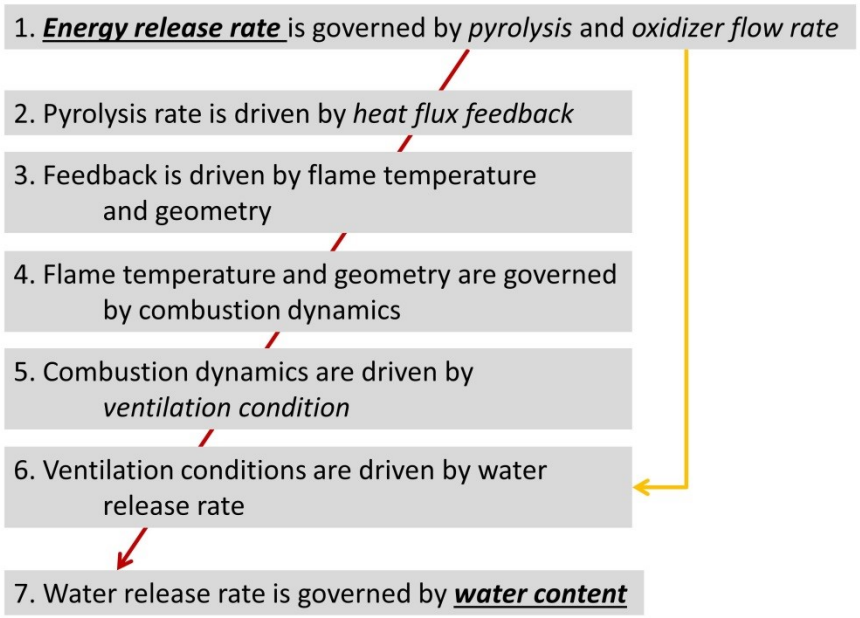


**Fig. 6.1. Schematic of the impact of the water release mechanism on the combustion behavior.**

For any fire (in the build environment or wildland), the ventilation condition is determined by the entrainment air and availability of oxygen. When the ventilation area (in a building) is small, oxygen is prevented from reaching the combustion zone. For wet fuel, a similar condition can be described. The released water displaces the oxygen, therefore hindering the combustion reaction. Finally, the water release mechanism is a function of the available water in the solid fuel, i.e. *FMC*. In Fig. 6.1, the red and yellow arrow indicate the pathways through which FMC influences the combustion behavior, by affecting the heat transfer (cooling solid and gases/flames reducing the pyrolysis rate) and by affecting the mass transfer (by displacing oxygen reducing the combustion efficiency and thus reaction intensity).

A preliminary study was conducted in 2013 [6.2] and [6.3] to gauge to what extent a full study should be conducted. The preliminary study showed first results of ignition behavior and burning dynamics of live vegetative fuels in the FPA. The result warranted a start of a full study that would go on for one year, including all seasons, and two generation (OG and NG) of foliage. As this is also a continuation of previous studies [6.4] and [6.5] that attempt to build a framework for the determination of flammability and burning characteristics of vegetation it is the intent to improve experimental protocols with additional modifications, such as the use of equivalent sample mass (for wet fuel).

Simeoni et al [6.6] summarized studies pertaining flammability and burning dynamics of forest fuel in great detail, however, not including influences of *FMC*. The studies evaluated flammability parameters (time to ignition, heat release rates, and mass loss rates) with respect to various test conditions, such as sample basket openness, species and airflow condition. In [6.4], Bartoli et al considered various main parameters influencing the combustion dynamics. Besides airflow and basket openness, species variation and sample loading variations were also considered. Thomas et al focused on the study of flammability of pine needle beds in [6.2] and [6.3] with respect to various test conditions (species, external heat flux, and FMC), supplementing the results found by Simeoni and Bartoli by studying North American needle species. The current study now added the *FMC* in more detail as a further test parameter. Jervis and Rein [6.7] first, evaluated the influence of *FMC* on the burning dynamics of *Pinus halepensis* needle samples in the FPA. Even though, the work in [6.7] and the current work have similarities both are supplementary to the other. Differences can be found in the sample properties, experimental set ups, and the bases of analysis.

In recent years, significant work on ignitibility of live foliage has been done at the Missoula Fire Science Laboratory in Missoula, Montana (US Forest Service Rocky Mountain Research Station). Jolly et al [6.8] have investigated and de-coupled the influence of dry mass on the *FMC* calculations by examining closely the chemical

composition of the foliage. Furthermore, they have related it to flammability (ignitibility) in [6.9] where they show a relationship between ignition time and foliar density. McAllister et al. [6.10, 6.11] have conducted extensive work using the Forced Ignition and Flame Spread Test (FIST), investigation seasonal trends in the ignition behavior of foliage. Furthermore, they proved a comprehensive review of various ignition models for wet fuel and compare their applicability to live forest fuel [6.10].

Several notable works studying flammability of live forest fuel in calorimeter that were also discussed in Chapter 1 are [6.12-6.19]. These authors have looked at energy release of live foliage as a function of *FMC*. Various test apparatuses, such as the Cone calorimeter [6.13, 6.16-6.18] intermediate scale calorimeter [6.12-6.15], or FPA [6.19] were employed. Furthermore, Baker [6.15] and Babrauskas [6.14] studied the energy release of full trees. Weise et al [6.13] have concluded that scaling of energy release between bench- and intermediate-scale combustion experiments was unsatisfactory. In the current work, scalability is reviewed.

### *6.1.3. Goals and Objectives*

The goal of this chapter is to assess the flammability in terms of ignition and burning behavior of live unconditioned foliage and determine any seasonal trend. The novel framework for live fuel flammability assessment from Chapter 5 is extended to unconditioned needles. A comparison of conditioned and unconditioned fuel flammability is made to analyze the effect of *FMC*. Finally, it is attempted to correlate the flammability assessment of unconditioned to fully conditioned foliage. This is achieved by determining the relationship between ignition time and *FMC* and the relationship between peak heat release rate and *FMC*. As was the case in Chapter 5, the live unconditioned flammability assessment is also compared to historic fire data to evaluate any correlation. The novel assessment presented in Chapter 5 and 6 results in the definition of live fuel flammability as a two dimensional parameter, depending on time (season) and *FMC*.

### *6.1.4. Chapter layout*

The Chapter is laid out to first describe important fuel and sample properties, as well as test conditions (Section 6.2). A linear relation between needle density (apparent) and *FMC* was discussed in Section 6.2.2. Similar to Chapter 4 and 5, the thermal behavior of the needles was discussed, with respect to increasing *FMC*. Section 6.3 assesses the flammability of unconditioned needles. The total live fuel flammability factors of dried and wet needles are compared. Following this, Section 6.4 analyzes the ignition and combustion behavior as a function of *FMC*. Empirical and semi-physical models for ignition and combustion behavior (pHRR) are explored. Finally, the developed correlations are validated in Section 6.5 with data obtained previously and in a different FPA (still PRI needles).

## ***6.2. Experimental description and critical parameter***

Analysis presented here is based on the same experimental campaign as outlined in Chapter 5, therefore, the reader is referred to that Chapter for detailed description (see Section 5.2). Additional properties and concepts critical for the current analysis are discussed here.

Experimentation was carried out in the FPA, using the same protocol as outlined in Chapter 2 with varying initial sample mass to account for the additional water mass.

### *6.2.1. Test conditions*

Only open sample baskets were used with live PRI needles (conditioned and not). The flow condition was always natural convection, to eliminate any additional convective influences. The heat flux was kept constant primarily at 25 $kW.m^{-2}$, unless stated otherwise. A significant difference to the previous chapter is the use of needles with varying *FMC*.

Samples were tested in the FPA with selected *FMC* ranges. For a monthly stock of needles, tests were conducted at the current *FMC* (unconditioned), followed by a set of tests at two conditioning periods, typically for 1-3 hours and 3-5 hours. Finally, one set of tests was conducted with samples that were conditioned for 24 hours, for a total of four *FMC* ranges.

Because it was ensured that the porosity was kept constant, the ignition and burning dynamics can be evaluated in terms of the sole influence of excess water mass. In other words, the amount of combustible material was kept constant, which allows the study of energy release as a function of the *FMC*. Evaluation of the ignition and burning dynamics of live forest fuel is carried out in a similar manner to the analysis performed in Chapter 5 (dried live PRI needles). The parameters of interest are: (1) Time to piloted ignition and (2) peak heat release rates (pHRR).

Time to piloted ignition is used to evaluate the ignition behavior of the fuel. Oxygen consumption calorimetry [6.20] is used to estimate the pHRR, as outlined in Chapter 2. These two parameters can be linked to critical wildfire behavior characteristics, fire spread and fire intensity, respectively, as was discussed previously.

Various dry particle properties ($k$, $\rho$, $c_p$, and $a$) have been discussed in Chapter 5. These also apply to the work presented in this Chapter. Furthermore, it is discussed how these dry properties change when the fuel is wet.

### *6.2.2. Sample initial mass and porosity*

This study aimed to evaluate the ignition behavior and burning dynamics in relation to *FMC* and seasonality, and therefore constant sample porosity (not to be confused with the needle porosity) had to be used, in order to eliminate influences from changing bed properties.

Authors of previous work (e.g. [6.13] and [6.17]) have eluded that, some inherent variability in their flammability results (e.g. ignition time) can be attributed to varying sample initial mass. Many have stated that future work should be conducted with constant initial sample mass. In this work, constant initial mass is interpreted as constant mass of combustible material, i.e. constant dry mass. Water mass, varying with *FMC*, was accounted for as additional non-combustible mass in the fuel matrix. Therefore, porosity is more accurately described with the dry bulk density, rather than the wet bulk density. The water mass in the needles had to be accounted for as excess weight that does not contribute to the combustible matter. To do this, the initial sample mass, used in the FPA experiments, was determined from an equivalent mass, which depended on the *FMC* and a dry reference mass [6.2].

$$m_{equiv} = m_{dry}(1 + FMC) \qquad \textbf{Eq. 6.1}$$

The dry reference mass, $m_{dry}$ was chosen to be 13.9 g, which corresponds to the amount of combustible material in unconditioned (~7% *FMC*) dead needle samples used in Chapter 3 and 4. The same mass was also used in Chapter 5 for conditioned live PRI needle samples. Appendix D1 lists some values for equivalent mass used. It also includes a statistical summary of sample dry mass. The sample mass is used in the bulk density calculation (see Chapter 2) which means that, when using the equivalent mass, it increases (volume of the basket is constant). Subsequently, this means that, the porosity reduces.

Using an equivalent mass essentially means that, the solid volume occupied by the needles (or the number of needles) in the basket is kept constant. At this stage, it is assumed that the volume of a single needle does not change during when dehydrated (shrinkage). This was accepted because needle diameter measurements (n=40) of unconditioned and conditioned needles showed a shrinkage of approximately 5%. Therefore, using the bulk density determined with the equivalent mass is not

appropriate. The correct mass that should be used is the dry mass ($m_{dry}$ = 13.9 g), which corresponds to the combustible material. When the dry bulk densities in Eq. 6.1 are used, the porosity stays relatively constant between 95-96.5%, depending on the apparent needle density. Both Bartoli [6.21] and Jervis [6.19] have demonstrated that ignition and combustion intensity is not significantly influenced by small variations of fuel loading in this range of porosities (under natural convection only).

### *6.2.3. Particle density*

The apparent density of unconditioned needles was measured (by liquid submersion) and is summarized in Table 6.1. When water is present, the density of needles was found equal or higher than for dry needles. Young NG needles are less influenced by the presence of water, compared to OG needles.

Table 6.1. Apparent density measurements of conditioned and unconditioned PRI needles.

| Type | Date | Density | | | |
|---|---|---|---|---|---|
| | | Conditioned | | Unconditioned | |
| | | Avg. [kg.m$^{-3}$] | St.dev. [%] | Avg. [kg.m$^{-3}$] | St.dev. [%] |
| OG | 17/04/2014 | 744.6 | 6.9 | 956.7 | 7.2 |
| | 07/05/2014 | 763.5 | 8.1 | 989.3 | 5.4 |
| | 02/06/2014 | 778.8 | 6.6 | 928.0 | 7.6 |
| | 07/07/2014 | 802.6 | 5.5 | 923.2 | 3.7 |
| | 04/08/2014 | 787.3 | 2.0 | 928.1 | 2.1 |
| | 27/08/2014 | 767.2 | 1.9 | 1009.9 | 3.5 |
| | 05/10/2014 | 835.5 | 4.6 | 941.8 | 3.3 |
| | 29/10/2014 | 815.8 | 3.2 | 959.5 | 2.8 |
| NG | 07/07/2014 | 974.3 | 3.4 | 984.4 | 3.9 |
| | 04/08/2014 | 979.0 | 4.4 | 984.9 | 2.6 |
| | 27/08/2014 | 1036.9 | 2.0 | 981.6 | 2.7 |
| | 05/10/2014 | 953.8 | 3.7 | 992.5 | 2.7 |
| | 29/10/2014 | 884.8 | 4.8 | 966.5 | 4.0 |
| | 04/12/2014 | 817.7 | 2.7 | 1037.1 | 3.6 |
| | 17/04/2015 | 779.1 | 2.9 | 1004.6 | 2.2 |

Thus, the density of needles is best described as a function of *FMC*. Correlations for wood show a linear increase with respect to *FMC* [6.22, 6.23]. Furthermore, Jolly et al [6.9] have also illustrated a linear relationship between foliar density and water content (wet weight).

In this study, PRI needle also exhibited a linear relationship with *FMC* (Fig. 6.2). However, this was found to be only true for mature needles. Young needles, as can also be observed from Table 6.1 behave dissimilar (approximately constant density). A detailed analysis is presented in Appendix D2. Only the final density-FMC model is presented here. This model is:

$$\rho_{FMC,all,mature} = 1.6\,FMC + \rho_{dry,all,mature} \qquad \textbf{Eq. 6.2}$$

and can be successfully used to predict the density of mature live wet needles independent of season (with 5% uncertainty). A comparison of measurements and Eq. 6.2 is given in Fig. 6.2.

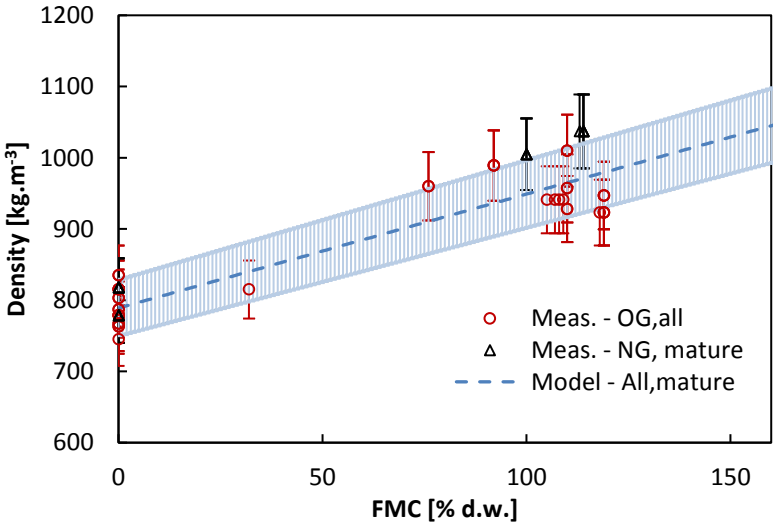


**Fig. 6.2. Comparison of measured density of mature PRI needles and estimated density (Eq. 7.3). Error bars indicate a 5% uncertainty.**

The relation between *FMC* and density is important to know and has significant implications. Particle density measurement of foliage can be obtained instantaneously and is inexpensive, whereas obtaining a *FMC* measurement requires time for conditioning and/or expensive equipment.

### *6.2.4. Thermal behavior of wet needles*

The impact of water in the solid phase was discussed in Chapter 1. From the summary given in Table 6.1 and the preceding discussion, one can deduce that, the thermal response of the needle will change, due to the fact that thermal mass is a function of density, which increases with *FMC*. If the density goes up, thermal mass increases and thus, time to ignition is longer, because it takes longer for the particle to reach its ignition temperature.

Such an evaluation can be illustrated with the thermal behavior as described by a *lumped capacitance analysis* [6.24]. It was concluded in Chapter 5 that, dry PRI needles have a thermally thin behavior, with $Bi_{rad,losses}$ = 0.077. Thus, a *lumped capacitance analysis* (uniform particle temperature profile; accurate when $Bi < 0.1$), can estimate the thermal evolution under the given heating conditions (radiant heating with losses due to natural convection and re-radiation).

The graph in Fig. 6.3 shows the thermal evolution ($\theta^*$) of the needles at three *FMC* levels (for three values of $\rho$ calculated according to Eq. 6.2). From a heat transfer perspective, it is evident that the needles at elevated *FMC* heat up slower. This slower heating is due to increased thermal mass, which was reduced by the increasing apparent density, which was in turn increased by the water content.

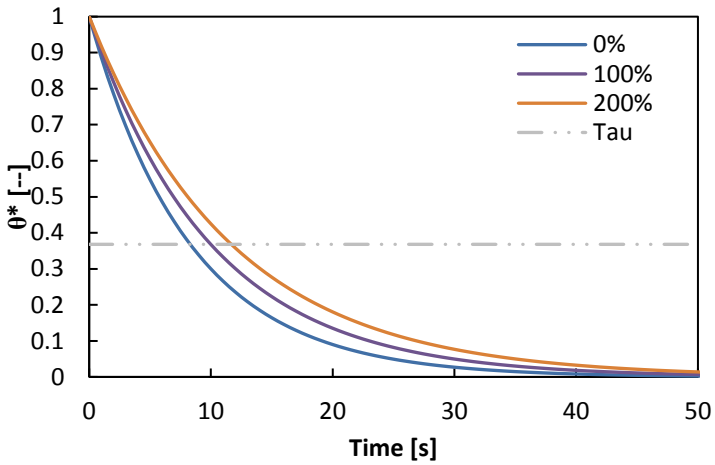


**Fig. 6.3. Thermal evolution of PRI needles with different FMC. Tau is the thermal time constant (see Chapter 4).**

Besides changing thermal properties, water is required to evaporate before ignition can commence. Future work should evaluate what the exact relation of these properties is for pine needles (or vegetative fuel in general), since no experimental evidence of the actual thermal behavior of wet pine needles was obtained here or elsewhere.

### *6.2.5. Fuel moisture content (FMC)*

The protocol and calculation (based on dry weight) are given in Chapter 2. Values for the *FMC* for all needle stocks (each month) are shown in Fig. 6.4. For each needle type, two measurements are shown. One measured in New Jersey immediately following collection and the second one in Edinburgh after arrival in the laboratory. The comparison was made in order to monitor if *FMC* was reduced in transit (due to drying). Overall, this was not the case.

Some differences exist between the *FMC* measurements. For example, the *FMC* for OG needles in July measured in NJ is much higher than what was measured in Edinburgh. This difference is because in NJ, a mix of old and new generation needles was measured. In Edinburgh the needles were separated. Similarly, for the NJ measurement in November, OG needles were green and brown (dead). In Edinburgh

these were separated into only green and only brown needles. That is why there are two measurement points (EDI – OG) in November. The lower one is the dead, brown needles, the higher value corresponds to the live, green needles.

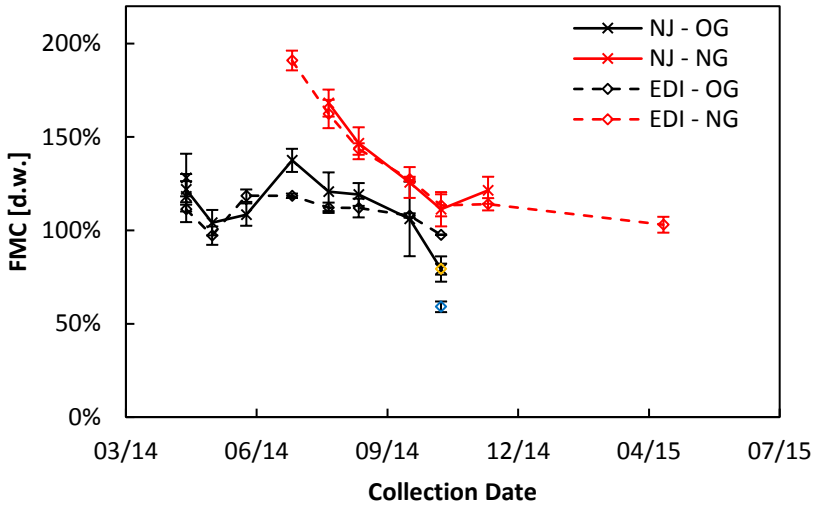


**Fig. 6.4. Comparison of FMC measurements done in NJ on the day of collection and at Univ. of Edinburgh at the day of arrival. The data points are referred to (from left to right) as: April 2014 – May – June – July – August – September – October – November – December – April 2015. "EDI – OG November" has three data points, black: live, blue: dead, yellow: mixed.**

Error bars in Fig. 6.4 correspond to one standard deviation of the measurements. Measurements done in NJ generally show a higher error than measurements done in Edinburgh. This is attributed to the measuring technique. In NJ samples were on the order of hundreds of grams, with little dissection of small debris and dead needle matter. Samples in Edinburgh were smaller, on the order of tens of grams, were free of any impurities (unwanted material) and care was taken that only healthy needles were included in the sample.

The spring dip (SD) was found to occur in May of 2014. The SD is associated with a valley in the *FMC* which occurs after the start of photosynthesis [6.8, 6.9, 6.25-6.27]. Jolly et al showed in [6.8] and [6.9] that this dip is not solely due to a reduction in water content but rather involves a change in chemical composition (dry mass). This

was not fully supported by density measurements discussed in Chapter 5, because a distinct rise in dry particle density was not observed.

Samples were tested at various residual *FMC*. The residual *FMC* was obtained by conditioning the sample for a designated time (< 24 hours). The conditioning periods were not always the same because needles release water at varying rates (see Fig. 5.7 in Chapter 5). During the conditioning period, the mass loss was periodically measured until a desired residual *FMC* (*FMC* after conditioning period) was achieved. This was somewhat arbitrary because it did not matter what the residual *FMC* was. However, the aim was to obtain ignition data over a wide range of *FMC* for a particular stock of needles. Generally, it was desired to have data points at 0%, 20-60%, 60-100%, and unconditioned *FMC*.

The condition technique was assessed (Chapter 5) in order to evaluate loss of volatiles during the drying process. Oven dried densities were approximately 7% lower than air dried densities, which means that, indeed some portion of extractives (e.g. essential oils) is lost in the drying process. This can have some adverse effect on the ignitability and combustibility of the fuel [6.7]; however an exact relation was not quantifiable.

The following section explores the flammability assessment that was introduced in Chapter 5, for unconditioned needles.

### *6.3. Flammability assessment with unconditioned foliage (as per Chapter 5)*

The assessment in Chapter 5 illustrated differences in seasonality of the flammability parameter, ignitibility and combustibility. Therefore, a system was proposed to estimate a total flammability factor accounting for both parameters. Results from combustion experiments with unconditioned needle samples are now assessed in the same fashion as was done with conditioned (0% *FMC*) needle samples in Chapter 5. Finally, the total flammability factors of conditioned and unconditioned needles are

compared. This comparison is made to illustrate effects of *FMC* on the flammability, since the *FMC* is also a seasonal parameter.

### *6.3.1. Individual flammability parameter*

#### Ignitibility

When testing unconditioned needles, the water content in the needles introduces a heat sink (besides altering effective properties), thus requiring additional energy to evaporate significant amount of water before ignition can occur. In the presence of a constant energy source, this results in longer ignition times. This is clearly identifiable in Fig. 6.5 for both OG and NG needles. (Remark: Unconditioned NG needles were not tested in July because of limited resources.) Overall, the water content (and release of it during heating) causes significant variability in the ignition time results, but is much longer than for fuel with 0% *FMC*.

*OG needles*

The ignition behavior of unconditioned OG needles was relatively constant over the summer months (Fig. 6.5). The longest ignition times are found for April 2014 samples and shortest for November 2014 with high fluctuations in between.

The low *FMC* during the SD does not correspond to the shortest ignition time (Fig. 6.5), which is an indication of the conclusion, that the SD is driven by an increase in dry mass and not in a reduction of water mass [6.9]. Although, ignition results from dried needles samples did not fully agree with this. Thus, there is likely a contribution of both factors, chemistry and *FMC*. As can be seen from the difference in ignition time of dry and wet needles it is evident that variation due to chemistry are small compared to the impact of water content. Time to ignition decreases in the spring before emerging NG needles. This correlates weakly to the decreasing ignition time of dry needles in this time period.

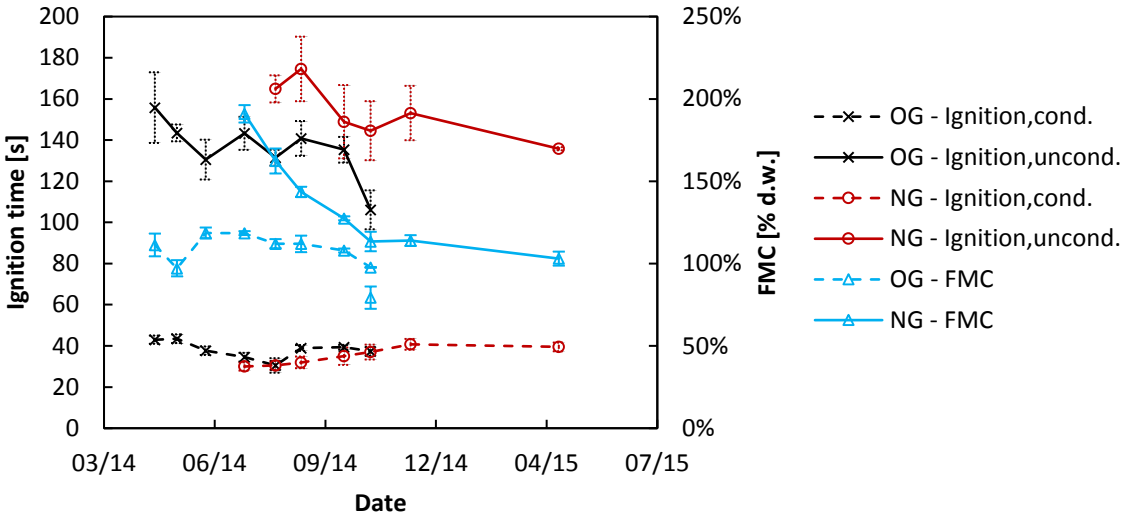


**Fig. 6.5. Seasonality of time to ignition of conditioned and unconditioned samples from April 2014 to April 2015. FMC is included for reference. Unconditioned needles were not tested in July because of limited resources.**

Overall, the decreasing trend of the ignition times of unconditioned OG needles can be weakly linked to the reduction in *FMC* over the test period.

*NG needles*

The high *FMC* for young NG needles is also not the sole driving mechanism for the ignition behavior. Ignition for August samples is slightly shorter, although within the error bars, than September samples. September-November results show decreasing trends; followed by a short peak in December. This peak also coincides with the peak ignition time for conditioned samples. The conditioned needles showed a continuously increasing trend from July to December (mature needles ignite slower). Thus, effects from *FMC* and chemical composition are competing, and they are not in balance. The effect of *FMC* on ignition time (unconditioned needles) dominates over the effects of changing chemical composition (conditioned needles).

It was discussed that dehydration rates are faster for young NG needles (Chapter 5). This can explain why the ignition time for these needles (August) is not significantly faster even though they have a much higher *FMC*.

### Combustibility

*OG needles*

Results of the pHRR estimations are presented in Fig. 6.6. Throughout the experimental period, OG needle *FMC* was relatively constant (100-120%) with the exception for the SD (May) where the *FMC* dropped to 90-100%. The drop in *FMC* does not correspond to any significant increase in combustibility. Values for pHRR are constant with minor fluctuations in July and August.

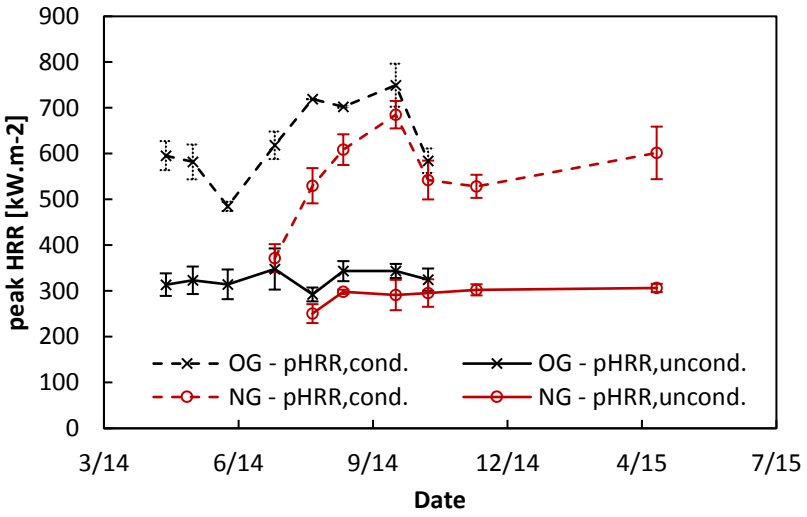


**Fig. 6.6. Seasonality of pHRR of conditioned and unconditioned samples from April 2014 to April 2015. Unconditioned needles were not tested in July because of limited resources.**

*NG needles*

NG samples in August have a *FMC* of approximately 150%, significantly higher than the *FMC* of OG needles, which can explain the reduced pHRR. NG sample in July had a *FMC* of around 190% and thus it can be assumed that, the pHRR of these samples is likely less than the one found from August samples (if igniting at all). Samples tested

in September and later (*FMC* < 140%) showed little variation in pHRR, similar to OG needles.

It is evident, and not unexpected, that, conditioned needle samples produce a higher pHRR compared to unconditioned needles (Fig. 6.6). The results confirm the initial discussion that water vapor in the gas phase reduces the combustion intensity due to oxygen displacement and cooling of the combustion gases and flames (reducing combustion efficiency and the heat flux feedback to the sample surface). These results are in agreement with Jervis and Rein [6.7] Furthermore, it can be observed that, pHRR is independent on the *FMC* in the range of typical seasonal levels, 90-140% (except August where *FMC* was around 150%), which masks seasonal effects that are observable for samples with 0% *FMC*.

NG samples tested in April 2015, which are considered mature needles at this stage, have comparable ignition and combustion intensity than OG samples tested in April 2014. Thus, as before, these can be considered equivalent and the flammability evolution of a needle for a full life cycle can be coupled together from the two data sets.

**Normalization of flammability parameter**

Normalization of each parameter was done with respect to the critical conditions found from dry needles. This condition reflects the worst-case scenario where the flammability is the highest. Normalized flammability parameter in Fig. 6.7, illustrate the fire hazard from the wet needles with respect to dry needle flammability. It shows that NG needles (black and red circles) are only marginally less flammable than OG needles (As per discussion in Chapter 5, the “first year” condition is a hypothetical case. Most likely, there will always be two or more generations on the tree; for evergreens).

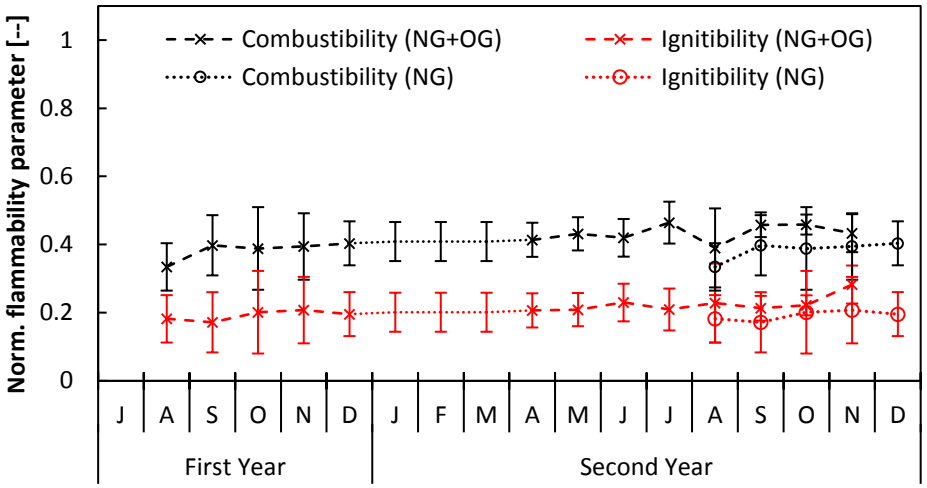


**Fig. 6.7. Seasonality of individual flammability parameter for OG and NG needles ("Dotted" section of the curve means that no tests were conducted in this period and data is interpolated between Dec. and April.).**

Overall, it can be concluded that, high *FMC* masks the effects that are observable for conditioned samples ($F_{tot,dry}$ is in the range 0.5-1.0) and drastically reduces the flammability (ignitibility and combustibility).

The fluctuation observed in Fig. 6.5 and Fig. 6.6 for wet needles (ignition time and pHRR, respectively) are less obvious in Fig. 6.7. This is because of the use of the critical condition for the normalization (translation to flammability). For example: ignition time variations over the test period for dried needles and wet needles are similar (Conditioned OG and NG: 11.2% and 12.3%, respectively; unconditioned OG and NG: 10.7 and 9.1%, respectively). However, a small rise in ignition time of dried needles still corresponds to a more flammable condition compared to a larger reduction in ignition time for wet needles (because it still ignites faster).

One may question the critical condition used for normalization (dried fuel). This was selected because if the "worst case" for wet fuel is used, one may not related the flammability of dried and wet fuel directly. Thus, a common condition is required. The overall "worst case" condition is a distinct condition which can be identified readily.

The preceding discussion considered unconditioned needles at their inherent FMC levels and the conclusion just stated is thus far only valid in the region of tested *FMC*. It needs to be determined to what extent such assumption holds true when the *FMC* is lowered, as might be the case in severe drought condition or other factor that increase the plant stress level (e.g. mountain beetle attack [6.28]). It is hypothesized that, there exists a *FMC* threshold at which other factors than water content become increasingly more important (e.g. fuel properties). The latter part of this chapter (Section 6.4) explores, at what level this might occur, by conducting combustion tests with partially dried needles (having a residual *FMC* lower than initial).

### *6.3.2. Flammability of OG and NG needles*

As done in Chapter 4, both flammability parameters are now combined to a flammability representation of the needle type (OG and NG). This is shown in Fig. 6.8 with a simple dynamic fuel load distribution ($w_{og}$ is not constant during the growing season; see discussion in Chapter 5).

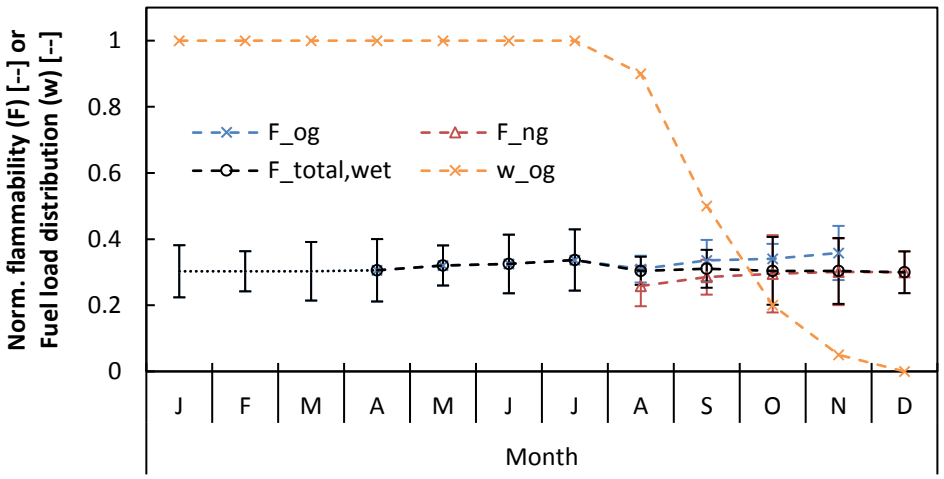


**Fig. 6.8. Seasonality of (1) flammability of OG (blue) and NG (red) needles (incl. ignitibility and combustibility parameter), and (2) total flammability factor (grey) of PRI foliage (incl. OG and ND needle flammability), and (3) the weighting coefficient $w_{og}$ (orange). ("Dotted" section of the curve means that no tests were conducted in this period and data is interpolated between Dec. and April.).**

It is evident from Fig. 6.8 that, the load distribution model is irrelevant for wet PRI needles, because the flammability of OG and NG needles is marginally different (compare blue and red curve). Thus, it is enough to consider for example only unconditioned mature needles in future flammability analysis, because they are more flammable compared to NG needles (conservative approach). This will be beneficial, because it means that experimental campaigns (testing live unconditioned needles) can be reduced to only one needle generation, as well as a single time of the year. This will relieve the financial burden and safe time.

### *6.3.3. Total flammability factor*

The OG and NG flammability factors are now averaged, to represent a total flammability factor that can be used to describe unconditioned live PRI foliage in relation to the critical condition (most flammable; dry fuel). The total flammability factor is plotted in Fig. 6.9, with historic fire data from the NJ Pine Barrens [6.29].

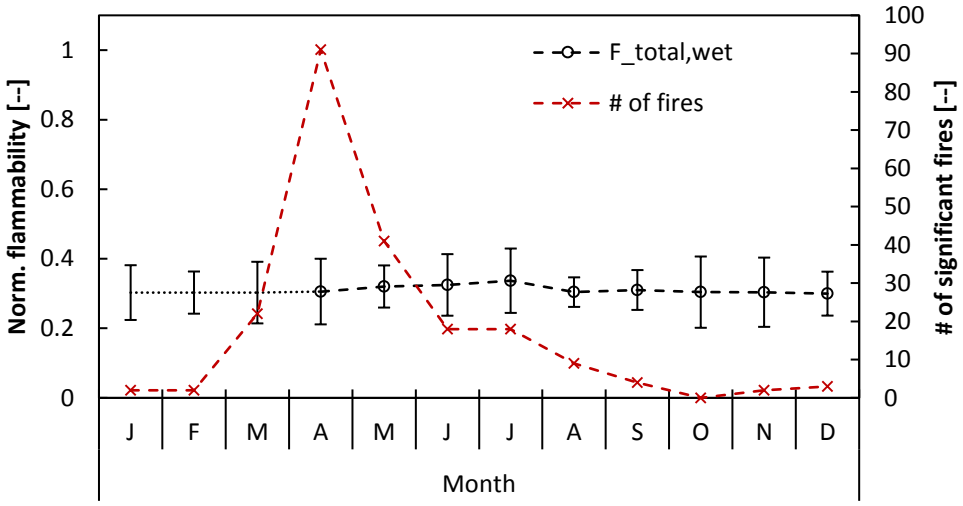


**Fig. 6.9. Total flammability factor compared to historic fire data [6.29]. ("Dotted" section of the curve means that no tests were conducted in this period and data is interpolated between Dec. and April.).**

Although a peak can be observed in July, it is minor, and falls within the variability of the ignition and pHRR measurements (error bars: standard deviation). There is no

variation of the flammability of wet PRI needles over the year. Therefore, as was the case with conditioned needles, unconditioned needle flammability is also not a driving factor behind the occurrence of the typical fire season.

### *6.3.4. Comparison of dry and wet fuel flammability factor*

A comparison of both flammability factors, for wet and dry foliage, is provided in Fig. 6.10. It shows that, trends are not the same. Nor are they on the same level. This is of course due to the selection of the critical condition. As was observed by the individual flammability parameters, the total flammability factor of the wet needles masks seasonal trends that were observed with dry fuel.

The selection of the condition used in the normalization is important. It was defined as the "worst-case" with fastest ignition and highest combustion intensity observed. If in future experimentation, additional fuel is tested and it is found that it ignites faster or burns more intense, the critical conditions must be re-evaluated to always reflect the "worst-case". This is because it is desired to have $F_{total}$ = 1 to reflect the most flammable condition.

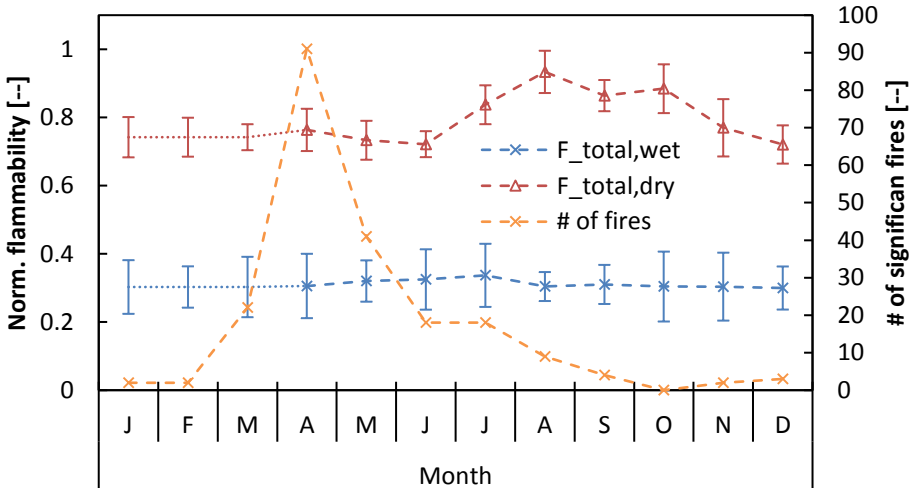


**Fig. 6.10. Comparison of total flammability factor for conditioned (red) and unconditioned (blue) PRI needles. Historic fire data [6.29] (orange). ("Dotted" section of the curve means that no tests were conducted in this period and data is interpolated between Dec. and April.).**

Dry and wet flammability factors represent the extremes that are possible, fully dehydrated and natural state, respectively. The question is which one is more appropriate to use in a characterization of live foliage? Both factors represent the same fuel. From a purely material stand point it is certainly the dehydrated state, because that reduces any adverse effects resulting from the dynamic nature of the water content. One may argue the other side of the coin and say that live foliage will naturally never be at 0% *FMC*. Both arguments have their validity, which leaves the only solution: flammability is a dynamic fuel parameter and must be defined in (at least) two dimensions, in time (seasonality) and *FMC*. Thus, the flammability at a given time of the year with a given *FMC*, $F_{total,FMC}$, can be defined as:

$$F_{total,FMC} = f(t, FMC) \quad \textbf{Eq. 6.3}$$

The two curves ($F_{total,dry}$, and $F_{total,wet}$) in Fig. 6.10 represent two boundary conditions, 0% and maximum *FMC*, respectively:

$$F_{total,dry} = f(t, 0) \quad \textbf{Eq. 6.4}$$

$$F_{total,wet} = f(t, FMC_{\max}) \quad \textbf{Eq. 6.5}$$

The latter equation, Eq. 6.5, may be further reduced to a constant, because it was found in Fig. 6.10 that variation in wet fuel flammability, $\Delta F_{total,wet} = 0.037$ are much smaller compared to variation in dry fuel flammability, $\Delta F_{total,dry} = 0.213$ Additionally, one may define the maximum *FMC*, $FMC_{max}$, as a function of time

$$FMC_{\max} = g(t) \quad \textbf{Eq. 6.6}$$

which can be deduced from an averaging of the results presented in Fig. 6.4, or the *FMC* history of PRI foliage given in Chapter 1. For PRI foliage, this is less critical,

because it was shown that the flammability is not influenced by the variability of $FMC_{max}$. However, other foliage may produce different results. A schematic of the flammability as a function of time (season) and *FMC* is illustrated in Fig. 6.11. Thus far, the two boundary conditions (0% and maximum *FMC*) have been identified and are idealized in the schematic.

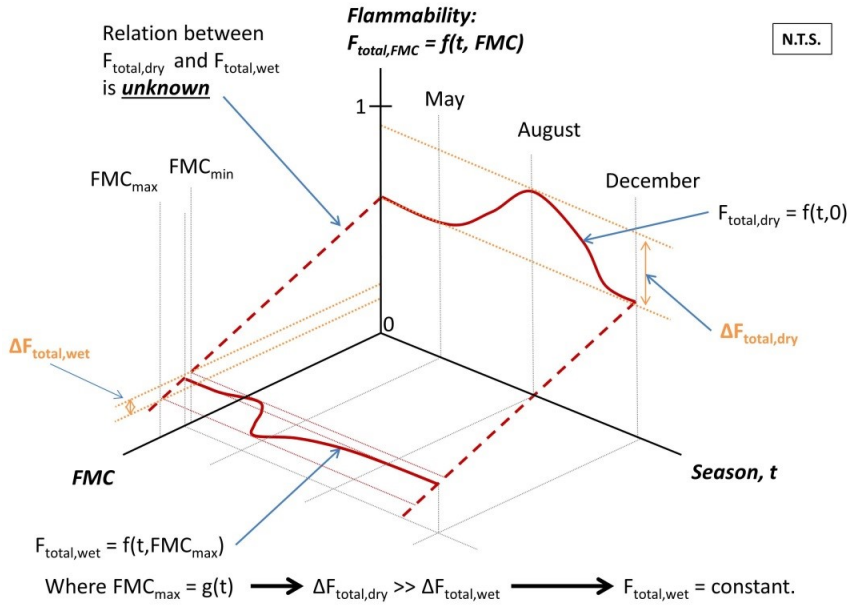


**Fig. 6.11. Schematic of live fuel flammability as a function of time (season) and FMC. The relationship between the boundary conditions is unknown.**

Still unknown is the relationship between these two boundaries, where 0% < *FMC* < $FMC_{max}$. The linear relation indicated by the red "dashed" line is selected arbitrarily at this point. This will be subject of the proceeding analysis. Furthermore, the following section will evaluate if a distinct FMC can be defined below which seasonal trends become important. This is achieved, by subjecting partially dried samples to combustion tests and evaluating the ignition and burning behavior as a function of *FMC*.

## *6.4. Using FMC as a predictor of ignition and combustion intensity*

The foregoing discussion identified that, seasonal trends of ignitability and combustibility, as determined by dry fuel, are masked by the *FMC* when the fuel is unconditioned. The level at which fuel composition becomes important is yet to be determined. The following analysis provides insight in what occurs between the two extremes of Fig. 6.10 and 6.11 (0% and max *FMC*), i.e. what is the ignition and combustion behavior between 0% to peak *FMC*?

### *6.4.1. Time to ignition as a function of FMC*

Several groups have illustrated that ignition time is a function of the *FMC*, for example [6.10, 6.13, 6.30, 6.31]. The variability of accuracy of correlations induces some differences in opinion and conclusions about the suitability to present the ignition time as a sole function of *FMC* for live forest fuel. It was shown in the previous chapter that influences due to state of growth exist. But it was also shown that high *FMC* masks these effects (Section 6.3). The following discussion explores how well the ignition results from FPA experiments compare with other works and to what extent a known semi-physical model can be used to predict the ignition behavior of live pine needle, as obtained here.

#### Empirical Correlation

At first all data points are plotted together in Fig. 6.12. This includes OG and NG needle samples over the entire period of the study at all *FMC* levels. In this graph a clear linear relation between ignition time and *FMC* is evident. The linear regression model indicates a good agreement with the data ($R^2 = 0.93$) and shows that *FMC* is a dominant parameter influencing the ignition dynamics. Simple empirical models have limited use but are an easy first approximation of a relationship. The following discussion will lead to an assessment of more sophisticated physics-based model.

The experimental results shown in Fig. 6.12, which include all test results (OG and NG needle samples), show some variability which can be attributed to the nature of the fuel, complexity of the ignition process [6.32-6.34], and test conditions (external heat flux and ambient conditions); but also due to some uncertainty in the *FMC* of each sample (gradient in the sample).

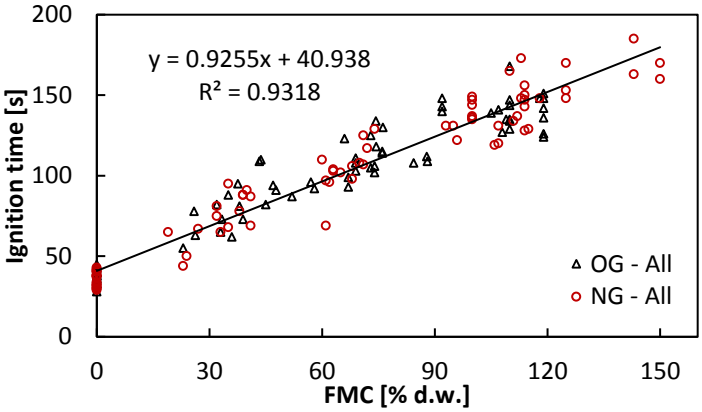


**Fig. 6.12. Time to ignition of all OG and NG needles plotted with respect to FMC (N = 152).**

Table 6.2 shows the averaged ignition time for all conditioned needles. The standard deviation highlights, that even at 0% *FMC* average variation can be up to 9%. A similar uncertainty was observed for dead needle samples in Chapter 3. Tests with conditioned needles were discussed in detail in Chapter 5. The maximum error was up to 12% (for NG needle sample tested in October). Putting this into perspective of the influence of *FMC*, the scatter in Fig. 6.12 can be considered acceptable, with $R^2 = 0.93$.

Table 6.2. Selected averaged ignition times for dry PRI needle samples (0% *FMC*).

| | Ignition Time [s] | | St.dev. [%] |
|---|---|---|---|
| | Mean | St.dev. | |
| OG, before SD | 43.3 | 2.1 | 4.85 |
| OG, after SD | 37.8 | 2.1 | 5.56 |
| OG, all | 38.1 | 2.1 | 5.51 |
| NG, young | 32.9 | 3.0 | 9.12 |
| NG, mature | 40.1 | 2.4 | 5.99 |
| NG, all | 35.0 | 2.8 | 8.00 |
| All | 36.6 | 2.4 | 6.56 |

Furthermore, this variation is much smaller than previously recorded results [6.10]. McAllister et al [6.10] contributed the variability to plant chemistry and formulated a new relation between ignition time, *FMC* and plant chemistry. This is not practical, because detailed chemical analysis is required. Neither is it necessary as suggested by results presented here. Ignition results obtained with the Cone Calorimeter by Weise et al. [6.13] also showed less variability ($R^2 = 0.91$). Moro [6.31] studied the ignition time as a function of *FMC* ($R^2 = 0.84$) of forest fuel (Erica arborea) over a long period (1989-2007). He used an epiradiator and showed a linear correlation between ignition and *FMC*. The test period spans almost 20 year, which is likely inducing a fraction of the uncertainty (long term effects, e.g. tree stand growth, or climate). McAllister et al [6.10] concluded in their work that, *FMC* alone could only explain 74-80% of the variability, depending on species.

The preceding paragraph indicates that one can find a wide range of variability in the ignition data available, with the current one being the one with least variability ($R^2 = 0.93$). It was discussed in several parts of this thesis that sample orientation (sample structure and preparation) is critical for accurate flammability estimations. In this respect, the Cone used by Weise et al [6.13], FPA used here or FIST used by McAllister et al [6.10], provide a sound basis, because they are standardized apparatuses where standard sample sizes are used. Although, sample preparation, e.g. initial mass, can still vary. Both the FPA (in this Chapter) and Cone (in [6.13]) are operated under natural convection conditions. The FIST in [6.10] is operated under forced convection condition. This will add additional heat and mass transfer mechanisms that might be the cause for the higher variability in results obtained by McAllister et al [6.10]. Impacts of forced convection can be reviewed in Chapter 3 and 4 of this thesis.

McAllister et al [6.10] found that ignition times of particles with the same *FMC* but collected at different times of the year (spring vs. summer) can be significantly different, almost 30%. They found ignition times to be longer in the spring compared

to summer and attributed plant chemistry. Findings from combustion tests with conditioned needle (OG) discussed in Chapter 5 also showed a similar trend (see brief summary of averaged ignition times in Table 6.2). Tests with unconditioned OG needles (Fig. 6.5) showed this as well. This trend is further assessed with data shown in Fig. 6.13by separating OG needle tests into two groups: "before SD" and "after SD".

*OG needles*

When only the OG results are separated, data into these two periods, small differences in the ignition times can be found. These are shown in Fig. 6.13. Needles appear to ignite faster after the SD occurred. This is the case for the entire range of *FMC* levels tested. Some variability and overlapping exists, however, the overall trend shows a distinction. Because the sample (bulk) properties and experimental conditions didn't change, this can be attributed to a change in particle properties, resulting from seasonal variations.

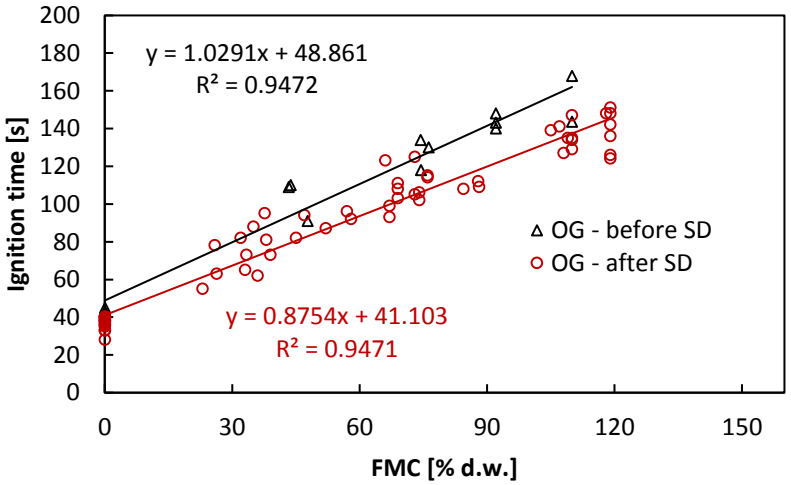


**Fig. 6.13. Time to ignition of OG samples plotted with respect to *FMC* and separated into data sets for a period before (and at) the SD and after the SD.**

*NG needle*

The ignition behavior of only NG needle samples with respect to *FMC* is given in Fig. 6.14. In this graph, ignition time data that was initially given in Fig. 6.12 was separated

into two groups. The first group corresponds to needles collected in 2014 (growing) and the second group to needles collected in April 2015 (mature). The difference in the trends of the ignition time is minor. When comparing the results of NG samples at 0% *FMC* (Table 6.2) a difference of around 7 s in ignition time between young and mature needles is apparent. Conclusively, this shows that the water content has a far more significant effect on the ignition behavior than the change in composition.

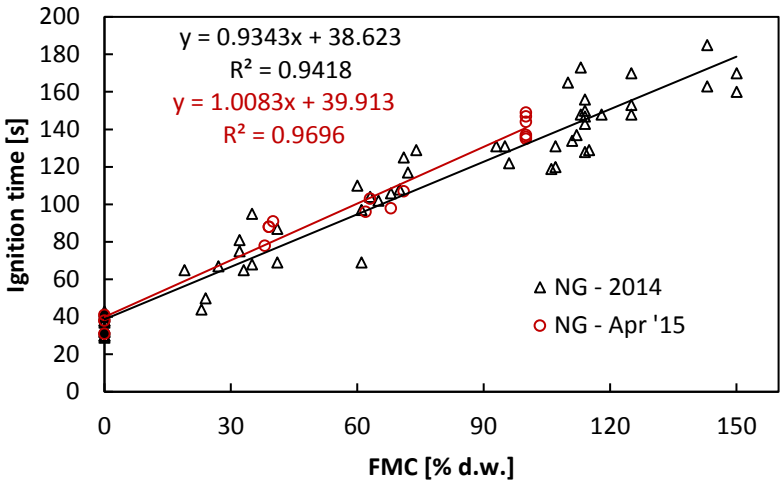


**Fig. 6.14. Time to ignition of NG samples plotted with respect to *FMC* and separated between 2014 and 2015 samples.**

Further separation can be made; time to ignition results from July 2014 and April 2015 NG samples are compared in Fig. 6.15. The former represents NG needles after the SD, the latter NG needles before the spring SD. Over the span of the *FMC* levels observed, July 2014 needles have faster ignition times compared to needles in April 2015. This correlates well with the observation of OG needles before and after the SD discussed earlier (Fig. 6.13) and findings from McAllister et al [6.10]. Unfortunately, there was not enough fuel in the July 2014 stock (for NG needles) to conduct more than three experiments. Thus, it is inconclusive if this behavior is typical. However, the comparison to OG needle samples strongly suggests that it is.

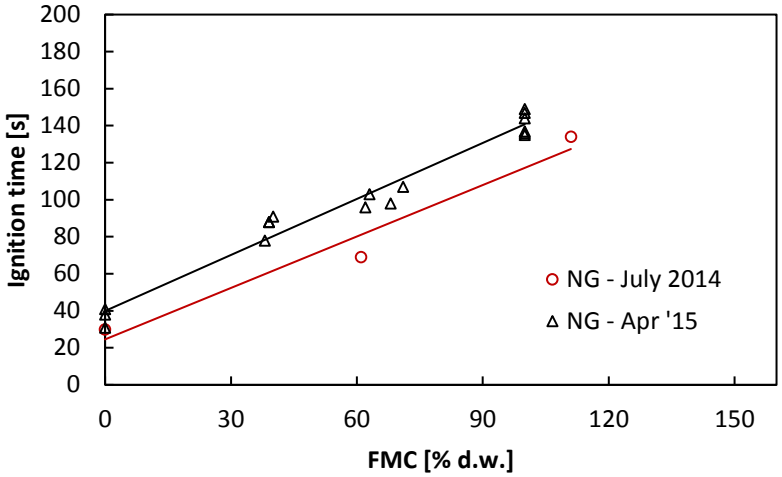


**Fig. 6.15. Time to ignition of NG samples in July 2014 and April 2015 with respect to *FMC*.**

The above discussion shows, that small seasonal effects exist even for wet needles. Most noticeably at times before and after the spring dip. In light of the complexity of the ignition process, dependence on experimental conditions and the strong influence of *FMC*, these effects can however be considered marginal.

Finally it is concluded that, a single linear model can be utilized to describe the relation between ignition time and *FMC*, based on the entire ignition data set (Fig. 6.12):

$$t_{ig,FMC,all} = 0.93\ FMC + t_{ig,dry,all} \qquad \textbf{Eq. 6.7}$$

The intercept of the correlation, $t_{ig,dry,all}$, refers to the averaged ignition time for all conditioned samples, 36.6 +/- 2.4 s, which is given in Table 6.2. Experimental data (separated into time periods discussed previously) are shown in Fig. 6.16 and compared to the model, with a 10% error. This error was chosen because it reflects the experimental error (one standard deviation) for all dry needle samples (Table 6.2).

The model slightly under-estimates a portion of the experimental results. When observed closely, results from tests that correspond to the time period before the spring dip (OG – before SD and NG – 2015 data series in Fig. 6.16) are the once that are

under-estimated. Thus, the model predicts the ignition more accurately in the summer and fall month (no tests were done in the winter). The under-estimation is acceptable, because it leans towards a slight conservative prediction.

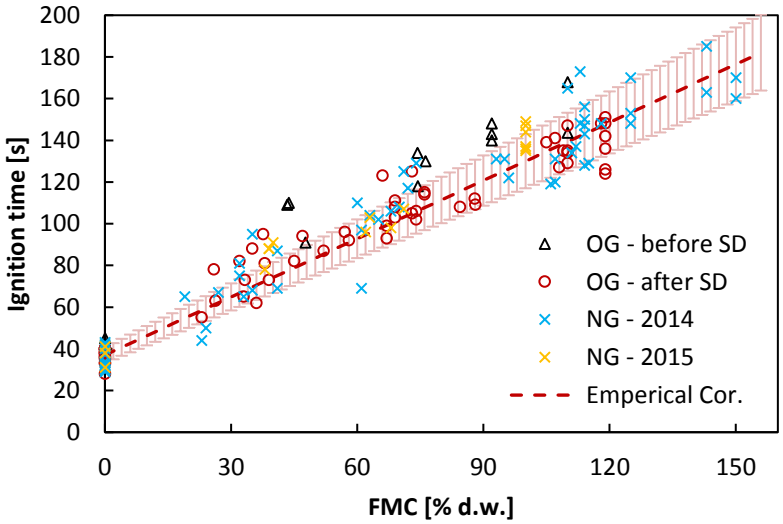


**Fig. 6.16. Experimental and estimated ignition time for OG and NG needles with respect to *FMC*.**

This correlation is surprisingly simple, but the reader is reminded, that the coefficients of correlation are specific for the test conditions (most significantly the heating rate), test apparatus, and fuel. Other linear models, for example from Weise et al [6.13], Dimitrakopoulos and Papaioannou [6.30], Moro [6.30], or McAllister et al [6.10] have different coefficients. Thus, extrapolating to other conditions should be done with caution.

### Semi-Physical Correlation

The coefficients of the regression model depend on many factors: external heat flux, heat losses, fuel (particle properties), sample properties, as well as experimental set-up. Therefore, empirical models are restricted to the conditions in which they were determined. Models based on physical parameters are more sophisticated and will be more useful, without conducting experiments for all conditions possible. McAllister et al [6.10] further suggest that, a semi-physical model developed by Pickard and Wraight

[6.35] is useful for further analysis, because it showed promising comparison to their experimental results with live Douglas-fir and Lodgepole pine foliage. They have also employed the modification that was adopted by Babrauskas [6.34]. Based on their results, this semi-physical model is used in the following analysis and comparison to PRI ignition data.

Pickard and Wraight [6.35] developed a semi-empirical correlation that is based on a summation of the time to ignition of dry fuel (time to reach a critical temperature) and the time it takes to evaporate water in the fuel:

$$t_{ign,PW} = t_{ign,dry} + \frac{\Delta h_{vap} d \rho_o FMC}{a_s \dot{q}"_{ext}} \qquad \textbf{Eq. 6.8}$$

This correlation was developed and validated for spontaneous ignition, assuming an absorptivity of one and neglecting any heat losses. Furthermore, this model was only developed for very thin material (cellulose sheets 0.05-0.78 mm thick). PRI pine needles are much thicker (diameter: 1.39 mm). They concluded that, for thick material, a significant temperature gradient will result in incomplete drying, i.e. water still remains in the fuel at ignition. It was concluded that dry PRI needles are thermally thin and that it is likely that wet needles also behave thermally thin because the internal thermal resistance reduces with increasing conductivity (due to water).

The experimentation in the current work was done for piloted ignition, which was explained to be faster than spontaneous ignition. This is a significant experimental difference, because spontaneous ignition allows for longer heating period compared to piloted ignition. This is often associated to a higher ignition temperature [6.1]. It needs to be assessed, if the model is still applicable. In this correlation the slope of the linear relationship is

$$slope_{PW} = \frac{\Delta h_{vap} d \rho_o}{a_s \dot{q}''_{ext}} \qquad \textbf{Eq. 6.9}$$

The heat of evaporation of water is 2,257 kJ.kg$^{-1}$, the diameter of the needle, $d$, is 1.39 mm and the global dry density, $\rho_o$, is 787 kg.m$^{-3}$ (from Chapter 5). The absorptivity was discussed in the previous Chapter and found to be 0.72 for live vegetation in the FPA. A heat flux of 25 kW.m$^{-2}$ was used for all tests. With these values, the slope is 137 and has the units of time (seconds). In order to compare it to the slope from the linear regression model (units: second per % *FMC*) found from the experimental data discussed here, the value needs to be divided by 100. This compares reasonably well to the slope found in the linear model (0.93), although it is slightly higher.

The higher slope means, that Pickard and Wraight's correlation (Eq. 6.8) tends to over-estimate the ignition time of PRI needles. The comparison to experimental data is shown in Fig. 6.17.

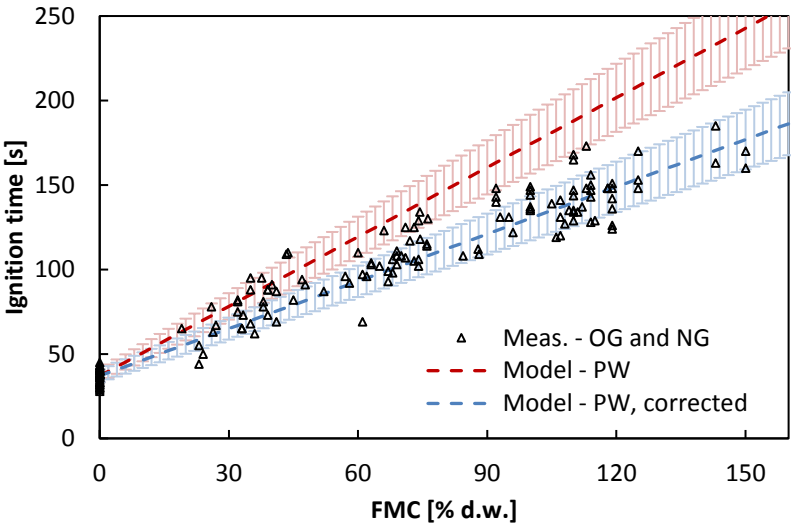


**Fig. 6.17. Experimental data and Pickard/Wraights (PW) [6.35] model predictions (PW: Eq. 6.8 and PW, corrected: Eq. 6.11).**

Constant parameters used in the calculation of the slope have some uncertainty, for example the diameter measurements (n=40) had a standard deviation of 0.09 mm,

which is roughly 7%. The more significant factors, however, are the ignition criterion and the assumption that all water is evaporated before ignition. Pickard and Wraight verified that this model applies to spontaneous ignition [6.35]. Piloted ignition is faster (which was discussed in Chapter 2). This change in ignition regime is to some extent accounted for by using dry needle ignition times corresponding to piloted ignition. Furthermore, the needles are physically thick compared to what this model was validated for, which means that the needles are most likely not fully dehydrated at the time of ignition (although a thermally thin behavior was estimated).

Pickard and Wraight's correlation (Eq. 6.8) should provide a better solution for spontaneous ignition, because the longer exposure time (until ignition) compared to piloted ignition results in higher water loss. So, considering water evaporation and pyrolysis as subsequent events leading to ignition might be a reasonable assumption. From this assumption one can deduce, that in case of piloted ignition (under the same heating condition) water remains in the particle at the time of ignition. In order to accommodate the difference in ignition regimes, and thus the state of saturation of the particle at the time of ignition, a correction factor, $C_B$, is included in the correlation (Eq. 6.8). This was first done by Babrauskas [6.34], who defined the correction factor, $C_B$ as:

$$C_B = 33{,}200(\dot{q}''_{ext})^{-2} - 8.7 \qquad \textbf{Eq. 6.10}$$

Which replaced $\Delta h_{vap}$ in Eq. 6.8. This correction factor, $C_B$, did however, not produce an acceptable correlation with the data set from FPA tests, likely due to the empirical nature of $C_B$. It was developed from much thicker samples of Monterey pine wood (9.0 mm). McAllister et al [6.10] were able to successfully use it with their experimentation (including a variable for surface absorptivity). This suggests that the correction factor, $C_B$, has limited applicability to live forest fuel. Therefore, the empirical correlation developed in this work (previous subsection) was utilized to obtain a unique correction factor, $C_T$, for this data set.

This correction factor, $C_T$, is in the range, 0-1; a correction factor of unity corresponds to the case where all water is evaporated before ignition. If $C_T < 1$, it indicates that, the particle has a residual *FMC* at the time of ignition. When the needles are wet, the water in the needle acts as a heat sink, which will absorb some of the energy that is otherwise utilized for raising the temperature. This further justifies the assumption that a thermal gradient is likely in live foliage, causing incomplete dehydration before ignition. However, it was also discussed that this effect competes against the effect of a likely higher conductivity (faster thermal response). The exact relation is unknown at this time. Further analysis is required to fully understand these phenomena. The new, corrected correlation has the form

$$t^*_{ign,PW} = t_{ign,dry} + \frac{C_T \Delta h_{vap} d \rho_o FMC}{a_s \dot{q}"_{ext}} \quad \textbf{Eq. 6.11}$$

In order to obtain a suitable value for $C_T$, Eq. 6.7 and Eq. 6.11 are set equal to each other:

$$t_{ign,FMC,all} = t^*_{ign,PW} \quad \textbf{Eq. 6.12}$$

Because all other parameters are known, one can solve for $C_T$, and thus deduce a value of the residual *FMC*.

$$0.93 = \frac{C_T \Delta h_{vap} d \rho_o}{a_s \dot{q}"_{ext}} \quad \textbf{Eq. 6.13}$$

$$C_T = 0.93 \left( \frac{\Delta h_{vap} d \rho_o}{a_s \dot{q}"_{ext}} \right)^{-1} = 0.678 \quad \textbf{Eq. 6.14}$$

This means that, the needles retain 32% of the initial *FMC* at the time of ignition, under the given heating rate. Jolly and Butler [6.36] conducted an experimental series with

live foliage to determine the ignition behavior in relation to water content and plant chemistry. In this series they were also able to determine the residual moisture content of live foliage after ignition. The results from these experiments are valuable in verifying the assumption that foliage does not fully dehydrate before igniting. The species tested was lodgepole pine (*Pinus contorta*) and extinguishing immediately after ignition was achieved by submersion of the burning fuel in a pure nitrogen gas stream. It was reported that the residual *FMC* is approximately 9.5% of the initial *FMC*, but can be as high as 30%. The correction factor, 0.68 (translating to 32% of the initial *FMC*) compares reasonably well with the findings of Jolly and Butler [6.36]. This correction factor, $C_T$, is unique to this data set and sensitive to fuel, experimental and heating conditions and should be used with caution when extrapolating to conditions other than the ones presented here.

From the discussion above it can be concluded that, the model will predict the ignition of live vegetation to an acceptable accuracy, which is shown in Fig. 6.18. A 10% error (as was done with the empirical model before) is shown to include most data points.

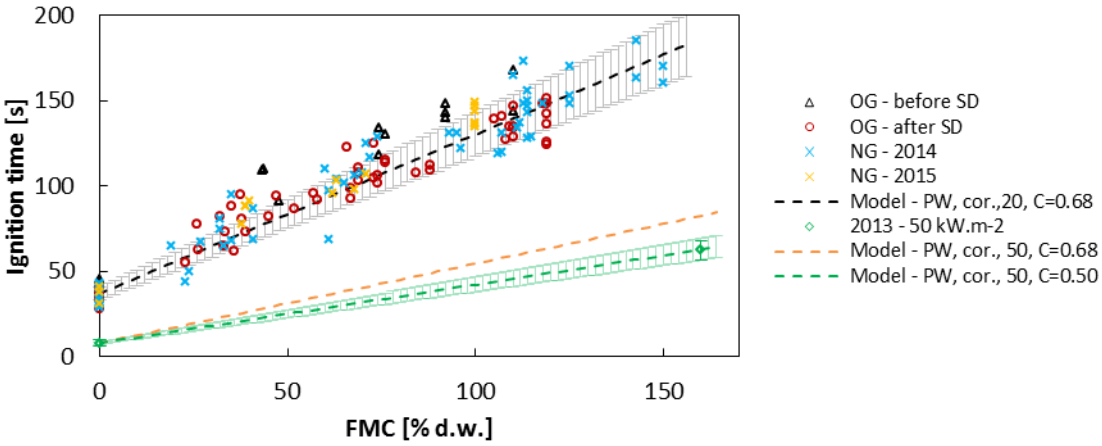


**Fig. 6.18. Experimental ignition data compared to modified Pickard and Wraight (PW) [6.35] semi-empirical ignition correlation (Eq. 6.11) for mature needles (OG and NG). Numbers (20, 50) correspond to external heat flux [kW.m$^{-2}$]. $C_T$ is the correction factor in Eq. 6.11. Ignition results "2013" are extracted from [6.2].**

A critical point to discuss is the dependence of the correlation to experimental conditions. In general, caution should be taken when using this correlation at

conditions dissimilar from the once tested here. At this stage no additional fuel loading was tested, however, Bartoli [6.21] and Jervis [6.20] have shown that, the ignition time is not significantly influenced by the fuel loading (in the range tested and for perforated sample holder). This is true for natural convection only, which was the condition in this work. This correlation should not be used in conjunction with forced convection conditions as this will add additional heat transfer mechanisms and therefore will change the ignition behavior (see Chapter 3 and 4).

It is likely that the correlation will change for different fuel species (changing coefficients). PRI was the only species tested in this experimental series. With this semi-empirical model, one can test the applicability to different heating conditions (external heat flux). Ignition times for conditioned and unconditioned PRI needles, tested at 50 kW.m$^{-2}$ external heat flux were reported in [6.2] (green marker in Fig. 6.18). The unconditioned needles had a *FMC* of 160%. Ignition times are summarized in Table 6.3, and compared to Eq. 6.11 evaluated at 50 kW.m$^{-2}$.

Table 6.3. Time to ignition for PRI needle samples tested at 50 kW.m$^{-2}$ extracted from [6.2].

| FMC [%] | Ignition time [s] | |
|---|---|---|
| | Average | St. Dev. |
| 0 | 8.0 | 2.0 |
| 160 | 62.3 | 5.9 |

Results are given in Fig. 6.18. The correlation (with $C_T$=0.68) over-predicts the ignition time at high *FMC* for this heating condition (orange dashed line). An explanation for this is a changing value for the correction factor, $C_T$, in Eq. 6.11. With faster heating rates, it is likely that, less water will be evaporated at the time of ignition, which will have the effect that, residual *FMC* at the time of ignition is higher compared to slower heating at 25 kW.m$^{-2}$. Therefore, the value of $C_T$ will reduce with increasing heat flux. A new value of $C_T$ can be calculated using the data from tests at 50 kW.m$^{-2}$. Applying the same methodology as described above, one can find a value of 0.50 for $C_T$ (green dashed line in Fig. 6.18).

The correlation at 50 $kW.m^{-2}$ heat flux compares well with the linear regression model found by McAllister et al [6.10], for *Pinus contorta* (Lodgepole pine), which was tested at the same heating rate. Their correlation has a slope of 0.3199, whereas, the corrected model from Pickard and Wraight (with $C_T = 0.50$) has a slope of 0.343 (6% difference). Minor difference can be attributed to species variation. Furthermore, tests in the FIST [6.10] are conducted under forced convection, which changes the heat transfer conditions and impacts the ignition behavior. These values for the slope also compare to what was found in [6.30] for pine species. Dimitrakopoulos and Papaioannou [6.30] obtained a slope of 0.322 for *Pinus brutia* (Brute pine) and 0.311 for *Pinus halepensis* (Aleppo pine).

The analysis highlights that a theoretical residual *FMC* can be estimated. It is suggested to conduct additional experimentation to calculated $C_T$ for a range of heating rates and conduct more experimentation similar to [6.36] in order to validate the correction factors.

The following section will analyze how the combustion dynamics change with respect to *FMC*. As already observed (Section 6.3.1), combustion intensity for unconditioned PRI needles is much lower than for needles with 0% *FMC*. The exact relationship will now be developed.

### *6.4.2. Peak HRR as a function of FMC*

Previous analysis of combustion tests with unconditioned needles showed that the *FMC* masks seasonal variations (Section 6.3). Seasonal variations were shown to exist when the sample was fully dehydrated. The question that arises is: at what FMC level is it important to consider these seasonal effects? Because similar trends (pHRR versus FMC) were found for both types of needles (OG and NG), data is combined in order to obtain a more global picture. Using this, the combustibility is evaluated independent of needle age (month). Peak HRR results for OG and NG samples are given in Fig. 6.19.

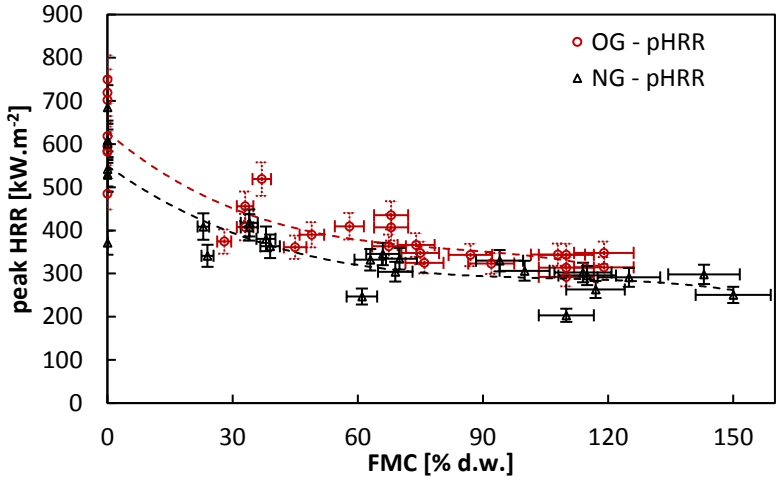


**Fig. 6.19. Peak HRR with respect to *FMC* separated into OG and NG sample tests.**

In this graph it can be observed that NG needles are slightly less combustible than OG needles over the entire range of *FMC*. Each data point in the following graphs is an averaged value from samples tested after the same conditioning period. Each data point includes 2-5 tests. The mean standard deviation for the *FMC* for each conditioning period was 6%, whereas the mean standard deviation for the measured pHRR was 7.5%. These variations are represented in the graphs by the error bars.

This difference was firstly attributed to change in chemical composition due to needle growth and secondly due to the climate changes from one year to the next (for mature NG needles). Thirdly, it was also discussed in Chapter 5 that there is a likelihood of changing hydraulic behavior between OG and NG needles, i.e. NG needles can release water vapor more rapidly. This influences the combustion dynamics in the gas phase and reduces the flame heat flux feedback to the surface, which governs the pyrolysis rate.

The distinction in the combustibility, although evident, is relatively small. For example the intercepts of the polynomial regression lines have a difference of approximately 12%. The variability of the results at 0% *FMC* is shown in Table 6.4 and indicates a 14.0% and 17.7% standard deviation for OG and NG needles, respectively. The

variability was associated to state of growth/decay. The averaged values show overlapping and therefore allow the assumption of one combined value.

Table 6.4. Averaged peak HRR measurements at 0% *FMC* for OG and NG needles.

| Type | Peak HRR [kW.m$^{-2}$] | | St.dev. [%] |
|---|---|---|---|
| | Avg. | St.dev. | |
| OG | 629.6 | 88.0 | 14.0 |
| NG | 552.6 | 97.5 | 17.7 |
| Combined | 593.6 | 97.6 | 16.5 |

OG and NG test results are therefore combined and presented in Fig. 6.20. A single polynomial regression line is fitted to the data, and is indicated in the graph. This regression model can be used to estimate the combustibility (in terms of peak HRR) of pine needles as a function of *FMC*, independent of needle age and seasonality. A 15% error indicates that most test results fall with in this range. For all test results at 0% an average pHRR value of 594 +/- 98 kW.m$^{-2}$ was found. The standard deviation is 16.5%, which also indicates that a 15% uncertainty level is acceptable. This average represents the y-intercept of the regression model (best fit):

$$\dot{q}''_{FMC,all} = -263.37\,FMC^3 + 740.52\,FMC^2 - 746.13\,FMC + \dot{q}''_{all,dry} \qquad \textbf{Eq. 6.15}$$

The $R^2$ value for this regression model is 0.77. In the graph (Fig. 6.20), the plateau indicates that the pHRR is independent of the *FMC* in that range. Such a plateau was also found by the initial study presented in [6.2]. Etlinger and Beall [6.12] and Weise et al [6.13] also described the pHRR with a polynomial regression model similar to the one given by Eq. 6.15 and observed a plateau, but at much higher *FMC* levels (>100%).

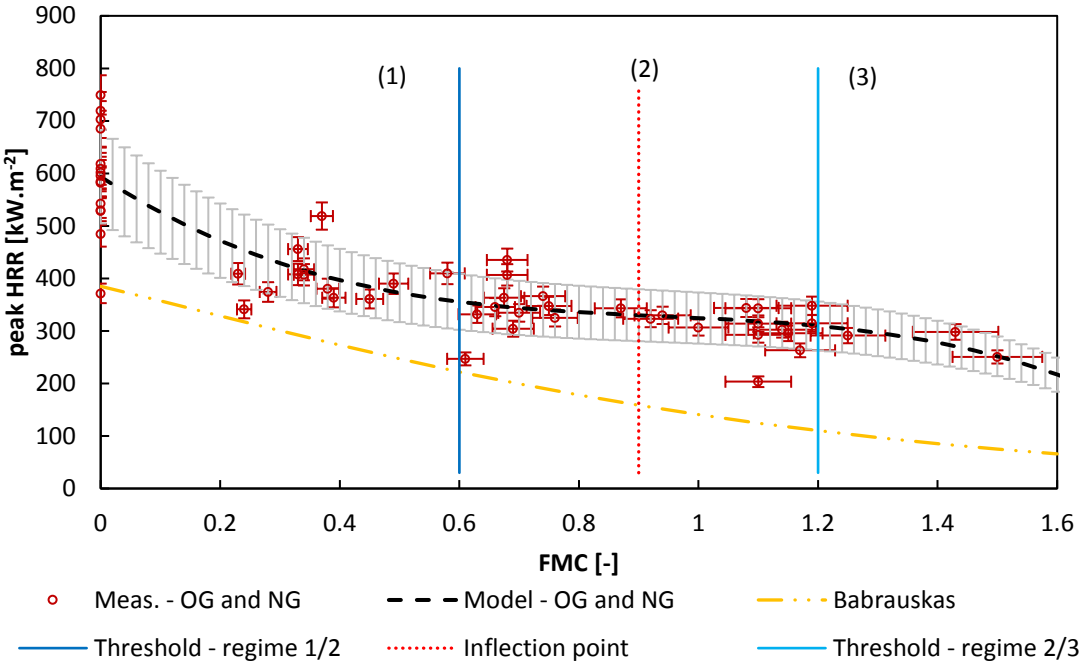


**Fig. 6.20. Measured and Predicted peak HRR with respect to FMC of all tests (OG and NG). "Babrauskas" (yellow "dashed-dotted" line) refers to Eq. 6.16 [6.14]. Regime (1): Combustion intensity is driven by FMC and plant chemistry variation. Regime (2): Combustion is independent of FMC and chemistry variation. Regime (3): Further reduction in combustion intensity due to FMC.**

Babrauskas [6.14] and Baker [6.15] found an exponential fit for their experimental fires, which is frequently used to estimate peak combustion intensity of trees. They burned full trees at different *FMC* in an intermediate scale calorimeter. The correlation is also included in Fig. 6.20 (yellow line):

$$\frac{\dot{q}_{peak}}{m_{wet}} = e^{5.8-0.017*FMC} \qquad \textbf{Eq. 6.16}$$

In this formula, the pHRR ($\dot{q}_{peak}$) is represented in [kW] and normalized by the sample initial wet mass, $m_{wet}$. The sample initial mass for the given study was the equivalent mass, $m_{eq}$, given by Eq. 6.1, which is a function of the *FMC*.

Their model under-predicts the pHRR of the FPA experiments. The poor correlation to the given experiments can be largely attributed to difference in scale, test conditions,

bulk properties and ignition scenario. But it might suggest that, the plateau is an artifact from experimental conditions (external heat flux was not removed after ignition). Further testing is however required to support this.

In Fig. 6.20, three regimes are identified, which represent ranges in which the combustion dynamics change.

**Regime (3); *FMC* > 120%**

Regime (3) is characterized by lowest combustibility and particles with *FMC* above 120%. Any detailed conclusions about this regime would be premature at this point, due to the lack of enough experimental data. It is also of less interest, because of the reduced hazard.

**Regime (2); 60% < *FMC* < 120%**

The inflection point in Fig. 6.20 occurs at approximately *FMC* = 90% and can be interpreted as the moisture of extinction. In this range, combustion is not influenced by fuel composition and approaches conditions where a sustained flaming state becomes unlikely. The results compare well with Dimitrakopoulos and Papaioannou [6.30] moisture of extinction for other pine species, which they found to be 89-138% for *Pinus halepensis*. Above this value, the determined, combustibility is low and sustained flaming cannot be expected. Baker [6.15] quoted that Douglas-fir trees self-extinguish when the *FMC* is above 80%. Given the nature of *FMC* measurements in [6.15] (outside needles of the tree only) and the averaging of the *FMC* over drying condition in this work, it can be concluded that, the inflection point (Fig. 6.20) and Baker's moisture of extinction compare well. This work adds more detail and helps determining a more concrete, quantifiable threshold based on bench-scale experiments.

The plateau (regime 2), corresponding to the range of about 60-120% FMC, and covers the full range of typical *FMC* levels for mature PRI needles (see Fig. 6.4; as well as other pine species, e.g. [6.25-6.27]). The independence of the pHRR from *FMC* in that range suggests that, unconditioned needles in the spring, during the SD where the *FMC* is 90-100%, are only marginally more dangerous as foliage during the rest of the year (from a combustibility point of view). Only when the *FMC* is extremely low, e.g. < 60% will severe conditions, in terms of combustion intensity occur (regime 1). Under normal conditions, such levels are not likely, but can be achieved under unusual external factors (drought or disease).

Ignitibility decreases during the entire range of *FMC*, therefore, it is the driving factor for hazardous condition in the range of *FMC*, regime (2). Even though, partially dried needles have similar combustion dynamics as unconditioned needles, they will pose a larger hazard with respect to ignition potential and/or flame spread. Below 60% *FMC* (regime 1), both ignitibility and combustibility are factors driving extreme fire behavior.

**Regime (1); *FMC* < 60%**

Regime (1) is the one of most interest, because if canopy fuel can reach this level of *FMC*, it will pose a severe risk, not only because the fuel will ignite with more ease, but also because the resulting combustion will be more intense. The graph in Fig. 6.21 shows the pHRR of selected OG needle samples, separated by month. Initially in Chapter 5, it was determined that October needles were the most combustible ones. This can be observed here. Furthermore, it can also be observed that, at elevated *FMC* (60-70%), October needles are still the most combustible ones. The same trend is true for June samples, which are the least flammable ones when tested fully dehydrated. These needle stay the least flammable until the data converges, around 60%. A similar, though less obvious behavior can be observed for NG needles (Appendix D3).

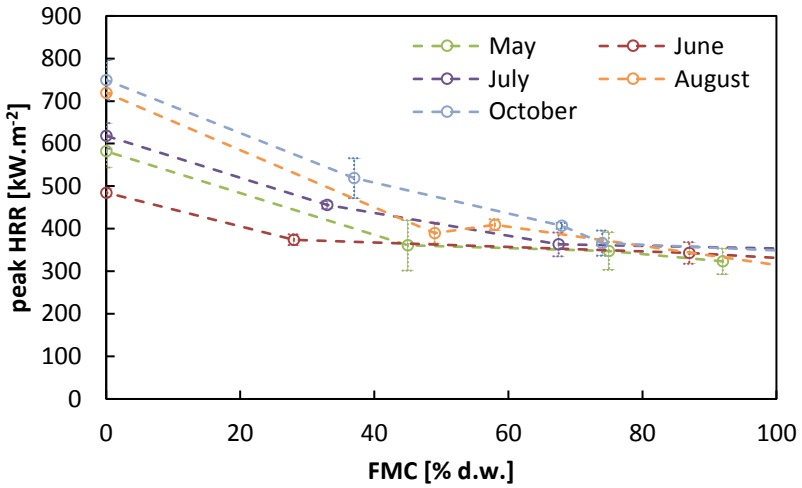


**Fig. 6.21. Selected pHRR results for OG needles, separated by the month that they were collected in.**

This observation provides the justification that, indeed, below 60% *FMC*, seasonal trends of the flammability must be considered. It is suggested that future research should focus on this range of *FMC* to provide more evidence of a critical *FMC*.

### Reaching a critical *FMC* (< 60%)

A critical factor that will govern fire severity is the pre-heating (or curing) condition. Under what fire behavior conditions can live fuel, located in the canopy be cured so that the *FMC* will fall under this critical threshold of roughly 60%? Elevated ambient temperature, low humidity, and high winds can certainly reduce the live *FMC*. But for healthy plants in non-drought conditions it is likely not enough. The likelihood of a significant reduction in *FMC* due to convective pre-heating from hot gases in a plume is much greater. Plume temperature can be much higher than ambient air, especially in the near field of the fire. Furthermore, the gases will travel at high velocity, creating an ideal environment for conditioning (not unlike a convection-oven, as used in the laboratory conditioning of needles).

A temporal aspect should also not be ignored. Curing of live foliage takes times. The better the curing condition the less time is required to reduce the *FMC* to below 60%. Sample dehydration curves presented in Chapter 5 showed that this can take between

two and four hours in a convection-oven at 60 °C, and that it depends on the state of growth of the foliage. Such times are certainly much longer than typical residence time (on the order of minutes) of a fire front moving through a forest (e.g. Mueller et al [6.37] showed a fire spread rate of < 0.245 $m.s^{-2}$). As the fire approaches unburned fuel particles, curing condition intensify, therefore, it is also a transient condition. In the near field, additional heat transfer and curing due to radiation will take place. Therefore, several aspects of wildfire behavior are causes for reaching conditions in which extreme fire behavior is more likely.

Curing conditions of live forest foliage should be investigated more, because it defines when extreme conditions are more likely. Therefore, it is crucial to understand what fire behavior mechanisms can cause the required pre-heating condition to reduce the *FMC* below 60%.

**Scaling up to intermediate-scale calorimetry and the importance of ventilation**

An interesting reflection of the results given in Fig. 6.20 can be observed in [6.12, 6.13]. Etlinger and Beall [6.12] and Weise et al [6.13], have observed similar trends for experiments conducted in an intermediate scale calorimeter. They also found an independence of the pHRR at elevated *FMC*. This leads to believe that results from small scale tests, such as the ones done with the FPA can, to some degree, be scaled up. Experimental results are however, not directly comparable, because significant difference exist, such as fuel/sample properties and test conditions.

Weise et al [6.13] concluded that correlation between bench scale and intermediate scale was weak-to-poor and they provide various arguments why, e.g. ignition scenario, sample properties, and heating condition.

There are significant improvements that can prove a better correlation between small and intermediate scale combustion tests. Weise et al [6.13] concluded that,

intermediate scale combustion tests resulted in higher pHRR (normalized by sample initial mass) compared to small scale. This can be explained by the confinement of the fuel matrix in the Cone Calorimeter (bench scale) test samples. Fuel was confined in a sample holder open only at the top surface. This limits the availability of oxygen. An oxygen limited combustion has lower combustion efficiency and can be associated with reduced energy release (intensity) as compared to well-ventilated combustion (see Chapter 3).

Ventilation controlled fires are generally associated to compartment fire dynamics, where doors and windows provide a limited area through which oxygen can reach the combustion zone inside the room [6.38]. Wildfires occur in the open and thus are commonly addressed as well-ventilated fire. Although this definition is acceptable in comparison to compartment fires, the definition of the ventilation condition is not on the same scale, because one has to consider forest fuel as a porous matrix, instead of solid fuel packages. The influence of the ventilation on the combustion dynamics is critical, especially for porous fuel beds. This is well illustrated by examination of combustion dynamics of wood cribs [6.1]. Recent studies that illustrate this are [6.39-6.43]. Similar mechanisms governing the combustion of wood cribs can be assimilated to forest fuels, for example litter or clumps of foliage on the tree, as McAllister and Finney illustrate [6.43].

For pine needle litter tested in bench scale calorimeter (e.g. FPA or Cone), Schemel et al [6.5] and Bartoli et al [6.4] have identified that sample holder, which have closed sides and bottom, hinder oxygen from reaching the inside of the porous fuel matrix. Bartoli et al [6.4] showed that the pHRR of pine needle litter using open mesh sample holder can be twice as high as for litter tested in closed basket holder (open only at the top surface). This however, also depends on particle and bulk properties. Open baskets were also used in the current study, which suggests that correlation to intermediate scale is likely better compared to what was found by Weise et al [6.13]. Such

correlation, however, has yet to be made in order to provide acceptable evidence for this hypothesis.

The fuel in [6.4] and [6.5] used dead dry needle litter as fuel source, which begs the question, if similar trends can be observed with unconditioned live fuel. Thomas et al [6.2] provide supportive evidence that, pHRR of unconditioned live fuels tested in the FPA is also dependent on the sample holder (ventilation condition). Even though, the dependence is not as strong as with dry fuel. The reason for this is the presence of significant amount of water vapor in the gas phase. The water vapor influences the combustion reaction, by cooling flammable gases and flames, as well as displacing oxygen. The displacement of oxygen is equivalent to blocking the entrainment air, which supplies the oxygen for the combustion reaction (or reducing the oxygen concentration as was done in Chapter 3).

Ventilation conditions are a key mechanism to understanding the combustion dynamics of vegetative fuels (or all fuel type and fire for that matter), as was made clear throughout parts of this thesis and in other works [6.2-6.6]. Because water release rate seems to be a governing parameter in controlling the combustion behavior of unconditioned foliage (by ways of controlling ventilation condition and heat flux feedback mechanism), it is suggested that this mechanism should be part of future explorations. Studying this mechanism will help understand the combustion dynamics and eventually might provide physical explanations why and at what FMC level the plateau and inflection point (moisture of extinction) occur. Ideally, such conditions are then linked to physical properties of the foliage at which point accurate prediction tools can be developed.

Summarizing, the ignition behavior and burning dynamics were described with respect to *FMC*. It was shown that, (1) a linear semi-physical model can be used to predict the ignition of live foliage; and (2) a polynomial regression model can be used to predict the combustion intensity of live foliage. The pHRR is dependent on the *FMC* only for

values below 60%, which corresponds to level until which plant chemistry is important. Above this level, the combustion intensity becomes independent of plant chemistry and *FMC*, until an upper limit of 120%. Only limited data is available above this level, thus extrapolation beyond this point can result in large uncertainty.

### 6.4.3. *The linkage between $F_{total,dry}$ and $F_{total,wet}$*

The relation between ignition behavior and *FMC*, as well as between the combustion behavior and *FMC* can be interpreted as the missing linkage between the boundary conditions that were found in Section 6.3.4 (0% and maximum *FMC*). Therefore, Fig. 6.11 can be reviewed with the additional knowledge attained.

A relation between the boundary condition will have a similar shape than the pHRR curve, which was found to be a polynomial regression. The ignition-FMC correlation was linear, therefore the change is constant (constant slope). Finally, the flammability is a function of time and *FMC* as illustrated in Fig. 6.22.

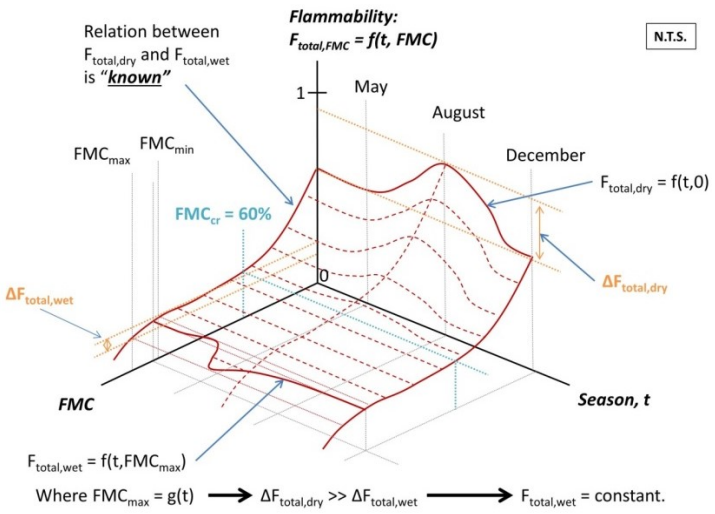


**Fig. 6.22. Schematic of the fuel flammability as a function of time (season) and *FMC* with knowledge of the relation between $F_{total,dry}$ and $F_{total,wet}$.**

The phrase "known" is in quotation, because the relationship is not yet fully understood. The models developed for ignition time and pHRR are averages over the

entire data sets, which included NG and OG needles, and no temporal distinction was made. It is however evident that, the relationship is not a linear one as first shown in Fig. 6.11. Further work is necessary to gain a full understanding.

In Fig. 6.22, influence of seasonal effects is observed until 60% *FMC*, indicated by the diminishing ridge (dashed contour lines) with increasing *FMC*. The variation in flammability at maximum *FMC*, $\Delta F_{total,wet}$, is small compare to the variation of dry fuel flammability, $\Delta F_{total,dry}$, illustrating the dominant effects of *FMC* over state of growth/decay.

Finally, it can be concluded that, flammability is a dynamic parameter changing with time and *FMC*. Neither dry fuel flammability nor wet fuel flammability is an adequate representation on their own, because either condition may occur, although the 0% *FMC* is less likely.

The fuel flammability assessment of PRI needles did not correlate to the typical fire season in the NJ Pine Barrens, which was attributed to the strong driver of weather. However, conducting this study with similar species from fire prone areas where the fire season coincides with the growing season may reveal different results. The fuel flammability is likely to be a contributing factor to extreme fire conditions, where the *FMC* is at a critical state. Even if it is not reaching the 60% threshold, foliage that is near it, will only require minimal fire behavior (induced by weather) to tip the balance and inflame an extreme fire scenario.

### *6.5. Validation of the ignition and pHRR correlations*

The last section investigates the validity of the discussed correlation with existing data from [6.2]. Two correlations, (1) a semi-physical mode predicting ignition time, and (2) an empirical model predicting the pHRR are validated over time and across multiple test apparatuses. This is done with data from Thomas et al [6.2]. Data from this test series was also obtained from FPA combustion tests conducted at the Fire

Laboratory of the Worcester Polytechnic Institute (WPI), MA, USA (the current test series was conducted in the Fire Laboratory at the University of Edinburgh, Scotland, UK).

Although both FPAs are comparable, minor differences exist (e.g. slightly different versions of the IR heating units). Although this might have an effect on the ignition times (absorptivity), it is assumed marginal, because the operating temperature of the units do not change drastically. Both studies were done with PRI needles at the same external heat flux and under natural convection.

### Ignition-FMC correlation

Only the corrected Pickard-Wraight model is used in the validation and results are shown in Fig. 6.23. The ignition-FMC correlation is not satisfactory over the entire range of *FMC* tested. Overall, the validation is marginally satisfactory.

Some tolerance in the comparison can be granted, because the 2013 samples were a mix of OG and NG needles. Furthermore, they were tested in a different FPA which induces additional uncertainty. Although these experimental differences exist, the data can be used to verify the acceptability of the correlation.

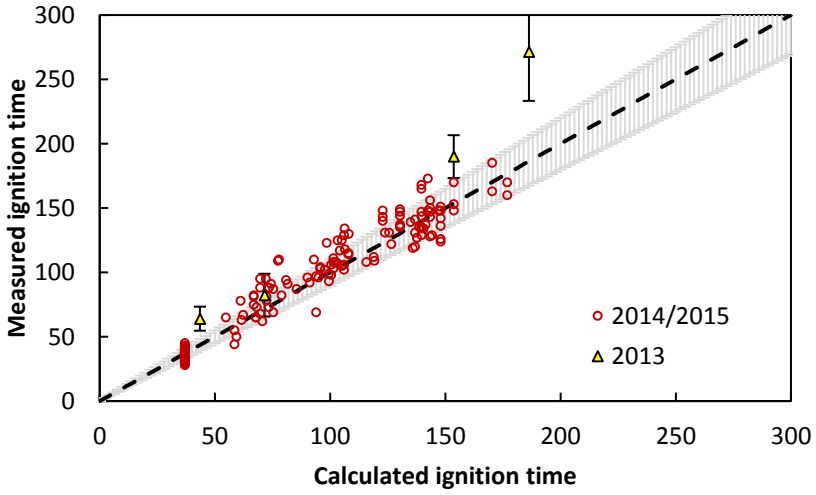


**Fig. 6.23. Calculated and measured ignition time [s] from two test series (2014/2015) and (2013) [1.45].**

The data point from the 2013 test series with the lowest ignition time is under-estimated with the correlation. This is likely, because these needles were dead ones. Attribution to the weak prediction is due to changing absorptivity and changing thermal behavior. Water storage between live and dead needles is different (dead: free water, live: free and bound water), therefore, it can be assumed that the water vapor release mechanism (a resistance to release water) changes as well. Furthermore, it is likely that chemical composition also plays a role. Both factors can influence the ignition behavior.

The data point from the 2013 test series with the longest ignition time is under-estimated. Reason for this is the nature of the ignition condition. For these test, ignition was first observed in a smoldering state prior to transitioning to a flaming state. Ignition conditions for tests in the 2014/2015 series, ignition was always due to piloted.

Therefore, it is likely that the correction factor, $C_T = 0.68$, does not represent the give condition, because the additional time given to water evaporation before ignition commences, means that the residual *FMC* is lower than what is assumed. Thus for this test, $C_T$ is likely to be close to 1. In fact, when $C_T = 1$, the prediction is acceptable with a percent difference of only 5.5%.

This further highlights that, (1) the original correlation by Pickard and Wraight [6.35] is more accurate for autoignition conditions, and (2) the importance of determining residual *FMC* at the time of ignition. The residual FMC is likely to change depending on initial *FMC*, particle size, and heating rate. Future experimentation should be conducted to investigate further relations.

**Peak HRR-FMC correlation**

Results obtained in the preliminary study conducted by Thomas et al in 2013 [6.2] indicated a trend similar to what was found in the full study. Calculated and measured pHRR are plotted against each other in Fig. 6.24. The prediction of the pHRR of 2013

data is marginally acceptable, because it under-predicts the pHRR (yellow marker). The predictions are slightly better at elevated *FMC*.

The under-prediction of the 2013 is due to the "dry" (or "zero") condition used in Eq. 6.15 (last term on the r.h.s.). For this test series, the lowest *FMC* tested was 7% and these needles were dead ones. Therefore, the under-estimation might only be an artifact of the used "zero" condition. Increasing the "zero" condition, as can be expected when the fuel is further dried, the predictions improve significantly (see for example Fig. 6.24, blue marker). These results where fitted so that the tests at 7% corresponds to the model.

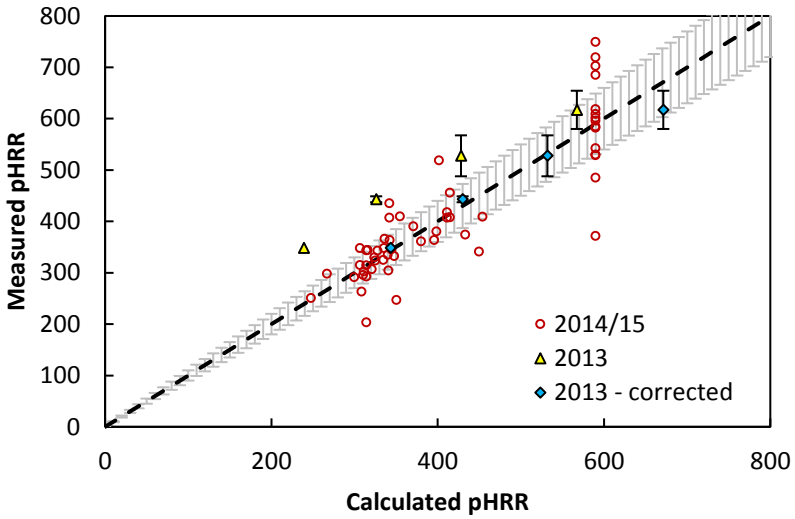


**Fig. 6.24. Calculated and measured pHRR (kW.m$^{-2}$) from two test series (2014/2015) and (2013) [6.2].**

The nature of obtaining HRR data (via calorimetry) has relatively high uncertainties on its own (see discussion in Chapter 2). Improvements in test protocols for conducting combustion experiments with the live vegetation will certainly increase the accuracy of the predictions in the future.

Overall, both correlations are at this time, only marginally satisfactory, mainly due to the lack of additional experimental result, but also due to scientific justification of the correction factor, $C_T$, used. However, improvements were discussed that will make

these correlations more robust and usable. Further testing with other species (and test conditions) should follow for a secondary validation, and to determine to what extent both models can be utilized to estimate ignitibility and combustibility with respect to *FMC* and apparent particle density.

### *6.6. Chapter summary and conclusions*

Work presented in this Chapter was part of the same experimental campaign described in Chapter 5. Several additional aspects of live fuel flammability were explored in this work. These aspects included the evaluation of the impact of *FMC* on the ignition behavior and combustion dynamics.

It was discussed that, the impact of *FMC* is twofold: (1) in the solid phase and (2) in the gas phase. In the solid phase, water in the fuel particle changes effective thermophysical properties. This changes the thermal response of the particle to a heating condition. It was found that dry PRI needles behave thermally thin and that wet needles are likely also to behave thermally thin due to an increase in thermal conductivity (i.e. reduced internal thermal resistance compared to external thermal resistance). This may, in part, explain why moist live foliage ignites readily. It is discussed that, the effects of different properties is competing. The exact relation between the properties and their impact is not evident and further evaluation is necessary. Additionally to changing effective properties of the fuel, water acts as a heat sink in the solid phase. Therefore, more energy is required to raise the temperature of the particle, which, under a constant heat source, results in delayed ignition.

When water is vaporized, it is released from the particle and enters the combustion zone. In a first instance, it dilutes the pyrolysis products and air mixture, causing delayed ignition. Furthermore, after ignition, it cools the flammable gas mixture and flames. This phenomenon reduces the combustibility of the gas mixture and heat flux feedback to the sample surface. It also displaces oxygen required for the combustion

reaction, which affects the combustion efficiency. The analysis of results is separated into two main parts: (1) flammability of unconditioned needles and comparison to dry fuel flammability, and (2) impact of *FMC* on the ignition and burning dynamics, providing a link between the two boundary condition (0% and maximum *FMC*).

First, the live fuel flammability assessment developed in Chapter 5 was extended to include unconditioned foliage (Section 6.3). This revealed that, neither ignitibility nor combustibility has significant seasonal trends. Furthermore, marginal differences in flammability were observed between OG and NG needles, Thus the total flammability factor of unconditioned PRI needles also did not correlate with historic fire data (from the NJ Pine Barrens). Finally, total flammability factors of conditioned and unconditioned needles were compared and a total flammability was defined as a function of time and *FMC*. The link between the two boundary conditions (0% and maximum *FMC*) was provided by studying the ignition and combustion behavior at intermediate *FMC* (0%-maximum), which was the subject of the second half of the chapter.

The ignition behavior and burning dynamics were described with respect to *FMC*. It was shown that, (1) a linear semi-physical model can be used to predict the ignition of live foliage ($R^2 = 0.93$); and (2) a polynomial regression model can be used to predict the combustion intensity of live foliage ($R^2 = 0.97$). The models obtained agree well with literature. In Section 6.3 it was explained that the *FMC* masks the seasonal trends of ignitibility and combustibility. Following this conclusion, the analysis in Section 6.4 was conducted to evaluate at what *FMC*, seasonal effects due to state of growth/decay become important. With the current experimental campaign, it was possible to deduce that, fuel composition plays a minor role in the ignition behavior compared to *FMC*. However, analyzing the peak combustion intensity as a function of *FMC* indicated that a *FMC* of 60% is a threshold level below which seasonal effects, due to plant chemistry, become important. Above this level and up to 120%, peak

combustion intensity is neither a function of *FMC* nor a function of seasonal variation in fuel properties.

In Section 6.5, previously obtained data (2013; also PRI needles) was used in a first validation, and revealed some differences between predicted and measured ignition time as well as pHRR. Reasons for the variations are explained, e.g. using two different FPAs in two different laboratories. Nevertheless, until further experimentation is conducted, both models can only be deemed marginally satisfactory.

Because typical *FMC* of unconditioned foliage is generally within the range where combustibility is constant (60-120% *FMC*), it can be concluded that, wildfire severity is less impacted by changes in seasonal flammability and *FMC* but more by local fire behavior. Such fire behavior scenarios need to have the ability of reducing the *FMC* of canopy foliage below 60%. This can be achieved with high plume temperature and/or strong winds. Which one is favorable is unknown.

It is suggested that future studies explore the exact mechanism of live foliage dehydration. Because, on the one hand, it will show what conditions are required to reach a critical *FMC* below 60%. On the other hand, it was shown in this work that, the water release mechanism is likely a dominant factor governing the combustion dynamics. The 60% *FMC* is not only a threshold at which combustion intensity increases, but also indicates a threshold below which ignition becomes more likely. Analyzing a semi-physical ignition model with experimental data suggests that, at high heating rates, residual *FMC* of needles might be as much as 50% of the initial *FMC*. Under normal conditioned in the summer, mature needles have a *FMC* between 110 and 120%. Therefore, a 50% reduction in the FMC corresponds to a 55-60% residual *FMC*, which is the threshold level. Finally, if a fire scenario is present that can pre-heat canopy fuel to such a level, particles may readily ignite and involve the canopy in the fire.

Such low levels of *FMC* can occur, for example due to disease, or severe drought. Therefore, in locations where tree stands are unhealthy or affected, this threshold level should be considered a warning sign at which extreme fire behavior is likely. Furthermore, if vegetation *FMC* is observed near this threshold, only minor fire behavior characteristics are required to tip the balance and inflame an extreme fire condition.

Many flammability studies have been conducted in the past; however, this is the first one providing a full picture of flammability as a function of time and *FMC*. The developed analysis can be easily extended to other species, which will lead to improved fuel flammability classification systems, Furthermore, implications of the assessment can be made in fire danger rating systems to account for hazardous conditions related to the canopy fuel.

### *6.7. References*

[6.1] J.G. Quintiere. Fundamental of Fire Phenomena. John Willey and Sons, Hoboken, NJ, USA, 2006.

[6.2] J.C. Thomas, A. Simeoni, M. Gallagher, N.S. Skowronski. An Experimental Study Evaluating the Burning Dynamics of Pitch Pine Needle Beds Using the FPA. Proceedings of the 11th International Symposium on Fire Safety Science, Christchurch, New Zealand, (2014) pp. 1406-1419.

[6.3] J.C. Thomas, J.N. Everett, A. Simeoni, N. Skowronski, J.L. Torero. Flammability Study of Pine Needle Beds. Proceedings of the 7th International Seminar on Fire and Explosion Hazards, Providence, RI, USA, (2013).

[6.4] P. Bartoli, A. Simeoni, H. Biteau, J.L. Torero, P.A. Santoni. Determination of main parameters influencing forest fuel combustion dynamics. Fire Safety Journal 46 (1-2) (2011) 27-33.

[6.5] C. Schemel, A Simeoni, H. Biteau, J. Riviera, J.L. Torero. A Calorimetric Study of Wildland Fuels. Experimental Thermal and Fluid Science 32 (7) (2008) 1381-1389.

[6.6] A. Simeoni, J.C. Thomas, P. Bartoli, P. Borowjeck, P. Reszka, F. Colella, P.A. Santoni, J.L. Torero, Flammability studies for wildland fuels using the Fire Propagation Apparatus. Fire Safety Journal 54 (2012) 203-2017.

[6.7] F.X. Jervis, G. Rein. Experimental study on the burning behavior of Pinus halepensis needles using small-scale fire calorimetry of live, aged and dead samples. Fire and Materials (2015)

[6.8] W.M. Jolly, A.M. Hadlow, K. Huguet. De-coupling seasonal changes in water content and dry matter to predict live conifer foliar moisture content. International Journal of Wildland Fire 23 (2014) 480-489.

[6.9] W.M. Jolly, J. Hintz, R.C. Kropp, E. Conrad. Physiological drivers of the live foliar moisture content 'spring dip' in Pinus resinosa and Pinus banksiana and their relationship to foliar flammability. Proceedings of the 7th International Conference on Forest Fire Research. Coimbra, Portugal (2014).

[6.10] S. McAllister, I. Grenfell, A. Hadlow, W.M. Jolly, M. Finney, J. Cohen. Piloted ignition of live forest fuels. Fire Safety Journal, 51 (2012) 133-142.

[6.11] S. McAllister, D.R. Weise. Effects of Season on Ignition of Three Species of Live Wildland Fuels using the FIST apparatus. Spring Technical Meeting of the Western States Section of the Combustion Institute, Pasadena, California, USA (2014).

[6.12] M.G. Etlinger. F.C. Beall. Development of a Laboratory Protocol for Fire Performance of Landscape Plants. Internation Journal of Wildland Fire 13 (2004) 479-488.

[6.13] D.R. Weise, R.H. White, F.C. Beall, M. Etlinger. Use of the Cone Calorimeter to Detect Seasonal Differences in Selected Combustion Characteristics of Ornamental Vegetation. International Journal of Wildland Fire 14 (2005) 321-338.

[6.14] V. Babrauskas. SFPE Handbook of Fire Protection Engineering – Heat Release Rate. 3rd ed. National Fire Protection Association, Quincy, MA, USA (2002).

[6.15] E.S. Baker. Burning characteristics of individual Douglas-Fir trees in the Wildland/Urban Interface. Worcester Polytechnic Institute, Worcester, MA, USA (2011). MS Thesis.

[6.16] R,H, White, D.R. Weise, K. Mackes, A.C. Dibble. Cone Calorimeter Testing on Vegetation: An Update. Proceedings of the 35th International Conference on Fire Safety. Columbus, OH, USA (2002) 1-12.

[6.17] R.H. White, W.C. Zipperer. Testing and Classification of Individual Plants for Fire Behavior: Plant Selection for the Wildand-Urban Interface. Internationa Journal of Wildland Fire 19 (2010) 213-227.

[6.18] A.C. Dibble, R.H. White, P.K. Lebow. Combustion characteristics of north-eastern USA vegetation tested in the cone calorimeter: invasive versus non-invasive plants. International Journal of Wildland Fire, 16 (2007) 426-443.

[6.19] F.X. Jervis, Application of Fire Calorimetry to Understand Factors Affecting flammability of Cellulosic Material: Pine Needles, Tree Leaves and Chipboard. University of Edinburgh, UK, 2012. Ph.D. Thesis.

[6.20] W.J. Parker, Calculations of the heat release rate by oxygen consumption for various applications, Report No. NBSIR 81-2427-1, US Department of Commerce, 1982.

[6.21] P. Bartoli. Feux de forêt: amélioration de la connaissance du couplage combustible-flamme. Universite de Corse-Pascal Paoli. 2011. Ph.D. Thesis.

[6.22] J.M. Cholin. Fire Protection Handbook – Wood and Wood-Based Products. 20th ed. National Fire Protection Association, Quincy, MA (2008).

[6.23] R. Bergman, et al. Wood Handbook: Wood as an Engineering Material. Department of Agriculture, Forest Service, Forest Products Laboratory. Madison, WI (2010).

[6.24] F.P. Incropera, D.P. DeWitt, T.L. Bergman, A.S. Lavine, Principles of Heat and Mass Transfer, John Wiley and Sons Ltd., Singapore, Singapore, 2013.

[6.25] C.R. Keyes. Foliar moisture contents of North American conifers. USDA Forest Service Proceedings RMRS-P-41 (2006) 395-399

[6.26] Chrosciewicz, Z. Foliar moisture content variations in four coniferous tree species of central Alberta. Canadian Journal of Forest Research 16 (1986) 157-162.

[6.27] M.E. Alexander. Foliar moisture content input in the Canadian forest fire behavior prediction system for areas outside of Canada. Proceedings of the 6th International Conference on Forest Fire Research. Coimbra, Portugal (2010).

[6.28] W.M. Jolly, R.A. Parsons, A.M. Hadlow, G.M. Cohn, S.S. McAllister, J.B. Popp, R.M. Hubbard, J.F. Negron. Relationships between moisture, chemistry, and ignition of Pinus contorta needles during the early stages of mountain pine beetle attack. Forest Ecology and Management 269 (2012) 52-59.

[6.29] New Jersey Office of Emergency Management. State of New Jersey 2014 Hazard Mitigation Plan Section 5.12 Wildfire. Tetra Tech, Inc. Morris Plains, NJ, USA (2014).

[6.30] A.P. Dimitrakopoulos, K.K. Papaioannou. Flammability Assessment of Mediterranean Forest Fuels, Fire Technology, 37(2) (2001) 143-152.

[6.31] C. Moro. Flammability measurements for Erica arborea, INRA, Le Ruscas (1989 – 2007), relation between ignition time and moisture content. EU FIRE LAB.<http://www.eufirelab.org/specific_view.php?unit=2&ID_encour=191&type=1>.

[6.32] J.Torero. SFPE Handbook of Fire Prevention Engineering – Flaming Ignition of Solid Fuels. 5th ed. Society of Fire Protection Engineers, London, UK, (2016).

[6.33] A.C. Fernandez-Pello. On Fire Ignition. Proceedings of the 10th International Symposium on Fire Safety Science, Maryland, USA (2011) 25-42.

[6.34] V. Babrauskas. Ignition Handbook. Fire Science Publishers, Issaquah, WA (2003).

[6.35] R.W.Pickard, H. Wraight, The effect of moisture on the ignition and flame Propagation of thin cellulosic materials, FR Note 450, Fire Research Station, Borehamwood, UK, 1961.

[6.36] W.M. Jolly. B.W. Butler. Final Report for JFSP-Funded Project entitled: "Linking Photosynthesis and Combustion Characteristics in Live Fuels: The Role of Soluble Carbohydrates in Fuel Preheating". JFSP Project ID: 10-1-08-6.

[6.37] E.V. Mueller, et al. An Experimental Approach to the Evaluation of Proscribed Fire Behavior. Advances in Forest Fire Research. Coimbra, Portugal (2014) 41-53.

[6.38] B. Karlsson, J.G. Quintiere. Enclosure Fire Dynamics. CRC Press LLC. London, UK (2000).

[6.39] A. Loennermark, H. Ingason. The Effect of Air Velocity on the Heat Release Rate and Fire Development during Fires in Tunnels. Proceedings of the 9th International Symposium on Fire Safety Science. Karlsruhe, Germany (2008) 701-712.

[6.40] O.A.O. Aljumaiah. Combustion Products of Ventilation Controlled Fires: Toxicity Assessment and Modelling. University of Leeds, Leeds, UK (2012) Ph.D. Thesis.

[6.41] S. McAllister, M. Finney. Effect of Crib Dimensions on Burning Rate. Proceedings of the 7th International Seminar on Fire and Explosion Hazards. Maryland, USA (2013).

[6.42] S. McAllister, M. Finney. The Effect of Wind on the Burning Rate of Wood Cribs. Fire Technology 52/4 (2016) 1035-1050.

[6.43] S. McAllister, M. Finney. Burning of Wood Cribs with Implications for Wildland Fires. Fire Technology (2015) (online only).

# Chapter 7

## *Summary of Key Findings, Direction of Future Research and Final Remarks*

The following conclusions, grouped by – *(1) Thermal behavior of the needles*, *(2) ignition behavior*, *(3) burning behavior*, and *(4) live fuel flammability assessment* – highlight the key findings of the thesis (Section 7.1). Section 7.2 and 7.3 provide guidance for future directions of this research and final remarks, respectively.

## *7.1. Summary of key findings*

### *7.1.1. Thermal behavior of the needles*

It was concluded that neglecting heat losses (convection and re-radiation) in the determination of the thermal behavior is a significant simplification and is only valid for a narrow range of conditions (high heating rate and natural convection). It results in an under-prediction of the heat flux level (heating rate) at which fine forest fuel particles start to deviate from a thermally thin behavior. For the two needle species tested (PS and PR) it was found that a "no loss" condition under-estimates this threshold by up to 31% for natural convection. For forced convection, it is much higher. Convective heat losses for fine particles (high *SVR*) can be significant due to prevailing wind in the open environment. Under radiative heating conditions, the convective heat losses dampen the heating rate and thus result in higher external thermal resistance compared to internal thermal resistance (i.e. they favor a thermally thin behavior).

The thermal behavior of dead and dried live needles was found to be thermally thin under radiative heating with convection cooling conditions. One exception was PR needles at 60 $kW.m^{-2}$ and natural convection. This was evaluated with a radiative Biot number assessment that includes heat losses due to re-radiation and convection. Understanding the thermal behavior of the particles is important, because it is a common assumption for modeling purposes that fine particles behave thermally thin. Knowing the limitations at what condition this assumption becomes unacceptable helps evaluate model uncertainties.

### *7.1.2. Ignition behavior*

**Effects of fuel properties**

It was discussed that fuel characterization is a key element in analyzing the flammability of vegetation. Such a characterization should be as detailed as possible, including properties such as ignition temperature ($T_{ig}$), *SVR*, thermal conductivity ($k$), particle density ($\rho$), specific heat ($c_p$), thermal diffusivity ($\alpha$) and absorptivity ($a$). It was found in this work that these properties can be used, in part, to explain results of the variations ignition time. For example, *SVR* was attributed as a driving factor behind the faster ignition of PS needles (high *SVR*). The technique employing geometric analysis to estimate the *SVR* showed fair agreement with an image analysis. The accuracy was around 10%. The simplicity of the technique makes it a useful tool which does not require much equipment.

The properties $k$, $\rho$, and $c_p$ govern the thermal response of a particle when subjected to a heating rate and thus also the ignition behavior (i.e. the time to reach ignition temperature). Species differences were observed in $\rho$ and $c_p$ which means that variations in ignition times can be expected due to variation in the thermal mass (or thermal inertia). For the two species tested in depth, PS and PR, the latter have the higher thermal mass ($\rho c_p$), which contributes to the longer ignition times observed for this species. Furthermore, this species also has significantly higher ignition temperature (PR: 340 °C, PS: 280 °C ), which further explains the longer ignition time.

It was found that dead needle density is lower than live (dried) needle density. Live (dried) needle density also showed seasonal trends. And finally young and mature needles showed differences. The exact reason is not evident but is likely due to composition (i.e. growth/decay) and internal needle porosity. For mature needles the variation over one year was ~5%. Growing needles are denser than mature needles and have a higher annual variation (~10%). The density decreases during the maturing process in the fall. The annual variation of mature needles may be considered

negligible because the experimental uncertainty was 2-8%. The variation of density for growing needles on the other hand is significant and showed a clear trend; the measurement uncertainty was 2-5%. Thus, a constant density should only be assumed for mature needle.

Live (wet) needle density was found to be linear with *FMC*. This was only observed for mature needles. Density for young growing needles was unaffected by the *FMC*, which suggests differences in composition and internal porosity. Effects of *FMC* outweighed the effects of seasonality for mature needles. An increasing ignition time with *FMC* can be associated, in part, to this increase in density however the heat of vaporization of water is anticipated to dominate.

Furthermore, it is suggested that young growing needles (dry and wet) can ignite faster because of the ability to release water with less resistance. Significant differences in dehydration rates (water) were observed. After three hours conditioning, the *FMC* of mature needles was approximately 48% of the initial *FMC*. After two hours conditioning, it was 63% for young needles.

Spectral dependence is observed for dead and live needles. The effective absorptivity/emissivity of dead and live needles was found to be different. It was found to be higher for live needles than for dead needles. For the given condition (FPA heating units) live needles have a mean absorptivity of 0.72 and dead needles 0.64. The higher absorptivity decreases the ignition time, which competes against the effects of other properties (e.g. $\rho$), which increase the ignition times. This competition is one of the reasons why no significant difference in ignition time was found between dead and live (dried) needles.

**Effects of external factors**

A forced convection impacts two mechanisms, heat and mass transfer. It impacts the net energy received by the particle due to convection cooling and mixing of pyrolysis

gases and air by varying the oxygen flow rate. An investigation was conducted to decouple these two affects and determine which one is the dominant mechanism driving the ignition behavior.

Increasing forced convection delays ignition due to cooling effects. This was observed to be true for low heating rates only. When the radiative heat flux is high enough, it dominates cooling effects and the ignition behavior is independent of the forced convection (airflow velocity). For the flow rates tested (6.67 and 13.3 $cm.s^{-1}$) the threshold was found to be around 40-45 $kW.m^{-2}$ for both species. This highlights the presence of two ignition regimes: (1) radiation/convection driven at low heating rates and (2) radiation only driven at high heating rates.

The cooling effects were further tested by varying the flow temperature. Increasing the temperature resulted in a decrease in ignition time. This is attributed to the increase in initial particle temperature which results in a shorter time to reach critical ignition temperature. Furthermore, convection cooling during the heating phase is reduced.

Increasing forced flow means that the oxygen mass flow rate into the mixing zone increases. Thus, it can delay the ignition by diluting the gas mixture (i.e. it takes longer to reach a LFL). It was concluded that the forced convection in the range tested did not increase the mixing time (of pyrolysis gases and air). This was tested by varying the oxygen concentration (14-23% $O_2$ by vol.) while keeping the flow magnitude constant; this varied the oxygen flow rate into the system, while keeping the heating conditions constant. No significant variation in ignition time (piloted) was observed for concentrations $\geq$ 17%. Below 17%, piloted ignition was no longer observed; only smoldering (transitioning to flaming) was observed as low as 14%. No further testing was done below this level. Thus, the dominant mechanism driving the ignition behavior is heat transfer. This means that the common assumption $t_{ig} \approx t_p$ is still valid for the given flow conditions and concentrations $\geq$ 17%. This is a useful simplification,

because the pyrolysis time is only a function of the fuel and heating and cooling rate (i.e. heat transfer).

Data produced from the FPA experimentation was used in a validation exercise of a simplified multiphase heat transfer model. This model is based on energy conservation principles and is intended as a predictive tool for ignition of porous fuel beds. The validation was performed with in-depth temperature, critical heat flux and ignition times at various forced convection flow rates and heat flux levels. In this model, in-depth radiation heat transfer is linearized with the Rosseland approximation. Convection heat transfer is either prescribed at the surface of the fuel bed (natural convection) or induced by advection (forced convection). Conduction was considered negligible due to the high porosity. It was concluded that the model can accurately predict ignition only when the flow rate is low ($Fr < 1.0$). Further validation is required to understand the full potential of this model.

It was concluded that *FMC* as a single variable to predict ignition is sufficient (<10% uncertainty). Such level of accuracy is acceptable in light of the complexity of the ignition process, measured *FMC*, sample preparation, test apparatus, and test conditions. It was shown that even the ignition time for dry fuel at natural convection has a variability of around 10%. It was shown that the time to ignition shows a linear relation to *FMC*, which can be assessed with a semi-physical model. It was assessed that needles will have a residual *FMC* at the time of ignition as is suggested by literature. Initial results showed that this residual *FMC* increases with increasing heating rate.

### *7.1.3. Burning behavior*

The effects of heat and mass transfer on the burning behavior was also assessed. For example, increasing the heat flux to the surface increases the pyrolysis rate, which results in a higher heat release rate. The heat release rate was unaffected by increasing external heat flux. This means that, after ignition the pyrolysis rate is driven by the

heat flux feedback from the flames and rate of smoldering. Increasing forced convection results in greater heat losses. However, the overall energy balance was such that heat gains (feedback from flames and smoldering) outweighed the losses.

The mass transfer is impacted by increasing forced convection which increases the heat release rate due to increased oxygen availability ($O_2$ flow rate). The increased $O_2$ flow rate also results in an increase in smoldering combustion. Both, flaming and smoldering combustion occur simultaneously and thus heat transfer from smoldering contributes to an increase in the pyrolysis rate.

Blocking entrainment air (quartz tube) from entering the combustion zone resulted in significant reduction in the combustion efficiency, which in turn resulted in lower combustion intensity. This condition (even with highest flow rate tested: 100 lpm air) is an oxygen limited combustion scenario, which results in significant incomplete combustion. This was identified by the change in CO and $CO_2$ generation rates. The oxygen limited combustion generates elevated CO levels and reduced $CO_2$ levels. Furthermore, pyrolysis in vitiated atmospheres showed a significantly higher production of CO compared to production in normal atmosphere.

When the oxygen concentration was reduced, a change in flaming regime was observed from diffusion to premixed type. The limiting oxygen concentration for the transition from diffusion to premixed type flaming was found between 17-19% $O_2$ (by vol.). A limiting concentration for premixed flame was not reached. At 14% $O_2$ premixed flames are still present and no further concentration was tested below this. Changing flaming regimes resulted in reduced heat flux feedback from the flames due to change in flame properties. It was concluded that heat release rates decrease with decreasing oxygen concentration due to the reduced heat flux feedback and reduction in the smoldering combustion. Convection heat losses were constant due to constant flow velocity and temperature.

At a given oxygen mass flow rate, the peak combustion intensity is significantly lower for tests in the confinement (using the quartz tube and 14-23% $O_2$) compared to test with varying flow magnitude in the open. This is due to lower pyrolysis rate (higher convective heat losses and lower heat flux feedback) and lower combustion efficiency.

The combustion efficiency was evaluated with the ratio of $CO/CO_2$. Combustion in the confinement resulted in significantly higher values of the ratio $CO/CO_2$ compared to samples tested in the open, indicating high levels of incomplete combustion (low combustion efficiency). The ratio is at least increased by tenfold. At worst it is increased 20-fold. In the open the ratio was around 1.0-1.5% (mean during flaming period). It is suggested that the elevated source of emissions from burning vegetation should consider a ventilation limited combustion besides smoldering combustion.

The peak combustion intensity was found to decrease with increasing *FMC* which is in line with literature. A polynomial regression model is proposed here. The data suggests three distinct *FMC* levels of interest. Regime (1) from 0-60%, regime (2) form 60-120% and regime (3) above 120%. Little data is available in region (3) that allows any significant conclusions. In regime (2), the combustion intensity is independent of the *FMC*. This indicates that, *FMC* masks seasonal effects. Below 60% FMC (regime (1)), combustion intensity increases drastically. Furthermore, results suggest that seasonal trends must be considered in this regime.

### *7.1.4. Live fuel flammability assessment*

Seasonal effects were assessed with unconditioned and conditioned needles. Dry fuel was tested in order to eliminate effects due to *FMC*. Conditioned needles indicated a rise in flammability during the growing season. Unconditioned needle flammability was significantly lower than conditioned needle flammability. Thus it was concluded that *FMC* masks seasonal trends due to state of growth/decay.

It was concluded that external factors (weather) are dominant factors that drive the occurrence of typical fire seasons compared to live fuel flammability. This is mainly because most fires start and travel on the ground in dead fuel beds and not in live foliage. *FMC* of dead fuel is governed by the environmental conditions, i.e. the weather. The live fuel flammability assessment (for dry and wet fuel) performed here did not reveal a significant correlation to the fire season (spring in the NJ Pine Barrens). For wet fuel, the flammability was found independent of season (i.e. constant). For dry fuel, the peak flammability occurs in August.

### *7.2. Direction of future research*

- Experimental protocols with the FPA have still room for improvements. The blockage device was a valuable modification in this work. However, it had the disadvantage that mass loss was impossible to determine when the blockage was used. Furthermore, the blockage was at the bottom edge of the sample. This forced the airflow into the bottom of the basket, but not out of the top surface of the sample. It is likely that a significant amount of the airflow escapes out the side of the sample basket. A new blockage should address these issues, for example by blocking the airflow at the level of the sample surface rather than the bottom.
- It was determined that the convective heat transfer coefficient is one of the most important variables when forced convection is present. This parameter strongly depends on the flow velocity used for the estimation. Only an estimated value was used in this work. Future work should employ sophisticated techniques such as particle image velocimetry (PIV), to obtain a more accurate value for the velocity. This will allow a more sound analysis of the convective heat transfer.
- Validation of the one-dimensional porous ignition model should continue. This should be done with additional fuel species. Furthermore, a new

validation should include bulk density and ambient temperature. Modifications of the model may be made to include for example *FMC*.

- Continue investigation in emission and link to fire behavior. The possibilities of ventilation controlled combustion in a realistic wildfire need to be determined.
- Continue experimentation to investigate the combustion efficiency and intensity for varying flow rate. Since it was shown that the combustion intensity depends on the heat flux feedback and smoldering it is beneficial to de-couple these two mechanisms and assess individual contribution.
- Conduct live fuel flammability assessments as outlined herein with a range of different species and apply a classification system. Evaluate if other pine species have similar season trends (dry fuel).
- Evaluate semi-physical ignition-FMC model (modified Pickard-Wraight correlation) with a range of heating rates and bulk densities. Develop supporting experimentation to determine residual FMC at ignition and develop a physical relationship for the correction factor $C_T$.
- Study the water (vapor) release mechanism of live foliage. Specifically difference for young growing and mature needles. This may be linked to pyrolysis gases release rates.

### *7.3. Final remarks*

The work presented in this work provides another stepping stone in the understanding the flammability of wildland fuel. Foremost, it illustrates that flammability (ignition and burning behavior) is not a constant property for these types of fuels, but significantly depends on a wide range of factors. Thus, it becomes a multi-dimensional parameter and should be quoted as such. Fuel flammability is an integral part in understanding fire behavior, which makes it critical for the mitigation of risks of wildfire. Research in this field is far from complete as community continues to seek a

unified methodology for an acceptable wildland fuel flammability assessment. To achieve this, one important question must be answered: what external conditions (heating rate, cooling rate, sample preparation, *FMC*, and others) should be used for a flammability assessment? This can only be answered by conducting large scale experimentation (field scale) with adequate measurement techniques to quantify fire behavior. This information can then be used more effectively in bench-scale flammability experimentation in order to define appropriate test conditions.

It was shown here that, live fuel flammability can be associated to the growing season. However, it did not correlate with the typical fire season (NJ Pine Barrens). This may be one reason why little catastrophic fires occur in this region as opposed to others (e.g. Western US). Of course, mitigation efforts (e.g. fuel treatments through prescribed burning) by the US Forest Service and authorities having jurisdictions also play a role. However, the assessment indicates a potential for extreme fire conditions, such as crowning, when weather conditions are favorable. It is likely that, the concurrence of a typical fire season and high live fuel flammability according to this assessment are a reason for the dramatic fire seasons in some regions (e.g. Western US). This should be examined with multiple species from various regions in order to understand why catastrophic fire seasons occur.

*This page is intentionally left blank.*

# Appendix

# Appendix

## Appendix A – Chapter 3

### Appendix A1 – Impact of gas temperature on $h_c$

The graph in Fig. A1.1. shows the relation between convective heat transfer coefficient and flow temperature at HF (13.4 $cm.s^{-1}$).

As an example, the convective heat transfer coefficient shown is a correlation for a bundle of cylinder in cross flow (see Chapter 1 and 4). Further details are be given in Chapter 4, in which the thermal behavior of the needles and sample are discussed in a non-dimensional analysis.

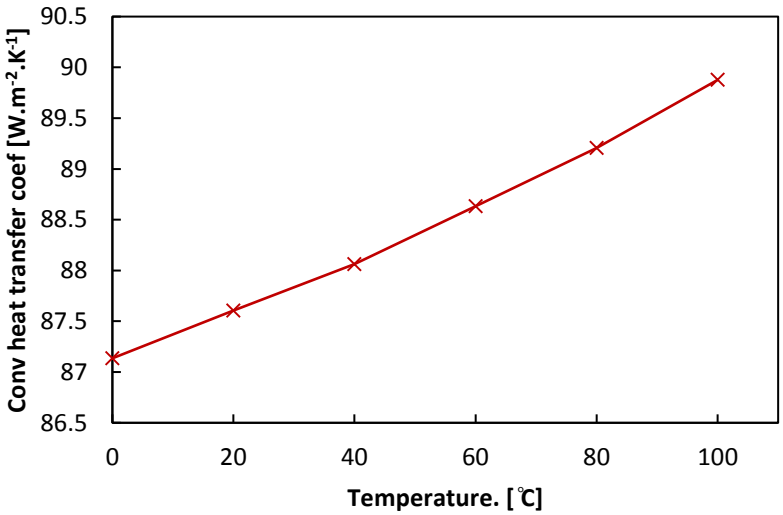


**Fig. A1.1. Heat transfer coefficient at 100 lpm inlet flow rate with respect to increasing flow temperature.**

## Appendix A2 – Calculation of forced oxygen flow rate

The oxygen flow rate can be calculated ($\dot{V}_{O_2} = y_{O_2}\dot{V}$) knowing the oxygen concentration, $y_{O_2}$, and magnitude of the volumetric flow rate, $\dot{V}$. The volumetric flow rate is converted into mass flow rate, $\dot{m}_{O_2}$, because pyrolysis rates, $\dot{m}_p$, are often reported in this manner. Prescribed flow rates used are 0, 50 and 100 lpm (NF, LF, HF condition, respectively). Oxygen concentration was varied between 14 and 23% (by vol.), $0.14 \leq y_{O_2} \leq 0.23$. Calculation results of the oxygen flow rates are presented in Fig. A2.1.

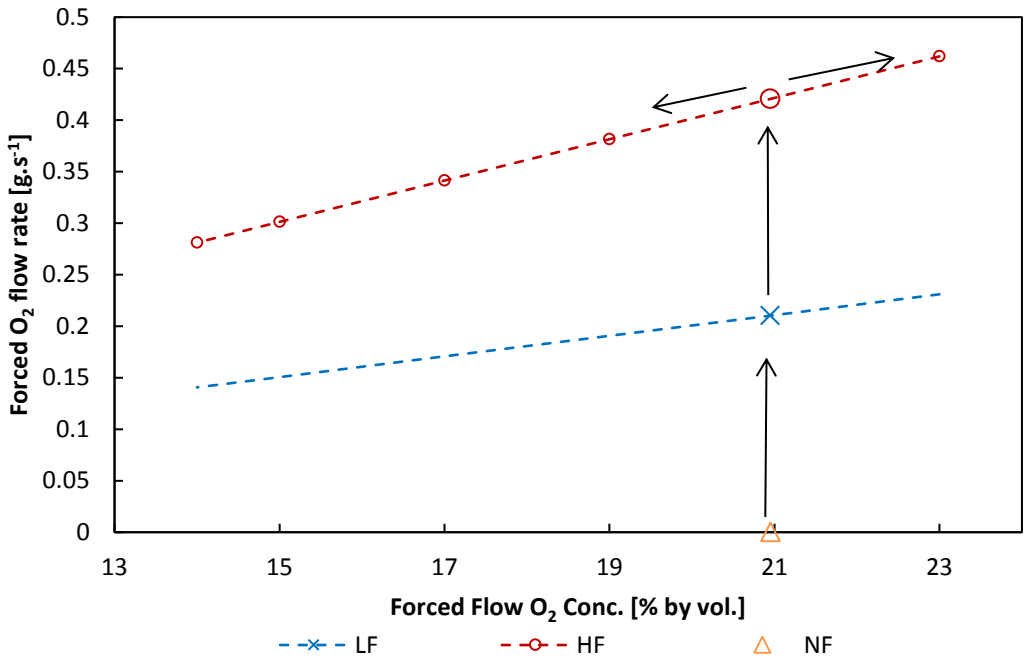


**Fig. A2.1. Oxygen flow rate with respect to the inlet flow oxygen concentration, for three inlet flow rates (NF, LF and HF). Markers indicate at which $O_2$ flow rates test were conducted. Enlarged markers indicate ambient condition.**

In this graph, the blue and red lines correspond to two different flow magnitudes (LF and HF). The arrows mark the pathways in which experimentation was carried out (First flow magnitude was increased from NF to LF to HF at ambient $O_2$ concentration, than $O_2$ concentration was varied for HF condition).

## Appendix A3 - Determination of length of flaming period for low oxygen concentration

The duration of flaming at low oxygen concentrations (< 17%) was estimated by evaluating the temperature in the duct. An example of the duct temperature evolution is given in Fig. A3.1. The time of flame out in this graph was determined by visual observation. The time of flame out corresponds to the steep decline of the temperature in the duct. Experiments at lower oxygen concentration, where the flames are not visible, had similar temperature curves (Fig. A3.2). It was not apparent, what exact moment corresponds to flame out, therefore, the estimation should be associated with some uncertainty. From Fig. A3.1., flame out corresponds to approximately the inflection point (or slightly after) of the temperature decay period. Therefore, this instant is used to approximate the time of flame extinction for tests where the flames are not visible.

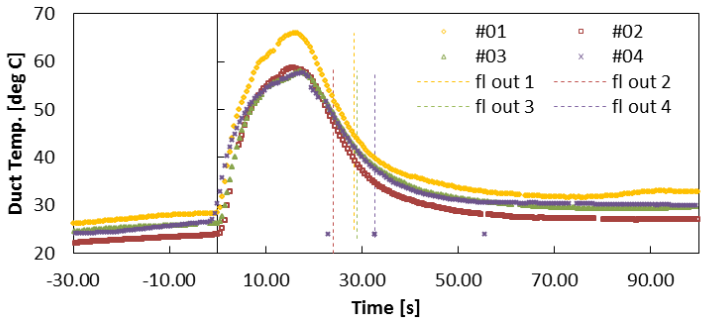


**Fig. A3.1. Typical duct temperature evolution for 4 repetitions of tests at ambient oxygen, no tube, 30 kW.m$^{-2}$, and 13.4 cm.s$^{-1}$. Flame out for each test is shown by the vertical dashed lines.**

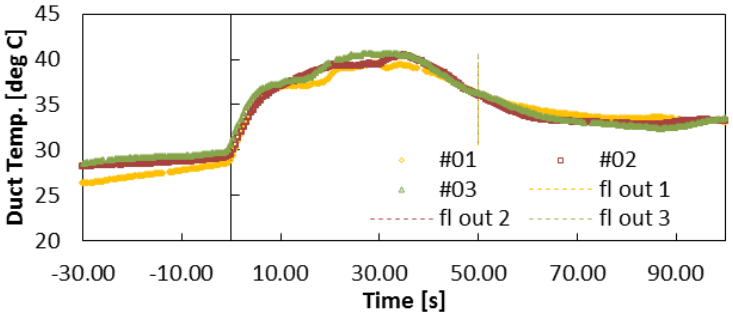


**Fig. A3.2. Typical duct temperature evolution for 3 repetitions of tests at 15% oxygen, tube, 30 kW.m$^{-2}$, and 13.4 cm.s$^{-1}$. Flame out for each test is shown by the vertical dashed lines.**

## Appendix A4 – CO and CO2 gen. rates for NF and HF conditions.

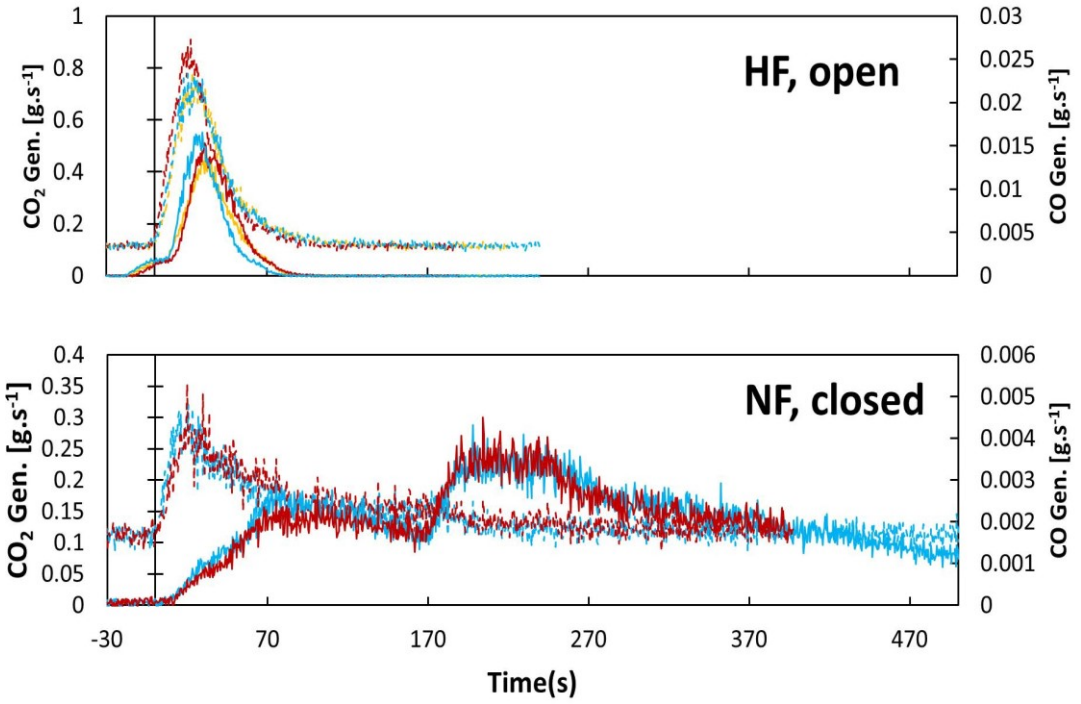


**Fig. A4.1. CO and $CO_2$ generation rates for tests with varying force airflow magnitude. Dashed lines are CO2 and solid lines are CO generation rates. Each color is one repetition. t=0s represents flaming ignition for each test.**

## Appendix B – Chapter 4

### Appendix B1 – Model discretization and computation domain

### Discretization

Table B1.1. gives the results of the time-step selection. A percent difference of less than 1% is considered acceptable. At low heat flux levels the ignition time is long. Therefore, resulting in lower error compared to high heat flux levels. A time-step of 0.05 s was found to be sufficiently small for the range of heat flux levels considered.

Table B1.1. Evaluation of time step selection with respect to time to ignition.

| | | $\Delta t$ [s] | $t_{ig}$ [s] | % Diff |
|---|---|---|---|---|
| low | 30 | 1 | 23.14 | |
| Heat flux | 30 | 0.5 | 22.88 | 1.12% |
| [kW.m$^{-2}$] | 30 | 0.1 | 22.67 | 0.91% |
| | 30 | 0.05 | 22.64 | 0.11% |
| high | 60 | 1 | 6.192 | |
| heat flux | 60 | 0.5 | 6.011 | 2.92% |
| [kW.m$^{-2}$] | 60 | 0.1 | 5.871 | 2.33% |
| | 60 | 0.05 | 5.854 | 0.30% |

Table B1.2. gives the results of the cell size selection at two time-step considerations. Again, a per cent difference of 1% is an acceptable error. The results of the analysis show that the cell size has to be on the order of $2.50 \times 10^{-5}$ m, or 0.025 mm, to produce computation error within the acceptable range.

Table B1.2. Evaluation of cell size with respect to time to ignition.

| | | $\Delta t$ [s]: | 0.1 | | 0.05 | | 0.1 - 0.05 |
|---|---|---|---|---|---|---|---|
| | | $\Delta x$ [m] | $t_{ig}$ [s] | %Diff | $t_{ig}$ [s] | %Diff | %Diff |
| low | 30 | 2.50E-03 | 21.10786 | - | 21.08203 | - | 0.12% |
| heat flux | 30 | 2.50E-04 | 22.74261 | 7.74% | 22.71642 | 7.75% | 0.12% |
| [kW.m$^{-2}$] | 30 | 2.50E-05 | 22.67036 | -0.32% | 22.64431 | -0.32% | 0.11% |
| high | 60 | 2.50E-03 | 5.706267 | - | 5.689833 | - | 0.29% |
| heat flux | 60 | 2.50E-04 | 5.838819 | 2.32% | 5.820986 | 2.31% | 0.31% |
| [kW.m$^{-2}$] | 60 | 2.50E-05 | 5.871418 | 0.56% | 5.853614 | 0.56% | 0.30% |

### Computational domain

The size of the computational domain can influence both the time to ignition and the in-depth temperature profile. The 1D model has a constraint at the front and back face. On the front face, it is the sample surface temperature, which is evaluated in each time step with initial condition of the ambient temperature. Because a semi-infinite behavior is assumed, the back face (of the computational domain) does not experience any heat losses. Therefore, the constraint is a constant temperature, which is the ambient temperature that is selected. The influence of the back face boundary constrain can be seen in Fig. B1.1. When the computational domain is set to the thickness of the sample (3.0 cm, solid line), the temperature profile is forced to match ambient conditions at this point. The result of the constraint is an inaccurate representation of what is occurring in this scenario. In order to overcome this issue, a larger domain needs to be selected (> 5.0 cm, dotted lines) until the boundary condition does not influence the simulation. At this point the curves give in Fig. B1.1 are only used for illustration purposes.

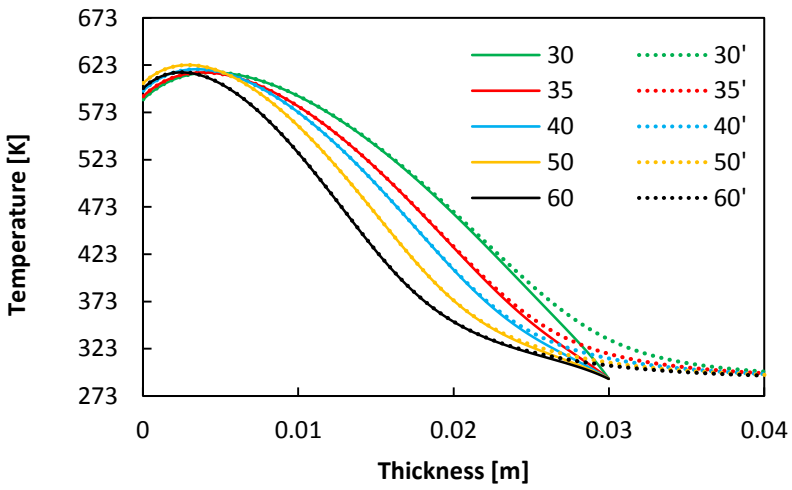


**Fig. B1.1. Simulation of the temperature profile of PR samples at various heat flux level [kW.m$^{-2}$]. Solid lines: 3 cm computational domain; Dotted lines: >5 cm computational domain. 0.0 m is the surface of the sample and 0.03 m is the back face.**

## Appendix B2 – Thermal evolution plotted against time

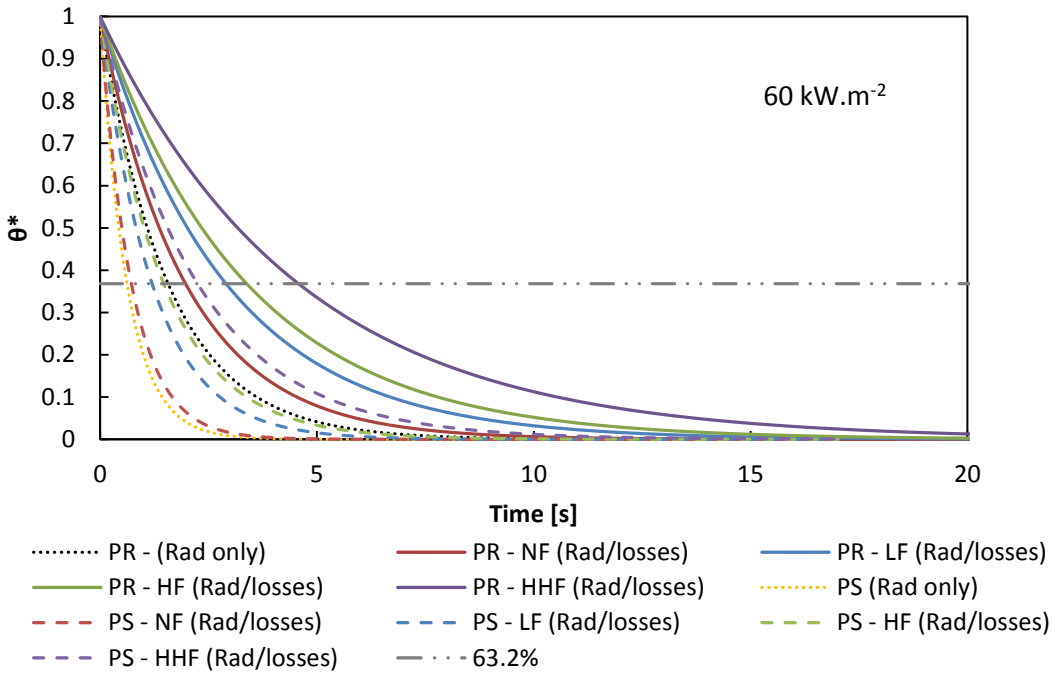


**Fig. B2.1. Thermal evolution (PS and PR) with respect to time for the radiation-losses boundary condition.**

## Appendix B3 – Thermal evolution at various heating rates

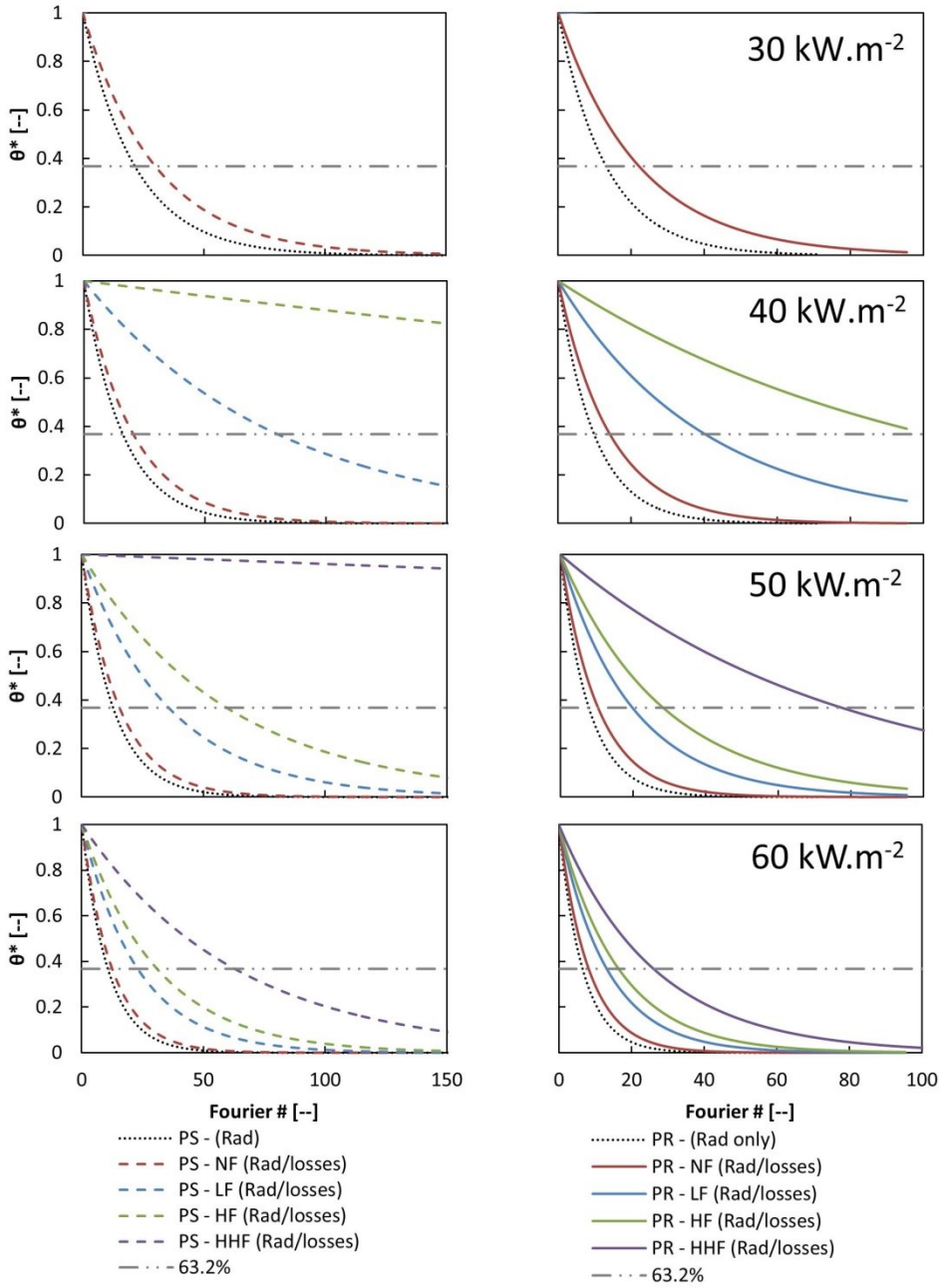


**Fig. B3.1. Thermal evolution (left: PS and right: PR) with respect to Fourier number for the radiation-losses boundary condition. Shown at various external heating conditions. The thermal evolution for the radiation-only boundary ("no-loss") condition is included**

The left hand side (Fig. B3.1) shows the evolution of the particle temperature of PS needles, and on the right hand side of PR needles, at the given external heat flux condition. The dotted lines in each graph are the evolutions determined with the "no loss" condition. When a line is not shown, for example blue, green and purple in the first row of plots (30 $kW.m^{-2}$), this means, that the critical heat flux condition (see Table 4.10) was not achieved and the particle did not heat up. The horizontal line corresponds to the condition when the particle has reached 63.2% of its equilibrium temperature. This condition is determined by the thermal time constant, $\tau$.

The thermal behavior when considering heat losses indicates, that, deviation from the "no loss" condition can be significant. Particles react slower to the heating when forced convection is present (different color lines in one graph). Furthermore, it can also be observed that, at one flow condition the deviation from the "no loss" condition increases with decreasing external heat flux (compare one color in different plots). The tendency describes the dominance of radiation over convection heat transfer.

The deviation from the "no loss" condition with increasing convection explains that, the "no loss" assumption is most feasible, when quiescent air is present.

## Appendix B4 – Some thermal time constants for "no loss" and "loss" condition

Table. B4.1. Summary of the thermal time constant for the radiation-only boundary condition.

| | Heat flux [kW.m$^{-2}$] | Radiation only ("no loss") | |
|---|---|---|---|
| | | PS | PR |
| $\tau_{rad}$ at heat flux [s] | 30 | 1.240 | 3.138 |
| | 40 | 0.930 | 2.354 |
| | 50 | 0.744 | 1.883 |
| | 60 | 0.620 | 1.569 |

Table. B4.2. Summary (PS and PR) of the thermal time constant for the radiation-losses boundary condition. Includes comparison to the "no-loss" boundary condition.

| | | Radiation/Convection (convection and radiation losses) | | | | | | | |
|---|---|---|---|---|---|---|---|---|---|
| | Heat flux [kW.m$^{-2}$] | PS | | | | PR | | | |
| | | Natural Conv. | Forced Convection | | | Natural Conv. | Forced Convection | | |
| | | NF | LF | HF | HHF | NF | LF | HF | HHF |
| $v$ [m.s$^{-1}$] | | 0 | 6.67 | 13.3 | 26.7 | 0 | 6.67 | 13.3 | 26.7 |
| $h_T$ [W.m$^{-2}$.K$^{-1}$] | | 20.83 | 71.30 | 85.27 | 106.96 | 24.44 | 55.18 | 64.30 | 78.86 |
| $\tau_{rad,losses}$ at heat flux [s] | 30 | 1.728 | -- | -- | -- | 5.296 | -- | -- | -- |
| | 40 | 1.180 | 1.180 | 3.372 | 6.946 | 3.390 | 7.586 | 11.997 | -- |
| | 50 | 0.896 | 1.769 | 2.432 | 5.6882 | 2.492 | 4.201 | 5.275 | 8.907 |
| | 60 | 0.722 | 1.199 | 1.467 | 2.248 | 1.971 | 2.905 | 3.381 | 4.577 |
| % Difference between $\tau_{rad}$ and $\tau_{rad,losses}$ | 30 | 39.3 | -- | -- | -- | 68.8 | -- | -- | -- |
| | 40 | 26.8 | 262.5 | 646.7 | -- | 44.0 | 222.3 | 409.7 | -- |
| | 50 | 20.4 | 137.7 | 225.6 | 663.5 | 32.4 | 123.1 | 180.1 | 373.0 |
| | 60 | 16.4 | 93.3 | 136.6 | 262.6 | 25.6 | 85.1 | 115.5 | 191.7 |

## Appendix B5 – Model performance (NF) at various time steps

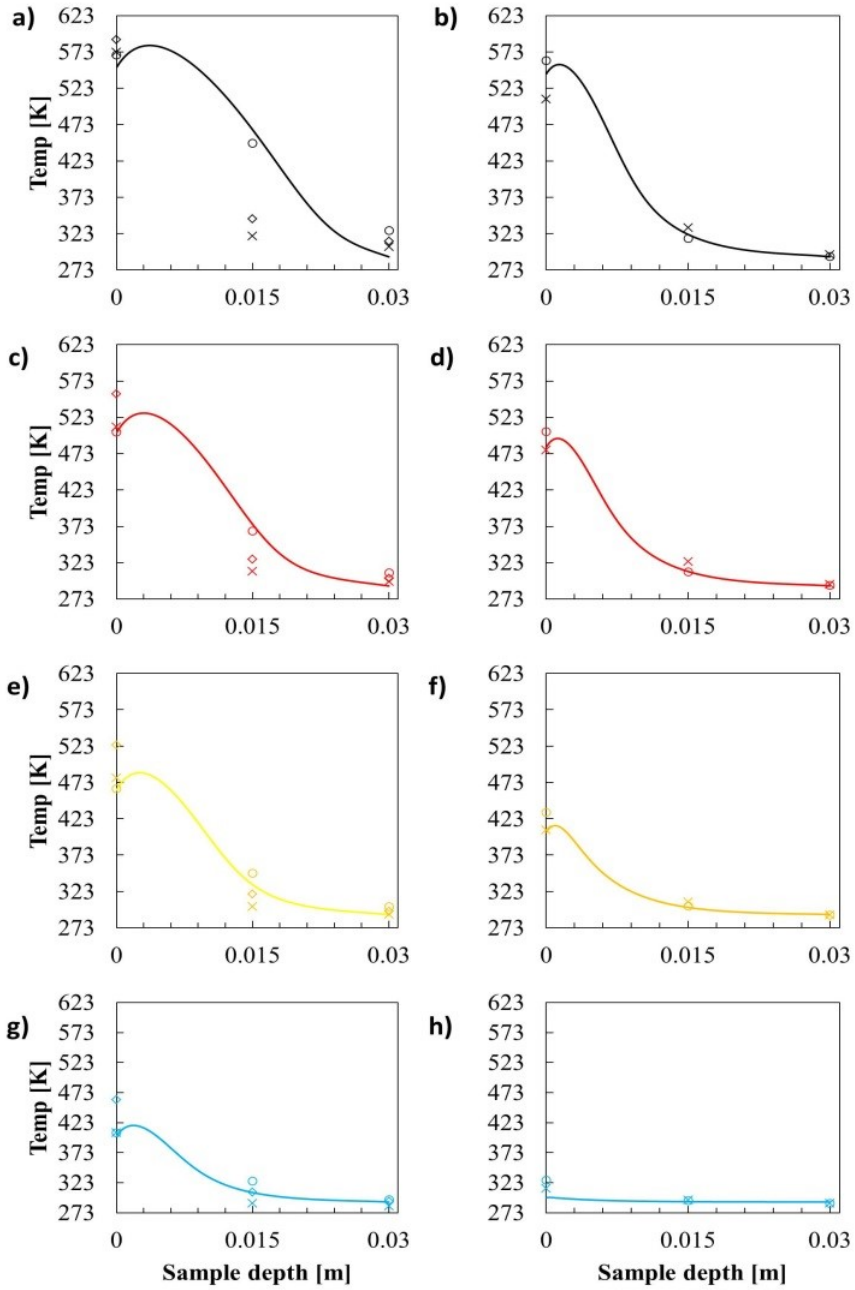


**Fig. B5.1. Temperature profile evolution at various times until ignition for PS samples exposed to 20 kW.m$^{-2}$ (a. ignition; c. 30 s; e. 20 s; g. 10 s.) and 60 kW.m$^{-2}$ (b. ignition; d. 5 s; f. 3 s; h. 1 s.). The data points indicate repeated experiments. Convection is natural.**

# Appendix C – Chapter 5

## Appendix C1 – Averaged density measurements of dried PRI needles.

Table. C1.1. Summary of averaged apparent needle densities at different stages of growth/decay.

| | Density [kg.m$^{-3}$] | | St.dev. [%] |
|---|---|---|---|
| | Mean | St.dev. | |
| NG, young (Jul-Nov) | 966 | 55 | 5.7 |
| NG, all | 918 | 94 | 10.2 |
| NG, mature | 798 | 27 | 3.4 |
| OG, all | 787 | 38 | 3.8 |
| All, mature | 789 | 28 | 3.6 |
| Dead (Nov) | 721 | 23 | 3.1 |
| Dead (ground) | 610 | 10 | 1.6 |

## Appendix C2 – Spectral Analysis of Live and Dead Pitch Pine Needles

This experimental series and report were produced by Dr. Marcos Chaos at FM Global.

### Experimental Details

*Spectral measurements*

The spectral reflectivity of pine needle samples (see below) was measured over a wide range of wavelengths, from ultraviolet to long infrared (0.25-20 μm). This range is similar to those of [1, 2] and much broader than those considered in other literature studies concerned with the spectral characteristics of vegetation (e.g., [3, 4]); however, it is necessary to ensure that the fraction of blackbody (or greybody) emissive power contained within the spectral band is as high as possible for temperatures typical of fires and bench-scale tests, such as those conducted in the FPA [2]. Two instruments were used to cover this spectral range: (1) ultraviolet, visible, and near infrared spectra (0.25-2.5 μm) were collected by a double-beam Shimadzu UV-3600 UV-Vis-NIR spectrophotometer equipped with a 6-cm diameter integrating sphere coated with barium sulfate ($BaSO_4$) and fitted with lead selenide and photomultiplier detectors; (2) mid- and long-infrared spectra (2-20 μm) were obtained with a Nicolet iS10 FT-IR spectrometer coupled with a 7.6-cm diameter gold-coated integrating sphere (Pike Technologies IntegratIR$^{TM}$) fitted with a mercury cadmium telluride (HgCdTe) detector. For measurements in the ultraviolet, visible, and near infrared spectral regions, a substitution method was employed wherein the reflectivity of the samples was compared to that of a calibrated reference (see Fig. C2.1.a.); measured values were corrected for substitution error [5]. For measurements in the mid- and long-infrared regions a flipper mirror could be switched to illuminate a calibrated reference or the sample so that no substitution was needed (the so-called Taylor method [6], see Fig. C2.1.b.). With known reflectivity, the emissivity (absorptivity) of the samples can be determined by invoking Kirchhoff's law [7, 8] (reflectivity and emissivity/absorptivity

are complimentary, i.e. emissivity = absorptivity = 1 - reflectivity). This approach assumes a completely opaque surface. The transmissivity of the prepared pine needle samples was measured using the apparatuses described above. Over the wavelength range considered the transmissivity was found to be negligible (< 0.5 %), which ensures that the samples were sufficiently thick so as to be optically opaque. It is noted that other studies that have investigated the spectral characteristics of pine needles (e.g., [4, 9, 10]) used samples consisting of a single layer of needles. In this case, corrections were needed to take into account the effect of void spaces between the needles; no such correction techniques were employed herein.

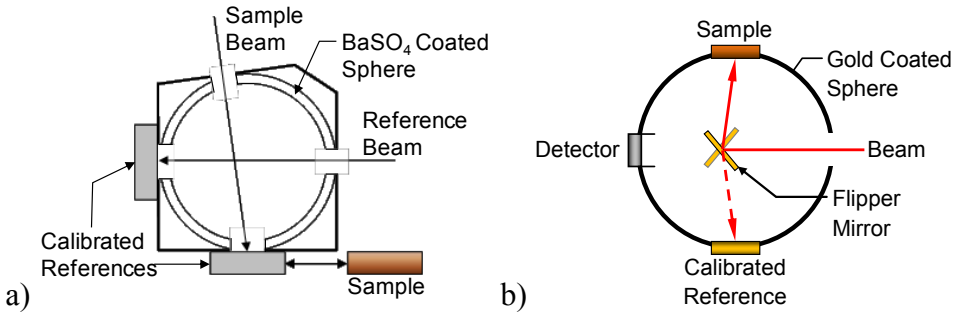


**Fig. C2.1. Spectral reflectivity measurement systems: (a) integrating sphere for measurements in the ultraviolet, visible, and near infrared; (b) integrating sphere for measurements in the mid- and long-infrared. The detectors for (a) are located 90° out of plane from the sample and reference beams.**

All reflectivity measurements were performed by illuminating the samples at 8° from their surface normal and collecting the total hemispherical reflectivity (i.e., directional-hemispherical measurement). It is noted that no attempt was made to separate the measured reflectivity into diffuse and specular components; all surfaces are assumed to be Lambertian (i.e., diffuse) so that specularly reflected light is negligible compared to the total hemispherical value. Two sets of scans were taken for each measurement: one for the calibrated reference (i.e. the "background" reading) immediately followed by the sample scan. The calibrated reference used for the ultraviolet, visible, and near infrared measurements was a NIST traceable Labsphere Spectralon® certified diffuse reflectance standard (component SRS-99-010, serial # 7A37B-4165); for the mid- and long-infrared measurements a NPL (National Physics Laboratory, UK) traceable

Avian gold certified diffuse reflectance standard (model RS-Au-02c, calibration # AT-20121201-IR1) was used. The uncertainty in the calibration values of the references is 2%; the uncertainty in the spectral measurements reported herein is estimated to be 5% due to photometric accuracy of the detectors used.

*Materials and Sample Preparation*

The materials considered in this study were pitch pine (*Pinus rigida*) needles collected from the Silas Little Experimental Forest in New Lisbon, NJ, USA; live (Fig. C2.2.a. and b.) and dead (Fig. C2.2.c. and d.) needles were used. The samples were collected from the field and sealed in plastic bags. Live needles were refrigerated whereas dead needles were kept at laboratory conditions (typically 20$^{o}$C and 45% relative humidity). The spectral measurements described herein were performed within one week of harvesting the samples. For the live needles, prior to collecting data, the samples were allowed to reach room temperature. No other sample conditioning was otherwise performed. As tested, the moisture content, on a dry mass basis, of live needles was 134.7 ± 6% whereas that for dead needles was 13.3 ± 0.7% (based on five repeat measurements performed on an A&D MX-50 Moisture Analyzer).

Needles were placed on sample holders with 25.4-mm diameter apertures (Fig. C2.2.); this aperture size ensured that the needles filled the sample ports of the integrating spheres used. Samples were prepared by arranging needles either in structured side-by-side (Fig. C2.2.a. and c.) or random (Fig. C2.2.b. and d.) orientations. Three samples of each orientation were assembled for a total of six samples each for live and dead needles. As mentioned above, sufficient needle layers were used to generate optically opaque samples. On average the thickness of the samples tested was 10 mm, approximately.

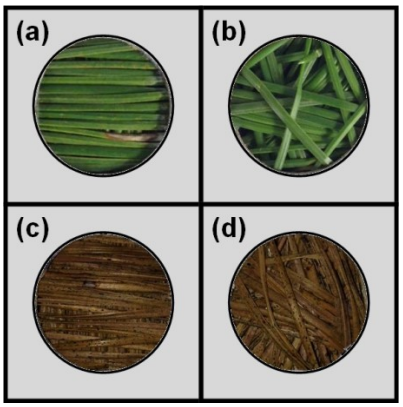


**Fig. C2.2. Representative *Pinus rigida* needle samples prepared for this study; live (a, b) and dead (c, d) needles arranged in structured (a, c) and random (b, d) orientations.**

## Results and Discussion

Spectral reflectivity measurements for live and dead needles are shown in Fig. C2.3.a. and b., respectively; highly non-grey spectral distributions are evident. The standard deviation of the six measurements taken for each of the needles is also represented in Fig. C2.3. There is noted variability (in excess of 40%), especially in the near infrared (~1-3 μm, 3300-10000 $cm^{-1}$) which indicates that the needles are not perfectly diffuse reflectors and directional effects are present. The samples used (see Fig. C2.2), however, are expected to be representative of and capture such effects, on average. Fig. C2.3. also includes data for remote sensing applications collected by the U.S. Geological Survey for live and dead lodgepole pine (*Pinus contorta*) needles [11]. Agreement with the present measurements is good, especially for the live needles. Although not shown for the sake of clarity, the present data are also in good agreement with those of Acem et al. [4] for Aleppo pine (*Pinus halepensis*) needles.

For live needles, in the visible wavelength range (~0.4-0.8 μm, 12500-25000 $cm^{-1}$), over 90% of the radiation is absorbed (i.e., low reflectivity) by pigments within the needle cells. The absorbed radiation energy is used by the needles in the photosynthesis process. A reflectivity peak near 0.55 μm (18200 $cm^{-1}$) can be discerned in Fig. C2.3.a., which is attributed to chlorophyll and gives the live needles their apparent

green color [12, 13]. For wavelengths greater than 0.7 μm (< 14285 $cm^{-1}$) reflectivity dramatically changes and is determined by the internal cell structure of the needles as well as the content of biochemicals (proteins, lignin, cellulose, etc.) and water [14]. There are strong water absorption bands present at 1.4 μm (7142 $cm^{-1}$) and 1.9 μm (5263 $cm^{-1}$) which lower the reflectivity of live needles at these wavelengths.

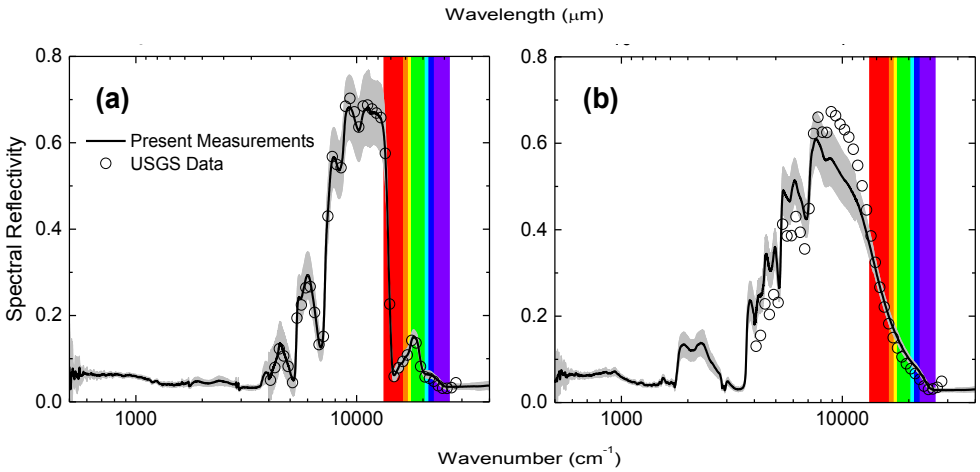


**Fig. C2.3. Spectral reflectivity of (a) live and (b) dead pine needles. Bold lines correspond to the average of all measurements performed in this study for Pinus rigida samples. Thin lines represent two standard deviations from the mean based on six samples. Symbols are data collected by Clark et al. [11] for lodgepole pine (Pinus contorta). In the plots the colormap regions denote the visible spectrum.**

Dead needles (see Fig. C2.3.b.) are characterized by an overall increase of reflectivity, when compared to live needles, for wavelengths beyond approximately 1.2 μm (< 8333 $cm^{-1}$), principally due to their much lower water content. This observation is properly illustrated by considering the 3.5–5.75 μm (1739-2857 $cm^{-1}$) spectral range where reflectivities of live and dead needles differ by a factor of two, approximately. The lack of water absorption helps reveal spectral characteristics (e.g., reflectivity peaks near 2 μm, 5000 $cm^{-1}$) due to structural biochemical molecules [1] as mentioned above. At shorter wavelengths, the reflectivity of dead needles is higher than that of live needles throughout most of the visible spectrum (~0.4-0.7 μm, 14285-25000 $cm^{-1}$) and lower for wavelengths between 0.7 and 1.2 μm (8333-14285 $cm^{-1}$). This

observation is consistent with the studies of [14, 15] and representative of damaged vegetation.

The spectral emissivity (absorptivity) for live and dead needles derived from the reflectivity data of Fig. C2.3. can be found in Fig. C2.4. As mentioned above, live and dead needles are highly non-grey absorbers/emitters and differ most notably in the near- and mid-infrared spectral regions. This behavior has direct implications in radiative energy balance calculations [2], which require that the spectral radiation environment interacting with the needles be taken into account. For example, the pine needles considered in the present study would absorb radiation more efficiently from low temperature sources (characterized by longer wavelengths) than from those at higher temperatures. On the other hand, emission of radiation (i.e., re-radiation) from the pine needles would be determined by their surface temperature, which may considerably differ from those of the radiation sources interacting with them. Therefore, one needs to determine the effective emissivity and absorptivity of the pine needles as a function of temperature.

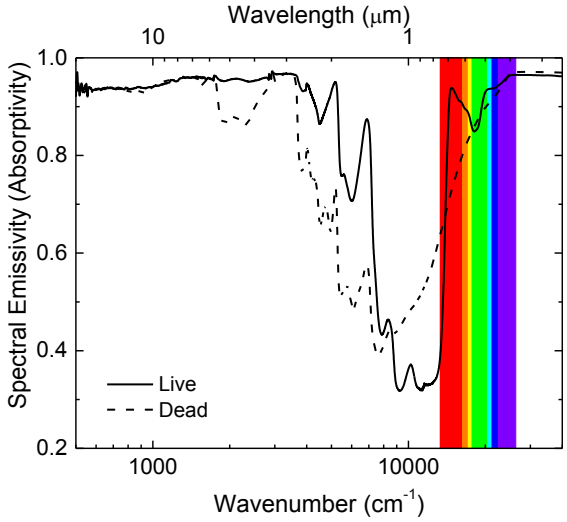


**Fig. C2.4. Spectral emissivity (absorptivity) of live and dead *Pinus rigida* needles; the colormap region denotes the visible spectrum.**

The discussion above indicates that even though, by Kirchhoff's law, the spectral emissivity and spectral absorptivity of the pine needles studied herein are equal (see Fig. C2.4.), their effective (i.e., spectrally averaged) emissivity and absorptivity may not necessarily be so. The effective emissivity, $\varepsilon_{eff}$, is strictly a function of the surface temperature of the material, $T_s$, and can be expressed as:

$$\varepsilon_{eff}(T_s) = \frac{\int \varepsilon(\lambda) I(\lambda, T_s) d\lambda}{\int I(\lambda, T_s) d\lambda} \tag{1}$$

Similarly, the effective absorptivity, $\alpha_{eff}$, is dependent on the radiation source temperature, $T_r$, and is given by:

$$\alpha_{eff}(T_r) = \frac{\int \alpha(\lambda) I(\lambda, T_r) d\lambda}{\int I(\lambda, T_r) d\lambda} \tag{2}$$

In Eqs. 1 and 2 $\varepsilon(\lambda)$ and $\alpha(\lambda)$ are the spectral emissivity and absorptivity, respectively (i.e., data shown in Fig. C2.4.; note that $\varepsilon(\lambda) = \alpha(\lambda)$), $\lambda$ is the wavelength, and $I(\lambda,T)$ is the spectral radiance of a body at a given temperature $T$ described by Planck's law:

$$I(\lambda, T) = \frac{h_p c^2}{\lambda^5} \left[ \exp\left( \frac{h_p c}{\lambda k_B T} \right) - 1 \right]^{-1} \tag{3}$$

where $h_p$ is Planck's constant, $c$ is the speed of light, and $k_B$ is Boltzmann's constant. Note that no temperature dependence has been assumed for $\varepsilon(\lambda)$ and $\alpha(\lambda)$ in Eqs. 1 and 2. As opposed to conducting or semi-conducting materials where electron movement (to fill conduction bands, for example) changes as a function of temperature, no such physical processes that may alter the surface characteristics occur in dielectric materials, such as the pine needles considered in this study. Therefore, the assumption of temperature independence for $\varepsilon(\lambda)$ and $\alpha(\lambda)$ is reasonable.

On the basis of the above discussion, Fig. C2.5. shows the results of Eqs. 1 and 2 as a function of temperature for the live and dead pine needles considered herein. As applied to bench-scale flammability tests conducted in the FPA, note that the FPA heaters radiate at temperatures of 2000 K < $T_r$ < 3000 K [2] where the effective absorptivity of live and dead needles differs by approximately 10 to 15% (on average, $\alpha_{eff}$ = 0.72 and 0.64 for live and dead needles, respectively, over this temperature range). On the other hand, typical surface temperatures are characterized by 300 K < $T_s$ < 1000 K for which the effective emissivity of live ($\varepsilon_{eff}$ = 0.95 on average) and dead ($\varepsilon_{eff}$ = 0.92 on average) needles differs by about 3%. Of course, the needles will char at higher temperatures; however, char spectrally behaves like a greybody with effective emissivity and absorptivity greater than approximately 0.8 [1, 2]. The results shown in Fig. C2.5 will have direct implications in interpretation of FPA data.

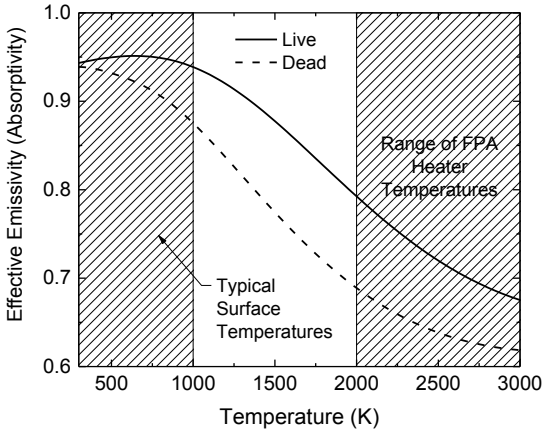


**Fig. C2.5. Effective emissivity and absorptivity of live and dead *Pinus rigida* needles as a function of temperature. Typical temperatures for surface emission and FPA heater radiation are shown by the shaded areas.**

## References

1. M. Försth, A. Roos, "Absorptivity and its dependence on heat source temperature and degree of thermal breakdown," Fire and Materials 35 (2011) 285-301. doi:10.1002/fam.1053

2. M. Chaos, “Spectral aspects of bench-scale flammability testing: Application to hardwood pyrolysis,” Fire Safety Science 11 (2014) in press. http://www.iafss.org/publications/fss/11/209
3. R.F. Kokaly, D.G. Despain, R.N. Clark, K.E. Livo, “Mapping vegetation in Yellowstone National Park using spectral feature analysis of AVIRIS data,” Remote Sensing of Environment 84 (2003) 437-456. doi: 10.1016/S0034-4257(02)00133-5
4. Z. Acem, G. Parent, B. Monod, G. Jeandel, P. Boulet, “Experimental study in the infrared of the radiative properties of pine needles,” Experimental Thermal and Fluid Science 34 (2010) 893-899. doi:10.1016/j.expthermflusci.2010.02.003
5. J.A. Jacquez, H.F. Kuppenheim, “Theory of the integrating sphere,” Journal of the Optical Society of America 45 (1955) 460-470. doi:10.1364/JOSA.45.000460
6. A.H. Taylor, “The measurement of diffuse reflection factors and a new absolute reflectometer,” Journal of the Optical Society of America 4 (1920) 9, doi:10.1364/JOSA.4.000009
7. G. Kirchhoff, “Über den zusammenhang zwischen emission und absorption von licht und wärme,” Monatsberichte der Akademie der Wissenschaften zu Berlin, sessions of Dec. 1859, 1860, 783-787.
8. G. Kirchhoff, “Über das verhältnis zwischen dem emissionsvermögen und dem absorptionsvermögen. der körper für wärme und licht,” Poggendorfs Annalen der Physik und Chemie 109 (1860) 275-301. (English translation by F. Guthrie: G. Kirchhoff, “On the relation between the radiating and the absorbing powers of different bodies for light and heat,” Philosophical Magazine Series 4 20 (1860) 1-21, doi:/10.1080/14786446008642901)
9. C.S.T. Daughtry, K.J. Ranson, L.L. Biehl, “A new technique to measure the spectral properties of conifer needles,” Remote Sensing of Environment 27 (1989) 81-92. doi:10.1016/0034-4257(89)90039-4
10. M.A. Mesarch, E.A. Walter-Shea, G.P. Asner, E.M. Middleton, S.S. Chan, “A revised measurement methodology for conifer needles spectral optical properties:

Evaluating the influence of gaps between elements," Remote Sensing of Environment 68 (1999) 177-192. doi:10.1016/S0034-4257(98)00124-2

11. R.N. Clark, G.A. Swayze, R. Wise, E. Livo, T. Hoefen, R. Kokaly, S.J. Sutley, USGS digital spectral library splib06a: U.S. Geological Survey, Digital Data Series 231, 2007, http://speclab.cr.usgs.gov/spectral.lib06
12. D.M. Gates, H.J. Keegan, J.C. Schleter, V.R. Weidner, "Spectral properties of plants," Applied Optics 4 (1965) 11-20. doi:10.1364/AO.4.000011
13. E.B. Knipling, "Physical and physiological basis for the reflectance of visible and near-infrared radiation from vegetation," Remote Sensing of Environment 1 (1970) 155-159. doi:10.1016/S0034-4257(70)80021-9
14. B.N. Rock, J.E. Vogelmann, D.L. Williams, A.F. Vogelmann, T. Hoshizaki, "Remote detection of forest damage: Plant responses to stress may have spectral 'signatures' that could be used to map, monitor, and measure forest damage," BioScience 36 (1986) 439-445. doi:10.2307/1310339
15. G.A. Carter, W.G. Cibula, T.R. Dell, "Spectral reflectance characteristics and digital imagery of a pine needle blight in the southeastern United States," Canadian Journal of Forest Research 26 (1996) 402-407. doi:10.1139/x26-045

## Appendix C3 – Ignition and pHRR plotted against apparent needle density

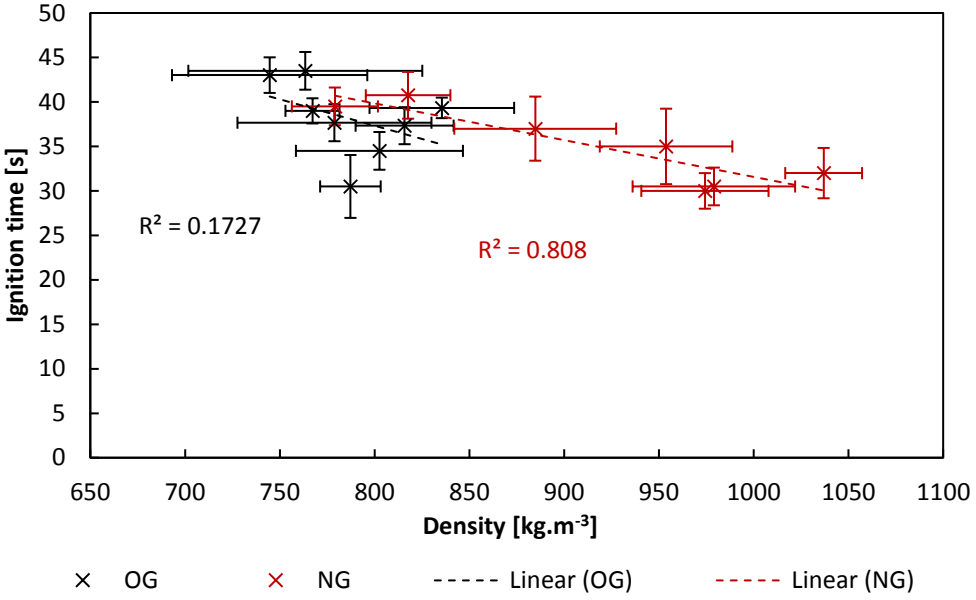


**Fig. C3.1. Time to ignition of 0% *FMC* samples plotted against apparent (dry) density.**

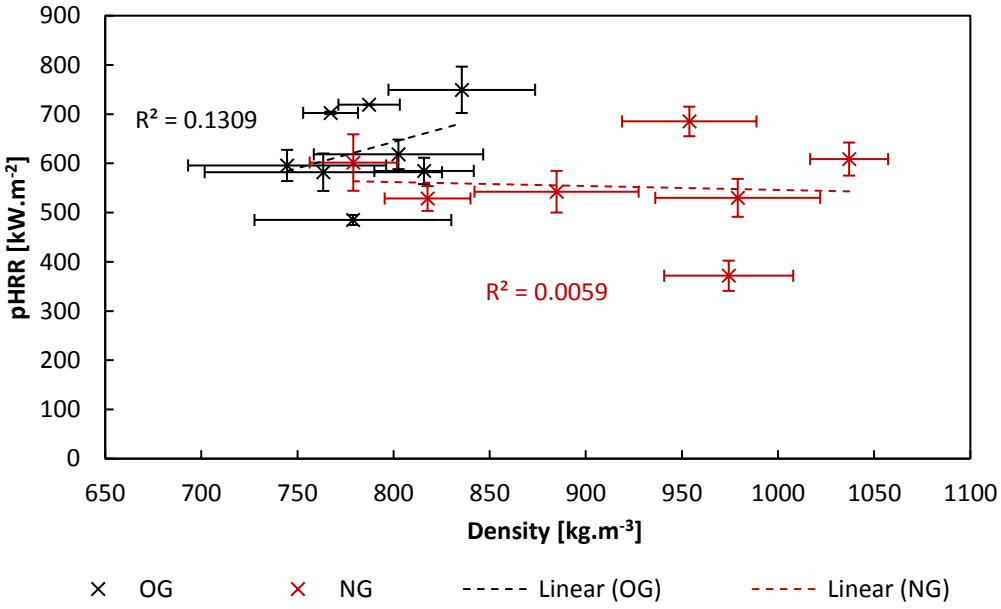


**Fig. C3.2. Peak HRR of 0% *FMC* samples plotted against apparent (dry) density.**

## Appendix C4 – Summary of density, ignition time and pHRR results with experimental error

Table. C4.1. Summary of ignition time (piloted) and pHRR obtained from FPA combustion tests with live (dried) PRI needles. Density measurements were obtained from liquid submersion technique.

| Type | Date | Density [kg.m$^{-3}$] | | Ignition time [s] | | pHRR [kW.m$^{-2}$] | |
|---|---|---|---|---|---|---|---|
| | | Avg. | St.dev. [%] | Avg. | St.dev. [%] | Avg. | St.dev. [%] |
| OG | 17/04/2014 | 744.6 | 6.9 | 43.0 | 4.6 | 595.7 | 5.3 |
| | 07/05/2014 | 763.5 | 8.1 | 43.5 | 4.9 | 582.0 | 6.5 |
| | 02/06/2014 | 778.8 | 6.6 | 37.7 | 5.5 | 484.8 | 2.1 |
| | 07/07/2014 | 802.6 | 5.5 | 34.5 | 6.1 | 618.3 | 4.9 |
| | 04/08/2014 | 787.3 | 2.0 | 30.5 | 11.6 | 719.1 | 0.0 |
| | 27/08/2014 | 767.2 | 1.9 | 39.0 | 3.6 | 702.6 | 0.3 |
| | 05/10/2014 | 835.5 | 4.6 | 39.3 | 2.9 | 749.4 | 6.3 |
| | 29/10/2014 | 815.8 | 3.2 | 37.3 | 5.6 | 584.6 | 4.6 |
| NG | 07/07/2014 | 974.3 | 3.4 | 30.0 | 6.7 | 371.6 | 8.3 |
| | 04/08/2014 | 979.0 | 4.4 | 30.5 | 7.0 | 529.9 | 7.3 |
| | 27/08/2014 | 1036.9 | 2.0 | 32.0 | 8.8 | 608.7 | 5.5 |
| | 05/10/2014 | 953.8 | 3.7 | 35.0 | 12.1 | 685.1 | 4.4 |
| | 29/10/2014 | 884.8 | 4.8 | 37.0 | 9.7 | 542.4 | 7.8 |
| | 04/12/2014 | 817.7 | 2.7 | 40.8 | 6.5 | 528.6 | 4.8 |
| | 17/04/2015 | 779.1 | 2.9 | 39.5 | 5.4 | 601.6 | 9.5 |

# Appendix D – Chapter 6

## Appendix D1 – Statistical summary of sample dry mass for all tests (OG and NG)

Table. D1.1. Equivalent mass for samples in the range of FMC under consideration.

| FMC | $m_{dry}$ [g] | $m_{eq}$ [g] |
|---|---|---|
| 0% | 13.89 | 13.89 |
| 30% | 13.89 | 18.06 |
| 60% | 13.89 | 22.22 |
| 90% | 13.89 | 26.39 |
| 120% | 13.89 | 30.56 |
| 150% | 13.89 | 34.73 |
| 180% | 13.89 | 38.89 |
| 210% | 13.89 | 43.06 |

Table. D1.2. Live needle sample (PRI) dry mass, averaged over all tests conducted.

| | Sample dry mass [g] | |
|---|---|---|
| | OG | NG |
| Mean | 14.22 | 14.09 |
| St. dev. | 0.60 | 0.71 |
| N | 75 | 77 |

## Appendix D2 – Apparent needle density as a function of *FMC*

*OG needles*

OG needles collected in June were dried for a certain period in order to obtain a residual *FMC* (depending on the length of conditioning) lower than the maximum. Immediately after the conditioning, density measurements were performed. The results (unconditioned, two residual *FMC*, and fully dried conditions) shown in Fig. D2.1., indicate a linear relation between needle density and *FMC*.

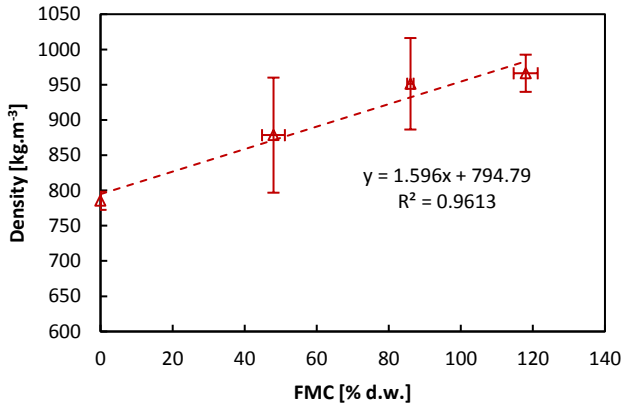


**Fig. D2.1. Density of June (OG) needles with respect to *FMC*. Highest FMC refers to unconditioned needles. Mid-values are two residual *FMC* after conditioning for several hours. 0% *FMC* is needles conditioned for 24 hrs.**

The intercept, 794.79, has the units of density [kg.m$^{-3}$] and can be taken as the dry needle density, which was found to be 785 +/- 13 kg.m$^{-3}$ for this needle stock (June) allowing the generalization of the relation for all needle stocks:

$$\rho_{FMC,OG,month} = 1.596\, FMC + \rho_{dry,OG,month} \qquad \textbf{Eq. 7.1}$$

In order to verify that this relation is true for needles at all seasons, unconditioned needle density was measured. The measurement results for OG needles are shown in Fig. D2.2 (red markers with color coded dashed lines for each stock). Some variability

exists, but it doesn't seem to follow any particular seasonal trend. Therefore, the variability is attributed to the measuring technique.

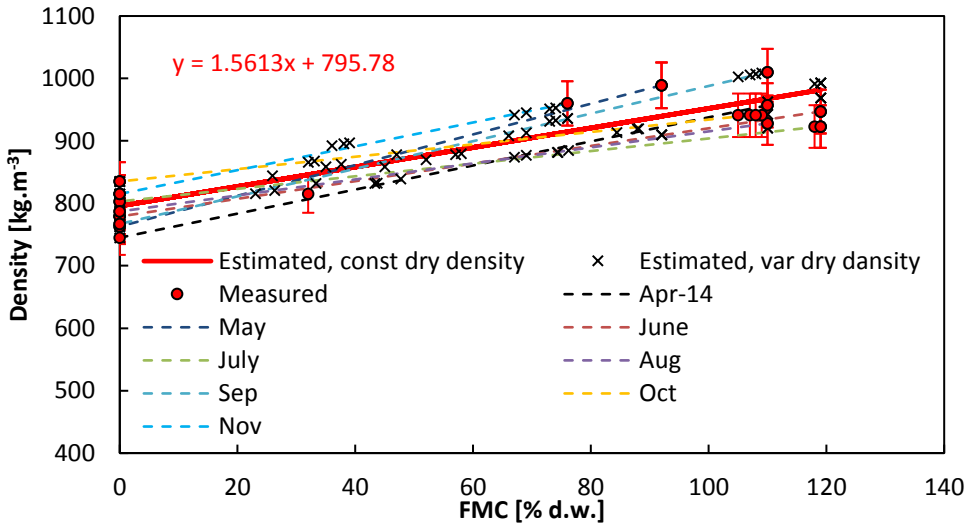


**Fig. D2.2. Density of OG needles with respect to *FMC*. Dashed lines are the correlations for each needle stock. Estimation with varying dry density refers to Eq. 7.1 and estimation with constant dry density, the simplified correlation, refers to Eq. 7.2.**

Applying the above correlation (Eq. 7.1) to individual needle stocks shows that it is acceptable to use, because the calculated values (x-marker) fall in the variability of the measured values. The thick red line in this graph is a global linear regression fit for all estimations of the density with each needle stock's dry density. This is very similar to the relationship that was initially found for needles collected in June (Eq. 7.1). For all OG needles a mean dry density of 787 +/- 38 kg.m$^{-3}$ was found (Table. D2.1.). Thus the needle density can be estimated from

$$\rho_{FMC,OG,all} = 1.6\, FMC + \rho_{dry,OG,all} \qquad \textbf{Eq. 7.2}$$

This relationship is shown in Fig. D2.3., with a 5% uncertainty. Since most measurements fall within the error bars, it is concluded, that such a model can be used to accurately (within 5%) estimate the density of OG needles at a given *FMC*. This model is independent of seasonal variation which makes it a very useful tool.

Furthermore, it illustrates that, for OG needles the influence of chemical variation on the density is small compared to the influence of water content.

Table. D2.1. Mean densities for oven dried OG and NG needles.

| | Density [kg.m$^{-3}$] | | St.dev. [%] |
|---|---|---|---|
| | Mean | St.dev. | |
| OG, all | 787 | 38 | 4.8 |
| NG, all | 918 | 31 | 3.4 |
| NG, young | 966 | 35 | 3.6 |
| NG, mature | 798 | 23 | 2.8 |
| All, mature | 789 | 17 | 2.1 |

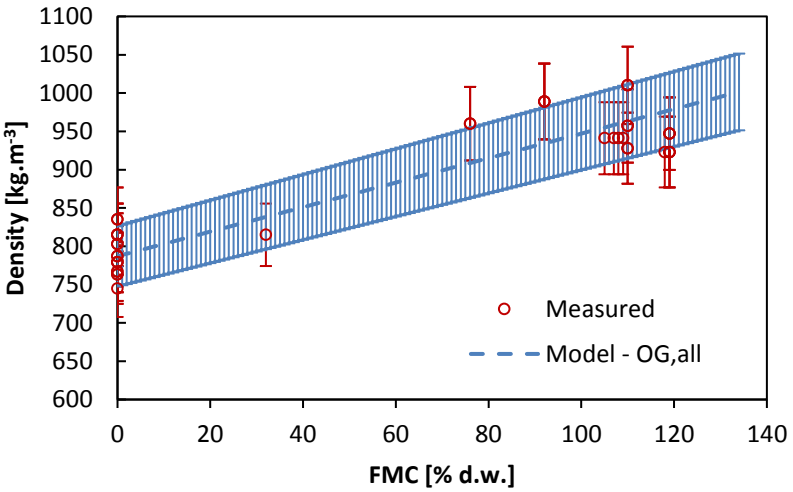


**Fig. D2.3. Global model prediction (Eq. 7.2) and measurement of OG needles with respect to FMC. Error bars indicate a 5% uncertainty.**

It describes that the density rise is governed by added water content of the needles. This compares to trends of (1) rising density of wood with increasing *FMC*, and (2) needle density at elevated FMC. Furthermore, it shows that seasonal variation in mature dry needle density is small compared to density variation due to water content and therefore will have a small influence on the combustion dynamics.

*NG needles*

The next step is to see if this model can be applied to NG needs as well. Density measurements of conditioned and unconditioned needles were collected and indicate a behavior dissimilar to OG needles (Fig. D2.4).

Densities of young NG needles (June – August) are essentially independent of *FMC*. In the final growth period (September) the density for dried needles is even higher than for wet needles. After the growth period (September), needles start to mature and the density-FMC relation becomes more like the one found for OG needles, i.e. dependent on the *FMC* (see November, December and April '15 measurements in Fig. D2.4.). For this reason the density-FMC relation is best described when separated into two groups: (1) growing/maturing period; and (2) fully matured period. These are indicated in Fig. D2.4. as the solid red and black linear regression lines, respectively. The model developed for OG needles (Eq. 7.2; also given in Fig. D2.4.) shows that it does not estimate the density of NG needles to an acceptable accuracy (using averaged density for all dry NG needles, see Table. D2.1.), for either young or mature needles.

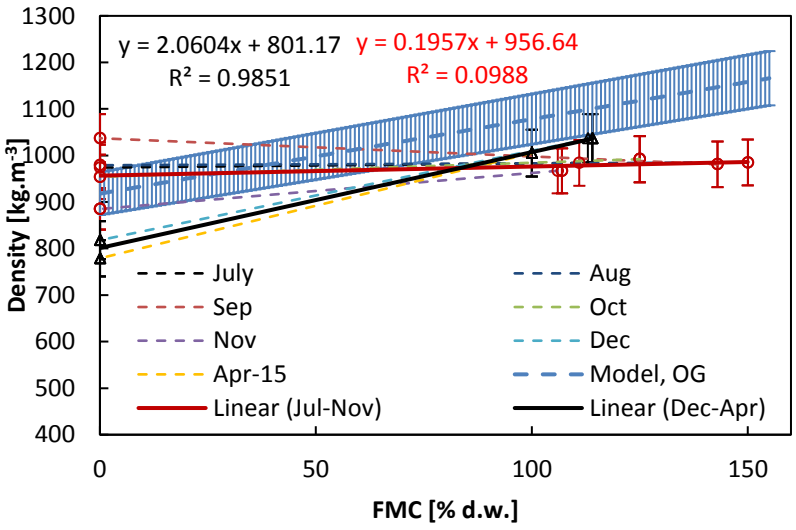


**Fig. D2.4. Measured and estimated densities of NG needles with respect to FMC. Dashed lines indicate the trend for each needle stock. The solid red line is the common trend for NG during growth and maturing period. Solid black line is the common trend of fully mature NG needles. The model (Model, OG) is the one found in Eq. 7.2 with the global dry density of NG needles. Error bars indicate a 5% uncertainty.**

Excluding young NG needles from the analysis, due to their dissimilar behavior, shows that Eq. 7.2 becomes applicable for mature NG needles. Thus, it can be concluded that the model

$$\rho_{FMC,all,mature} = 1.6\, FMC + \rho_{dry,all,mature} \qquad \textbf{Eq. 7.3}$$

can be successfully used to predict the density of mature live wet needles independent of season (with 5% uncertainty). A comparison of measurements and Eq. 7.3 is given in Fig. D2.5.

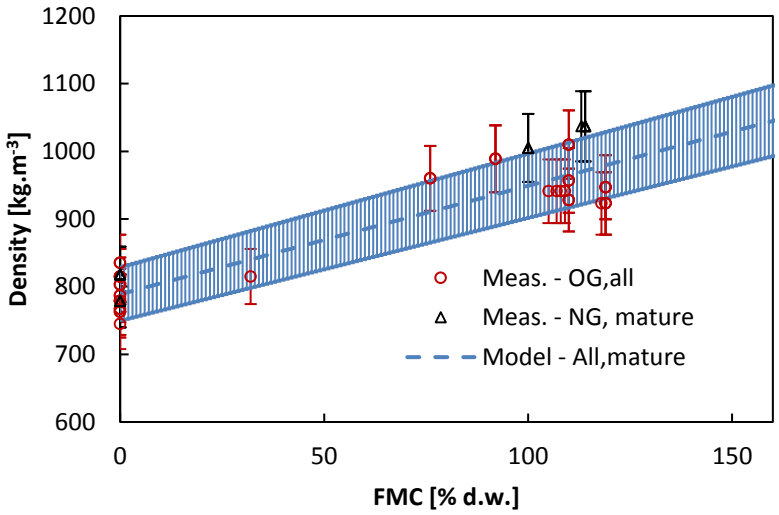


**Fig. D2.5. Comparison of measured density of mature PRI needles and estimated density (Eq. 7.3). Error bars indicate a 5% uncertainty.**

The relation between *FMC* and density is important to know and has significant implications. Particle density measurement of foliage can be obtained instantaneously and is inexpensive, whereas obtaining a *FMC* measurement requires time for conditioning and/or expensive equipment.

## Appendix D3 – Peak HRR versus *FMC* for NG needle (separated)

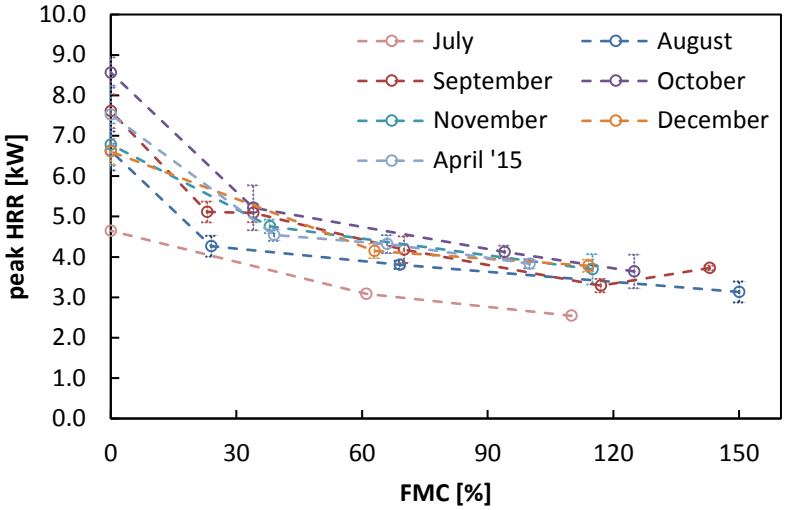


**Fig. D3.1. Peak HRR results for NG needles, separated by the month that they were collected in.**